Nonlinear Enhancement of Optical Spectroscopy in the Mid-infrared

Thesis by

Mingchen Liu

Caltech

In Partial Fulfillment of the Requirements for

the Degree of

Doctor of Philosophy

CALIFORNIA INSTITUTE OF TECHNOLOGY

Pasadena, California

2024

(Defended Jan 19, 2024)

© 2024

Mingchen Liu
ORCID: 0000-0002-0649-8976

ACKNOWLEDGEMENTS

This dissertation stands as a testament to the extraordinary support I have received, which has been pivotal in reaching this milestone in my life.

Foremost, I extend my profound gratitude to my advisor, Alireza Marandi. His decision to welcome me into this prestigious program has allowed me the privilege to collaborate with some of the brightest minds in the field. Alireza's extensive knowledge in optics and his acute judgement to experimental, simulation, and theoretical challenges have been invaluable to my growth. I fondly recall the late nights and early mornings spent with him near the optical table, meticulously aligning and optimizing a free-space OPO. His technical mentorship was crucial to my research, but it was his unwavering consideration, patience, and understanding—especially during challenging times such as the pandemic—that I value even more deeply. The lessons I have learned from him are immeasurable, and my gratitude is endless.

I am also very thankful to Professors Mitchio Okumura, Lihong Wang, and Changhuei Yang for their service as members of my graduate committee. They provided precious input to this thesis. A special acknowledgment to Professor Okumura for not only chairing the committee but also for inviting me to present at his group meeting, marking my first "invited talk".

I extend heartfelt appreciation to Robert Gray for his kindness, intelligence, humility, and tireless work ethic. His readiness to assist played a crucial role in the success of my thesis. Similarly, Arkadev Roy's profound knowledge and productivity have greatly influenced my research, and his sharp insights have been particularly enlightening.

My time at Caltech has been enriched by the camaraderie and intellectual exchange with my fellow Marandi group students, including Christian Leefmans, Luis Ledezma, Ryoto Sekine, Gordon Li, James Williams, and Selina Zhou, as well as our postdoctoral scholars Joong Hwan Bhang, Saman Jahani, Qiushi Guo, Midya Parto, Rajveer Nehra, Luis Costa, and Nicolas Englebert.

I am grateful to Dr. Cheng Shen (group of Professor Changhuei Yang), Dr. Zhiquan Yuan, and Dr. Lue Wu (group of Professor Kerry Vahala) for their generosity in lending equipment

that significantly advanced my experiments. A special note of appreciation goes to my roommate Dr. Cheng Shen, not just for his professional support, but for the invaluable assistance and guidance he has offered me in both my career and personal life.

I am equally grateful for the guidance and support I received prior to Caltech, which paved the way for my doctoral journey. My heartfelt appreciation goes to my undergraduate research advisor, Professor Jiahui Peng, and my summer research internship advisor, Professor Alexei Sokolov. Their invaluable mentorship was instrumental in securing my opportunity to pursue a PhD at Caltech. I also wish to express my gratitude to Professor Peifeng Chen, my course instructor, and Professor Zhengyan Li, my undergraduate thesis advisor, for their profound impact on my academic development. A special note of gratitude goes to my undergraduate roommates, Chang Xu and Wudi Zheng. Their excellence has been a constant source of inspiration, and our friendship, which began in China, has flourished across continents to North America.

Although limitations in space preclude the mention of every individual's name who has contributed to my journey, I earnestly thank all my educators, peers, and friends. Your collective support has profoundly influenced my path, leaving a lasting imprint for which I am eternally thankful.

I extend my deepest gratitude to my girlfriend, Yilin Luo, whose unwavering support have been the bedrock of my resilience throughout this journey. The life of a PhD student is often grueling and, at times, desperate. Yet, it is her companionship that have infused even the darkest days with color and meaning. Her love and steadfast support have been an indispensable anchor for me, providing solace and strength during the most challenging times.

Lastly, but most importantly, I owe an immeasurable debt of gratitude to my parents, Mr. Liu and Dr. Shi. Their unconditional love, care, and support have been my guiding lights. Words fall short in expressing my deep appreciation for their sacrifices and belief in my dreams.

ABSTRACT

Optical spectroscopy has long been a cornerstone in studying material properties, playing a pivotal role in the advancement of science and technology. It remains crucial in both research and industry, particularly in the mid-infrared (MIR) region, known for its unique molecular fingerprint capabilities. The emergence of optical frequency comb technology has set the stage for dual-comb spectroscopy (DCS) to revolutionize optical spectroscopy with its potential superiority in speed, resolution, sensitivity, precision, and compactness. However, practical implementation of DCS in the MIR region faces challenges due to its demanding requirements for sources, inefficient photodetection, and dynamic range limitations, despite an exciting prospect.

This dissertation explores the use of quadratic optical nonlinearity to tackle these challenges. By manipulating energy and information flows between photons of different frequencies through nonlinear optics, we leverage well-developed near-infrared (NIR) sources, detectors, and optics to address difficulties in the MIR region. We first demonstrate optical parametric oscillators in the regime of simulton (quadratic soliton pair), achieving a high-power broadband MIR frequency comb with a remarkably high NIR-to-MIR power conversion efficiency. We also introduce cross-comb spectroscopy (CCS), which upconverts the MIR frequency comb to the NIR region and allows MIR spectral analysis with NIR photodetection. This novel approach can offer superior signal-to-noise ratio (SNR), dynamic range, and detection efficiency compared to conventional DCS, while providing wavelength flexibility. Additionally, we present a new method to facilitate the detection of trace samples with short-pulse optical parametric amplifiers, which can significantly enhance SNR and limit of detection of existing methods.

Overall, this research demonstrates the capabilities of quadratic nonlinearity in enabling high-performance optical sensing in spectral regions where sources, detectors, and optics are less developed.

PUBLISHED CONTENT AND CONTRIBUTIONS

[1] **M. Liu**, R. M. Gray, A. Roy, K. A. Ingold, E. Sorokin, I. Sorokina, P. G. Schunemann, and A. Marandi, "High-Power Mid-IR Few-Cycle Frequency Comb from Quadratic Solitons in an Optical Parametric Oscillator," Laser Photonics Rev (2022), 16, 2200453.
DOI: https://doi.org/10.1002/lpor.202200453
M. Liu contributed to the conception of the project, built the setup, performed the measurements, analyzed the results, conducted theoretical analysis, participated in numerical simulation, and led the writing of the manuscript.

[2] **M. Liu**, R. M. Gray, A. Roy, C. R. Markus, and A. Marandi, "Mid-Infrared Cross-Comb Spectroscopy," Nature Communications 14.1 (2023): 1044.
DOI: https://doi.org/10.1038/s41467-023-36811-7
M. Liu led the conception of the project, designed the experiment, built the setup, performed the measurements, analyzed the results, conducted theoretical analysis and numerical simulation, and led the writing of the manuscript.

[3] **M. Liu**, R. M. Gray, A. Roy, L. Ledezma, and A. Marandi, "Optical-Parametric-Amplification-Enhanced Background-Free Spectroscopy," arXiv preprint arXiv: 2401.01016 (2024).
DOI: https://doi.org/10.48550/arXiv.2401.01016
M. Liu conceived the project, conducted theoretical analysis and numerical simulation, analyzed the results, and led the writing of the manuscript.

[4] **M. Liu**, R. M. Gray, A. Roy, K. A. Ingold, E. Sorokin, I. Sorokina, P. G. Schunemann, and A. Marandi, "Quadratic Soliton Frequency Comb at 4 µm from an OP-GaP-based Optical Parametric Oscillator," in Conference on Lasers and Electro-Optics (2020), p. SF3R.4.
DOI: https://doi.org/10.1364/CLEO_SI.2020.SF3R.4
M. Liu contributed to the conception of the project, built the setup, performed the measurements, analyzed the results, conducted theoretical analysis, participated in numerical simulation, and led the writing of the manuscript.

[5] **M. Liu**, R. M. Gray, A. Roy, K. A. Ingold, E. Sorokin, I. Sorokina, P. G. Schunemann, and A. Marandi, "0.5-W Few-Cycle Frequency Comb at 4 µm from an Efficient Simulton-based Optical Parametric Oscillator," in Conference on Lasers and Electro-Optics (2021), p. STh1L.3.
DOI: https://doi.org/10.1364/CLEO_SI.2021.STh1L.3
M. Liu contributed to the conception of the project, built the setup, performed the measurements, analyzed the results, conducted theoretical analysis, participated in numerical simulation, and led the writing of the manuscript.

[6] **M. Liu**, R. M. Gray, A. Roy, and A. Marandi, "Mid-Infrared Cross-Comb Spectroscopy using Sum-Frequency Sampling," in Conference on Lasers and Electro-Optics (2021), p. SM3A.4.

DOI: https://doi.org/10.1364/CLEO_SI.2021.SM3A.4
M. Liu led the conception of the project, performed the CCS measurements, analyzed the results, conducted theoretical analysis and numerical simulation, and led the writing of the manuscript.

[7] **M. Liu**, R. M. Gray, A. Roy, and A. Marandi, "Cross-Comb Spectroscopy using Sum-Frequency Sampling in the Mid-IR," in Optical Sensors and Sensing Congress (2021), p. JTu4D.5.
DOI: https://doi.org/10.1364/AIS.2021.JTu4D.5
M. Liu led the conception of the project, performed the CCS measurements, analyzed the results, conducted theoretical analysis and numerical simulation, and led the writing of the manuscript.

TABLE OF CONTENTS

LIST OF ILLUSTRATIONS AND/OR TABLES

NOMENCLATURE

BFS. Background-free spectroscopy.

CCD. Charge-Coupled Device.

CCS. Cross-comb spectroscopy.

CMOS. Complementary Metal Oxide Semiconductor.

CEO. Carrier-envelope offset.

CEP. Carrier–envelope phase

CW. Continuous wave.

DAS. Direct absorption spectroscopy.

DCS. Dual-comb spectroscopy.

DFG. Difference frequency generation.

DN. Detector noise.

DR. Dynamic range.

FC. Frequency comb (OFC, optical frequency comb).

FID. Free-induction decay.

FTIR. Fourier transform infrared spectroscopy.

FOM. Figure of merit.

FSR. Free-spectral range.

FTS. Fourier transform spectrometer/spectroscopy.

FWHM. Full-width at half-maximum.

FWM. Four-wave mixing; $\chi(3)$ interaction.

GDD. Group Delay Dispersion.

GVD. Group velocity dispersion.

GVM. Group velocity mismatch.

IR. Infrared.

LOD. Limit of detection.

MCT. Mercury cadmium telluride (HgCdTe).

MDC. minimum detectable concentration.

MIR. (Mid-IR). Mid-infrared.

NEP. Noise equivalent power.

NIR. (Near-IR). Near-infrared.

OFC. Optical frequency comb

OPA. Optical parametric amplification/amplifier.

OPD. Optical path difference.

OPG. Optical parametric generation/generator.

OPO. Optical parametric oscillation/oscillator.

OSA. Optical spectrum analyzer.

PPLN. Periodically poled lithium niobate.

QCL. Quantum cascade lasers.

QPM. Quasi phase-matching.

REP. Repetition rate.

RF. Radio frequency.

RIN. Relative intensity noise.

SCG. Supercontinuum generation.

SFG. Sum frequency generation.

SHG. Second harmonic generation.

SN. Shot noise.

SNR. Signal to Noise Ratio.

SOA. Semiconductor optical amplifier.

TFLN. Thin-film lithium niobate.

TOD. Third Order Dispersion.

TWM. Three-wave mixing; $\chi(2)$ interaction.

C h a p t e r   1

INTRODUCTION

1.1. Optical spectroscopy

Advances in science and technology are always driven by a deeper understanding of the basic properties of matter, and such an understanding is invariably facilitated by improved measurement techniques. Optical spectroscopy stands as a foundational tool for examining the physical, chemical, and structural properties of materials, playing a pivotal role in the evolution of modern science. In 1670, Newton dispersed sunlight into a spectrum of colors using a prism [1], marking the inception of the history of optical spectroscopy. This discovery is considered a key moment that opened the door to modern optics.

Nevertheless, the practical optical spectrometer was not constructed until the early nineteenth century. Joseph Fraunhofer built the first one based on gratings, through which he discovered fixed dark lines in the solar spectrum [2], known as Fraunhofer lines, around 1814. By comparing the measurements between the sun and the other stars, he concluded that these lines originate in the nature of the celestial bodies themselves which carry signature to each. This study opened the area of astronomical spectroscopy, a crucial tool for modern astronomy.

This spectroscopy study has even more profound implications. About 45 years later, Kirchhoff and Bunsen noticed that several Fraunhofer lines coincide with characteristic emission lines identified in the spectra of heated elements, and people began to realize that those bright or dark lines are related to atoms of different elements. One such element is hydrogen, the simplest yet vital. In the early twentieth century, the development of optical spectrometers led to the discovery of different spectral series of hydrogen. These spectral measurements provide the first direct experimental evidence for Bohr's model, the foundation of quantum theory, whose significance to modern science cannot be overstated.

 Nowadays, optical spectroscopy continues to serve as a workhorse in different fields of research and industry, spanning from laboratories in physics, chemistry, and biology to factories in food, pharmaceuticals, and semiconductors. For example, at Caltech, optical

spectrometers are not only found in labs specifically focused on optics but also in physics, astronomy, chemistry, biology, mineralogy, and geology labs—virtually anywhere people need to study or identify materials. Moreover, spectrometers are not confined to Earth; they are also extensively employed in space. For example, the James Webb Space Telescope is equipped with multiple optical spectrometers, covering a range from visible to mid-infrared wavelengths.

In the future, we expect optical spectroscopy to continue enabling scientific breakthroughs, much like it has done in the past. However, compared to hundreds of years ago, today's demands on optical spectroscopy are much greater in terms of resolution and speed to push the limits of science and technology even further. In the time domain, transient events in various fields can occur at durations much smaller than 1 second. In fact, the era of pico-second (ps, 10^{-12} s) and femto-second (fs, 10^{-15} s), or even atto-second (as, 10^{-18} s), began decades ago, as reflected by the Nobel Prize in chemistry in 1999 for femtosecond spectroscopy and the Nobel Prize in Physics in 2023 for attosecond pulses. In the frequency domain, typical molecular fingerprint absorption has a width around 1 GHz at atmospheric pressure, which can be much narrower under lower pressure. For measurements of fine structure or Doppler-free spectra, a resolution around 10 MHz or even smaller may be required. All of these can pose significant challenges for existing methods of optical spectroscopy.

Therefore, the question arises: can traditional optical spectroscopy handle these challenges? If not, why, and what limits them? Moreover, if there is any new technique that can overcome these limits and bring optical spectroscopy to the next level? If yes, what are the new challenges along the way? To address these questions, the rest of this chapter will first provide a quick discussion about traditional optical spectrometers and their limitations. It will then introduce optical frequency comb and dual-comb spectroscopy. Following that, I will summarize some challenges of this new technique despite its great potential, and explain how we use the weapon of nonlinear optics to tackle them, which is the key thread of this dissertation.

1.2. Traditional optical spectrometers

| Optical Source | Sample | Spectrometer | Detector |
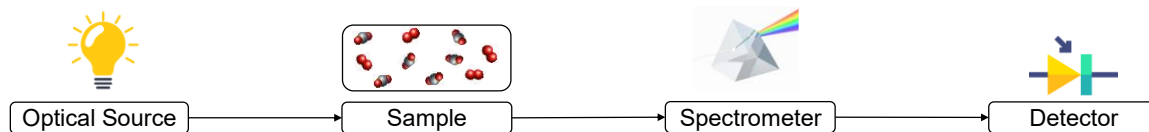
Figure 1.1: **Typical structure of an optical spectroscopy system.**

Generally, an optical spectroscopy system comprises four parts: an optical source, samples (if applicable), a spectrometer and a detector, as shown in Figure 1.1. While all parts are important, the spectrometer is the core of the system, which resolves the optical wavelength (frequency). Traditional optical spectrometers can be classified into two categories: those based on dispersion by diffraction gratings and those using interferometers and Fourier transform. The latter type is commonly known as Fourier transform spectrometer/spectroscopy (FTS) or Fourier transform infrared (FTIR) spectroscopy. Figure 1.2 provides a simple comparison of their typical best performance, preferred wavelength range, and structure illustrations. In grating spectrometers, one or more gratings are usually mounted on a rotational stage. Light at different wavelength is directed to an exit slit and detected as the stage rotates to different angles. In interferometers, one mirror is mounted on a translation stage and scanned to generated interference patterns ('interferogram') as a function of optical path difference. Although these two types of spectrometers work quite differently and have disparate components, they share a common reliance on mechanical movement.

(a)

	Diffraction Grating	Interferometer (FTIR)
Typical best resolution	~ 10 GHz	~ 3 GHz
Typical acquisition time at best res	> 10 s	> 10 s
Popular wavelength range	Visible and Near-IR	Mid-IR

(b)
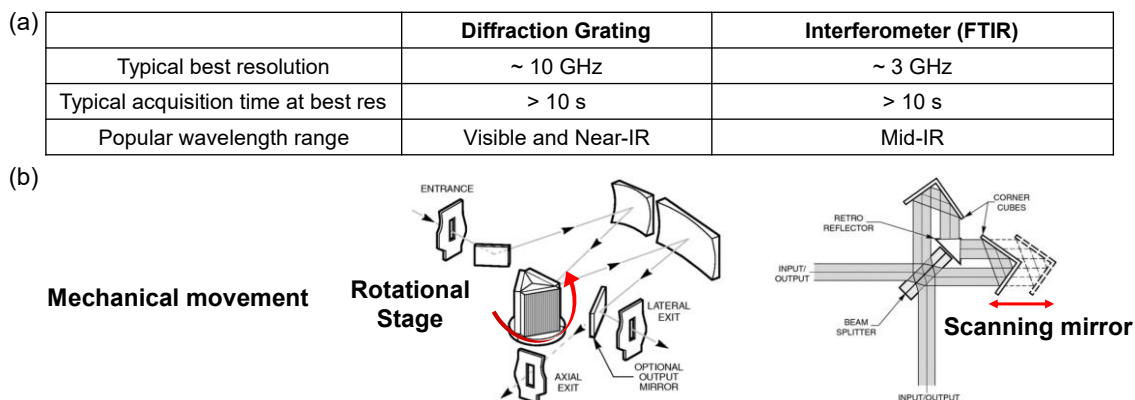
Figure 1.2: **Traditional MIR optical spectrometers.** **a** Comparison of typical parameters. **b** Structure illustrations of grating-based spectrometer (left) and FTS (right). Photo credits:

Cornerstone 260 Monochromator and MIR8035 modular FT-IR spectrometers series, Oriel® Instrument, a Newport Corporation Brand.

In real-life optics, mechanical movement is almost always unpleasant to manage. First, it is slow. At least centimeter-level displacement is required to make a meaningful rotation or translation for spectroscopy, which takes time on the order of second. Second, it adds to complexities and difficulties in optical alignments and system maintenance. Generally, except for the optical path length or angles, we want to keep everything else of the system, especially the optical alignment, consistent during the mechanical scans to generate a clean spectrum or interferogram. Unfortunately, achieving this strictly in practice is impossible, and people have to take additional measures to compensate and calibrate imperfections. Moreover, the mechanical parts often occupy significant space, whose size is challenging to decrease.

In contrast to the 'awkwardness' of the mechanical part, the optical and electrical parts of the spectrometer can be much 'smarter.' Generating optical or electrical signals with a repetition rate of MHz or even GHz is not challenging these days, and they can operate stably without requiring cumbersome control or periodic calibration/maintenance. Furthermore, substantial progress has been made in miniaturizing them, so their physical size can be or has already been well reduced. Comparatively, when we assess the mechanical part alongside the optical or electrical part, it becomes evident that mechanical movement imposes bottlenecks on the entire spectrometer system in many aspects, including resolution, speed, complexity, stability, and footprint.

While a comprehensive analysis and comparison of these two types of spectrometers is important and useful, it can be extensive and involved, which has been done nicely in some excellent references [3,4]. Therefore, a systematic expansion on this topic is not the goal here and beyond the scope of this thesis. Instead, I will delve further into FTS, driven by two reasons. First, FTS is more directly dependent on and limited by mechanical movement. Second, it holds dominance in the mid-infrared wavelength range (MIR, ~2-20 µm) due to its superior signal-to-noise ratio (SNR) and resolution compared to the other type. The MIR range, often referred to as "molecular fingerprint region," plays a vital role in detection,

identification, and quantification of molecules, featuring fundamental rotational-vibrational transitions that are much stronger than elsewhere. Hence, it is of particular interest in optical spectroscopy, which aligns with the main focus of this thesis. In the MIR, FTS stands out as the best among traditional techniques, and further discussion about FTS can explicitly show the fundamental limitations of conventional optical spectrometers.

Building on these motivations, we now continue to a more detailed discussion of FTS. The basic physics behind FTS is not intricate. It essentially follows the Wiener-Khinchin Theorem (or the more general cross-correlation theorem), stating that the power spectral density (spectral intensity) of the optical field is equal to the Fourier transform of the autocorrelation of the field, up to some constants. Naturally, the optical frequency resolution of the system is inversely proportional to the maximal optical path difference (OPD) that can be scanned. This relationship mirrors the basic connection between the time domain and the frequency domain taught in signal and system classes. For example, a 1-cm OPD leads to a resolution of 1-cm^{-1} (30 GHz). This figure happens to be close to what a typical bench-top commercial FTIR system can offer, which may require a room of ~0.3 m^3 and cost around 10k USD. Besides, typical speed of the translation stage is on the order of 1 cm/s, resulting in one complete scanning taking about a few seconds for spectrum acquisition at a 1-cm^{-1} resolution. These values are fine for routine measurements, where obtaining rough spectral information at a slow rate is acceptable. However, something much finer and faster is required to be able to continue pushing back the frontiers of science, as discussed previously.

One can always increase the OPD (the length of the delay line) to achieve higher resolution. Decent progress has been made and a resolution up to ~30 MHz (10^{-3} cm^{-1}) has been achieved [5]. Such a resolution marks the highest commercially available state-of-the-art FTIRs and is advertised as "the ultimate instrument for the high-resolution IR spectroscopy." Although it does provide an option for some research projects, its impact is limited in more scenarios. Firstly, the price of a 30-MHz resolution is an OPD as long as 10 meters. The entire system can occupy a large room and cost more than 700k USD. Such a long delay line requires different measures to achieve clean scanning, with additional

strict requirements on environment, calibration, and maintenance. This prevents its usage in more research labs, let alone industries. Second, and more fundamentally, it does not effectively improve the trade-off between resolution and speed, despite the engineering excellence. It takes at least 400 s to acquire one interferogram (for the highest resolution), limited by the mirror speed in the same way as old systems. Moreover, one interferogram generally does not provide enough SNR, and people usually need to average multiple ones in practice. For instance, 100 interferograms will take this system about half a day (4×10^4 s ≈ 11 h)! This prohibits the superior resolution from being utilized on most dynamic processes. In short, this 'ultimate' FTS is limited to just a small number of laboratories for static measurements.

Certainly, one can speed up the spectrometer by decreasing the OPD. However, that is just the other end of the trade-off. Let us say we want to obtain 100 interferograms in one second, then, the OPD needs to be decreased to 1/25 cm assuming a mirror speed of 2 cm/s. An OPD of 1/25 cm leads to a resolution of 25-cm^{-1} (0.75 THz). It cannot be denied that such a resolution can be useful in a few cases, but overall, it is too low for most of applications. For example, if we use this to detect CO_2 molecules in the air, you can only see a few discrete points on the absorption spectrum without enough signatures, which can hardly help you to identify it. Although a shorter OPD makes the engineering of the system easier, unlike the case of longer OPD, the return of it is limited and even undesired. In brief, we want higher speed without compromising resolution, which is barely possible with the traditional FTS.

While I explain that FTS is fundamentally limited by the mechanical movement, one may argue that grating spectrometers may not have to rely on it. It is true, thanks to the techniques of CCD (Charge-Coupled Device) and CMOS (Complementary Metal Oxide Semiconductor), but only in the visible and part of the near-infrared (NIR) range (~400-1000 nm) where these sensors work. Outside of this range, at least for now, there are no practical detector arrays as good as them. Unfortunately, 400-1000 nm is just a small fraction of the optical spectrum, and many crucial applications of optical spectroscopy lie beyond it, such as the aforementioned molecular fingerprint region (MIR). Moreover, even

within the favorable region of CCD and CMOS, although the speed of spectrometers can be boosted, their resolution is still limited by the geometry of the system and the detector array, which does not exceed what FTS can provide. Hence, our argument about the fundamental limitation of traditional optical spectrometers holds for most cases, despite some exceptions in a limited bandwidth.

It seems that we are stuck in a trade-off caused by mechanical movement. Shifting within this trade-off can demand considerable effort but may not yield sufficient rewards. In essence, we desire simultaneously better resolution and higher speed, as well as a smaller footprint and lower price, if possible. To this end, we must break from these limitations, with the help of something fundamentally different to eliminate the need for mechanical movement.

But how? Here comes a revolutionary technique, the optical frequency comb.

1.3. Optical frequency comb

Optical frequency combs (OFC or FC) were experimentally demonstrated in the late 1990s, thanks to the development of low-noise mode-locked lasers and the precision control of phase and frequency of the generated optical pulses [6–8]. Over the past three decades, they have found a multitude of applications, including but not limited to spectroscopy [9], length metrology [10], LIDAR [11], optical clockwork [12], telecommunications [13], attoscience [14], astronomy [15], and remote sensing [16]. Among them, high-precision sensing, especially high-precision spectroscopy that we are most interested in for this thesis, is one of the most representative fields that OFC has been revolutionizing. Notably, half of the Nobel Prize in Physics 2005 was shared by John L. Hall and Theodor W. Hänsch, for their contributions to the development of laser-based precision spectroscopy, including the optical frequency comb techniques.
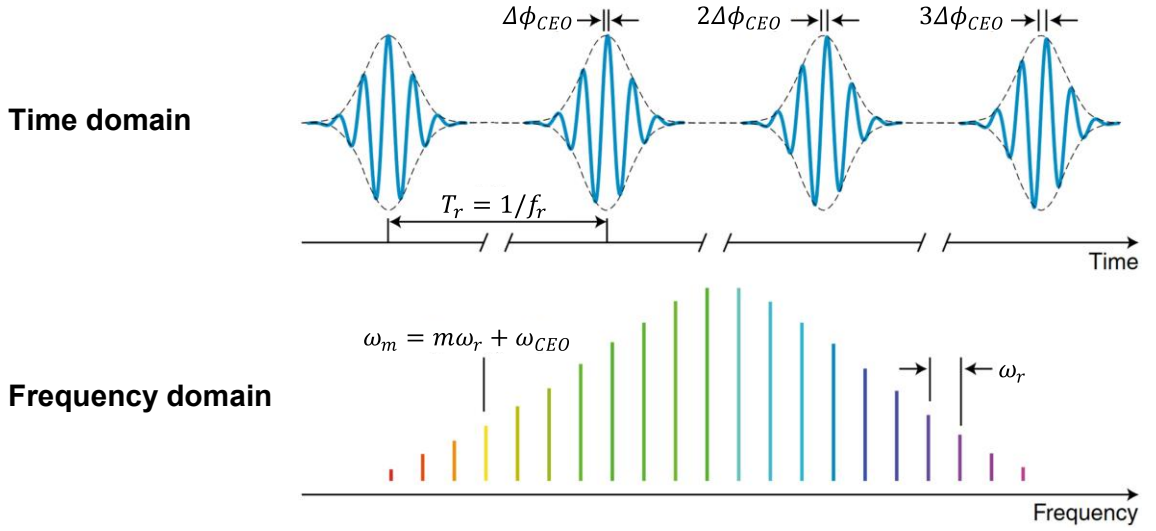
Figure 1.3: **Diagram of a frequency comb in the time and frequency domains.**

The theory of OFC is rather straightforward, and we generally describe it in both the time domain and the frequency domain, as illustrated in Figure 1.3. In the time domain, it is just a series of short optical pulses with a constant repetition period (T_r):

$$e(t) = \sum_{m=-\infty}^{m=+\infty} a(t - mT_r) \exp(im\Delta\phi_{CEO}) \exp(i\omega_0 t). \tag{1.1}$$

Ideally, every pulse shares the same temporal envelope, $a(t)$, the width of which is generally in the range of fs to ps. While the shape of the envelop is expected to strictly remain the same, there can be a non-zero but stable shift of the relative phase between the carrier and the envelop from pulse to pulse. The relative phase is defined as the carrier-envelope offset (CEO) phase (ϕ_{CEO}) or sometimes called the carrier–envelope phase (CEP), and the shift in it every period is denoted by $\Delta\phi_{CEO}$. ω_0 denotes the carrier frequency of the optical field, generally around the order of 100 THz (10^{14} Hz), which can also be understood as the center frequency of the spectrum.

In the frequency domain, an OFC is a set of individual lines with a constant spacing between each line, which can be described as:

$$E(\omega) = A(\omega - \omega_0) \sum_{m=-\infty}^{m=+\infty} \delta(\omega - \omega_{CEO} - m\omega_r). \qquad (1.2)$$

$A(\omega)$ denotes the spectral envelope, which is the Fourier transform of temporal envelope $a(t)$. The Dirac delta functions represent the series of frequencies extending beneath the spectral envelope, which resembles a comb and thus leads to the name of "frequency comb." Note that $E(\omega)$ is simply the Fourier transform of $e(t)$ up to constants, although they are not written strictly for the sake of clarity. The frequency of the mth comb lines is:

$$\omega_m = m\omega_r + \omega_{CEO}. \qquad (1.3)$$

ω_r and ω_{CEO} denote the repetition rate (frequency) and the carrier-envelope offset frequency of the OFC, respectively. They are related to their corresponding temporal parameters by:

$$\omega_r = \frac{2\pi}{T_r} \qquad (1.4)$$

$$\omega_{CEO} = \frac{\Delta\phi_{CEO}}{T_r}. \qquad (1.5)$$

Here we use angular frequency ω in rad/s, but ordinary frequency f in Hz is also often used. They are simply related by a factor of 2π: $\omega_{r\ or\ ceo} = 2\pi f_{r\ or\ ceo}$. f_r is generally in the range of 10 MHz to 10 GHz, so T_r is generally in the range of 100 ns to 100 ps). In principle, f_{ceo} can be any value, but we restrict it to be non-negative and smaller than f_r as it is defined as an "offset frequency."

Although these properties of OFC look simple, they have profound implications. Accurate measurements of optical frequency used to be quite challenging because we lacked accurate wavemeter or oscilloscope at such high frequencies (10^{14} Hz). However, in the context of frequency comb, once you know two parameters, f_r and f_{ceo}, accurately, in principle you can know frequencies of all comb lines with the same accuracy. As mentioned, f_r and f_{ceo} generally fall in the category of radio frequency (RF), for which accurate measurement and control are readily available. Therefore, OFC bridges the gap between the RF domain and the optical domain, allowing for the transfer of much more

mature capabilities from the former to the latter. This is one of the fundamental reasons why OFC paves the way for high-precision metrology, including optical spectroscopy.

The properties of OFC may seem very appealing. However, how exactly can they be helpful? If we put it back into the context of Fig. 1, it just acts as an optical source, albeit a nice one, after which we still need a spectrometer to resolve its wavelength to provide spectra. If we continue using traditional spectrometers, we will still be faced with the dilemma of the mechanical movement. It is true that employing just one set of OFC as the source will not significantly improve the situation in spite of some benefits. However, if we can add one more set of OFC to play the role of a spectrometer, an incredible difference can be made. This technique is called dual-comb spectroscopy.

1.4. Dual-comb spectroscopy

Dual-comb spectroscopy (DCS) was first experimentally demonstrated in the optical domain around the early 2000s following the invention of frequency combs [16–18]. The concept of DCS is illustrated in Figure 1.4. Two combs are almost identical except a slightly shifted repetition rates, the difference of which is denoted by δf_{rep} and generally ranges from ~100 Hz to ~100 kHz. The second comb can be combined with the first one either before they are transmitted through the sample together, or after the first comb is transmitted through the sample alone, and then they are interfered on a photodetector directly. Just similar to OFC, the physics underlying the detection is not complicated and can be described in two domains.
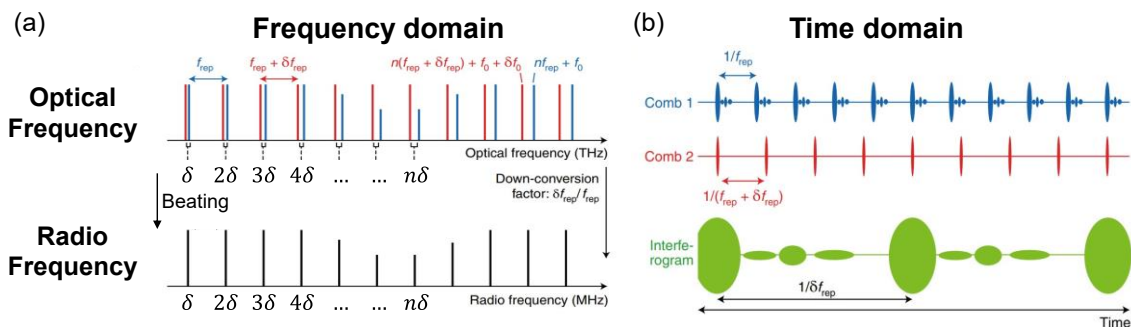
Figure 1.4: **Illustration of dual-comb spectroscopy. a** time domain. **b** frequency domain. This figure is adapted from ref. [9].

In the frequency domain, each pair of the comb teeth will generate a beat note as a result of heterodyne interference, and the frequencies of those beat notes can be unique and increase with a step of δf_{rep}. Interestingly, the beat notes can be also regarded as a "frequency comb" with a "repetition rate" (frequency spacing) of δf_{rep}. Unlike the original optical combs, the RF comb can be directly detected by a photodetector as its frequencies are in the RF domain. In other words, the "RF frequency comb" is a down-converted mapping of the optical frequency combs that can be easily accessible by RF electronics. One can obtain the response of the sample, the target of interest in most scenarios, by comparing the RF comb when the sample is present or absent in the optical path.

The picture of the time domain is nothing fundamentally different from traditional FTS. One pulse is scanned through the other to generate an interferogram, the Fourier transform of which is the power spectrum of the optical field. However, the biggest and most important difference is that the scan of the temporal delay (OPD), is "automatically" achieved as a result of the repetition rate difference, which does not require any mechanical part at all! This is one of the fundamental reasons, and perhaps the most important one, why DCS can significantly outperform conventional spectrometers.

As quite a few paragraphs have been spent on complaining how mechanical movement impedes traditional methods, now it is much easier to explain how DCS is superior. First of all, the speed can be improved by many orders of magnitude. Let us reuse the aforementioned example of the best state-of-the-art FTIR, which takes > 400 s to acquire one spectrum with a resolution of 30 MHz. In contrast, for a recently demonstrated interleaved DCS system, it can acquire one spectrum with a resolution of 20 MHz in only 36 ms, faster by a factor of 10^4! The speed of DCS is more of a free choice of a parameter that needs to be balanced between the detection bandwidth, instead of something strictly dictated by the speed of translation stage. Second, the maximal OPD can be greatly extended without difficulties from long delay lines, which is now only limited by the nature of frequency combs. In principle, the interleaved DCS can realize a frequency resolution limited only by the absolute comb-tooth linewidth, which can be ~kHz or even lower. This level of optical resolution is practically inaccessible with traditional methods. Moreover,

the footprint and price can also be significantly decreased, which now are only limited by the optical sources and electronics. Although there is still a long way towards fully-integrated and cheap DCS systems, good progress has been made.

More details about DCS can be found in later chapters where it is compared to cross-comb spectroscopy. Nevertheless, a complete discussion about its theory, performance, advantages, implementations, and applications can be another ten theses and is out of the scope of this one. There are multiple excellent reviews [9,19,20], though this technique is still evolving fast.

In short, DCS is a promising and powerful tool that has started a revolution in traditional optical metrology. Although DCS is still under active research and in the early stage of the development, it has already started to play a role in the real world besides excellent lab demonstrations. For example, some data of the HITRAN database is now from DCS, which was worse or even unavailable with traditional methods. There are also some startups featuring the applications of DCS in chemistry research, environment monitoring and gas leakage detection.

It looks like we have got what we need to substitute for traditional methods to keep pushing the boundary of optical spectroscopy and subsequently related science and technology. In theory, DCS is expected to be capable of much more than just those aspects above and promises more significant impacts. However, at this stage, its full potential is yet to be realized and there are still many practical challenges that prevent fulfillments of most of its capability. In consequence, DCS is still not superior to their traditional counterparts in terms of availability, flexibility, bandwidth, SNR, and efficiency, in many important scenarios, especially in the MIR region. However, the principle spectral region of interest for molecular spectroscopy is at wavelengths greater than 3 μm, though DCS does have applications in the near-IR and visible regions. In the next section, we will first restate the importance of MIR domain and then discuss some of those practical challenges encountered there. Afterwards, we introduce how we are going to tackle them, in order to fully unlock the potential of DCS.

1.5. Motivations and challenges of mid-IR dual-comb spectroscopy

Let us revisit the motivation of optical spectroscopy and explain why we care so much about the MIR region. The most basic function of optical spectroscopy is to measure the spectrum of a certain light source itself, e.g., sunlight. In this sense, different wavelength ranges are of presumably similar importance, as every wavelength can be a target of interest. However, more often, we use optical spectroscopy to detect, identify or study the properties of a certain sample or material, in which the optical source is a tool instead of the goal. For such purposes, particularly the detection and identification of trace samples, we naturally want to work in the wavelength region where samples exhibit their strongest characteristic responses, typically absorption or emission. Most molecules, especially gaseous ones, have their strongest absorption cross-sections in the MIR region. If we describe the vibrational transitions of molecules as imperfect harmonic oscillators, the fundamental frequencies usually lie in the MIR range, which are at least two orders of magnitude higher than their overtones (higher orders or sum frequencies, usually in the NIR or visible range) [21]. For example, the absorption intensity of CO_2 around 4.3 µm is stronger than that around 1.96 µm by a factor of 10^4. In fact, many applications heavily rely on MIR spectroscopy for the identification and quantification of trace biomarkers, toxic vapors, or pollutants. For instance, environmental monitoring [22], medical breath analysis [23], and isotopologues measurements [24]. In addition, MIR spectroscopy also plays an important role in atmospheric sensing [25] and communication [26] because it contains two transparent windows of the Earth's atmosphere (3-5 µm and 8-13 µm).

From those crucial motivations and unprecedented potential of DCS, we can see an exciting prospect of employing DCS in the MIR region. However, MIR DCS still remains limited and challenging, lacking either SNR and dynamic range, or wavelength flexibility and energy efficiency. To summarize those challenges, let us revisit Fig. 1.

The first challenge is the optical source, lasing in MIR [27]. In contrast to the fundamental molecular ro-vibrational bands in the MIR, wavelengths of most mature mode-locked lasers are in the NIR region. For example, Ti:sapphire (Ti:Al_2O_3) lasers around 800 nm, Ytterbium-doped (Yb:) fiber lasers around 1 µm, and Erbium-doped (Er:) fiber lasers

around 1.5 µm. To date, among relatively mature techniques, Cr:ZnS(Se) lasers are believed to have the longest direct lasing wavelength, around 2 µm. These mode-locked lasers are technically mature and commercially available that can generate decent frequency combs, but they do not provide direct access to the MIR region.

After the source and sample comes the spectrometer. In the context of DCS, the role of spectrometer is played by another set of frequency comb besides the source one. There are significant challenges in relating and synchronizing the two combs. However, these challenges are general to any wavelength range, and they are usually solved in the NIR domain and by special ways of MIR frequency comb generation. Hence, here they are not counted as additional challenge on top of the first one, MIR comb generation.

The last component is the detector, which constitutes the second challenge. MIR detectors generally have an order(s)-of-magnitude worse performance and order(s)-of-magnitude higher price compared to their NIR counterparts [28]. More seriously, the typical MIR detector, MCT (mercury cadmium telluride, HgCdTe), has a cut-off wavelength around 13 µm, making detection of longer wavelength even more challenging.

There is another challenge regarding the trace amount of the sample. Although it is not specific to DCS or MIR wavelength, it is usually more prominent as a result of less advanced sources and detectors in the MIR range. Many applications require the detection and analysis of samples at a concentration as low as parts-per-million (ppm, 10^{-6}) and parts-per-billion (ppb, 10^{-9}), or even lower. Such minute amounts of samples will apply a minimal change to the optical sources, which can be extremely challenging to discern from the strong background.

These challenges may seem somewhat unrelated. However, we tackle them with the same methodology, second-order (quadratic) optical nonlinearity, despite different specific nonlinear processes. Those solutions constitute a major part of this dissertation, which will be overviewed in the next section.

1.6. Overview of this dissertation

This thesis addresses some of the pressing challenges in mid-IR spectroscopy, particularly in dual-comb spectroscopy, through the employment of quadratic optical nonlinearity. Its structure is outlined in Figure 1.5.
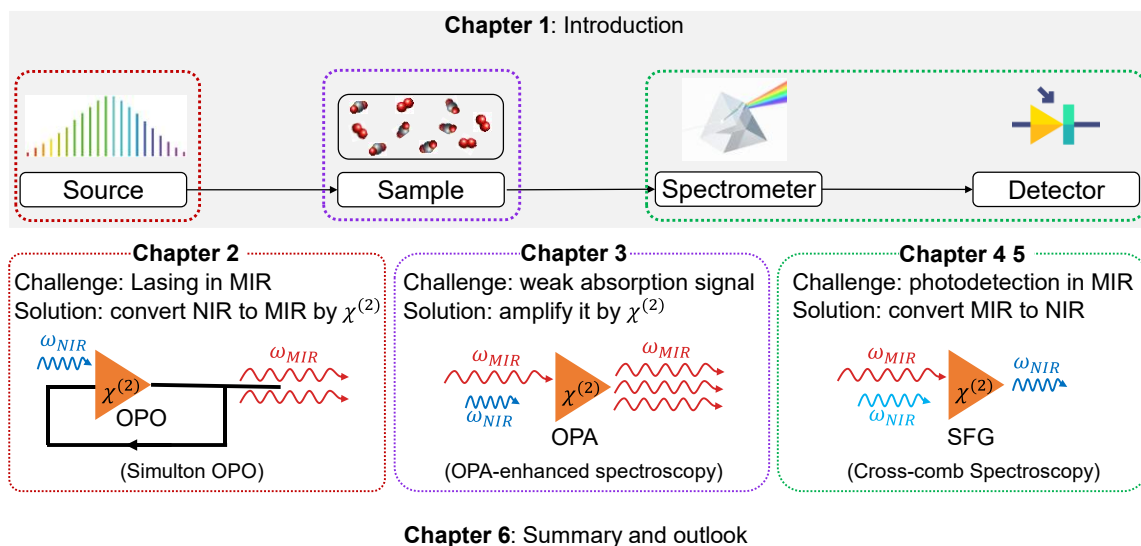
Figure 1.5: **Thesis structure diagram.**

The first chapter serves as an introduction, delineating motivations and challenges, and providing an overview of the solutions.

Chapter 2 presents a synchronously-pumped degenerate optical parametric oscillator (OPO) operating in the regime of simulton (quadratic soliton pairs). This approach addresses the first challenge: MIR frequency comb generation. As direct lasing in MIR is challenging, the standard approach to generate MIR frequency combs is parametric down-conversion of NIR frequency combs. Traditional methods, however, often fall short in terms of either power and efficiency or wavelength coverage. Our simulton-based OPO achieves a MIR frequency comb with a record high power and efficiency, as well as broad instantaneous bandwidth.

Chapter 3 proposes a new method to surmount the third challenge: detecting trace molecules. This approach starts with the suppression of the spectral background using a linear interferometer, followed by temporal-selective amplification of the faint molecular response through a short-pulse optical parametric amplifier. Theoretically and numerically,

this method is demonstrated to be able to enhance SNR and LOD (limit of detection) for broadband vibrational spectroscopy by order(s) of magnitude compared to existed methods.

Chapters 4-5 are dedicated to cross-comb spectroscopy (CCS), our innovative solution to the second challenge: MIR photodetection. If we can use optical nonlinearity to down-convert NIR photons to MIR photons, we can leverage optical nonlinearity again to up-convert the MIR photons back into NIR photons. This strategy allows us to take advantage of the NIR photodetectors to capture the information probed and carried by MIR photons. Beyond advantages in detection wavelength, CCS can also offer superior SNR and dynamic range compared to conventional DCS. Due to the complexity of introducing a new technique, this topic is divided into two chapters: the first focuses on general theories, while the second details our experimental implementation.

The last chapter concludes this thesis, summarizing the key findings and offering insights into future prospects for these endeavors.

C h a p t e r   2

HIGH-POWER MID-IR FEW-CYCLE FREQUENCY COMB FROM QUADRATIC SOLITONS IN AN OPTICAL PARAMETRIC OSCILLATOR

Powerful and efficient optical frequency combs in the mid-infrared (MIR) spectral region are highly desirable for a broad range of applications. Despite extensive efforts utilizing various techniques, MIR frequency comb sources are still lacking power, efficiency, or bandwidth for many applications. In this chapter, we discuss the generation of an intrinsically locked frequency comb source centered at 4.18 µm from an optical parametric oscillator (OPO) operating in the simulton regime, in which formation of purely quadratic solitons lead to enhanced performance. We show advantages of operation in the simulton regime in direct experimental comparisons to the conventional regime, which are also supported by simulation and theory. We achieve 565 mW of average power, 900 nm of instantaneous 3-dB bandwidth, 350% slope efficiency, and 44% conversion efficiency, a performance that is superior to previous OPO demonstrations and other sources in this wavelength range. This work opens a new avenue toward MIR frequency comb generation with high power and efficiency and suggests the great potential of soliton generation based on quadratic nonlinearity in the MIR spectral region.

2.1. Introduction

Optical frequency comb generation in the mid-infrared (MIR) spectral region (3-25 µm) has been a subject of intensive research over the past decades, driven by its numerous

applications ranging from precise sensing to fundamental science [27], of which notable examples are molecular spectroscopy [9,18], astronomical spectrograph calibration [29,30], and high-harmonic generation [31,32]. Referred to as the "molecular fingerprint region," the MIR portion of the electromagnetic spectrum contains strong rovibrational absorption features of many molecules, the detection of which is useful for a plethora of applications such as medicine, environmental science, agriculture, energy, and defense. In particular, the 3-5 µm band is of high interest as it contains strong absorptions of many important molecules, including greenhouse gases (e.g., carbon dioxide at ~4.2 µm, nitrous oxide at ~4.5 µm and methane at ~3.3 µm), species used in breath analysis (e.g., ethane at ~3.3 µm and carbon monoxide at ~4.7 µm) and major air pollutants (e.g., nitrogen dioxide at ~3.5 µm and sulfur dioxide at ~4 µm) [33,34]. Given its significance, it is highly desirable to produce frequency combs in this band with great power, efficiency, bandwidth, and stability.

The most widely used techniques to produce MIR frequency combs include difference frequency generation (DFG), optical parametric oscillators (OPO), quantum cascade lasers (QCL), microresonators, supercontinuum generation (SCG), and direct MIR lasing. DFG-based sources feature single-pass configuration and passive cancellation of the carrier-envelope offset frequency (f_{ceo}) [35–37] but are limited by their relatively low powers and efficiencies. QCLs have been demonstrated to be a promising alternative to optical nonlinear methods for frequency comb generation [38–40] but currently exhibit narrow instantaneous bandwidth and limited spectral coverage. Other MIR frequency comb sources, including microresonators [41], SCG [42,43] and direct MIR lasing [44] are still facing challenges to reach beyond 3.5 µm.

Compared to other techniques, OPOs have high powers and efficiencies with broad spectral coverages and wide tuning ranges [45–50]. Among the various OPO configurations, synchronously pumped degenerate OPOs have been demonstrated to be particularly promising, featuring high conversion efficiencies [51,52], two-octave-wide spectra [53], few-cycle pulses [54], scalability to a multi-GHZ repetition rate [55], and more importantly, intrinsic phase and frequency locking of the output to the pump [56]. However, the

demonstrated OPOs with a wavelength coverage beyond 3 µm have either a MIR conversion efficiency smaller than 20% [45,47–49,51] or a limited MIR output power under 250 mW [52,53].

Recently, there has been increasing interest in realization of purely dissipative cavity solitons [57,58] with the promise of frequency comb sources outside the well-developed near-IR region. The temporal simulton, a special form of quadratic solitons characterized by the generation of simultaneous bright-dark solitons of the signal at ω and the pump at 2ω [59,60], has emerged as a novel state of operation in OPOs [61,62]. The simulton-based OPO can be considered as a combination of a degenerate optical parametric amplifier (OPA) and a positively detuned cavity, in which a double balance of energy and timing is achieved [62], as illustrated in Figure 2.1(a)-(d). While the energy balance results from the interplay of dissipation and amplification, the timing balance is rooted in the compensation of cavity detuning by the nonlinear acceleration. Running in an uncommon high-gain low-finesse regime, simulton-based OPOs feature even higher power and efficiency as well as favorable power-dependent bandwidth scaling without losing any advantages of conventional OPOs. Although operation in the simulton regime has offered a promising new avenue for frequency comb generation in the MIR spectral region, it has remained challenging to extend it to longer wavelengths due to an incomplete understanding of its formation requirements and challenges in experiment.

In this chapter, we demonstrate an OPO working in the simulton regime which generates a frequency comb centered at 4.18 µm with a high average power of 565 mW, a record conversion efficiency of 44%, an instantaneous full-width at half-maximum (FWHM) bandwidth from 3.6 µm to 4.5 µm, and pulses of 45-fs duration, making it an outstanding mid-IR frequency comb source. A direct experimental comparison between the simulton and conventional regimes under the exact same pump condition attributes many of these outstanding characteristics to the simulton formation. Moreover, we perform numerical simulations to capture the behavior exhibited by different regimes of the OPO, which agree well with our experimental results. The simulation also indicates a pathway to further improve the performance of the simulton-based OPO. Lastly, we highlight key features of

the simulton build-up dynamics and offer a discussion on the impact of the pump carrier-envelope offset frequency on simulton formation, with many practical implications. This work presents a powerful scheme for MIR frequency comb generation and demonstrates its potential to be extended to longer wavelengths and integrated platforms [63].

2.2. Experimental setup

The experimental setup of the MIR OPO is illustrated in Figure 2.1(e). For the pump, another OPO based on periodically poled lithium niobate with a 250-MHz repetition rate generating pulses centered at 2.09 µm is used. Its average power reaches up to 1290 mW with a FWHM bandwidth around 155 nm. The MIR OPO cavity consists of a bowtie resonator with a tunable cold-cavity time of ~4 ns that can be scanned or locked around the pump repetition period using a piezoelectric actuator. The input coupler (M1) is a flat dielectric-coated mirror that is highly transmissive for the pump range (around 2.09 µm) and highly reflective for the signal range (around 4.18 µm). The focusing and collimating of the beams are provided by two concave gold mirrors (M2 and M3) with a 24-mm radius of curvature, which have a high reflection for both signal and pump. The nonlinear gain is provided by a plane-parallel orientation-patterned gallium phosphide (OP-GaP) crystal with a length of 0.5 mm and a poling period of 92.7 µm for type-0 phase matching at room temperature. The crystal has a broadband anti-reflection coating for both the signal and pump range. The output coupler (M4) is a dielectric mirror coated for broadband transmission (T=25%) from 3.5 µm to 5.5 µm, the value of which is chosen based on a rough experimental optimization of the output coupling using a coated pellicle beamsplitter [52]. The length of the OPO is locked using the "dither-and-lock" procedure described in reference [56].
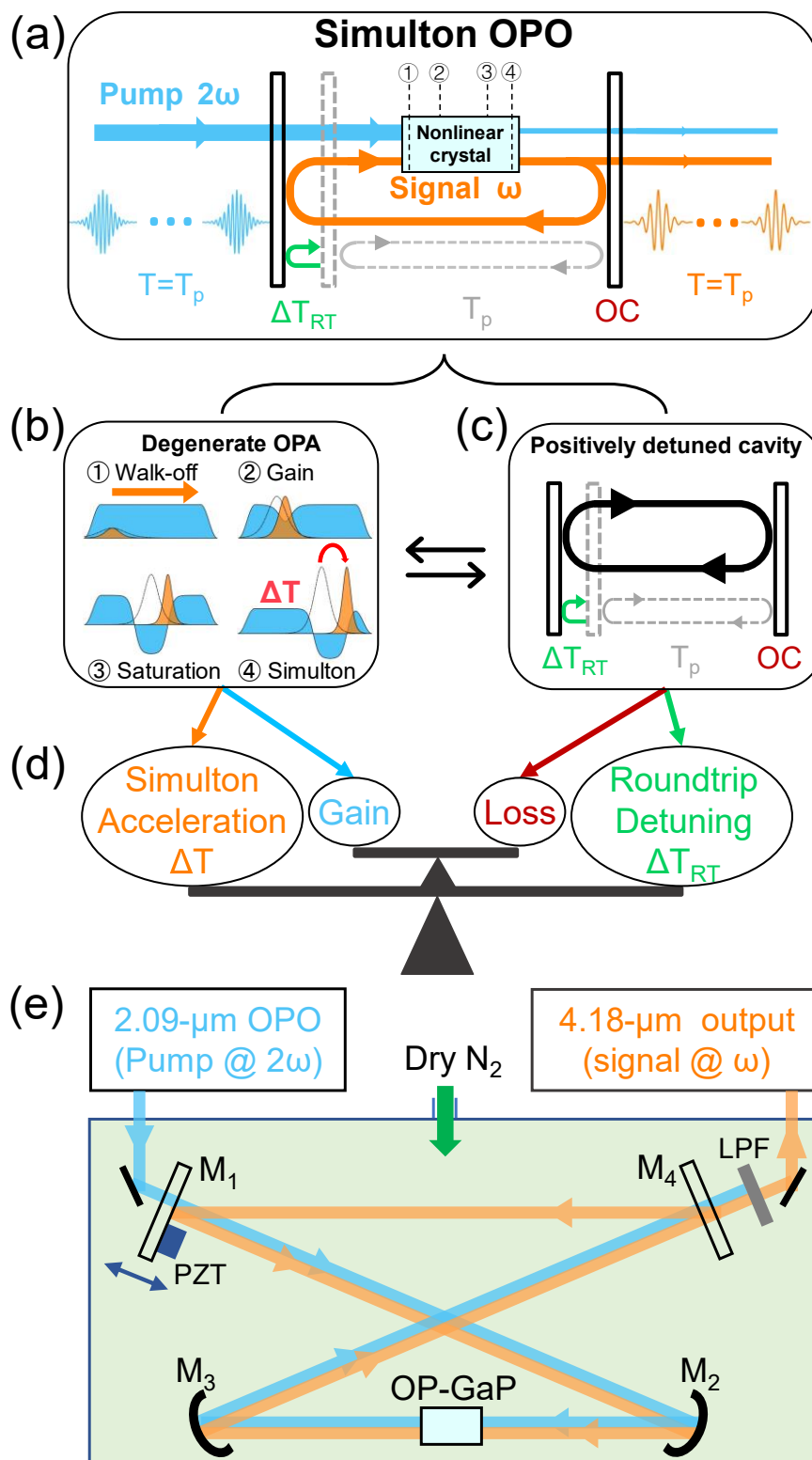
Figure 2.1: **The simulton-based OPO. (a)** Simplified diagram of the oscillator. Tp: Repetition period of the pump pulse and the signal pulse, which is also the cold-cavity

round-trip time of the degenerate OPO working in the perfectly synchronous (conventional) regime. ΔTRT: positive timing mismatch between the cavity time of the simulton OPO and Tp. OC, partial output coupler. The oscillator can be considered a combination of **(b)** a degenerate OPA and **(c)** a positively detuned cavity, striking **(d)** a double balance of timing and energy. **(b)** Illustration of simulton formation: signal (orange) at ω and pump (blue) at 2ω. For comparison, uncolored solid lines denote a perfectly synchronous (ΔTRT=0) half-harmonic pulse undergoing linear propagation. ①: on each roundtrip, a small group delay, ΔTRT, is acquired by the resonating signal pulse with respect to the newly in-coupled pump pulse due to the detuning of the cavity roundtrip time. ②③: Passing though the crystal, the signal is amplified by extracting gain from the pump until the pump is depleted, meanwhile accumulating a simulton group advance. ④: Once depleted, the pump forms a dark soliton and co-propagates with the signal at the simulton velocity. **(e)** Schematic of the 4.18-µm OPO cavity. The cavity length is controlled by mounting M1 on a piezo stage (PZT). The whole cavity resides in a box purged with dry nitrogen to reduce the effects of atmospheric absorption on the OPO operation. Although the OPO can still run without purging, degenerate operation is not possible due to the strong absorption of carbon dioxide centered at 4.2 µm, prohibiting the OPO from operating in the simulton regime. We also contain the measurement instruments for characterization of the OPO output in the purging box to limit the artifacts caused by the atmospheric absorption. LPF, long-pass filer.

2.3. Simulation modeling

Here, we describe the methodology behind the simulations used for numerical modeling of our experiment. Using the notation of [62], the coupled wave equations describing the phase-matched nonlinear interaction of pump and signal in the crystal are given by:

$$d_z A_\omega(z,t) = \kappa A_{2\omega} A_\omega^* - \frac{\alpha_\omega}{2} + \widehat{\mathcal{D}}_\omega A_\omega \tag{2.1}$$

$$d_z A_{2\omega}(z,t) = -\kappa A_\omega^2 - \frac{\alpha_{2\omega}}{2} - u \frac{\partial A_{2\omega}}{\partial t} + \widehat{\mathcal{D}}_{2\omega} A_{2\omega} \tag{2.2}$$

where the time coordinate is taken to be comoving with the group velocity of the signal wave. Additionally, the pump envelope phase has been shifted by $\pi/2$ to ensure real solutions, neglecting higher order dispersion. Here, subscripts ω and 2ω refer to the signal and pump, respectively. A_j, j ε {ω, 2ω} describes the field envelope and is normalized such that $|A_j|^2$ gives the instantaneous power. κ is the nonlinear coupling coefficient which governs the strength of the nonlinear interaction, given by $\sqrt{2\eta_0}\omega d_{eff}/(w_0 n_\omega \sqrt{\pi n_{2\omega}} c)$ where η_0 is the impedance of free space, d_{eff} is the effective nonlinearity, n_j is the refractive index, and w_0 is the Gaussian beam waist in the crystal. α_j is the absorption

coefficient, given by the material loss in the crystal. u is the walk-off parameter between pump and signal. Finally, $\widehat{\mathcal{D}}_j = \sum_{m=2}^{\infty} \left[\frac{(-i)^{m+1} \beta_\omega^{(m)}}{m!} \right] \partial_t^m$ is the dispersion operator.

Simulations of the field envelope evolutions in the crystal are performed using the split-step Fourier method, in which the OPA process in the crystal is divided into fifty segments. In each segment, we solve the linear and nonlinear portions of the coupled wave equations as lumped elements. The nonlinear step is computed by solving the nonlinear terms in the coupled wave equations using the fourth-order Runge-Kutta method. This is followed by a linear filter containing the dispersion and loss for the crystal, which is applied in the frequency domain to the pump and signal. We calculate four orders of dispersion for both pump and signal from the Sellmeier equation given in [64].

The roundtrip propagation is modeled by a linear feedback loop which contains the frequency-dependent losses as well as the dispersion for all cavity elements. Specifically, for the nth roundtrip, the signal at the input of the crystal $A_\omega^{n+1}(0, t)$ is related to the output of the OPA process, $A_\omega^n(L, t)$ by the equation:

$$A_\omega^{n+1}(0, t) = \mathcal{F}^{-1}\{e^{-\frac{\alpha(\Omega)}{2}} e^{-i\Phi(\Omega)} \mathcal{F}\{A_\omega^n(L, t)\}\}. \tag{2.3}$$

Here, Ω is the normalized Fourier frequency and $\mathcal{F}$ and $\mathcal{F}^{-1}$ are the Fourier transform and inverse Fourier transform, respectively. $\alpha(\Omega)$ gives the round-trip loss of the signal, including the frequency-dependent losses from the output coupling, the AR coatings on the crystal interfaces, the cavity mirrors, and the residual atmospheric gases in the cavity after purging, modeled using data provided from the HITRAN database [65]. Similarly, $\Phi(\Omega) = \Delta T_{RT}(\pi c / \lambda_{2\omega} + \Omega) + \Delta\Phi(\Omega)$ gives the round-trip phase accumulated by the signal, measured relative to a perfectly synchronous signal pulse, as mentioned in the main text. ΔT_{RT} is the detuning and contributes to both a constant phase term, $\frac{\Delta T_{RT} \pi c}{\lambda_{2\omega}}$, and a linear phase term, $\Delta T_{RT}\Omega$, which accounts for the timing delay. Here, c is the speed of light and $\lambda_{2\omega}$ is the wavelength of the pump. $\Delta\Phi(\Omega)$ accounts for higher-order contributions to the phase due to the dispersion of the cavity mirrors, the AR coatings on the crystal, and the residual gas in the cavity.
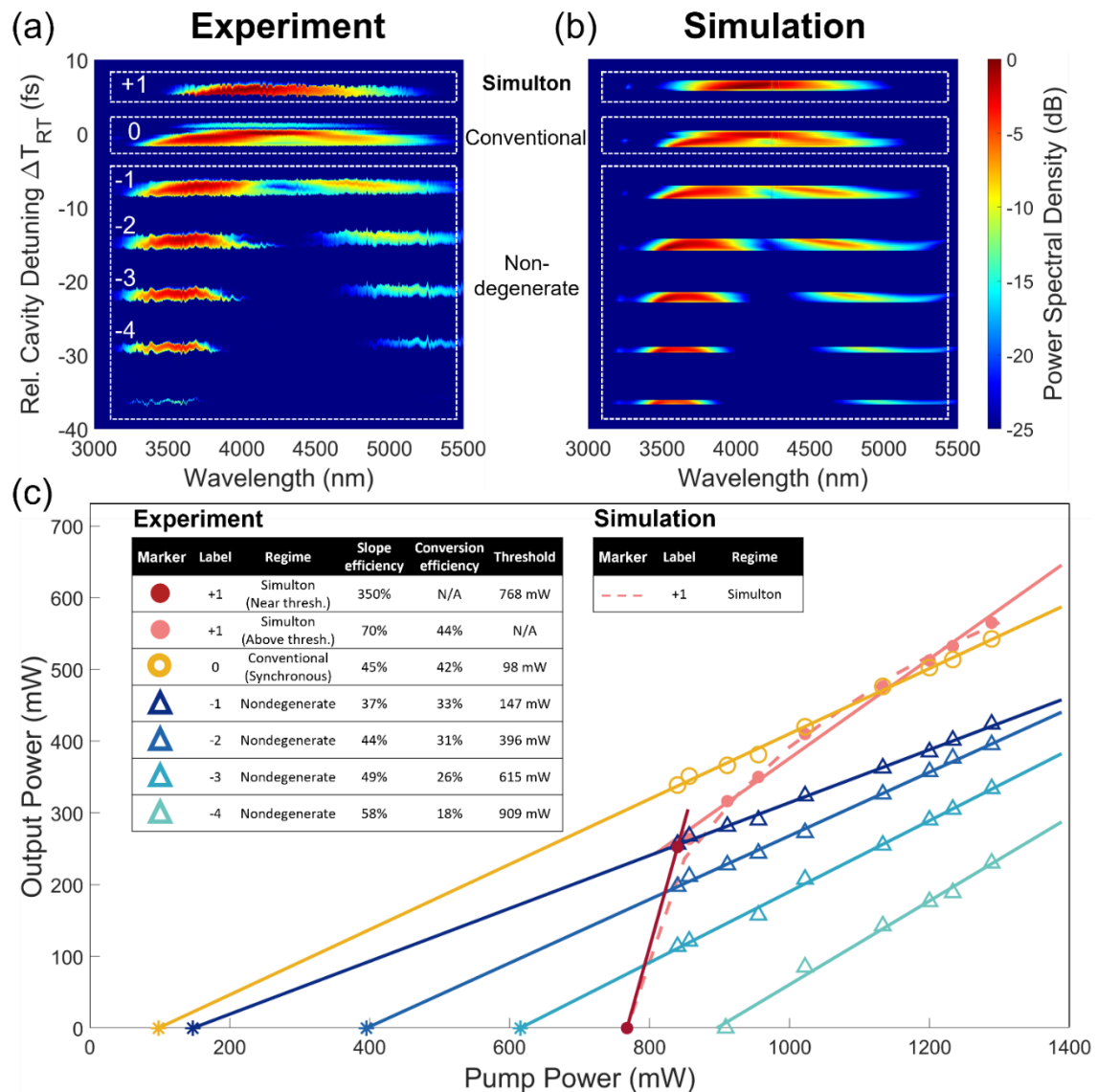
Figure 2.2: **Signal spectrum as a function of cavity detuning and output-input power.**
(a) Measured signal spectrum as a function of cavity detuning at the highest pump power of 1290 mW, labeled with resonance numbers. The y-axis denotes the relative cavity detuning, the zero of which is set at the center of the conventional resonance. **(b)** Simulated signal spectrum as a function of cavity detuning corresponding to (a), with the three identified regimes indicated on the left. **(c)** Output-input power dependencies for each resonance measured with locked cavity lengths. Filled circle, unfilled circles and triangles denote experimental measured points of simulton (+1), conventional (0), and non-degenerate (-1 to -4) resonances, respectively. Solid lines represent their linear fitting for estimation of their slope efficiencies. Note that the thresholds of resonance 0, -1, -2 and -3 cannot be directly measured since the pump is not stable at such low powers; therefore, they are instead estimated by extrapolations of their linearly fitted lines, denoted by asterisks. Two slope efficiencies, one just above the threshold (dark red solid line) and the

other well above the threshold (pink solid line), are estimated for the simulton resonance, given its distinct behavior from other resonances. Conversion efficiencies for all resonances are calculated at the highest pump power of 1290 mW. The simulation corresponding to resonance +1 is denoted by the pink dashed curve.

2.4. Results

Because the parametric gain is phase-sensitive, the signal of the OPO only oscillates around the cavity lengths where it acquires a 0 or π phase shift relative to the pump on each roundtrip. This results in signal resonances at a discrete set of cavity lengths, which are separated by about half the signal center wavelength. In the context of this paper, the cavity length is denoted by the deviation of the cold-cavity round-trip time from the repetition period of the pump pulses, i.e., ΔT_{RT}. Depending on the ΔT_{RT}, the different resonances can be classified into three regimes of operation: simulton ($\Delta T_{RT} > 0$), conventional ($\Delta T_{RT} \cong 0$, also referred to as "synchronous"), and nondegenerate ($\Delta T_{RT} < 0$) [61,62]. Note that the positive ΔT_{RT} corresponds to a longer cavity length. Figure 2.2(a) shows the measured output spectrum as a function of relative cavity timing detuning (ΔT_{RT}) at the highest pump power of 1290 mW. When the cold cavity is most nearly synchronized to the pump repetition period ($\Delta T_{RT} \cong 0$), the OPO is identified to run in the conventional (synchronous) regime (labeled "0"), which has a degenerate spectrum and the lowest threshold. One additional degenerate resonance, the simulton regime (labeled "+1"), is found when the cavity is positively detuned. Conversely, when the cavity is negatively detuned, the OPO operates in the nondegenerate regime, with the output spectra split into distinguishable signal and idler bands (labeled "−1, −2, −3, −4"). With parameters comparable to the experiment, a simulation of the output spectrum as a function of ΔT_{RT} is conducted, which is depicted in Figure 2b. The simulation exhibits a good agreement with the experimental result for all three regimes.

Figure 2.3(c) present output-input power dependencies for each resonance measured with locked cavity lengths. With the lowest threshold, the conventional regime has a slope efficiency of 45% and a conversion efficiency of 42%. For the nondegenerate resonances, as ΔT_{RT} becomes increasingly negative, the thresholds increase uniformly, with conversion efficiencies decreasing and limited to less than 35%. In contrast, the simulton resonance

has an irregularly located high threshold and the highest conversion efficiency of 44%. Furthermore, it measures a ~350% slope efficiency near the threshold and a ~70% slope efficiency well above the threshold, much higher than those of the conventional and nondegenerate regimes.

To demonstrate the difference between the power-dependent bandwidth scaling of the conventional and simulton regimes, we measure spectra of the signal at each output power corresponding to the experimental points in Figure 2.2(c), the results of which are shown in Figure 2.3(a)-(c). In the simulton regime, as the power increases, the bandwidth of the signal spectrum increases if the pump power is not too high (Figure 2.3(a)), while in the conventional regime, it monotonically decreases (Figure 2.3(b)). These tendencies are in accordance with the simulton theory [62] and conventional box-pulse scaling [61]. It should be noted that at the three highest pump powers, the signal bandwidth of the simulton regime stops broadening further, which also agrees with our theoretical prediction that the simulton theory would fail if the signal is too far above threshold [61]. This transition from simulton scaling to box-pulse scaling far above threshold also accounts for the observed nonlinear reduction in the simulton slope efficiency in Figure 2.2(c). Nonetheless, at high pump power around 1200 mW, the simulton regime wins about 40% in bandwidth. This power-dependent signal spectral characterization shows that the simulton regime outperforms the conventional regime not only in power and efficiency but also in spectral bandwidth. At the highest available pump power of 1290 mW, the FWHM bandwidth of the signal spectra for simulton and conventional regimes are 14 THz and 10 THz, which can support pulses as short as 22 fs and 32 fs, respectively. Figure 3d depicts the interferometric autocorrelation of the simulton pulse measured by a two-photon extended-InGaAs detector, together with its fitted pulse intensity. This measurement corresponds to a FWHM pulse width of ~45 fs, assuming no chirp. However, chirp exists due to the dispersion from the substrates of the output coupler (1-mm ZnSe) and two long pass filters (1-mm Ge and 1-mm Si) in the path to the autocorrelator.
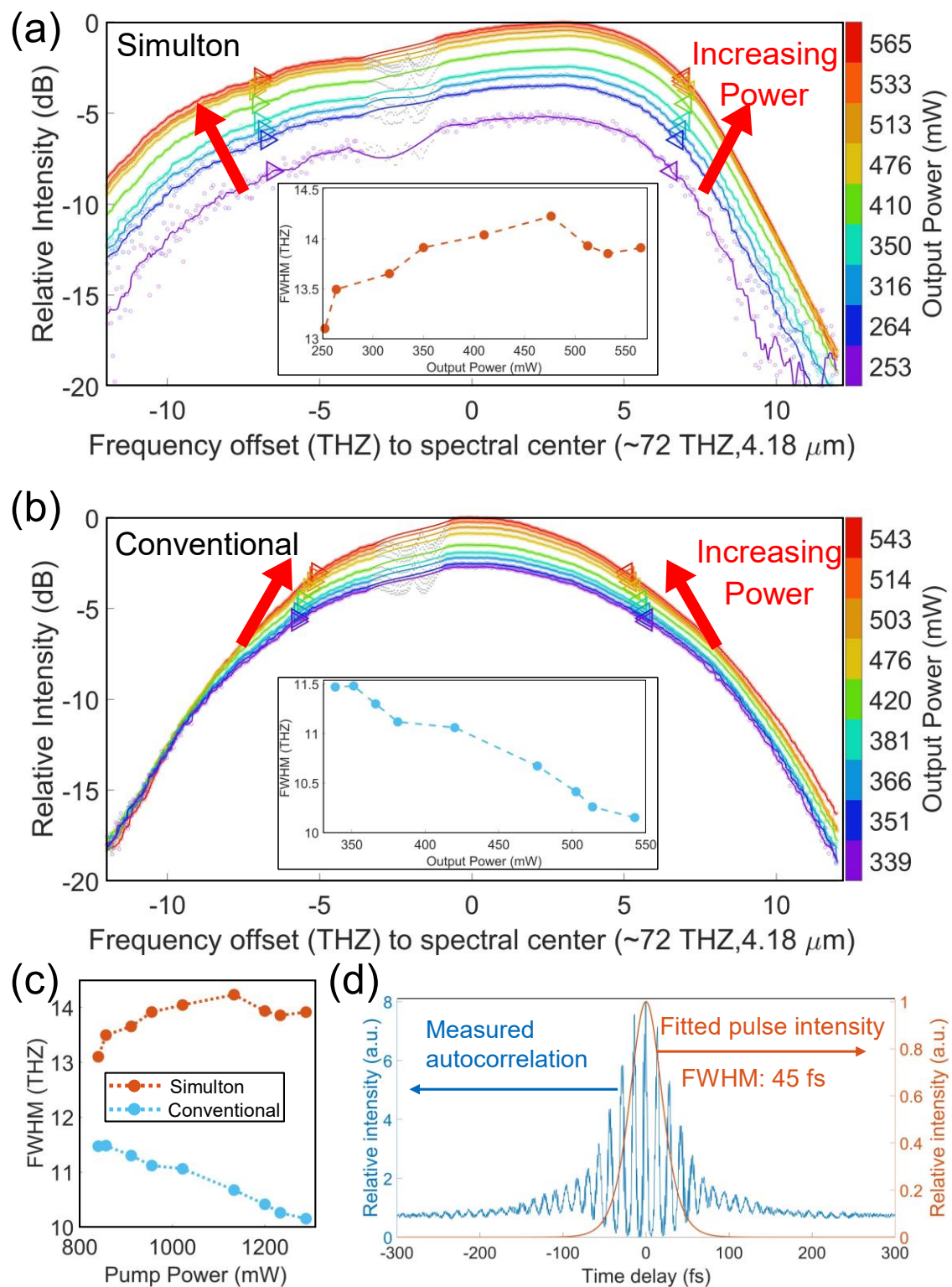
Figure 2.3: **Spectra as a function of output power and autocorrelations. (a), (b)** Spectra recorded as a function of output power for the OPO working in the (a) simulton regime and

(b) conventional (synchronous) regime. The signal power and corresponding FWHM bandwidth for each curve are presented in the insets. The FWHM bandwidths are also denoted by the triangular arrows on the curves. The unfilled circles denote the raw data points obtained by the Fourier-transform infrared spectroscopy (FTIR), and curves present the interpolation of them for a better visualization of results and estimation of FWHM bandwidths. Note that a portion of the raw data near the strong atmospheric absorption around 4.2 µm is discarded during the interpolation, which is denoted by smaller filled grey circles. **(c)** FWHM bandwidths of the signal spectra as a function of pump power for both regimes, corresponding to (a) and (b). Solid circles denote experimentally measured points and dotted curves are to guide the eye. **(d)** Two-photon interferometric autocorrelation (blue) and fitted intensity (red) of the signal pulse at the highest pump power of 1290 mW, for the OPO working in the simulton regime.
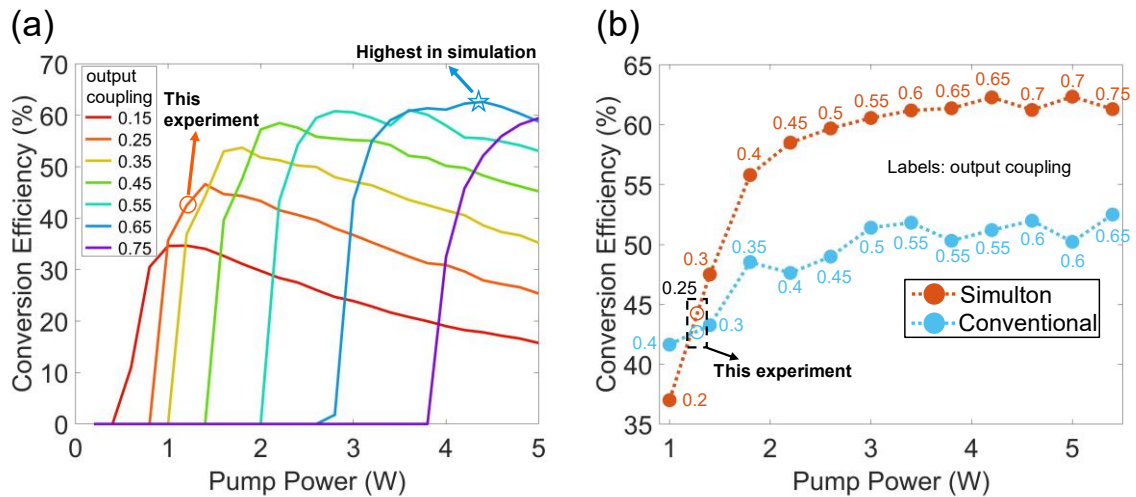
Figure 2.4: **Numerical simulation of the simulton OPO with different output coupling ratio. (a)** Conversion efficiency (in percentage) as a function of pump power. Curves in different colors denote different output coupling ratio (in decimal), as indicated in the legend box. The orange circle denotes the result that is realized in our experiment, and the blue pentagram denotes the suggested highest conversion efficiency that can be achieved by this simulton-OPO. **(b)** Highest conversion efficiency (in percentage) that the OPO can achieve under different pump power. The red circles denote the results (in percentage) in the simulton regime, labeled with the output coupling ratio (red decimal) that should be used. The blue circles, as a comparison to the red ones, denote the results in the conventional regime, also labeled with the corresponding output coupling ratio (blue decimal). The unfilled red and blue circles denote our experimental results of simulton and conventional regime, respectively.

In this experiment, the efficiency advantage of the simulton regime is limited by the available pump power. To further demonstrate the efficiency potential of the simulton regime, we use numerical simulations with higher pump power under different output coupling ratios, and the results are shown in Figure 2.4(a). As suggested by the simulation,

higher output coupling should be employed with higher pump power to realize higher conversion efficiency, and the conversion efficiency can be improved to as high as 63% if 4.2-W pump power and 0.65(65%) output coupling ratio are used. This simulation result can also be used as a design rule for choosing the output coupling of the simulton OPO under different available pump powers. Figure 2.4(b) presents the highest possible conversion efficiency that the simulton regime can reach under different pump powers (red circles), with the labels of the corresponding output coupling (red decimals). As a comparison, under each pump power, the highest conversion efficiencies that the conventional regime can achieve are also plotted in Figure 2.4(b) (blue circles), labeled with the corresponding output coupling ratios (blue decimals). The comparison shows that the return of the simulton regime can increase sharply with increasing pump power. It is worth noting that the pump intensity used in the simulation is similar to those of the previously demonstrated experiments [53,66], which is expected to be below the damage threshold of OP-GaP.

2.5. Discussion

As is evident from our experimental and theoretical results, developing a better understanding of simulton formation is crucial for further improvement of the OPO performance. Here, we use our simulation results to build upon the understanding of simulton formation dynamics presented in [37] and offer practical tools for optimizing simulton performance. We begin with a discussion of the relationship between the simulton formation dynamics and the high slope efficiencies and conversion efficiencies offered by this regime. Figure 2.5(a) shows schematically the interaction between pump (blue) and signal (orange) in the single-pass OPA process which occurs each roundtrip in the OPO. From the crystal input (left) to its output (right), the signal walks through the pump, depleting it and extracting gain in the process. Two terms contribute to the walk-off, the product of the group velocity mismatch (GVM), u, with the crystal length, L, and the nonlinear timing advance due to simulton acceleration, ΔT, leading to a combined walk-off of $uL + \Delta T$ relative to the signal starting position. This walk-off along the fast time axis and simultaneous depletion of the pump by the signal determines the available gain for the

signal. For the signal to resonate above threshold, the gain extracted in consecutive roundtrips must consistently overcome the loss.
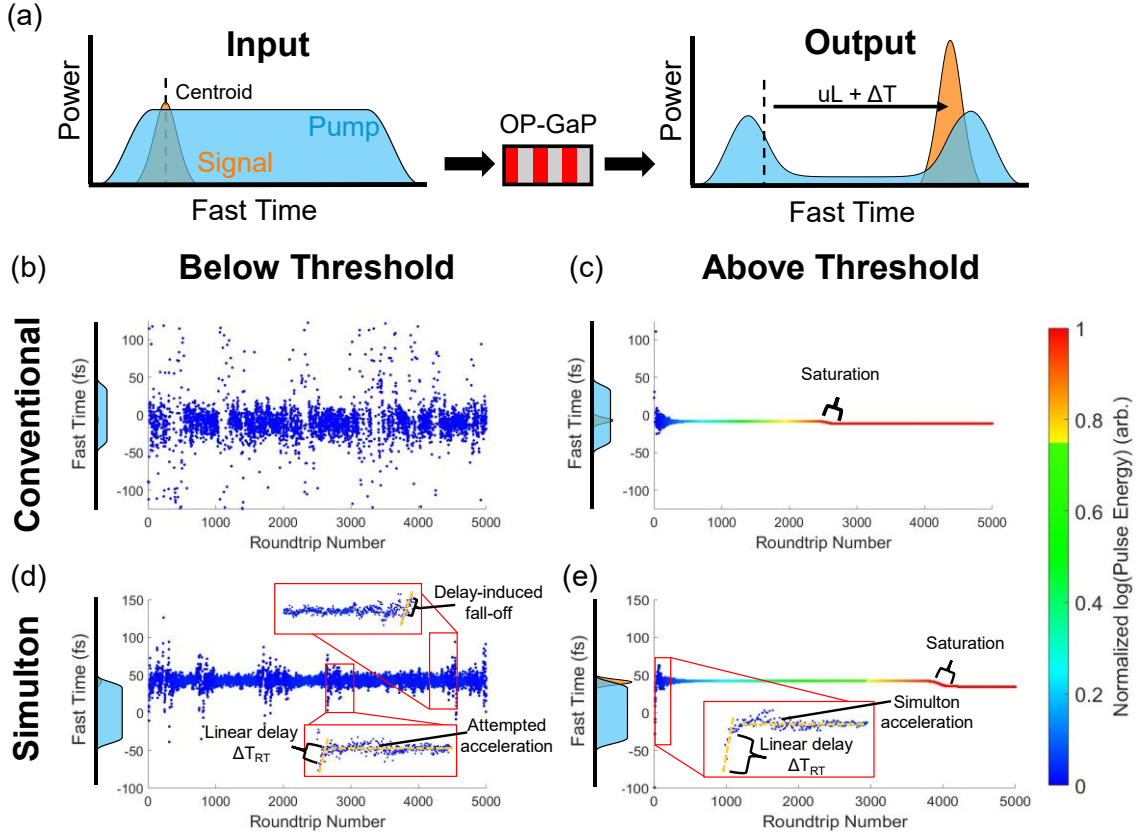
Figure 2.5: **Depiction of simulton formation dynamics as compared to the conventional regime. (a)** Schematic illustration of the pump-signal interaction in the crystal. Between the input (left) and output (right) facets of the crystal, the signal (orange) walks through the pump (blue) from its starting point according to product of the GVM, u, with the crystal length, L, plus any timing advance, ΔT, due to simulton acceleration. This walk-off and concurrent pump depletion define a gain window for the signal along the fast time axis. (b-e) Simulated comparison of simulton (b, c) and conventional (d, e) signal centroid positions along the fast time axis as a function of roundtrip number in the below (b, d) and above (c, e) threshold cases. The normalized logarithm of the pulse energy is indicated by the color of each point. **(b)** The conventional case below threshold has few discernible features as noise and loss dominate; noise amplified by the pump is unable to build up. **(c)** Above threshold, the noise quickly builds into a strong signal pulse. A small timing shift is observed when the gain saturates. **(d)** For the simulton, noise amplified by the pump experiences a linear delay due to the cavity detuning ΔT_{RT}. Below threshold, since the gain cannot enable sufficient acceleration for the timing condition to be satisfied, the delay results in the signal falling out of the gain window before signal build up can be achieved. **(e)** The simulton goes above threshold when the gain is sufficient for the simulton

acceleration to compensate the linear delay and enable signal build up. As in the conventional case, a small timing shift is observed when the gain saturates.

Figure 2.5(b)-(e) shows the signal centroid position at the input facet of the crystal as a function of roundtrip, with the color indicating the normalized logarithm of the pulse energy, to illustrate the signal build up dynamics in the conventional and simulton regimes. In the conventional case (Figure 2.5(b)-(c)), there is no timing condition, so the signal goes above threshold as soon as the gain experienced through the linear walk-off, uL, equals the loss. This results in there being no clear trends in the dynamics of the signal below threshold, as shown in Figure 2.5(b), with amplified noise being unable to build up. Above threshold, the noise quickly grows into a strong signal pulse, located near the center of the gain window set by the pump (Figure 2.5(c)). In the simulton case (Figure 2.5(d)-(e)), however, the cavity detuning, ΔT_{RT}, creates a linear delay which causes the amplified signal noise to move away from the gain window set by the pump. Since the simulton acceleration relies on pump depletion by the leading edge of the signal and subsequent back-conversion of the trailing edge, going above threshold requires that the simulton build up enough to accelerate and satisfy the timing condition before falling out of the gain window due to the linear delay. This intertwines the simulton energy and timing conditions, as large simulton acceleration requires the presence of high enough signal gain. Figure 5d shows the case of the below threshold simulton, in which the delayed and amplified noise attempts to build up but ultimately does not experience enough gain to sufficiently accelerate and falls off. By contrast, Figure 5e shows the simulton build-up above threshold, in which the simulton acceleration leads to a timing advance, ΔT, which compensates the delay, ΔT_{RT}. Unlike the conventional case, the simulton just above threshold builds up near the edge of the gain window. These observations correspond to important features of the simulton. First, the high threshold for the simulton is a consequence of the requirement for there to be high gain for the timing condition to be satisfied. The burst slope efficiency of the simulton near threshold then results as the acceleration pulls the simulton to the center of the gain window. Once well-confined to the gain window, the longer walk-off for the simulton due to the additional nonlinear acceleration term, ΔT, suggests that simulton operation can often enable more efficient extraction of the pump gain. This gives rise to

observed trends of slope efficiencies and overall conversion efficiencies for simulton operation that exceed what is observed for conventional OPO operation. Practically, one should match uL + ΔT to the length of the gain window defined by the pump for optimum signal generation.
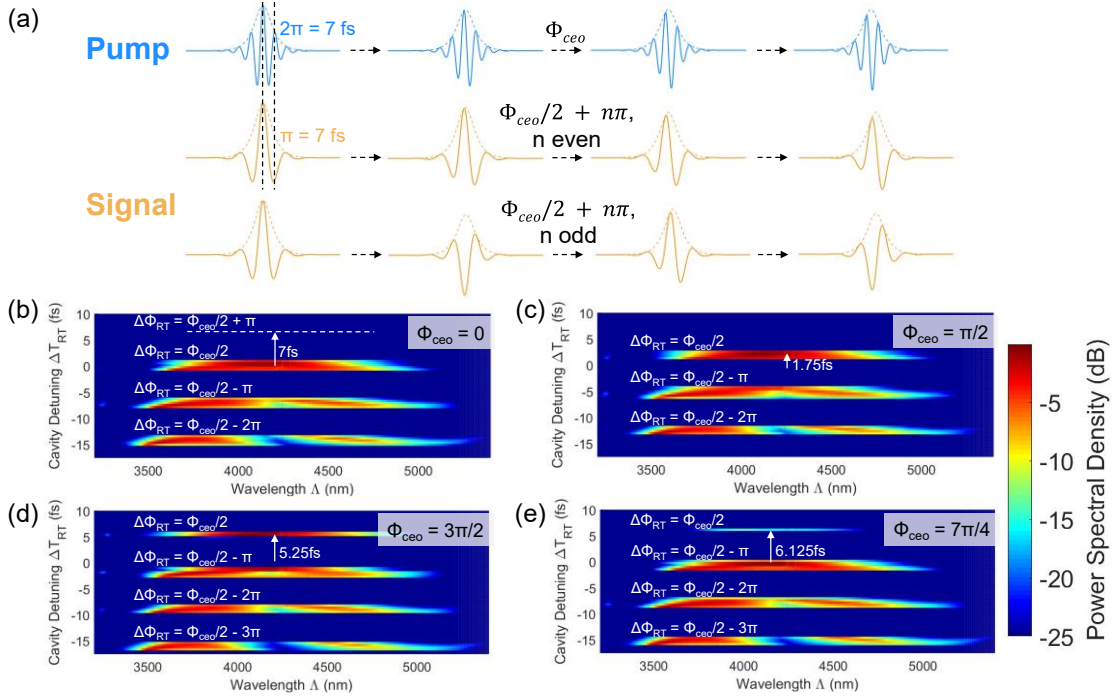
Figure 2.6: **Simulated impact of the carrier-envelope offset phase, Φceo, on simulton performance.** **(a)** Illustration of the pump-signal phase relationships for the OPO resonances. For a pulse-to-pulse phase slip of Φ_{ceo} in the pump, the OPO can resonate when the roundtrip phase accumulation, $\Delta\Phi_{RT}$, is $\Phi_{ceo}/2 + n\pi$, where n is an integer, with π signal phase corresponding to a detuning of 7 fs between resonances. The upper signal branch depicts the case of n even, where a pulse-to-pulse phase of $\Phi_{ceo}/2$ is accrued, while the lower shows n odd, which adds an additional π phase shift between consecutive pulses. **(b)** First three cavity resonances for $\Phi_{ceo} = 0$, showing that no simulton behavior is observed, with the topmost resonance occurring at $\Delta T_{RT} = 0$ and exhibiting both strongly degenerate and nondegenerate features. **(c)** As Φ_{ceo} is increased to $\pi/2$, simulton-like behavior is observed as the topmost resonance becomes more positively detuned. **(d)** Example of a strongly degenerate simulton at $\Phi_{ceo} = 3\pi/2$, showing that tuning of Φ_{ceo} to this region can enable optimum simulton performance for the given gain. **(e)** As Φ_{ceo} is further increased beyond $7\pi/4$, the simulton disappears as the timing condition can no longer be satisfied by the gain, which is why no simulton resonance is observed in panel (b) at the $\Phi_{ceo}/2 + \pi$ resonance, indicated by the white, dashed line.

An additional parameter which is critical to simulton formation is the carrier-envelope offset frequency (fceo) of the pump, the impact of which is illustrated in Figure 2.6. The

pump fceo imposes a phase Φ_{ceo} between consecutive pump pulses. Due to the aforementioned phase-sensitive gain which demands a relative phase of 0 or π between pump and signal for signal build-up, this pulse-to-pulse phase shift in the pump must be mirrored in the signal, as shown in Figure 2.6(a). For signal resonance to occur, the phase accumulated in the roundtrip must be $\Phi_{ceo}/2 + n\pi$, where n is an integer, with π signal phase corresponding to a detuning of 7 fs between resonances for the 4.18 μm OPO. The case for n even is shown by the upper signal branch while the case where n is odd, in which the signal accumulates an additional phase shift of π between pulses, is depicted in the lower signal branch. The signal roundtrip phase accumulation, $\Phi(\Omega)$, relative to a perfectly synchronous signal pulse is given by $\Phi(\Omega) = \Delta T_{RT}(\pi c/\lambda 2\omega + \Omega) + \Delta\Phi(\Omega)$, where Ω is the normalized frequency, ΔT_{RT} is the detuning as defined previously, c is the speed of light, $\lambda_{2\omega}$ is the pump wavelength, and $\Delta\Phi(\Omega)$ represents the higher-order effects of dispersion from mirrors and additional cavity elements [37]. From this equation, we see the required pulse-to-pulse phase shift for the signal can be achieved through varying ΔT_{RT} such that the constant phase term $\Delta\Phi_{RT} = \Delta T_{RT}\pi c/\lambda 2\omega = \Phi_{ceo}/2 + \pi n$, the desired phase shift. In other words, Φceo determines the detuning values where the OPO can resonate. However, varying ΔT_{RT} also causes a change in the signal timing, modeled through the linear phase term $\Delta T_{RT}\Omega$, and consequently the simulton threshold and slope efficiency. This implies that, through tuning of the pump fceo, one can adjust the timing of the signal resonances to optimize simulton performance.

Figure 2.6(b)-(e) show the simulated signal resonances for a few values of Φ_{ceo}. As the focus of this study is on simulton behavior, only the first few resonances are shown. Resonance labels denote the roundtrip phase, $\Delta\Phi_{RT}$, acquired by the signal, and an additional label denotes the timing shift from 0 fs of the most positively detuned resonance with $\Delta\Phi_{RT} = \Phi_{ceo}/2$. As seen in Figure 2.6(b), when $\Phi_{ceo} = 0$, the signal at $\Delta\Phi_{RT} = \Phi_{ceo}/2$ is a typical conventional resonance with $\Delta T_{RT} = 0$. Note that no simulton exists at the expected location, $\Delta\Phi_{RT} = \Phi_{ceo}/2 + \pi$ (shown by the white, dashed line), due to a lack of gain. For values between 0 and π, the $\Delta\Phi_{RT} = \Phi_{ceo}/2$ resonance becomes simulton-like but still behaves more like a conventional OPO, with both non-degenerate and degenerate regions as shown in Figure 2.6(c). Beyond $\Phi_{ceo} = \pi$, a strong simulton is observed, like that

shown in Figure 2.6(d) for $\Phi_{ceo} = 3\pi/2$. In tandem with the $\Delta\Phi_{RT} = \Phi_{ceo}/2$ resonance transitioning from more conventional behavior to the simulton regime, we also observe strengthening of the degenerate side of the $\Delta\Phi_{RT} = \Phi_{ceo}/2 - \pi$ resonance such that it behaves more like a conventional OPO as it approaches $\Delta T_{RT} = 0$. Finally, as exemplified by Figure 2.6(e), when Φ_{ceo} is greater than 1.5π, the power in the resonance quickly drops off as the gain struggles to satisfy the timing condition, with the OPO repeating the resonance structure shown in Figure 2.6(b) as Φ_{ceo} approaches 2π. Our experiment corroborates these findings, as we observe such a shift in simulton behavior as the Φ_{ceo} is varied, with presented data representing the strongest observed simulton. This suggests that, for given experimental values of gain and loss, Φ_{ceo} can be a crucial experimental parameter for optimizing simulton performance.

2.6. Summary

In summary, we present the generation of a high-power and efficient MIR frequency comb centered at 4.18 μm based on an OPO operating in the simulton regime, achieving 565-mW average power together with a 14-THz instantaneous FWHM bandwidth, sub-three-cycle pulses, a 350% slope efficiency near the threshold, a 70% slope efficiency above the threshold, and a record high 44% conversion efficiency. By a direct comparison with the conventional regime in terms of cavity detuning, output power, threshold, slope and conversion efficiency, instantaneous bandwidth, and bandwidth scaling, we are able to ascribe the favorable performances of this novel regime to the simulton formation, based on the agreement between the experiment, simulation, and theory. The performance of this simulton OPO is expected to be further improved by tuning the pump and optimizing dispersion and loss within the cavity. Especially, the numerical simulation suggests that a conversion efficiency >60% can be achieved if 4-W pump power and 65% output coupling are employed. Finally, we further explore simulton build-up dynamics and analyze the impact of the pump f_{ceo} on simulton formation, and we tie these results to practical design considerations for a simulton OPO. In addition, we want to emphasize that the half-harmonic signal of femtosecond degenerate OPOs are frequency combs that are intrinsically phase- and frequency- locked to their pump combs, which is well-established in previous works [51,56,67]. Very recently, we have used the OPO presented in this work

as the comb source for a dual-comb-based spectroscopy experiment in the mid-IR [68], enabled by its comb character and intrinsic locking. Moreover, it is experimentally shown that the CEO frequency noise can be reduced by 6 dB through the half-harmonic generation [69].

In short, this work paves the way to realization of a compelling new source of ultrashort-pulse frequency combs in the mid-infrared region which can benefit numerous applications, for example, spectroscopy methods that require high-power, broad-band and short-pulse MIR frequency combs [67,68]. This work sheds new lights on soliton generation based on the quadratic nonlinearity, and its potential in the MIR region. Recent advances in integrated quadratic platforms [58,63,70] promise on-chip realization of such sources in the future.

C h a p t e r   3

OPTICAL-PARAMETRIC-AMPLIFICATION-ENHANCED BACKGROUND-FREE SPECTROSCOPY

M. Liu conceived the project, conducted theoretical analysis and numerical simulation, analyzed the results, and led the writing of the manuscript.

Traditional absorption spectroscopy has fundamental difficulty in resolving small absorbance from strong background due to the instability of laser sources. Existing background-free methods in broadband vibrational spectroscopy help to alleviate this problem but face challenges in realizing either low extinction ratios or time-resolved field measurements. In this chapter, we introduce optical-parametric-amplification-enhanced background-free spectroscopy, in which the excitation background is first suppressed by an interferometer and then the free-induction decay that carries molecular signatures is selectively amplified. We show that this method can further improve the limit of detection in linear interferometry by order(s) of magnitude without requiring lower extinction ratios or time-resolved measurement, which can benefit sensing applications in detecting trace species.

3.1. Introduction

Optical absorption spectroscopy is a powerful and versatile tool to study properties of different materials. The absorption information is typically contained in the change of the radiation source and deciphered by comparison between at least two measurements of the optical spectrum. Detecting trace samples with low concentrations is important and can push the limits of a wide range of applications, such as breath analysis [71], industrial control [72] and environmental monitoring [73]. However, in traditional absorption spectroscopy, detection of tiny absorption dips on top of a large background is a

fundamental challenge, which is limited by the noise and stability of the light source, as well as the dynamic range of the whole detection system.

There are some existing background-free spectroscopy (BFS) methods, including photoacoustic spectroscopy [74,75], Faraday rotation spectroscopy [76,77], and laser-induced fluorescence spectroscopy [78]. Nevertheless, they are limited either in access to narrow resonances and quantitative measurement capabilities or only applicable to a small class of molecules and narrow wavelength range. These challenges have limited such techniques to prototypical demonstrations in laboratory settings in contrast to more standard infrared spectroscopy techniques like Fourier transform infrared spectroscopy (FTIR).

Recently, to realize a background-free detection in broadband infrared (ro-vibrational) spectroscopy, two types of approaches have been proposed and demonstrated. The first is temporal gating based on short excitation pulses and nonlinear wave mixing [79–83], in which the excitation background is detected and separated from the free-induction decay (FID) signal directly in the time domain. However, time-resolved measurements require not only accurate synchronization (femto- or even atto-second level) and scanning between two independent pulse trains but also super short pulses, which may have to be shorter than one optical cycle of the excitation pulse. These components are challenging to realize and necessitate substantial efforts.

The second is broadband linear interferometry [84–86], which is motivated by LIGO [87], dual-beam interferometry [88] and some narrowband laser absorption spectroscopy works [89,90]. In this approach, a Mach-Zehnder-like or Michelson-like interferometer arranged for destructive interference is used to coherently subtract the background from the optical field using a sign-inverted replica before the optical power arrives at the photodetector, which converts absorption from dips to peaks in spectra. However, this method is directly limited by the realistic intensity extinction ratio (Field unbalanced factor), which necessitates locking and additional components in the setup to control and practically difficult to further decrease. Therefore, the advantage of this BFS method over direct

absorption spectroscopy (DAS) is limited to only a ~10 times improvement in SNR [84,86] and is not experimentally demonstrable in some cases [85].

In this work, we propose a new method, optical-parametric-amplification-enhanced background-free spectroscopy (OPA-BFS). We discuss it in the context of ro-vibrational spectroscopy, but it is also potentially applicable to other kinds of absorption spectroscopy. First, similar to refs. [84–86], the sample is interrogated by short pulses (generally mid-IR), the background excitation of which is suppressed by an interferometer. Next, the output from the interferometer, which includes sample response and residual background, is amplified by a short-pulse optical parametric amplifier (OPA). The pump pulses (generally near-IR) of the OPA are kept at a chosen delay relative to the signal pulses (output from the interferometer), so they can amplify a strong part of the FID field while being far away from the center of the original excitation pulses to avoid residual background. We theoretically and numerically demonstrate that this method can further improve the SNR and limit of detection (LOD) of the above-mentioned broadband linear BFS by orders of magnitude, without requiring a lower extinction ratio or time-resolved measurements which can be experimentally challenging. On one hand, while OPA-BFS amplifies the absorption signal of the samples and make it more detectable, there is no limitation on the type of spectrometer used for spectrum acquisition; one can either use a typical frequency-domain spectrometer, like a grating-based OSA, monochromator, or FTIR, or a time-domain spectrometer, such as dual-comb spectroscopy [19], electro-optic sampling [82,91] or cross-comb spectroscopy [83]. In comparison, existing BFS by temporal gating [79,81–83] is less flexible because it demands time-resolved spectrometry, which can have some advantages over traditional frequency-domain spectrometry but requires more experimental effort. On the other hand, thanks to the temporal gating provided by short-pulse nonlinearity, OPA-BFS is not limited by and has a relaxed requirement on the extinction ratio of the destructive interference compared to existing broadband BFS based on linear interferometry. Although extinction ratios of ~10^{-4} have been demonstrated [84–86], achieving further extinction remains technically challenging due to misalignment, substrate thickness mismatch and environment noise [85], which strictly limits the advantages of linear BFS.
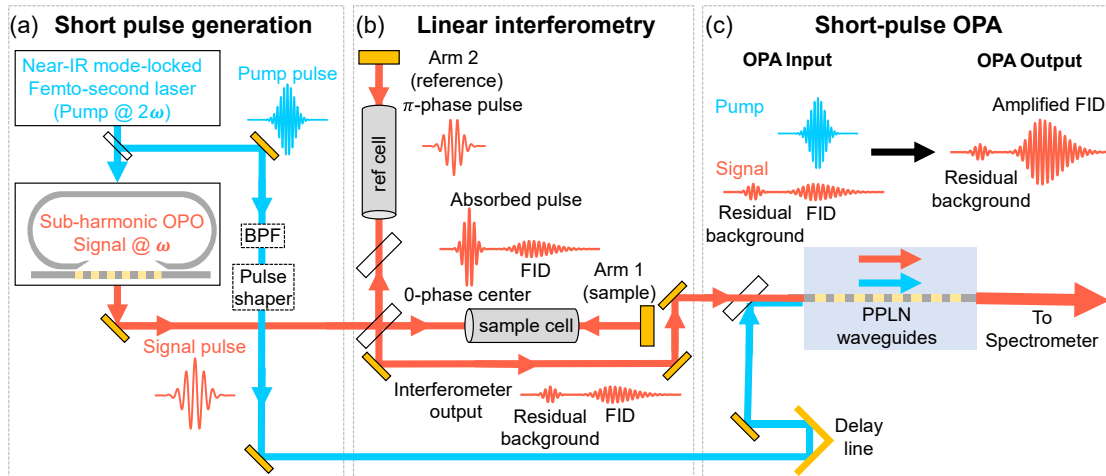
Figure 3.1: **OPA-enhanced background-free spectroscopy (OPA-BFS). (a)** short pulse generation. BPF: bandpass filter. BPF and pulse shaper may be required to change and control the profile and pulse width of the original pump pulse because the short-pulse OPA in (c) may need a pump pulse with a longer pulse width and a different profile. **(b)** Linear interferometry. While a Michelson-like interferometer is illustrated here, a Mach-Zehnder-like interferometer can also work. For clarity, we only present the most important components of the interferometer; more details, especially regarding dispersion compensation and delay locking, can be found in refs. [84–86]. Note that we make a very short and clean separation between the excitation pulse (center) and FID radiation for clarity of the illustration, which is not always the case in practice. However, this will not influence our following analysis and arguments, as there will always be part of the FID radiation that is far enough from the excitation pulse center and thus can be separated well. **(c)** Short-pulse OPA. Here, we show the illustration of an OPA based on nanophotonic periodically-poled lithium niobate (PPLN) waveguides [63,70], which was recently demonstrated with unprecedented high gain and broad bandwidth. However, it can also be any other platform or material that can support short-pulse OPA with high parametric gain.

3.2. System architecture

The architecture of OPA-BFS is presented in Figure 3.1, which is composed of three parts: short pulse generation, linear interferometry, and short-pulse OPA. While OPA-BFS does not require any specific technique for the pulse generation, Figure 3.1(a) illustrates a sub-harmonic optical parametric oscillator (OPO) synchronously pumped by a short-pulse mode-locked laser (typically a fiber laser), which is a common way to generate short mid-IR pulses[62,49,92,53,93]. One important advantage of synchronously-pumped OPOs is that the timing and phase of signal pulses and pump pulses are intrinsically locked, which can exempt additional efforts in their control for the short-pulse OPA [56]. The second step is to use the signal pulses (generally mid-IR) to interrogate the sample with a detection

background suppressed by linear interferometry, as illustrated in Figure 3.1(b). The output of the interferometer consists of two parts, the residual pulse center (background) which cannot be fully eliminated by the interferometer and the subsequent FID signal which carries the spectral information of the sample. Compared to the residual background (originally the excitation pulse) that is much more localized in the time domain (pulse width of ~10-100 fs), the FID signal can typically last at least hundreds of ps and sometimes have a local maxima at a relative delay of 10-100 ps [79,80,94,95]. This can be understood equivalently in the frequency domain; while femtosecond pulses can have a bandwidth as broad as tens of THz, a typical vibrational absorption has a linewidth on the order of magnitude of only 10 GHz at room temperature and atmospheric pressure, which can be even smaller at lower pressure or temperature. The output of the interferometer is then sent to a short-pulse OPA (Figure 3.1 (c)) as the signal to be amplified. The pump pulse is held at a chosen delay with respect to the signal such that it overlaps with a strong portion of the FID but is far away from the excitation center. Therefore, the FID carrying useful sample signatures is amplified while the residual background is not, as it does not temporally overlap with the pump pulse. This can further improve the SNR of the absorption spectrum and make a trace sample detectable that cannot be detected by DAS or linear BFS.
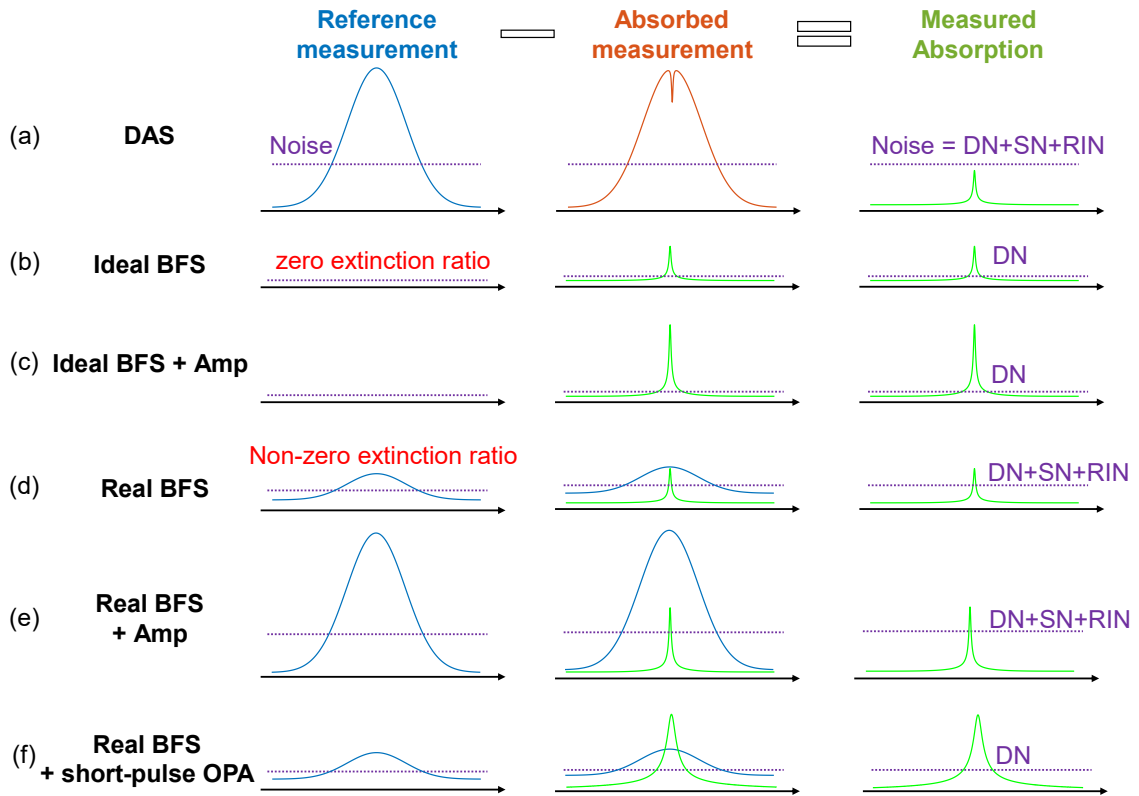
Figure 3.2: **Qualitative comparison between different spectroscopy schemes.** (**a**) DAS.
(**b**) Ideal (linear) BFS. (**c**) Ideal BFS followed by an ideal general frequency-domain
amplifier (GA). (**d**) Real BFS. (**e**) Real BFS followed by a GA. (**f**) Real BFS followed by
a short-pulse OPA.

3.3. Qualitative comparison

Figure 3.2 qualitatively compares different spectroscopy schemes in detecting small
absorption (trace sample) to show the advantage of OPA-BFS. In traditional DAS (Figure
3.2(a)), one must compare two measurements, one without sample (reference measurement,
blue curve) and one with sample (absorbed measurement, red curve), the difference of
which is the absorption signal of interest (green curve). There are three primary kinds of
noise: detector noise (DN), shot noise (SN), and relative intensity noise (RIN), and any of
them may dominate and limit the detection depending on the power incident on the detector.
The noise level for each spectrum is denoted by the purple dashed line. Generally, if we
assume a high source power which can saturate the detector, the RIN will dominate and
fundamentally limit the detection. Therefore, one cannot detect an absorption dip smaller
than the RIN, which is proportional to the full power of the light source (excitation

background). In ideal BFS (Figure 3.2(b)) where the background is fully eliminated in the reference measurement, the absorption is a bright peak instead of a dark dip in the absorbed measurement. In this case of perfect background elimination, the power arriving at the detector is from the absorption, the signal of interest, so a noise proportional to (smaller than) the signal does not limit the detection of the existence of the absorption. Therefore, we do not consider RIN as the limiting factor in this ideal case. In principle, SN may still limit the detection. However, here we focus on the case that SN is negligible compared to the DN, which is typically the case for less-advanced detectors, especially in MIR wavelength range. This is why we only indicate DN there (same for Figure 3.2(c) and (f)). As absorption is a positive peak instead of a negative dip in BFS, it is natural to add an amplifier after it, which can further improve the detectability of the signal (Figure 3.2(c)). Note that the amplifier here refers to a general ideal frequency-domain amplifier (GA) which does not bring in extra noise and has no temporal features. In these two ideal cases, the LOD (defined as minimum detectable absorbance) is decided by the available source power and amplification, which is free from detector saturation and RIN.

However, these two ideal cases are not realistic because the extinction ratio in real linear interferometry is always non-zero and results in a residual background. Although linear BFS can increase the SNR to some extent (Figure 3.2(d)), the residual background can still fundamentally limit the LOD via SN or RIN at high power like DAS and prevents detection of lower absorption. Moreover, adding a general (frequency-domain) amplifier after the linear interferometry is not helpful in the RIN-limited regime because the noise (SN and RIN) from the residual background is also amplified by the same factor as the absorption signal (Fig. 2(e)). In contrast, a short-pulse OPA can make a difference (Figure 3.2(f)). Upon a proper timing of the pump pulse, one can amplify only the FID (absorption signal) but avoid the excitation pulse center (residual background), which will remain almost the same. Thus, OPA-BFS can further increase the SNR in addition to the enhancement from linear BFS, and the LOD of OPA-BFS is fundamentally limited by the available source power and OPA amplification.

3.4. Theoretical model of BFS based on linear interferometry

To further demonstrate the advantages of OPA-BFS quantitatively, we conduct theoretical analysis and numerical simulation for different detection schemes and types of samples. The mathematical models for BFS of linear interferometry and noise analysis are based on refs. [84–86,96]. Specifically, some important parameters are adapted from a recent state-of-the-art experimental result reported in ref. [86], including the Field unbalanced factor $\delta = 10^{-2}$ and RIN ratio $\sigma_r = 10^{-2}$. Note that those numbers are very close to the experimental results in ref. [86] but with a simpler value for ease of presentation. More importantly, for linear BFS, the model using those two parameters gives a theoretical LOD of absorbance equal to $\delta\sigma_r = 10^{-4}$, which agrees with what is experimentally demonstrated in ref. [86].

The amplitudes of electric field in the sample arm ("Arm 1," subscript "spa") and reference arm ("Arm 2," subscript "rfa") are described as:

$$E_{spa} = E_0 e^{-\frac{A}{2}} \tag{3.1}$$

$$E_{rfa} = -E_0(1 + \delta). \tag{3.2}$$

In the equation of E_{spa}, A denotes a small absorbance ($A \ll 1$). In the equation of E_{rfa}, the negative sign denotes a π phase change (destructive interference), and δ is the Field unbalanced factor, which is assumed real in this work. Note that we assume a small absorbance $A \ll \delta$. Also, we assume a power $P_0 = cE_0^2$, where c is a proportional constant and will be omitted in the following derivation. Therefore, the total optical power entering the interferometer is approximately $2P_0$. At the output of the interferometer, the amplitude and power of the combined field are:

$$E = E_{spa} + E_{rfa} = -E_0\left(1 - e^{-\frac{A}{2}} + \delta\right) \cong -E_0\left(\frac{A}{2} + \delta\right) \tag{3.3}$$

$$P = E^2 = E_0^2\left(\frac{A}{2} + \delta\right)^2 \cong P_0(\delta^2 + A\delta). \tag{3.4}$$

Therefore, in BFS, the optical power incident on the detector of the reference (without sample, A=0) and absorbed measurements is:

$$P_{ref}^{BFS} = P_0(\delta^2) \tag{3.5}$$

$$P_{abs}^{BFS} = P_0(\delta^2 + A\delta). \tag{3.6}$$

The absorption signal, i.e., the difference between these two measurements, is:

$$P_s^{BFS} = P_0(A\delta). \tag{3.7}$$

Similarly, for direct absorption spectroscopy (DAS), we have:

$$P_{ref}^{DAS} = P_0 \tag{3.8}$$

$$P_{abs}^{DAS} = P_0 e^{-A} \cong P_0(1 - A) \tag{3.9}$$

$$P_s^{BFS} = P_0 A. \tag{3.10}$$

As for the noise,

$$P_N = \sqrt{P_{DN}^2 + P_{SN}^2 + P_{RIN}^2} = \sqrt{P_{DN}^2 + P_0 h\nu(\Delta f)^{-1} + (P_t \sigma_r)^2}. \tag{3.11}$$

Here, P_{DN}, P_{SN}, and P_{RIN} denote the detector noise (DN), shot noise (SN), and relative intensity noise (RIN), respectively. P_t denotes the average total power incident on the detector, and σ_r denotes the RIN. h is Planck's constant, ν is the optical frequency, and Δf is the measurement bandwidth (reciprocal of the measurement time for each spectral element).

In this work, we assume that shot noise is negligible compared to the other two kinds of noise, which is generally the case for less-advanced detectors, especially in the MIR range. Note that this assumption agrees with the results of some previous experimental works, for example, ref. [86]. Next, we define a "detectable signal" as having a SNR=1 ($P_s = P_n$). Hence, for BFS at high powers, when RIN dominates, we have:

$$P_s = P_0(A_{LOD}^{BFS}\delta) = P_N = P_0(\delta^2)\sigma_r \tag{3.12}$$

$$A_{LOD}^{BFS} = \delta\sigma_r. \tag{3.13}$$

For DAS, we have

$$P_s = P_0 A_{LOD}^{DAS} = P_N = P_0 \sigma_r \tag{3.14}$$

$$A_{LOD}^{DAS} = \sigma_r. \tag{3.15}$$

The above derivation shows that, in the RIN-limited regime, $P_s^{BFS} = \delta P_s^{DAS}$ and $P_N^{BFS} = \delta^2 P_N^{DAS}$, giving the conclusion $A_{LOD}^{BFS} = \delta A_{LOD}^{DAS}$. This shows the SNR advantage of BFS in

the RIN-limited regime, as δ is generally very small ($\delta \ll 1$), and also highlights the benefits of reducing the Field unbalanced factor or at least suppressing its effect.

3.5. Simulation model and parameters

The simulation of OPA is based on solution of the coupled wave equations using the Fourier split step method [61,62], the parameters of which are based on previous experimental demonstrations of high-gain OPA in thin-film lithium niobate [63]. The absorption of molecules is modeled based on data from the HITRAN database [65], using a Lorentz oscillator model for the line profile.

3.5.1. Simulation model

Simulation of the optical parametric amplification (OPA) process between the pump at frequency 2ω and signal at frequency ω in the nonlinear crystal is based on solving the coupled wave equations as in ref. [62], which are given as:

$$\partial_z E_\omega(z,t) = \kappa E_{2\omega} E_\omega^* - \frac{\alpha_\omega}{2} + \widehat{D}_\omega E_\omega \tag{3.16}$$

$$\partial_z E_{2\omega}(z,t) = -\kappa E_\omega^2 - \frac{\alpha_{2\omega}}{2} - \Delta\beta' \partial_t E_{2\omega} + \widehat{D}_{2\omega} E_{2\omega} \tag{3.17}$$

where we have taken the time coordinate, t, to be co-moving with the signal. Additionally, the pump envelope phase has been shifted by $\pi/2$ to ensure real solutions if higher orders of dispersion are not considered. In these equations, the subscripts ω and 2ω are used to denote the signal and pump, respectively. E_i, $i \in \{\omega, 2\omega\}$, denotes the electric field amplitude, normalized such that $|E_i|^2$ gives the instantaneous power. The nonlinear coupling coefficient is given by $\kappa = \sqrt{2\eta_0}\omega d_{eff}/(w n_\omega \sqrt{\pi n_{2\omega}}c)$, where η_0 is the impedance of free space, d_{eff} is the effective nonlinearity, w is the beam radius where a symmetric Gaussian mode has been assumed, n_i is the refractive index, and c is the speed of light. α_i is the absorption coefficient, which accounts for losses incurred during propagation in the waveguide. The group velocity mismatch between pump and signal is given by $\Delta\beta'$. Finally, $\widehat{D}_i = \sum_{m=2}^{\infty}[\frac{(-i)^{m+1}\beta_m^{(m)}}{m!}]$ is the dispersion operator, which describes the material dispersion experienced by the pump and signal during propagation in the waveguide. In our simulation, we consider up to third order dispersion.

For simulating the signal response to propagation through the sample, we use a Lorentz oscillator model to compute the complex refractive index of the gas of interest. Specifically, we find the index, $n(\omega)$ as:

$$n^2(\omega) = 1 + \sum_{ij} \frac{f_{ij} N_j q^2}{2\varepsilon_0 m_e \left(\omega_{ij}^2 - \omega^2 + i\gamma_{ij}\omega\right)}. \tag{3.18}$$

Here, the indices i,j refer to the upper and lower state of the transition, f_{ij} is the oscillator strength, N_j is the number density of molecules in state j, q is the electron charge, ε_0 is the vacuum permittivity, m_e is the mass of the electron, ω_{ij} is the center frequency of the transition, and γ_{ij} is the linewidth. $n(\omega)$ may be separated into its real and imaginary components,

$$n(\omega) = n'(\omega) - i\kappa(\omega) \tag{3.19}$$

where the imaginary part, $\kappa(\omega)$ defines the absorption experienced because of the interaction of light with the sample, and $n'(\omega)$ accounts for the signal dispersion. The Lorentz oscillator defined as such allows us the flexibility to simulate multiple gases, as presented in the results of the main text, using parameters provided by the HITRAN database [65]. Additionally, we may use this model to define mock samples with arbitrary linewidths, strengths, and center frequencies to investigate theoretically more easily the consequence of these various parameters on the system response.

3.5.2. Waveguide parameters

The parameters used for simulating the nonlinearity are based on OPA in a thin-film lithium niobate waveguide, as in ref. [63].We consider a 700-nm thin film deposited on a silica substrate. The waveguide is taken to have a width of 1800 nm, and an etch depth of 375 nm. This gives rise to the following simulation parameters:

$\beta_\omega^{(2)}$	$\beta_\omega^{(3)}$	$\beta_{2\omega}^{(2)}$	$\beta_{2\omega}^{(3)}$	$\alpha_\omega, \alpha_{2\omega}$	$\Delta\beta'$	L	d_{eff} [52]	n_ω	$n_{2\omega}$	Beam Radius
20.3 fs^2/mm	-1196.4 fs^3/mm	119.3 fs^2/mm	20.3 fs^2/mm	0.023	0.4637 fs/mm	6 mm	18.7 pm/V	1.854	2.057	0.8 μm

3.5.3. Signal (mid-IR) pulse

Center frequency	Pulse Shape	Pulse width	Average power	Repetition rate
143. 4 THz (2.09µm)	Sech	40 fs	1000 mW	250 MHz

The average power of 1000 mW leads to a power per spectral element ~0.1-1 mW/0.1nm around the center wavelength of the signal spectrum, which can just reach the assumed detector saturation (1 mW) (for DAS) and make the detection RIN-limited (for DAS, BFS, and BFS+GA). Note that we use the same signal parameters for all simulations in this work.

3.5.4. Pump pulse

We use different pump pulses for different samples. Note that the repetition rate of all pump pulses is the same as that of the signal pulse, 250 MHz.

For mock sample:

Center frequency	Pulse Shape	Pulse width	Average power	Delay of pulse center
286.9 THz (1.045µm)	Rectangular	50 ps	500 mW	25 ps

For NH_3:

Center frequency	Pulse Shape	Pulse width	Average power	Delay of pulse center
286.9 THz (1.045µm)	Rectangular	20 ps	250 mW	12 ps

For CO_2:

Center frequency	Pulse Shape	Pulse width	Average power	Delay of pulse center
286.9 THz (1.045μm)	Sech	5 ps	100 mW	25 ps

3.5.5. Noise and Field unbalance factor

Field unbalance factor δ	RIN σ_r	Detector noise	Detection bandwidth	Spectrometer resolution (Width of element)
10^{-2}	10^{-2}	1 pW/(Hz$^{1/2}$)	1 kHz	0.1 nm

These parameters are either adapted from the experimental values of refs. [84–86] or from typical values of commercial devices.

3.6. Results and discussion
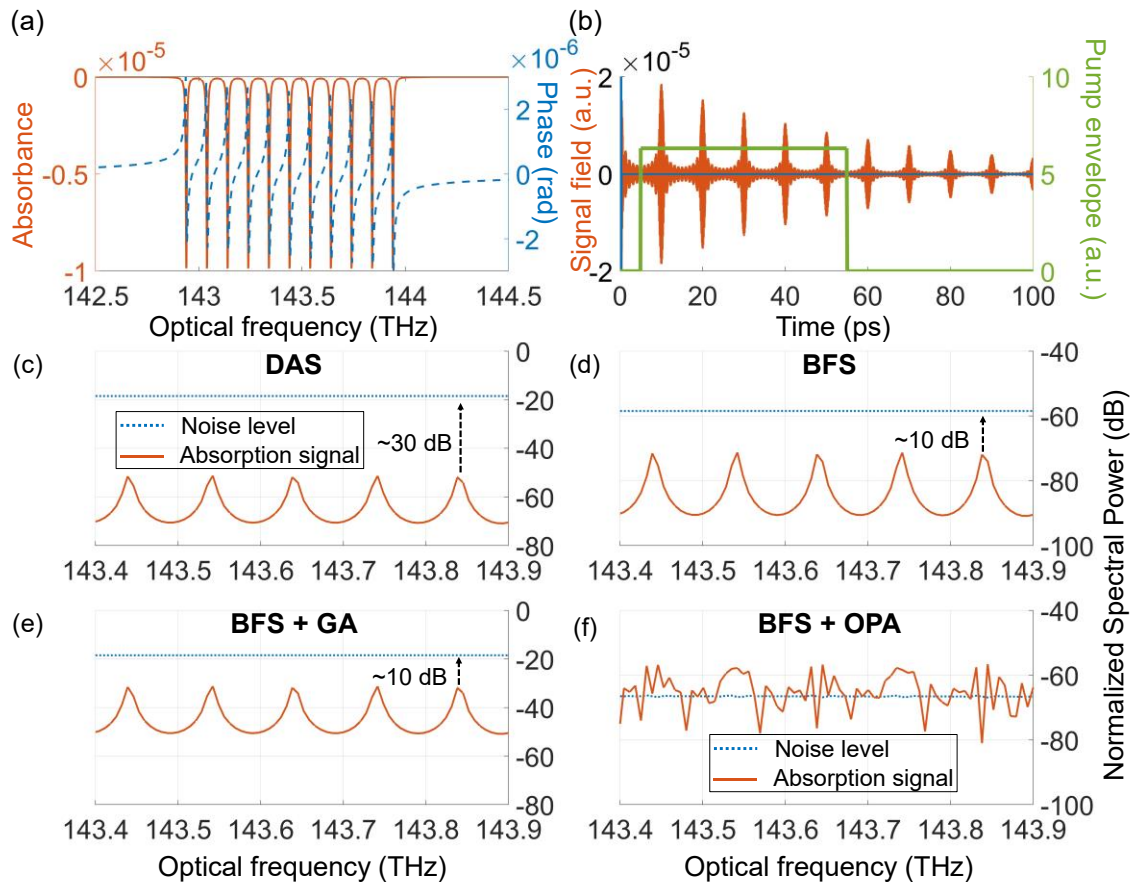
Figure 3.3: **OPA-BFS for a mock sample. (a)** Intensity (absorbance, red solid curve) and phase (blue dashed curve) of 11 Lorentzian transitions assumed for the mock sample. **(b)** FID field of the signal pulse (red curve, left y-axis) that probed the sample in the interferometer (see "Arm 1" in Fig. 1(b)). Note that, to show the weak and long FID, the y scale (intensity) is zoomed in and x scale (time) is zoomed out; therefore the stronger and narrower background residual (blue curve) cannot be seen clearly here. The yellow curve (right y-axis) denotes the envelope of the pump pulse. **(c)-(f)** Spectral noise level (blue dotted curves) and ideal absorption signal (red solid curves) in different detection schemes. The absorption signal is the difference between the reference measurement (without sample) and the absorbed measurement (with sample), and the noise level is an incoherent addition (quadratic mean) of the total noise level (including DN, SN, and RIN) in these two measurements. Note that we zoom into the central five transitions to show the details more clearly.

First, we conduct a simulation for a mock sample to give a simple and clear illustration. The mock sample is set to have 11 equally strong and equally spaced Lorentzian transitions with the same linewidth of 6 GHz. Those transitions are distributed from 143 THz to 144

THz, with a peak absorbance of 10^{-5} as shown in Figure 3.3(a), together with the phase profile. We use a sech signal (excitation) pulse with a center wavelength of 2.09 µm (143.4 THz) and a 40-fs pulse width to interact with the sample in the interferometer. The output of the interferometer consists of two parts, the residual background (excitation pulse) and FID, part of which is shown in Figure 3.3(b) (red curve, left y-axis). One can observe a pattern in the FID with a period of 10 ps, which is a result of the coherent addition of reradiation of those transitions with a 100-GHz spacing [79,94,95]. To amplify the FID, we use a rectangular pump pulse with a center wavelength of 1.045 µm (286.9 THz) and pulse width of 50 ps, the envelope of which is denoted by the yellow curve (right y-axis) in Figure 3.3(b). Note that we keep the center of the rectangular pump pulse at a delay of 30 ps with respect to the center of the signal pulse (zero of the time axis), by which the pump can cover a strong part of the FID while avoiding the residual background.

While more detailed figures about the simulation can be found in the next section (supplementary results), the results of the absorption signal and noise level in different detection schemes are presented in Figure 3.3(c)-(f). Note that we assume a grating-based spectrometer for detection of the 2.09-µm signal spectra with a resolution of 0.1 nm. Also, we assume a high enough average power for the 2.09-µm excitation pulse such that the peak of its spectrum can just saturate the detector of the spectrometer, and all the spectral power is normalized to it and presented on a logarithmic scale. Therefore, the noise level is about -20 dB in DAS (Figure 3.3(c)), which is dominated by RIN, corresponding to a $\sigma_r = 10^{-2}$. As we set an absorbance of 10^{-5}, the absorption signal level is -50 dB, which is 30-dB weaker than the noise level and thus undetectable in DAS. In linear BFS, while the absorption signal will be lowered by δ, the background will be suppressed by δ^2 as will the RIN (See the section of theoretical model for detailed derivation). Therefore, the SNR can be increased by $1/\delta$ if the RIN still dominates, which is the case for our example here. As shown in Figure 3.3(d)), compared to DAS, the noise level in BFS is suppressed by 40 dB ($\delta^2 = 10^{-4}$) and now around -60 dB, and the signal level is lowered by 20 dB ($\delta = 10^{-2}$) and now -70 dB. Obviously, although the SNR has been increased by 20 dB ($1/\delta$), the signal is still below the noise level and thus still undetectable. This agrees with

the fact that the absorbance we set here (10^{-5}) is lower than the LOD of the linear BFS ($\delta\sigma_r = 10^{-4}$). Next, we try to amplify the output of the interferometer with an ideal general amplifier (GA) with a power gain of 40 dB, and the result is shown in Figure 3.3(e). Compared to BFS, while the signal is amplified by 40 dB, the noise level is also amplified by the same factor; therefore, the SNR is not increased. We assume a power gain of 40 dB because it corresponds to $(1/\delta)^2$, which will bring the output spectra back to the saturation level of the spectrometer. One can apply a higher power gain if the spectrometer saturation is not considered, but it still cannot increase the SNR. Finally, Figure 3.3(f) presents the result of OPA-BFS. The absorption signal reaches above -60 dB, which is amplified by about 10 dB in the frequency domain. This frequency-domain amplification factor is much less than that of the GA in panel (e) because the OPA pump pulse only covers a small temporal range of the whole FID. However, as the pump pulse avoids the residual background in the time domain, the noise is not amplified like GA, by which the SNR is effectively increased compared to linear BFS. In fact, we even observe a decrease in the noise, because part of the energy of the residual background pulse (2.09 µm) flows to the pump wavelength (1.045 µm) via second harmonic generation (SHG). The SHG here is prominent since the signal pulse is set with a relatively high power because we want to work in the RIN-limited regime. Even if we ignore the SHG effect, the absorption signal reaches above -60 dB, the same as the noise in the linear BFS (see Figure 3.3(d)), and so will still be detectable (SNR >= 1). In this case, the LOD will be limited by the amplification of the OPA instead of the RIN or detector saturation. There is some observed broadening and distortion of the resolved peaks, which is mainly due to the finite temporal window of the pump pulse and the phase-sensitive nature of the OPA gain. Nevertheless, the basic spectral information, including the center frequencies and relative intensities of the transitions, are well preserved. One can always try to apply a longer pump pulse to cover a wider temporal range to alleviate this problem. However, for a given average power of the pump, there is a trade-off between the peak power (temporal gain) and width (temporal window) of the pump pulse.
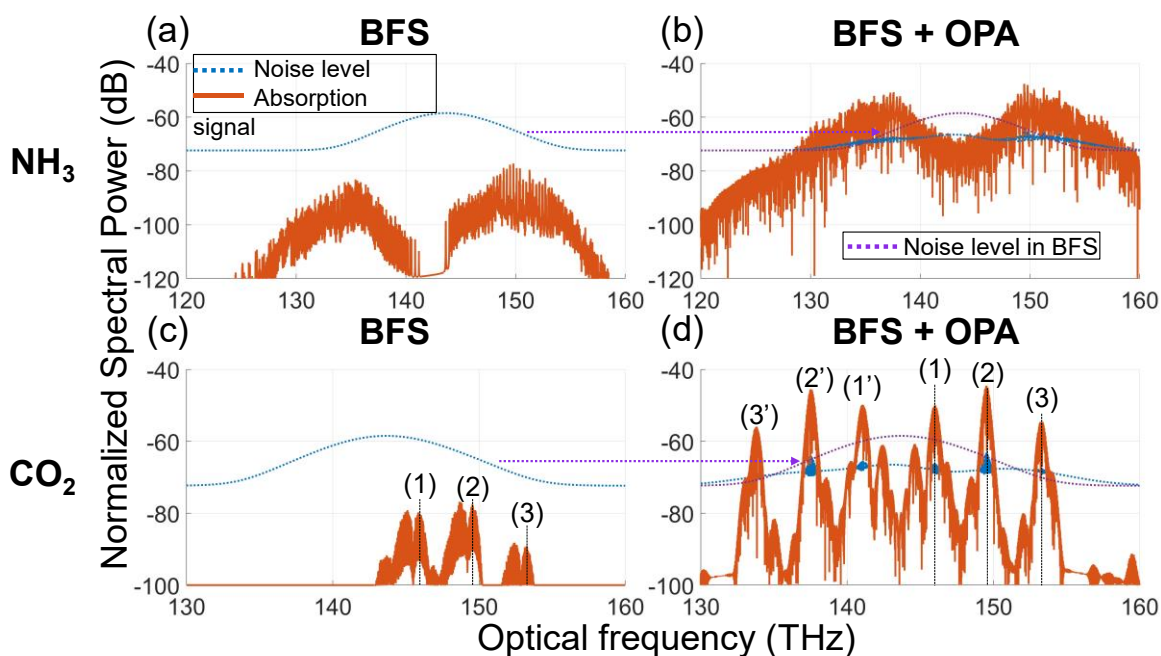
Figure 3.4: **BFS and OPA-BFS for NH3 ((a)-(b)) and CO2 ((c)-(d)) around 143.4 THz.** The purple dotted lines in (b) and (d) denote the noise level in corresponding BFS spectra (blue dotted curves in (a) and (c)). Note that there are some weak transitions missing around the center of the NH_3 absorption (141-142 THz) due to data missing from HITRAN database.

For further demonstration of OPA-BFS, we conduct simulation with real molecules. As we have shown that the SNR of BFS can be higher than that of DAS and cannot be further increased by an ideal GA, here we only present the results of BFS and OPA-BFS. Note that the parameters for the linear BFS and noise are the same as those of the last example. Results for NH_3 are shown in Figure 3.4(a)-(b). We set the transition at 151.3 THz, the strongest one around the center frequency of our excitation pulse (143.4 THz), to have an absorbance of 10^{-5}, so the absorbance of other nearby transitions is smaller than 10^{-5}. Therefore, all transitions are below the LOD of the linear BFS (see Figure 3.4 (a)). Here, we continue to use a rectangular pump pulse but with a shorter pulse width of 20 ps, the center of which is held at a delay of 12 ps. As shown in Figure 3.4(b), the absorption signal is above the noise level and well detectable in OPA-BFS. As before, the noise level in OPA-BFS (blue dashed curve) is decreased because of SHG. However, the absorption signal here is also higher than the original noise level in BFS (purple dashed line) and thus still detectable even if we do not consider the SHG effect. The same is observed in the case

of CO_2 (see Figure 3.4(c)-(d)). For CO_2, there are three groups of transitions of close to 143.4 THz, which are around 145.8 THz, 149.6 THz, and 153.3 THz, as labeled in Figure 3.4(c). The transition at 149.6 THz, the strongest among the three groups, is set to have an absorbance of 10^{-5}. Here, different from previous cases, we use a sech pump pulse with a pulse width of 5 ps at a relative delay of 25 ps to amplify the FID. Figure 3.4 Figure 3.4(d) shows that OPA-BFS makes the absorption signal stronger than the noise and thus readily detectable. Although there are some distortions to the absorption profile as we use a relatively short pump pulse for higher gain, the center of each transition group is well captured (see the labels corresponding to panel (c)), which can be enough for detection and identification of the molecule. Notably, new frequency components (labeled (1'), (2'), and (3')) are found on the other half of the spectrum. They are idler radiation generated in the OPA and thus symmetric to their corresponding signal frequencies with respect to the center frequency (143.4 THz). If we also include the radiation around the idler frequencies into our detection, the SNR and LOD can be further enhanced. In short, for both molecules, we demonstrate that OPA can enhance the LOD of linear BFS by more than one order of magnitude, considering that the absorbance for both molecules is less than or equal to 10^{-5}.

Note that the obtained absorption signal in OPA-BFS depends on many parameters, including the power, profile, width, and center delay of the pump pulse, and we only show one possibility for each example above. Also, different molecules may have strong FID at different time delays. For an efficient multispecies detection, one can split the pump pulse into multiple replicas and use multiple delay lines to control them to cover different time windows. Moreover, there is a trade-off between temporal gain and spectral resolution, the essence of which is the trade-off between width and peak power of pump pulse with a fixed average power. A complete and systematic discussion and optimization of those parameters is useful but involved, so they are beyond the scope of this work and will be the subject of future works.
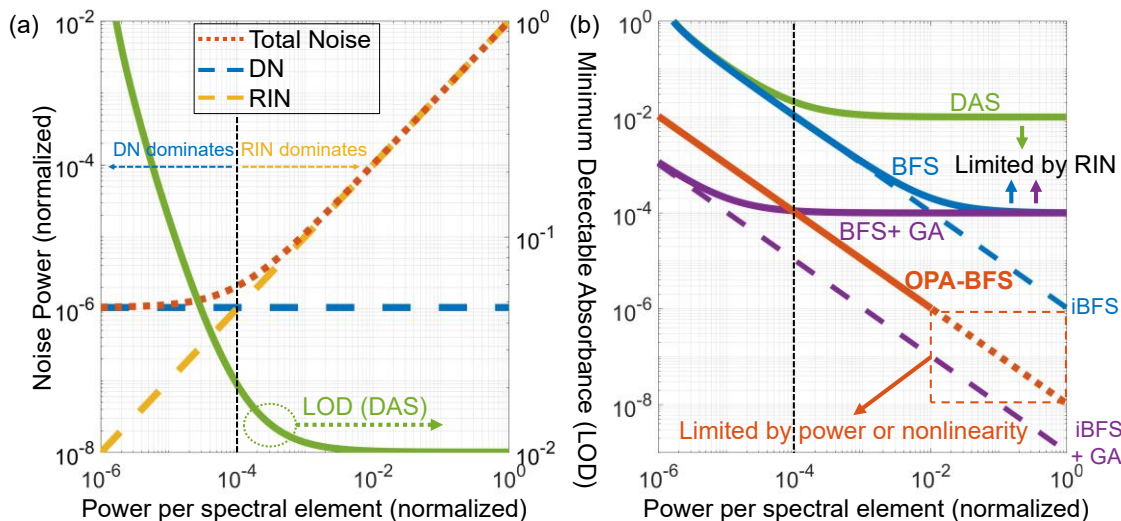
Figure 3.5: **Noise and LOD scaling with excitation power of different spectroscopy schemes. (a)** Detector noise (DN, blue dashed line), relative intensity noise (RIN, yellow dashed line) and total noise (red dotted curve) in DAS (left y-axis). Green curve (right y-axis) denotes the limit of detection (minimum detectable absorbance, SNR=1) of DAS. **(b)** LOD scaling with excitation power of different schemes. Solid curves: DAS (green, same as the green solid curve in (a)), BFS (blue), BFS+GA (purple), and OPA-BFS (red). Dashed curves: ideal BFS (iBFS, blue) and iBFS+GA (purple).

We finally investigate how the noise and LOD scale with excitation power for different detection schemes, which are presented in Figure 3.5. Here, we assume a detector saturation power of 0.1 mW and all power displayed is normalized to it. More details and parameters for this calculation can be found in previous sections. Figure 3.5 (a) first depicts the scaling of the noise (left y-axis) for DAS as an example. In DAS, the total noise is dominated by detector noise (DN) or RIN when the relative excitation power is smaller or larger than 10^{-4}, respectively. This power scaling is basically similar to Fig. 1 of ref. [96] despite two differences. One is that we do not consider dynamic range of the whole detection system. The other is that the shot noise in our case is negligible and thus not shown in the figure, which is consistent with the finding in ref. [86]. If we define "detectable" as SNR=1, the corresponding LOD for DAS can be calculated and is denoted by the green solid curve (right y-axis). While higher power leads to a lower LOD when the DN dominates, the LOD stops decreasing and converges to 10^{-2} (σ_r) as the RIN dominates. Following DAS, the LOD scaling of other schemes is depicted in Figure 3.5 (b). The LOD of BFS (blue solid curve) can be lower than that of DAS because of the RIN

suppression, but it is still ultimately limited by RIN and converges to a fixed lower bound of 10^{-4} ($\sigma_r\delta$). An ideal general amplifier can decrease LOD of BFS at low power (purple solid curve), but it stops helping at higher power as the detector becomes saturated and the detection is limited by the RIN in the same way as the case without amplification. Finally, the red solid curve denotes the LOD of OPA-BFS. At low power, OPA is not as helpful as GA due to a gain penalty we set with it, since short-pulse OPA amplifies only a part of the signal in the time domain. However, OPA-BFS outperforms GA-BFS and linear BFS at higher power as its LOD continues to scale down because it is not limited by RIN. When the excitation power per spectral element is higher than a specific limit, which would vary case by case and we set 10^{-2} in this figure, further scaling down of the LOD in OPA-BFS (dotted red curve) depends on the availability of the total excitation pulse power or on having enough parametric gain for a high-power signal input. Note that two dashed lines, blue for ideal BFS (iBFS) and purple for iBFS+GA, are also displayed as useful references although they are not practical. In short, although BFS can lower the LOD of DAS to some extent, it is still limited by RIN at high powers due to a non-zero extinction ratio. While a general amplifier cannot effectively help, a short-pulse OPA can further lower the LOD of BFS by order(s) of magnitude.

The above discussion shows how short-pulse OPA-BFS can be practically useful compared to GA-BFS due to its ability to selectively amplify a portion of the time-domain signal, resulting in temporal gating. This motivates consideration of the method in comparison to other nonlinear sensing techniques, which may also provide temporal gating or up-conversion capabilities. One distinct advantage of OPA is its unique ability to achieve exponential amplification in the signal due to the conversion of photons from the pump [97,98], with amplification factors on the order of 100 dB/cm having been readily achieved [63]. This makes its gain and efficiency much higher than techniques based on, for example, second-harmonic generation or sum-frequency generation for the measurement of ultraweak signals [82,83,91], for which the output photon number cannot exceed the input signal photon number, placing a fundamental limit on the potential amplification [99]. OPA-BFS may also be considered in the non-degenerate regime, where signal up- or down-

conversion is possible in addition to amplification and background can be intrinsically zero even without linear interferometry.

3.7. Supplementary results
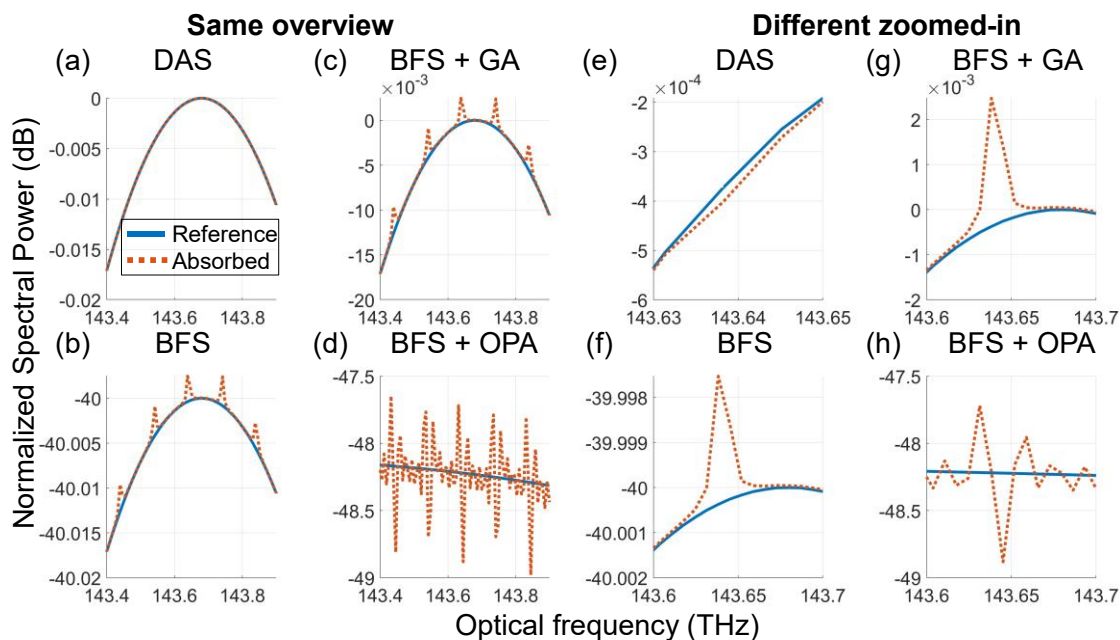
Figure 3.6: **Spectra of mock sample simulation.** Spectra of reference measurements (without sample) and absorbed measurements (with sample) for different spectroscopy schemes: (a)(e) DAS, (b)(f) BFS, (c)(g) BFS+GA and (d)(h) BFS+OPA.
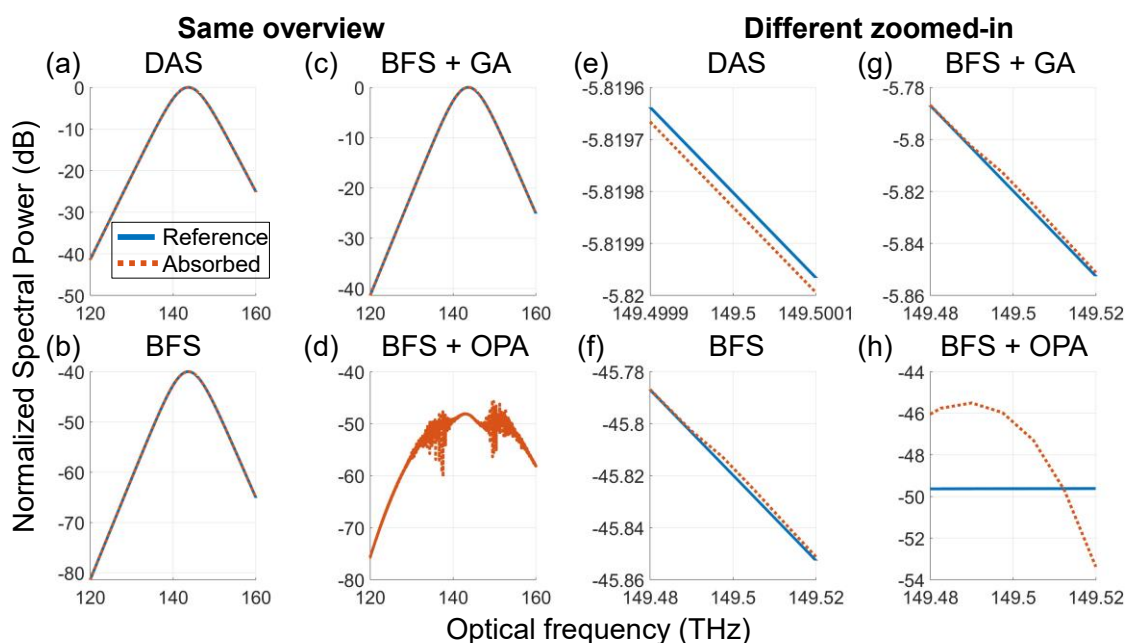
Figure 3.7: **Spectra of NH₃ simulation.** Spectra of reference measurements (without sample) and absorbed measurements (with sample) for different spectroscopy schemes: (a)(e) DAS, (b)(f) BFS, (c)(g) BFS+GA and (d)(h) BFS+OPA.
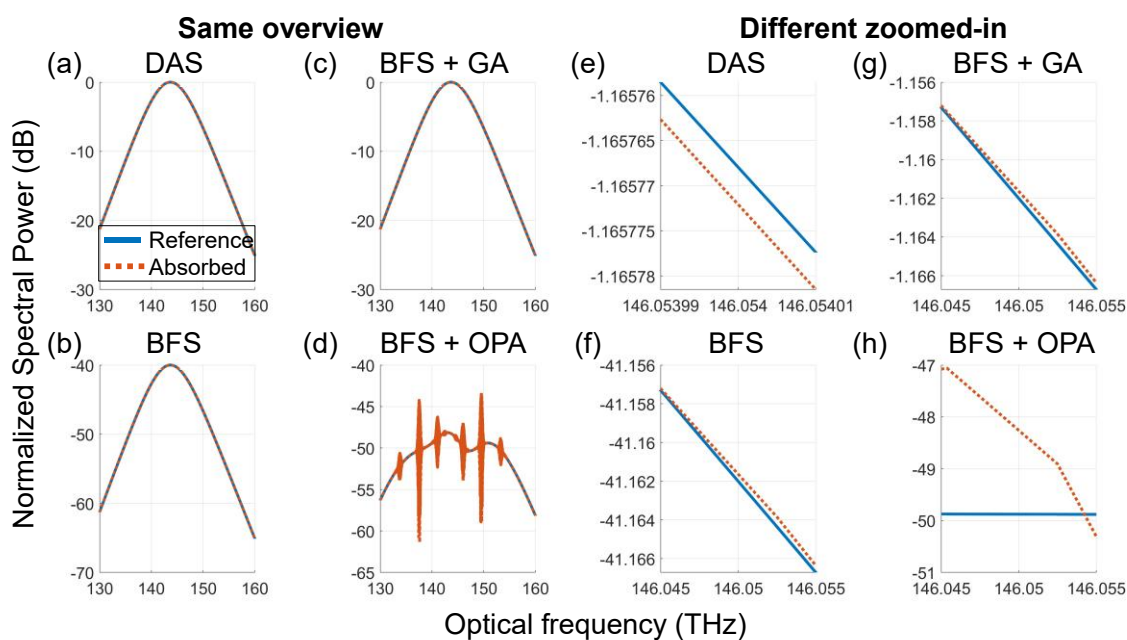
Figure 3.8: **Spectra of CO₂ simulation.** Spectra of reference measurements (without sample) and absorbed measurements (with sample) for different spectroscopy schemes: (a)(e) DAS, (b)(f) BFS, (c)(g) BFS+GA and (d)(h) BFS+OPA.

Figure 3.6, Figure 3.7, and Figure 3.8 present more results of simulation for mock sample, NH3, and CO2, respectively. Panels (a)-(d) depict the spectra of reference measurements (without sample) and absorbed measurements (with sample) for different spectroscopy schemes in the same optical frequency range as the corresponding figures of the main text, in which the absorption signal is the difference between these two measurements. Note that the two curves in the panels (a) of Figure 3.6, Figure 3.7, and Figure 3.8, as well as panels (b)-(c) of Figure 3.7 and Figure 3.8, are not visibly distinguishable because the absorption is tiny compared to the background. Therefore, we further zoomed in differently for different detection schemes to show the spectral difference, depicted in panels (e)-(h). Note that while panels (f)-(h) (BFS, BFS+GA, BFS+OPA) use the same zoom, panels (e) (DAS) are particularly more zoomed in to show the smaller difference.
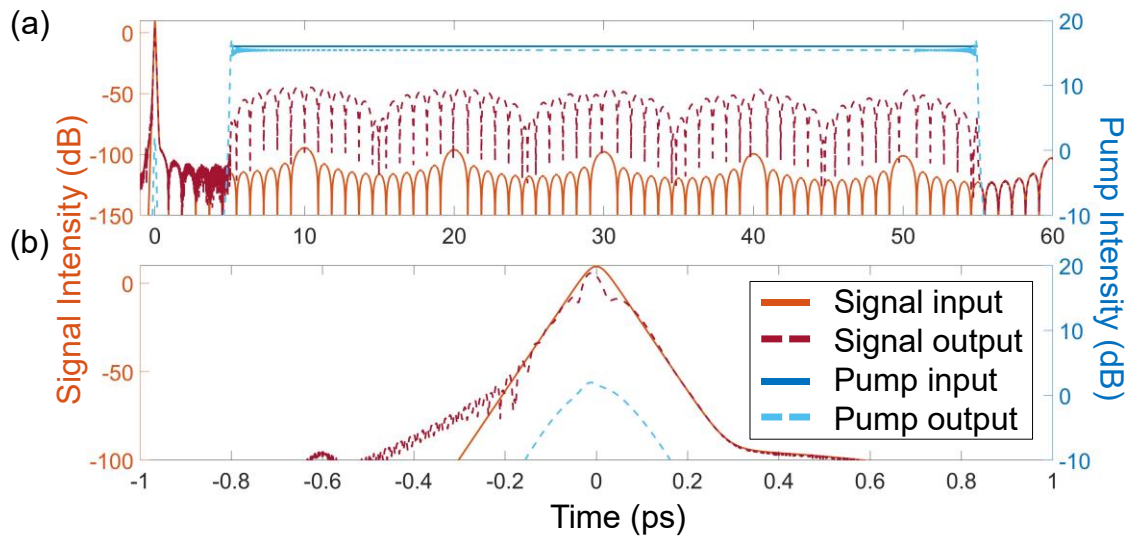
Figure 3.9: **Time domain of mock sample simulation. (a)** Time-domain overview from −1 ps to 60 ps. There is about a 50-dB gain for the signal field that temporally overlaps with the pump field. **(b)** Time domain zoomed into [−1,+1] ps, the center of the signal pulse.
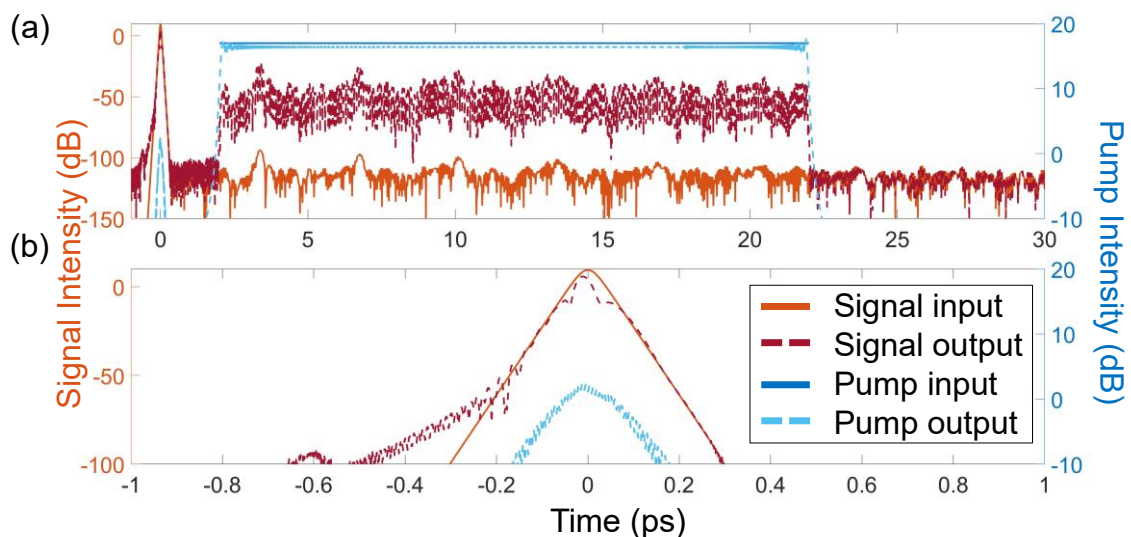
Figure 3.10: **Time domain of NH₃ simulation. (a)** Time-domain overview from −1 ps to 30 ps. There is about a 50-dB gain for the signal field that temporally overlaps with the pump field. **(b)** Time domain zoomed into [−1,+1] ps, the center of the signal pulse.
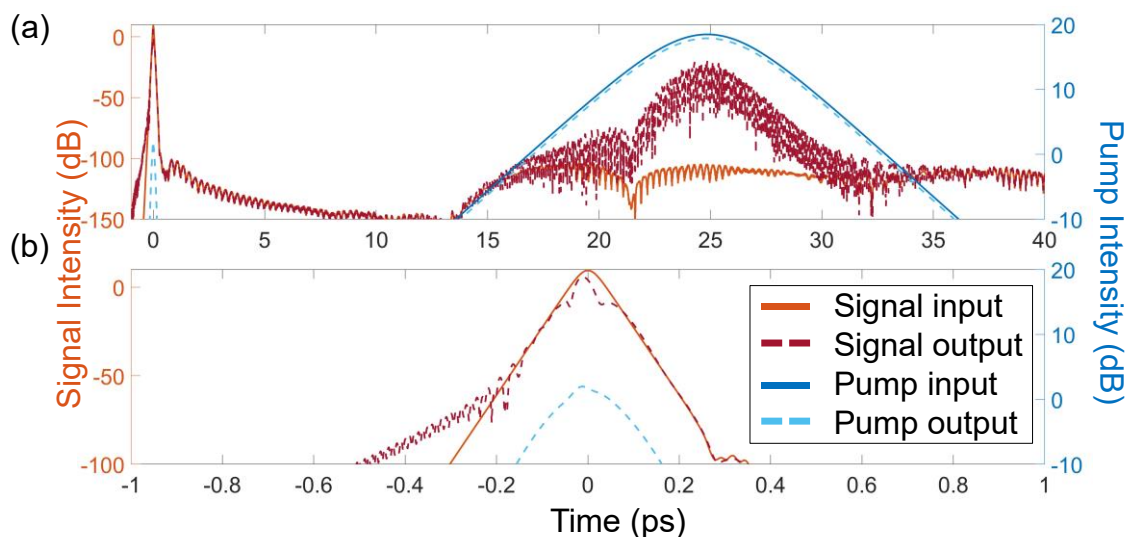
Figure 3.11: **Time domain of CO₂ simulation. (a)** Time-domain overview from −1 ps to 40 ps. There is about a 50-dB gain for the signal field that temporally overlaps with the pump field. **(b)** Time domain zoomed into [−1,+1] ps, the center of the signal pulse.

Figure 3.9, Figure 3.10, and Figure 3.11 show the time domain signal of the absorbed measurement in OPA-BFS. Panel (a) of each figure is a time-domain overview and mostly presents the FID part of the signal field that overlaps with the pump field, where the signal field is amplified by the pump field, i.e., energy flows from pump to signal. In contrast,

panel (b) zooms into the center of the signal pulse (excitation background), where one can observe decrease in the signal field and generation of new pump field because energy flows from the signal field to the pump field as a result of SHG.

3.8. Summary

In summary, we introduce a new method named OPA-BFS. While it can achieve a higher SNR and lower LOD in broadband vibrational spectroscopy, it does not require a lower extinction ratio or time-resolved measurements, which is experimentally challenging but has remained essential to existing BFS works. OPA-BFS not only combines and improves upon many merits of demonstrated techniques for background-free vibration spectroscopy, including both linear and nonlinear ones, but also circumvents some of their practical challenges. This work sheds new light on the potential for detection of trace molecules enhanced by optical nonlinearity, which can enable new limits in broadband vibrational spectroscopy and benefit numerous applications. Recently, there have been substantial advances in high-power and broadband mid-IR femtosecond pulse generation[53,62,92] and unprecedented optical nonlinearity enabled by lithium niobate nanophotonics [63,70,100], which can enable experimental realization of this technique on both free-space and on-chip platforms.

Chapter 4

CROSS-COMB SPECTROSCOPY (THEORY)

Dual-comb spectroscopy has been proven beneficial in molecular characterization but remains challenging in the mid-infrared region due to difficulties in source generation and efficient photodetection. Here we introduce cross-comb spectroscopy, in which a mid-infrared comb is upconverted via sum-frequency generation with a near-infrared comb of a shifted repetition rate and then interfered with a spectral extension of the near-infrared comb. We measure CO_2 absorption around 4.25 µm with a 1-µm photodetector, exhibiting a 233-cm^{-1} instantaneous bandwidth, 28000 comb lines, a single-shot SNR of 167 and a figure of merit of 2.4×10^6 Hz$^{1/2}$. We show that cross-comb spectroscopy can have superior signal-to-noise ratio, sensitivity, dynamic range, and detection efficiency compared to other dual-comb-based methods and mitigate the limits of the excitation background and detector saturation. This approach offers an adaptable and powerful spectroscopic method outside the well-developed near-IR region and opens new avenues to high-performance frequency-comb-based sensing with wavelength flexibility.

This chapter introduces cross-comb spectroscopy, emphasizing its theoretical foundations and numerical analysis, and sets the stage for addressing the experimental aspects in the following chapter. We will first provide an overview of this novel technique by concisely describing its architecture, the principle of tooth mapping, and its advantages over other

methods. Subsequently, we will delve deeper into these topics, offering detailed derivations and thorough discussions.

4.1. Introduction

Dual-comb spectroscopy (DCS), based on two mutually locked frequency comb (FC) sources in the same wavelength range, has become a compelling alternative to traditional Fourier-transform infrared spectroscopy (FTIR) with advantages in resolution, precision, sensitivity, speed, and bandwidth [9,19,20]. Over the past decade, significant efforts have focused on its extension to the mid-infrared (MIR) spectral region (3-25 µm) [27,67,101–104], where strong molecular signatures are located, making it promising for numerous applications in physical, chemical, biological, and medical sciences or technologies. However, generating two mutually locked broadband frequency comb sources in the MIR has posed a significant challenge. In addition, photodetectors in the MIR usually suffer from lower sensitivity, higher noise, and slower response times, and generally require cooling, compared to their well-developed near-infrared (NIR) counterparts. Moreover, photodetection above 13 µm [28] remains a significant challenge.

On the other hand, the signal-to-noise ratio (SNR), sensitivity (detection limit) and dynamic range (DR) of DCS have been limited by noise from strong excitation background [82,96], especially for detection of trace molecules. To detect a weaker absorption, one can apply a higher excitation power, but the stronger background signal from it will in turn decreases the dynamic range, which is an undesirable trade-off in DCS. Additionally, the sensitivity can still be limited by the detector saturation. Therefore, although significant progress has been made toward broadband and high-power (>100 mW) MIR frequency combs [35,36,39,45,48,53,92], the MIR DCS does not yet take full advantage of such sources since typical MIR detectors saturate at ~1 mW. Recently, some works have been demonstrated to alleviate the background issue by linear interferometry [84,85].

To overcome those obstacles, one effective path is to upconvert the MIR FC to the NIR region using short pulses and capture the wealth of molecular information available in the MIR with NIR photodetectors. Electro-optic sampling (EOS) is one recent successful example of this approach [82,91], in which ultrashort NIR pulses are used to directly detect

the electric field of MIR pulses in the time domain. However, this method necessitates very short NIR pulses with durations shorter than the optical cycle of the carrier frequency of the MIR pulses [105,106], whose generation and dispersion control require substantial efforts. Besides, the detection is based on field-dependent polarization rotation of the NIR sampling pulses, which adds additional components to the measurement setup. Moreover, to get higher SNR and sensitivity in EOS, some additional efforts may be required to independently tune the power and spectrum of different spectral parts of the ultrashort NIR pulses [107,108].

In addition to EOS, one can also upconvert the MIR frequency comb using a high-power NIR continuous-wave (C.W.) laser and perform standard DCS in the NIR region [109]. Nonetheless, this method has not yet been demonstrated to exhibit a favorable signal-to-noise ratio (SNR) and bandwidth compared to direct MIR DCS, mainly owing to its low upconversion efficiency because of the low peak power of C.W. lasers. More essentially, this method is still constrained by the above-mentioned limits of the general DCS as there is no temporal gating.

In this work, we introduce cross-comb spectroscopy (CCS), which can be considered a general form of frequency-converted DCS. Specifically, we show that short-pulse CCS can fundamentally have better SNR, sensitivity, DR, and detection efficiency compared to DCS or C.W. upconversion DCS, and does not require ultrashort NIR pulses and ellipsometry like EOS. We experimentally demonstrate a MIR measurement of ambient CO_2 around 4 μm with a NIR 1-μm detector, which exhibits a high temporal SNR and a high figure of merit (FOM) [96]. Moreover, in CCS, detector saturation can be circumvented since the detection process has been divided into two parts, upconversion (by local FC) and interference (by readout FC), which can be tuned independently. In addition, upon a proper setting of the power, the detection can fully utilize the DR of the detector, which does not have to be sacrificed for higher sensitivity. Provided suitable comb sources and strong upconversion capabilities are available, this method can be extended to any wavelength range and promises a superior performance that can break the limits of conventional methods, especially for longer wavelengths.

4.2. Overview of architecture, tooth mapping, and advantages

4.2.1. Architecture of the CCS system

The general architecture of CCS for upconversion is illustrated in Figure 4.1(a). The spectral information contained in the MIR (target) FC is upconverted to the NIR region via sum-frequency-generation (SFG) with a NIR (local) FC of a slightly shifted repetition rate (shifted by δ). The SFG output is then interfered with the spectral extension of the local FC (readout FC) to transfer the MIR information into the radio frequency (RF) domain. Like DCS, it is possible to realize a one-to-one mapping between the MIR FC teeth and the RF comb teeth, which are easily accessed with a single NIR detector and RF measurement. To obtain a tooth-resolved absorption spectrum of the target FC, the minimum required aggregate bandwidth of the local and readout FC is equal to the bandwidth of the target FC, which eliminates the need found in EOS for super-short NIR pulse generation and measurement of polarization rotation.
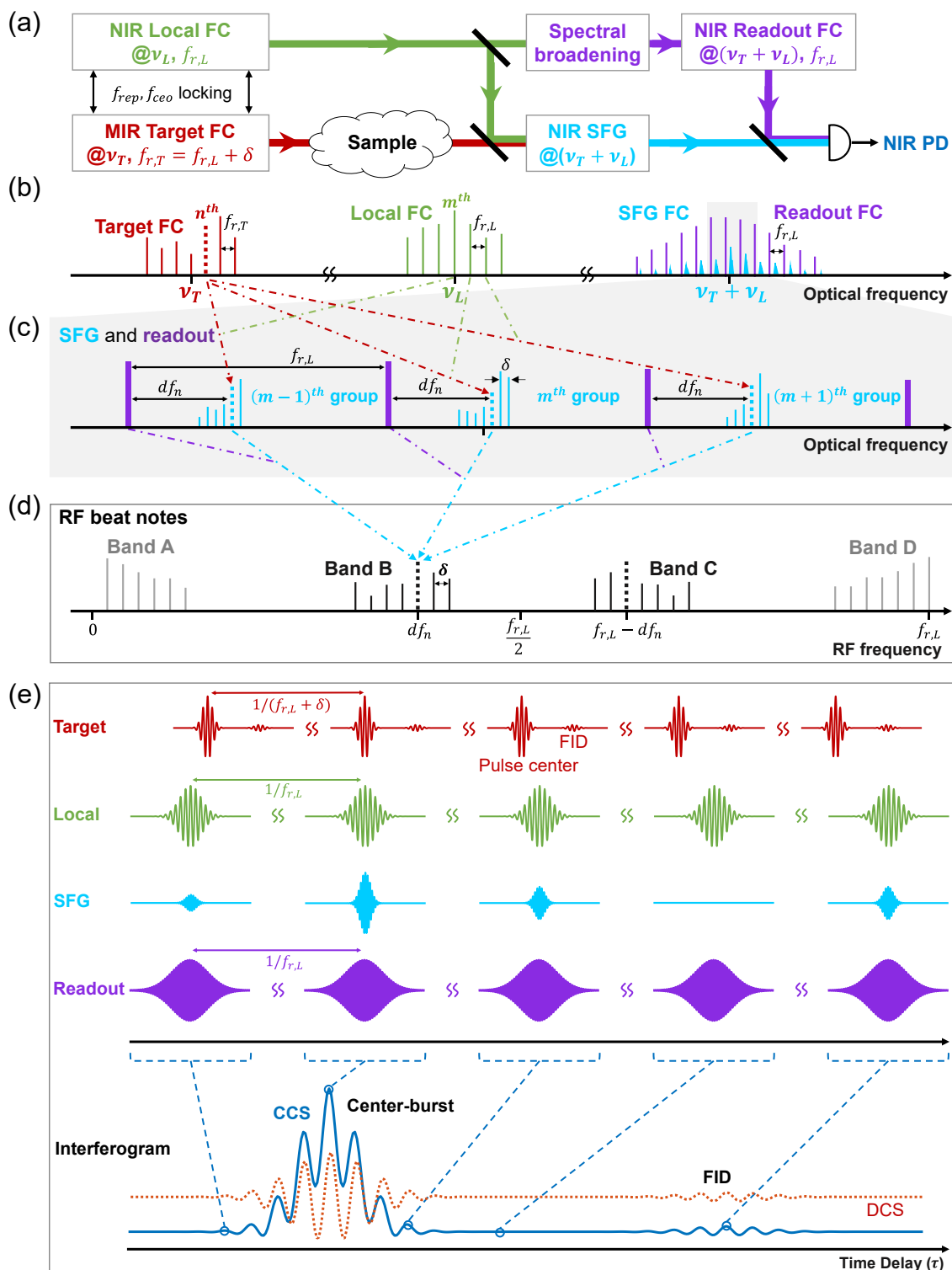
Figure 4.1: **Cross-comb spectroscopy. (a)** Schematic of the setup. ν_L and ν_T, center optical frequencies of the NIR local FC and MIR target FCs. f_{ceo} and f_{rep}, carrier–envelope offset frequency and repetition rate of a FC. $f_{r,L}$ and $f_{r,T}$, repetition rate of the local FC and the

target FC. δ, difference between $f_{r,L}$ and $f_{r,T}$. PD, photodetector. **(b)-(d)** Principle of the tooth mapping in frequency domain. An example target tooth, together with its corresponding SFG teeth and RF teeth, is denoted by a dashed line to demonstrate the one-to-one mapping. n (m): index of the example tooth of the target FC (local FC). **(b)** Optical spectra. **(c)** Zoomed-in view of the grey-shadowed area in (b). df_n denotes the distance of the SFG teeth (dashed lines) generated by the n_{th} target tooth from their respective closest readout tooth. **(d)** Heterodyne beat notes in the RF domain, obtained by square-law detection of the interference between the SFG FC and readout FC with a single NIR detector. Band B (C) is the result of the beating between SFG teeth with their nearest (second nearest) readout tooth, while band A (D) is the result of the beating between two SFG teeth from the same SFG group (two adjacent SFG groups). The arrows denote the optical tooth pairs in **(c)** that contribute to the dashed RF tooth. **(e)** CCS in time domain. In addition to the typical CCS interferogram (solid blue curve), a typical DCS interferogram (dashed red curve) is plotted for comparison. Note that this illustration describes the case where the target, local and readout FCs are all short pulses, which is not necessary for general CCS. While the DCS interferogram baseline is delay-independent since the envelopes of two pulses are delay-independent, the envelope of the SFG signal in CCS is delay-dependent, which gives a delay-dependent baseline and makes the interferogram "vertically asymmetric." This time-domain delay-dependent baseline in CCS interferogram corresponds to band A and D in frequency domain, which can be canceled out via balanced detection. More details can be found in following sections. FID, free induction decay.

4.2.2. One-to-one comb tooth mapping

Figure 4.1 illustrates the operation principle of CCS using sum-frequency sampling. In Figure 4.1(b), each pair of comb teeth from the local FC (green) and target FC (red) generates an SFG tooth at a unique frequency, the set of which is referred to as the SFG FC (blue). The teeth of the SFG FC cluster into different frequency groups that are evenly spaced by the repetition rate of the local FC (f_{rL}) [110] and follow specific patterns (see Figure 4.1(c) and Section 4.3.2). Within a frequency group, the SFG teeth are separated by δ, and each tooth represents a unique tooth of the target comb. Across all SFG groups, teeth generated by the same tooth of the target comb are all at the same relative frequency position in each group. These characteristics enable one-to-one mapping from the MIR domain to the RF domain. To realize this, a readout FC (purple), which is a spectral extension of the local FC, is employed to beat with the SFG FC on a NIR photodetector. For SFG teeth that are generated by the same target tooth, they share the same unique distance to their respective closest readout tooth and are therefore mapped to the same RF

tooth, which creates a unique mapping of the target tooth from the mid-IR domain to the RF domain. To explain those patterns more clearly, let us use an arbitrarily chosen target tooth as an example, labeled as the nth target tooth and denoted by a dashed line in Figure 4.1(b). The process of its mapping from the mid-IR domain to the RF domain, including SFG and heterodyne beating, is shown by arrows in Figure 4.1(b)-(d). Like all other target teeth, it mixes with different local teeth and generates multiple SFG teeth that are distributed across SFG groups and separated by f_{rL}. They share the same unique distance to their closest readout tooth, as denoted by df_n in Figure 4.1 (c). Thus, the dashed tooth in RF band B is the unique mapping of the n_{th} target tooth (Figure 4.1(d)), as is its mirror image in RF band C.

The resultant RF FC contains four distinguishable bands (Figure 4.1(d)) [105]. While band A and D correspond to the envelope of the SFG pulses (intensity cross-correlation between the target FC and local FC) and thus lack useful spectral information, the above shows that band B (or its mirror image band C) contains a one-to-one mapping from the target FC (multiplied by the local and readout FCs) to the RF FC. To interrogate the spectral response of the sample in the target FC path, one can compare the measured RF band B (or C) with the corresponding sample-free result. Balanced detection can eliminate band A and D since they are common-mode signals, which would double the bandwidth for band B and C. Figure 4.1(e) presents the same principle of CCS in the time domain. The target pulses are sampled by the local pulses, generating SFG pulses, which then interfere with the readout pulses, leading to the RF interferogram. More detailed descriptions can be found in Section 4.3 and Section 4.4.
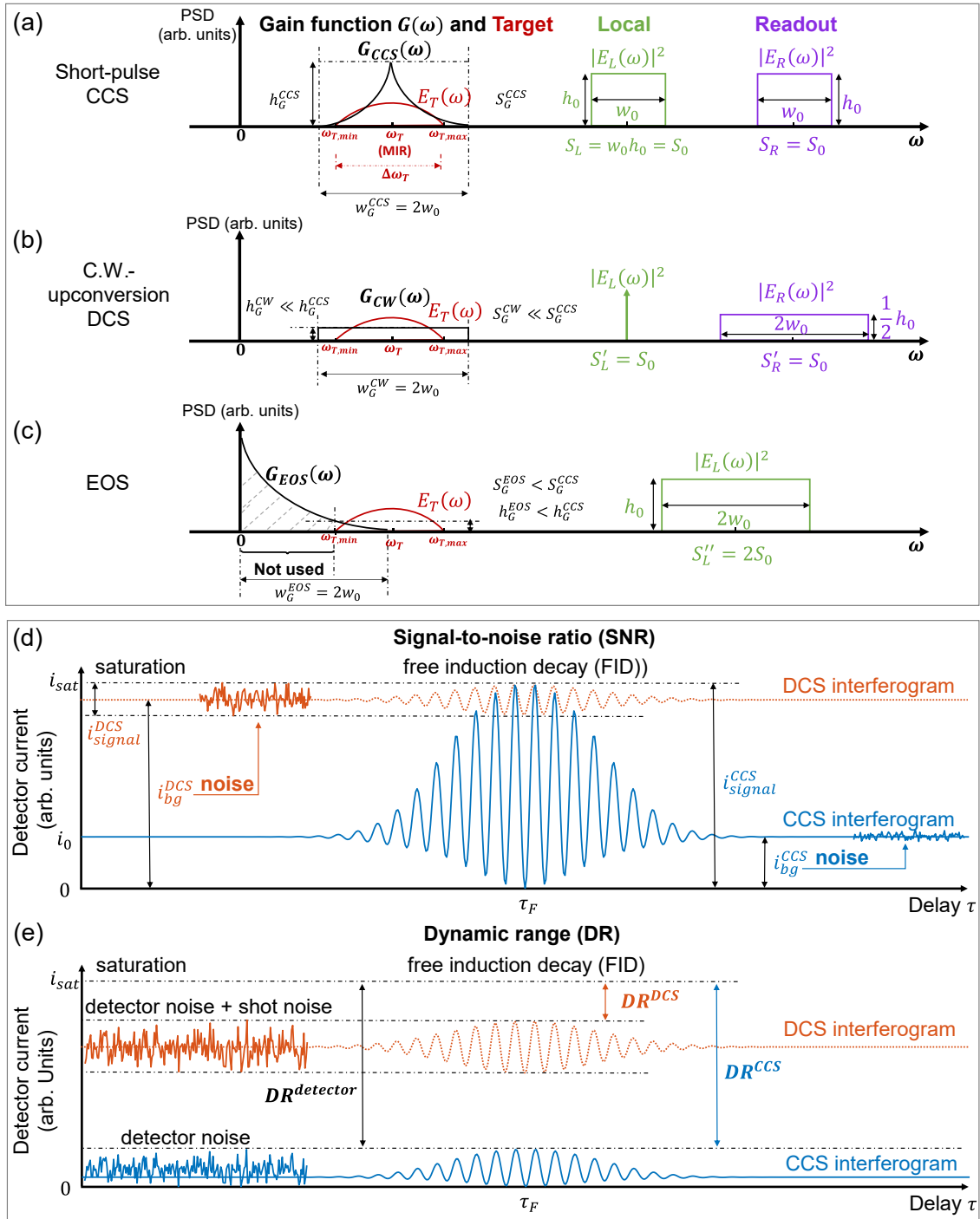
Figure 4.2: **Comparison of detection efficiency, bandwidth, SNR and DR between short-pulse CCS and other dual-comb-based techniques. (a)-(c)** Power gain function $G(\omega)$ for quantification of detection efficiency and bandwidth for three upconversion methods: short-pulse CCS **(a)**, C.W. upconversion DCS **(b)**, and EOS **(c)**. The spectral amplitude of the target ($E_T(\omega)$) and spectral intensities of the local ($|E_L(\omega)|^2$) and readout ($|E_R(\omega)|^2$) FCs are denoted by curves in red, green, and purple, respectively. The

instrument response function $H(\omega)$ is the convolution of $E_L^*(-\omega)$ and $E_R(\omega)$, and its spectral intensity ($G(\omega) = |H(\omega)|^2$) is denoted by the black curve for each method. **(a)** Short-pulse CCS. h_0, w_0 and $S_{L(R)}$ denote the height (PSD), width (bandwidth), and area (total average power) of the local (readout) spectrum, respectively. $\Delta\omega_T, \omega_{T,min}, \omega_T, \omega_{T,max}$ denote the bandwidth and minimal, center, and maximum optical frequency of the target spectrum to be detected, respectively. w_G, h_G and S_G denote the width, maxima, and total area under $G(\omega)$, respectively. **(b)** C.W. upconversion DCS. **(c)** EOS. The grey-dashed area of $G_{EOS}(\omega)$ denotes the part not effectively used in detection since it does not overlap with the target spectrum. **(d)-(e)** Comparison between DCS (red curves) and CCS (blue curves) interferograms at FID. **(d)** SNR comparison. Here we assume enough optical power for both techniques to saturate the detector for highest SNR. In DCS, the weak FID must be accompanied by the strong background from the excitation pulse center, which only contributes to noise here. Contrarily, CCS is free from such a background and can get an interference pattern of higher visibility with smaller noise. i_{signal}, the range of the beating signal. i_{bg}, the background current; i_{sat}, the saturation level of the detector. **(e)** DR comparison. Here we assume enough optical power for both techniques to detect an identical level of weak absorption. In DCS, a large part of the detector DR is occupied by the background. The higher the sensitivity (lower detection limit) reached, the larger the background, and the smaller the remaining DR. However, in principle, CCS does not have such problem and can make use of a larger part of the detector DR.

4.2.3. Detection efficiency and bandwidth

Figure 4.2(a)-(c) compares CCS with the other two upconversion methods in terms of detection efficiency and bandwidth. To quantify their performance, we define a power gain function $G(\omega) = |H(\omega)|^2$, where $H(\omega) = E_L^*(-\omega) \otimes E_R(\omega)$ is the instrument response function, in which $E_L(\omega)$ and $E_R(\omega)$ denote spectral envelopes (Fourier transforms of a single pulse) of the local and readout FCs, respectively. The width w_G, maximum value h_G and total area S_G of $G(\omega)$ can quantify the bandwidth, highest gain, and total gain of the detection, respectively. For short-pulse CCS (panel (a)), we set the spectra of the local and readout FCs to be both rectangular functions with the same height, width, and area. Their corresponding $G_{CCS}(\omega)$ (black curve) has a width equal to the sum of their bandwidths, which is required to be larger that of the target spectrum $E_T(\omega)$ (red curve), i.e., $\Delta\omega_T$, to detect the whole target band. As for the C.W. upconversion DCS (panel (b)), if we keep the average power of the local FC identical to that of the short-pulse CCS, the local spectrum can be approximated by a Dirac-delta function as it has a finite area, a near-zero bandwidth and a near-infinite spectral density. For a fair comparison, we keep the total

average power and the total optical bandwidth of the local FC and readout FC the same as for CCS. To this end, the bandwidth of the readout FC is doubled, and its spectral intensity is halved. As shown in Figure 4.2(b), although $G_{CW}(\omega)$ has the same bandwidth, h_G^{CW} and S_G^{CW} are both much smaller than those of CCS by a factor proportional to the peak power ratio between a short pulse and C.W. laser of the same average power. This detection gain advantage of CCS is rooted in the much higher peak power that (femtosecond) short pulses can offer for the nonlinear wavelength-conversion process, compared to C.W. lasers.

EOS (Figure 4.2(c)) is slightly different as it uses only one "local FC" to play the role of both the local FC and readout FC of the prior methods (see also Figure 4.3 and Section 4.4). Again, to keep the total bandwidth and total power the same as those of short-pulse CCS for a fair comparison, we double the bandwidth of the $E_L(\omega)$ here and keep its height unchanged. Note that the $H(\omega)$ in this case is the autoconvolution of the $E_L(\omega)$. As shown in Figure 4.2(c), although the nominal bandwidth of $G_{EOS}(\omega)$ is the same as the others, most of it is not effectively utilized (grey-dashed shadow) as it does not overlap with the target spectrum ($E_T(\omega)$). To cover the whole $E_T(\omega)$, the local bandwidth is required to be larger than $\omega_{T,max}$ instead of just $\Delta\omega_T$ (as is the case for the other two methods), which causes experimental challenges and is an ineffective use of bandwidth. For example, to detect a 30-THz MIR band from 60 THz to 90 THz (5-3.33 µm), EOS would require very short local pulses with a bandwidth of at least 90 THz, i.e., 155-245 THz (1.22-1.93 µm) if it is centered around 200 THz (1.5 µm). Meanwhile, CCS only needs a total bandwidth of 30 THz. Moreover, since only the part of $G_{EOS}(\omega)$ that overlaps with $E_T(w)$ contributes to the detection, its effective h_G and S_G are much smaller than their nominal values and depend on the values of $\omega_{T,min}$ and $\omega_{T,max}$. Using the parameters from the previous example, h_G and S_G of EOS are calculated to be 4/9 and 4/27 those of CCS, respectively, even though EOS can be more experimentally demanding. Additional details regarding this part can be found in Section 4.4 and 4.5.

4.2.4. Wavelength conversion and temporal gating

The optical nonlinearity can provide CCS with advantages over DCS in two ways. The first is wavelength conversion. Generally, photodetection in the NIR has a better performance, a lower cost, and does not require cooling. Also, typical commercial MIR detectors have a cut-off wavelength around 13 µm and are limited for detection of longer wavelengths. Converting MIR information to the NIR can get around these limitations.

Second, and more importantly, strong nonlinearity from short pulses gives rise to a temporal gating [82] effect that can endow CCS with better SNR, sensitivity, and dynamic range compared to DCS. To demonstrate such advantages, we compare CCS and DCS directly at the free induction decay (FID) part of their interferograms. The FID is the sample's reradiation which contains molecular signatures [79,80,95], and isolating it from the center-burst has been demonstrated to provide the absorption spectrum with a better detection performance [82]. Therefore, the SNR and dynamic range of the two techniques at the FID can be a good indicator of their sensing capability, the comparisons of which are illustrated in Figure 4.2(d)(e), based on our simplified theoretical model (Section 4.6). Note that, in this paper, "FID" refers to either the tail in the electric field of the target pulse (relative to the "pulse center," see "Target" in Figure 4.1(e)) or its corresponding part of the interferogram (relative to the "center-burst," see "Interferogram" in Figure 4.1(e)). In DCS (red dotted curve in Figure 4.2(d)), the weak FID beating must be on top of a strong background (the "direct-current" baseline), most of which comes from the power of the strong center of the excitation pulse which only contributes to the noise (shot noise and RIN) here but not the signal (interference). This kind of baseline is referred to as background signal (power), and this kind of noise is referred as "background noise" in the following text. On the contrary, the FID beating in CCS is independent of any extra background (blue curve in Figure 4.2(d)), because the FID part of target pulse is temporally isolated from the strong pulse center by the short local pulses (see Figure 4.1(e)). In other words, it is possible to get an "ideal" interference pattern with full interferometric visibility (SNR) at the FID in CCS, while that of the DCS is greatly limited by the background noise from excitation pulse center; the lower the absorption to detect, the higher the excitation

power (background) that must be used, and the larger this difference can be. Note that saturation at the center-burst part of the interferogram is ignored for both cases.

The SNR comparison naturally leads to a comparison of sensitivity, i.e., the minimal detectable absorption. In DCS, higher optical power gives higher SNR and sensitivity, which are ultimately limited by the detection saturation (or relative intensity noise (RIN) of the sources) [96]. However, as CCS detects the FID in a "background-free" manner, its fundamental limitation is the nonlinear upconversion capability. That is, the upconverted weak FID signal just must be stronger than the detector noise (NEP) to be detectable, instead of the shot noise or RIN from the strong background as in DCS. Therefore, CCS is not fundamentally limited by the detector saturation or extra noise from the strong excitation background, which sets a hard boundary for DCS.

Figure 4.2(e) illustrates the dynamic range comparison. In CCS, as mentioned before, the detector noise limits the weak side of the absorption signal, and the FID detection can utilize the full DR of the detector. Meanwhile, the background in DCS occupies a large part of the detector DR, which inevitably decreases the room for the FID. In fact, a weaker absorption would require a higher excitation (background) to provide sufficient SNR for detection, which occupies more of the detector DR, further decreasing the DR of the FID (absorption). However, this "sensitivity-DR tradeoff" does not exist in CCS as the excitation background is excluded in the FID detection. In principle, CCS can take advantage of the full DR of the detector. It should be noted that, although we assume here an FID signal that is clearly separated from the pulse center for clarity of our theoretical model, our arguments hold for general cases and do not rely on special temporal features of FID that could be unique to some molecules. See Section 4.7 for a more detailed discussion.

Among the three upconversion methods, C.W. upconversion DCS can only have the advantage of wavelength conversion, since the C.W. laser cannot provide any temporal gating and it is still basically a DCS detection. As for EOS, one may think it can have all discussed advantages since it uses even shorter pulses for upconversion than CCS. However, this is not fully true since its "local and readout pulses" come from the same

pulse; therefore, some additional efforts may be required to independently tune their power and spectra [107,108] so that, for a very weak FID, the readout power will not saturate the detector before enough local power is applied for upconversion. However, in CCS, as the local pulses and readout pulses are inherently separated, their powers can be independently tuned directly according to the absorption to be detected, and hence the detector saturation can be easily avoided. In short, the flexibility of short-pulse CCS can utilize the full advantages offered by the optical nonlinearity. A detailed discussion for this topic can be found in Sections 4.6 (theoretical model) and Section 4.7 (simulation).

4.2.5. Comparison between CCS and other dual-comb-based techniques

CCS has many advantages compared to other dual-comb-based techniques despite their similarities. Figure 4.3(a)-(d) illustrates dual-comb-based spectroscopic techniques in the MIR, including DCS, C.W. upconversion DCS, dual-comb EOS, and CCS. In all four techniques, two combs of slightly detuned repetition rates are employed to replace the mechanical scanning stage used in traditional FTIR techniques. In fact, CCS can be considered the general form of frequency-converted DCS. C.W. upconversion DCS and dual-comb EOS are essentially two special cases of the CCS; the former uses a very narrow-band local "FC" with only one "comb tooth," and the latter uses a very broadband local FC (very short local pulses) which also functions as the readout FC (Section 3). The features of these four techniques are summarized in Figure 4.3(e). Compared to MIR DCS, CCS is free from requiring a second MIR FC as well as the poor performance of MIR detectors, and it can have enhanced performance from temporal gating. Compared to C.W. upconversion DCS, CCS features much higher upconversion efficiency and temporal gating, thanks to the short local pulses. Compared to EOS, CCS does not require ultrashort sampling pulses and ellipsometry to detect polarization rotation, which can be experimentally challenging. CCS can also mitigate the limitation from detection saturation in a more direct way, so it can be more resource-efficient and flexible. Moreover, using an independent readout FC can potentially bring more phase information and favorable signal scaling for strong attenuation [111].
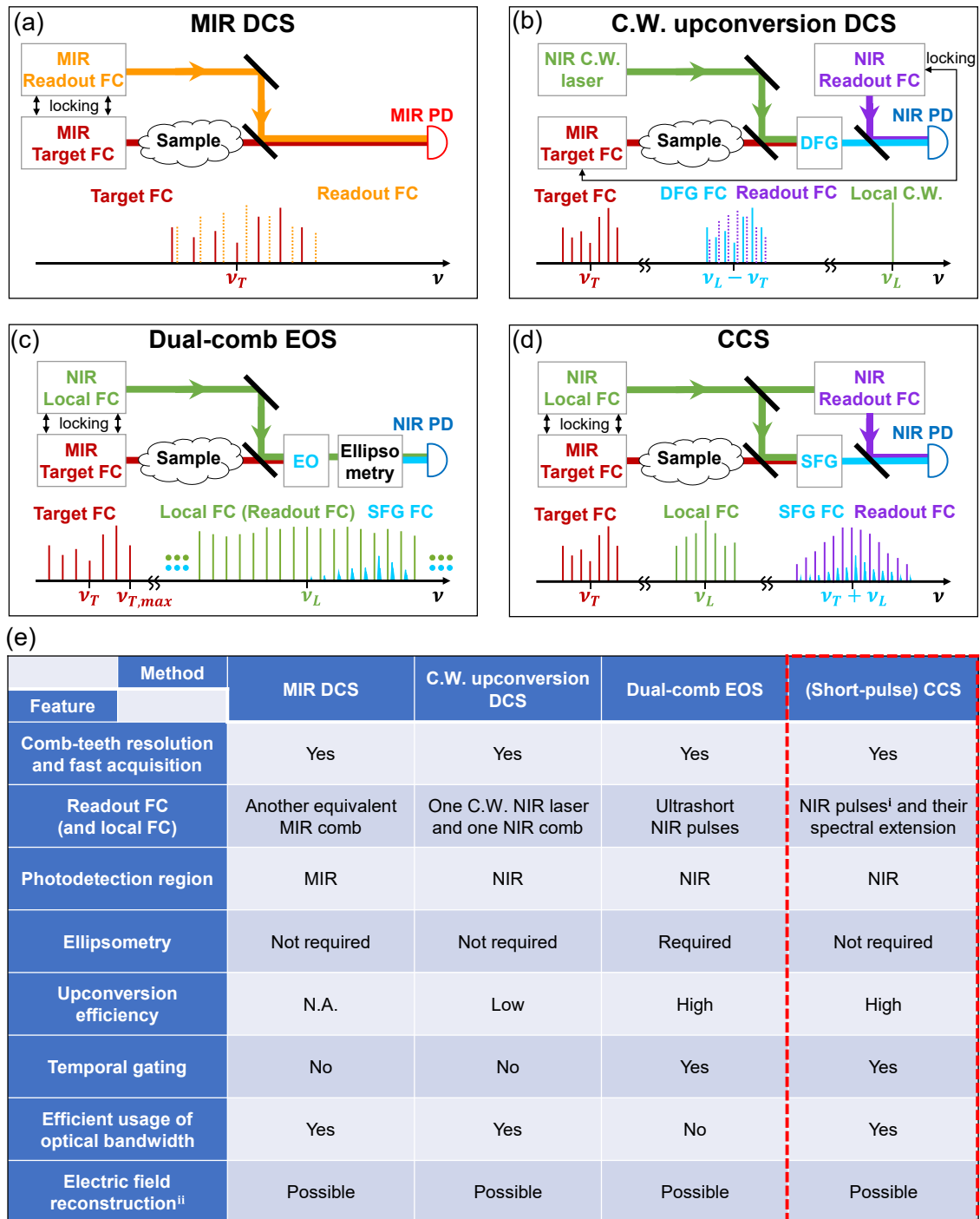
Figure 4.3: Comparison of principles and features of different dual-comb-based techniques for MIR spectroscopy. (a)-(d) Simplified schematics of different techniques. **(a)** General dual-comb spectroscopy with an asymmetric (dispersive) configuration [19]. The second MIR FC, which does not pass through the sample, is often referred to as the "local FC" or "slave FC" in other works. However, in the context of this work, it is named the "MIR readout FC" since it samples the MIR target FC linearly, by which a linear cross-

correlation signal is generated to give the spectral information of the target FC. **(b)** C.W. upconversion DCS. The MIR target FC is generated by the DFG between the NIR C.W. laser and the "master NIR comb" [109], which is not shown in this simplified schematic. This method can be considered as a special case of CCS, in which the "local FC" contains only one "comb tooth." Note that using an SFG or DFG process for the nonlinear upconversion of the MIR target FC does not make a fundamental difference. **(c)** Dual-comb EOS. It can also be considered as a special case of CCS, in which the local FC is so broadband that it also serves as the readout FC. The lower-frequency part of the local FC can be regarded as an effective "local FC," while the higher-frequency part can be regarded as an effective "readout FC," in the context of CCS. **(d)** General cross-comb spectroscopy. **(e)** Table comparing features of different techniques. (i) In principle, CCS does not require short pulses as the NIR local FC. However, the (short) local pulses enhance the upconversion efficiency and enable temporal gating. (ii) If the electric field of the readout FC (and local FC if applicable) is (are) known, all four techniques can fully reconstruct the electric field of the target pulse. However, this extra information is not necessary for the purpose of general absorption spectroscopy.

4.3. One-to-one tooth mapping from target FC to RF FC

4.3.1. Target FC and local FC

The electric field of the local FC can be described by:

$$e_L(t) = \sum_m A_m^L \exp(i\phi_m^L) \exp(-i2\pi\nu_m t) = \sum_m L_m \exp(-i2\pi\nu_m t) \qquad (4.1)$$

where L_m denotes the complex amplitude that encodes both the intensity and phase of the mth local comb tooth with optical frequency ν_m, and the spatial dependence is omitted here. The superscript "L" of A_m^L and ϕ_m^L denotes local FC, and the subscript "m" corresponds to the mth comb tooth. In addition, for the optical frequency ν_m, we have:

$$\nu_m = mf_{r,L} + f_{ceo,L} \qquad (4.2)$$

where $f_{r,L}$ and $f_{ceo,L}$ are the repetition rate and carrier-envelope offset (CEO) frequency of the local FC, respectively.

Sometimes it is not convenient to directly use "m" to index comb teeth, since the first tooth usually occurs at very large m. To be specific, for the first tooth of a practical frequency comb, $m_{first} \sim 10^6$. For convenience, here we define the effective tooth index, m', which starts at 1. If we use m_{first} to denote the tooth index of the first local tooth, we have:

$$v_{m'=1} = v_{m_{first}} = (m_{first} - 1)f_{r,L} + 1 \times f_{r,L} + f_{ceo,L}$$
$$= 1 \times f_{r,L} + f_{ceo,L} + v_{start,L} \tag{4.3}$$

where $v_{startL} = (m_{first} - 1)f_{rL}$.

Then, for any m'^{th} teeth (m' starts from 1),

$$v_{m'} = m'f_{r,L} + f_{ceo,L} + v_{start,L}. \tag{4.4}$$

Like the local FC, we use X_n to denote the complex amplitude of the nth target comb tooth with the optical frequency v_n. We have:

$$e_T(t) = \sum_n X_n \exp(-i2\pi v_n t), v_n = n(f_{r,L} + \delta) + f_{ceo,T} \tag{4.5}$$

where δ denotes the repetition rate detuning between the local and target FC, i.e., $f_{r,T} = f_{r,L} + \delta$.

Similarly, we can also define the effective tooth index for target comb teeth,

$$v_{n'} = n'f_{r,T} + f_{ceo,T} + v_{start,T}, \quad v_{start,T} = (n_{first} - 1)f_{r,T}. \tag{4.6}$$

Using the notation introduced above, the frequency-domain picture of cross-comb spectroscopy is depicted in Figure 4.4. To make a concise and clear illustration, only three teeth are included for both FC, and simple random numbers are assigned to their optical frequencies, which are of arbitrary unit (Figure 4.4(a)). Note that generality is not lost by assigning $f_{ceo,L} = 0$, since in practice it is just the relative f_{ceo} between the two FCs that matters. Although only a small number of comb teeth and simple random numbers are used for the following illustrations and equations, the conclusions still hold when scaled to practical numbers.

4.3.2. SFG FC

Because of the slightly detuned repetition rates between the local and target FCs, each pair of teeth from them will generate an SFG tooth at a unique frequency, the set of which are referred to as the SFG FC. The electrical field of a certain SFG tooth can be described by (phase-matching effect is not included here):

$$E_{n,m}^{sfg} = L_m X_n \exp\left(-i2\pi v_{n,m}^{sfg} t\right), v_{n,m}^{sfg} = v_n + v_m. \qquad (4.7)$$
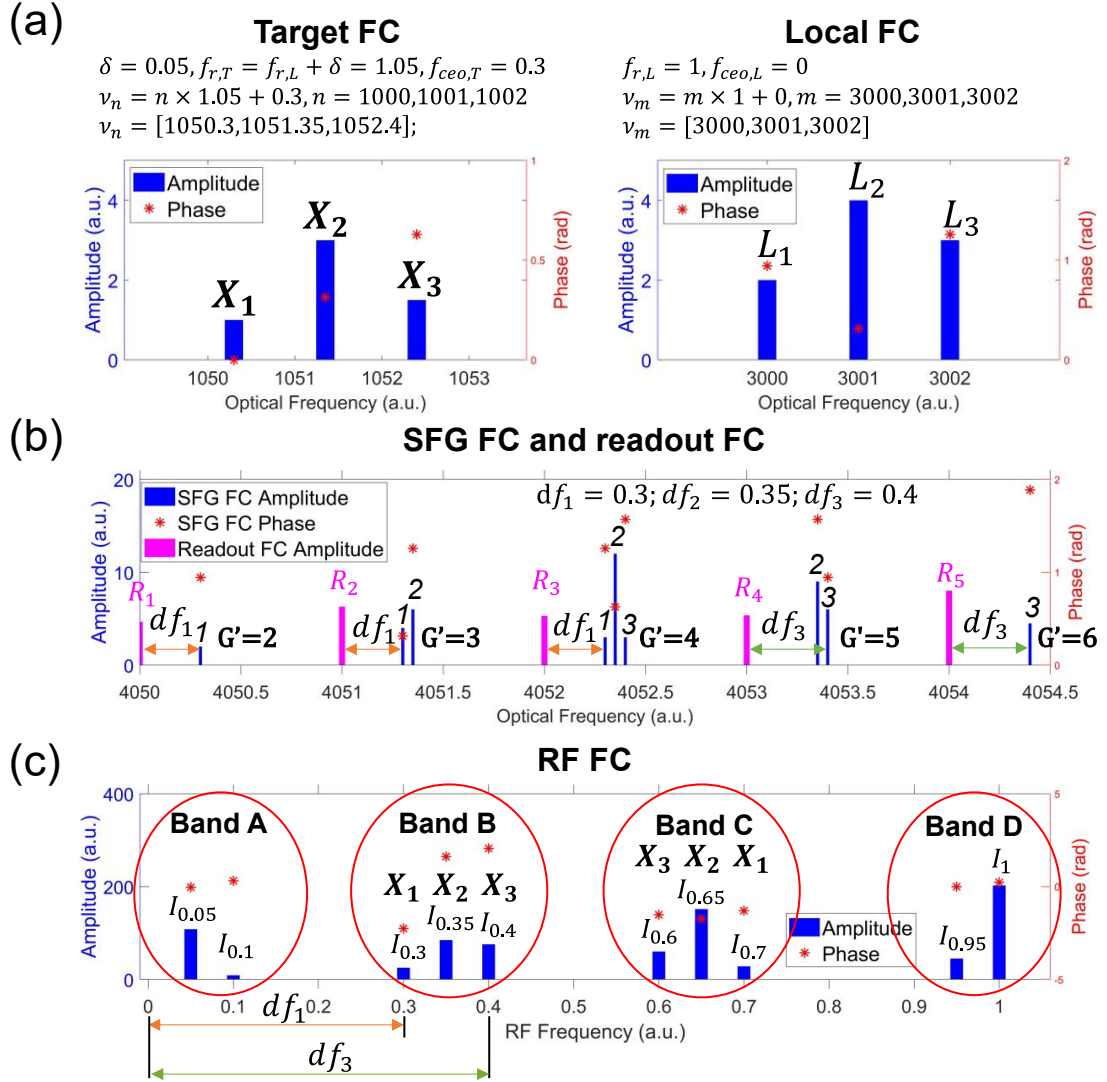
Figure 4.4: **Quantitative illustration of one-to-one tooth mapping of cross-comb spectroscopy.** **(a)** Target FC and local FC. Effective tooth indices are used to label each comb tooth in the plot. **(b)** SFG FC and readout FC. Each SFG tooth is labeled by the effective tooth index ("1," "2," or "3") of the corresponding target tooth. The phase for the readout FC is assumed to be constant for each tooth and is thus not shown in the plot. $df_{n'}$ denotes the primary readout frequency for the n'^{th} (effective tooth index) target tooth. Each SFG group is labeled by its effective group index G'. **(c)** RF FC. Every RF comb tooth in band B and band C is labeled with its corresponding target tooth.

As shown in Figure 4.4(b), the resultant SFG comb teeth cluster into different frequency groups [110], which can be indexed by the group index $G = n + m$ (or effective group

index $G' = n' + m'$), and the groups are evenly spaced by $f_{r,L} = 1$. The group G' is generated by the SFG between the ... $(n'-1)^{th}, n'^{th}, (n'+1)^{th}$ ... target teeth and the ... $(m'+1)^{th}, m'^{th}, (m'-1)^{th}$ ... local teeth. Note that the center group, with $G' = 4$, contains information about all the target teeth, in spite of the fact that different target teeth are modulated by different local teeth (see also Figure 4.1). Such a group that contains the information for all target teeth is called a "complete (SFG) group" in the following context. It is readily seen that the number of complete groups formed is determined by the number of local teeth relative to target teeth.

More patterns can be observed within SFG groups. Firstly, SFG teeth in a single group are separated by δ. Secondly, mixing with different local teeth, a given target tooth will generate multiple SFG teeth, which are all at the same relative frequency position in their respective SFG groups. To illustrate the second pattern, each SFG tooth in Figure 4.4(b) is labeled by its corresponding target tooth ("1," "2," or "3"). The pattern is made clearer still if readout teeth are introduced as frequency references (see next subsection). These patterns make it possible to do one-to-one mapping between the MIR and RF domains.

4.3.3. Readout FC

To read out the spectral information of the target FC contained in the SFG FC, another comb, referred to as the readout FC, is employed to beat with the SFG FC on a square-law photodetector. The readout FC is effectively a spectral extension of the local FC and therefore inherits its f_{rep} and f_{ceo}. As shown in the Figure 4.4(b), readout comb teeth can be regarded as "boundary markers" for SFG groups, since they share the same constant distance $f_{r,L}$ between each unit. For a certain SFG group, we name its closest (second closest) readout tooth as its "primary (secondary) readout tooth." For a certain SFG tooth within a SFG group, we name the frequency difference between the tooth and its primary (secondary) readout tooth as its "primary (secondary) readout frequency," and the sum of its primary and secondary readout frequencies is $f_{r,L}$. As shown in the illustration, the SFG teeth generated by the same target tooth always have the same primary readout frequency, even though they are distributed in different SFG groups and correspond to different primary readout teeth. Also, SFG teeth generated by different target teeth have different

primary readout frequencies, denoted by df_n, in the illustration. These two patterns are very important and provide the foundations for the one-to-one mapping.

As with the local and target FCs, we use "R_q" to denote the complex amplitude of the qth comb tooth of the readout FC:

$$e_R(t) = \sum_q R_q \exp(-i2\pi v_q t), v_q = qf_{r,R} + f_{ceo,R}. \tag{4.8}$$

Also, we can define the effective tooth index for readout comb teeth:

$$v_{q'} = q'f_{r,R} + f_{ceo,R} + v_{start,R}, \; v_{start,R} = (R_{first} - 1)f_{r,R}. \tag{4.9}$$

Note that $f_{ceo,R} = f_{ceo,L}$ and $f_{r,R} = f_{r,L}$.

4.3.4. RF FC, one-to-one mapping, and absorption spectrum

Based on the SFG and readout comb teeth in the optical domain, one can calculate the resultant RF spectrum detected by a single square-law detector. The bandwidth of the detector is assumed to be "1" ($f_{r,L}$), which means that the highest RF frequency the detector can detect is the repetition rate of the local FC, $f_{r,L}$. This is a common condition for many works in dual-comb spectroscopy. To calculate the RF signal (photocurrent) at a given RF frequency, one must sum the contributions from all the comb tooth pairs that can generate heterodyne beating at this frequency:

$$I_{f_0} = \sum_{f^{rf}=f_0} A_1 A_2^*, f^{rf} = v_1 - v_2 = f_0. \tag{4.10}$$

A_1 and A_2 denote the complex amplitude of the two involved comb teeth, which can be from the SFG or readout FC. The RF frequency of the beating signal, f_{rf}, is equal to the difference between the optical frequencies of the two involved comb teeth. Following these equations, for the case of this illustration, the RF signal at different frequencies can be calculated:

$$Band \; A \begin{cases} I_{0.05} = (L_1 L_2^* + L_2 L_3^*)(X_1^* X_2 + X_2^* X_3) \\ I_{0.1} = (L_1 L_3^*) X_1^* X_3 \end{cases} \tag{4.11}$$

$$Band\ B \begin{cases} I_{0.3} = (L_1 R_1^* + L_2 R_2^* + L_3 R_3^*)X_1 \\ I_{0.35} = (L_1 R_2^* + L_2 R_3^* + L_3 R_4^*)X_2 \\ I_{0.4} = (L_1 R_3^* + L_2 R_4^* + L_3 R_5^*)X_3 \end{cases} \tag{4.12}$$

$$Band\ C \begin{cases} I_{0.6} = (R_4 S_1^* + R_5 S_2^* + R_6 S_3^*)X_3^* \\ I_{0.65} = (R_3 S_1^* + R_4 S_2^* + R_5 S_3^*)X_2^* \\ I_{0.7} = (R_2 S_1^* + R_3 S_2^* + R_4 S_3^*)X_1^* \end{cases} \tag{4.13}$$

$$Band\ D \begin{cases} I_{0.95} = L_3 L_1^* (X_1 X_2^* + X_2 X_3^*) \\ I_1 = (L_2 L_1^* + L_3 L_2^*)(X_1^* X_1 + X_2^* X_2 + X_3^* X_3) + \left(\sum_{q=1}^{4} R_q^* R_{q+1} \right). \end{cases} \tag{4.14}$$

Note that, for simplicity, here we use subscript effective tooth indices "1,2,3," "1,2,3," and "1,2,3,4,5,6" (m', n', q') to index different comb teeth of the target FC, local FC and readout FC, respectively. The resulting teeth are also illustrated in Figure 4.4(c) and are referred to as the "RF FC."

As shown in the illustration, RF FC comb teeth can be classified into four bands [105]. Band A consists of the intra-group beat notes, which are generated by two SFG teeth from the same SFG group. Band D is also composed of beat notes generated by two SFG teeth, but the two teeth are from two different adjacent SFG groups. Note that the frequency component with $f^{rf} = f_{rL} = 1$ is a special component in band D which also includes the contribution from beatings between two readout teeth. Band A and band D result from only the SFG FC (excluding $f_{rf} = 1$) and correspond to the envelope of the SFG pulses (cross-correlation signal between target and local FC) in the time domain, which does not contain much useful information for our purpose. In contrast, band B, consisting of beat notes between SFG teeth and their primary readout teeth, is a one-to-one mapping of the original target FC. As demonstrated in the equations, the complex amplitude of a certain band B RF tooth is related to and directly proportional to that of only one target tooth, although it is generally modulated by more than one local tooth and readout tooth. Like band B, band C is also a one-to-one mapping of the original target FC, resulting from beating between SFG teeth and their secondary readout teeth. Band B and C contain the exact same information regarding the target FC, which are mirror images of each other, reflected about $f_{r,L}/2$ in the RF domain.

Based on the one-to-one mapping, the absorption spectrum in the MIR region interrogated by the target FC, including both amplitude and phase, can be obtained by comparing the RF band B (C) measured with the sample in the path and the corresponding result measured without the sample in the path (reference).

4.3.5. Universality

In our experiment, we use a MIR synchronously pumped degenerate OPO (centered at 4.18 µm) and Er-doped fiber laser (centered at 1.55 µm) as the target FC and local FC, respectively. The readout FC is a band-pass filtered portion of a supercontinuum pumped by the local FC, which is generated in a photonic crystal fiber (PCF). It should be noted that the scheme of cross-comb spectroscopy (CCS) does not have any limitation on the laser techniques used for the frequency comb generation. However, the current implementation benefits from the intrinsic phase locking of the mid-IR comb to the Yb: fiber laser pump. Also, as a special case of CCS, the local FC or readout FC can be replaced by a "frequency comb" with only one tooth, i.e., a C.W. laser. This is explained in depth later.

Moreover, in this derivation, we demonstrate the frequency-up-conversion one-to-one comb tooth mapping by SFG. In fact, it is also possible to realize one-to-one mapping by difference frequency generation (DFG), the derivation of which is very similar. This may be useful in the application of frequency-comb-based spectroscopy in the ultraviolet spectral range or for even shorter wavelengths.

4.3.6. Bandwidth requirements for local FC and readout FC

To realize one-to-one mapping for all teeth of the target FC, local FC and readout FC, one must satisfy some requirements which will be discussed in detail in this subsection. To provide a concise discussion, we continue to use the simple illustration above, keeping the number of target teeth to be three but varying the number of local teeth to be 2, 3, or 4. The results are shown in the Figure 4.5. N, M, and Q denotes the number of teeth of the target, local and readout FCs, respectively.
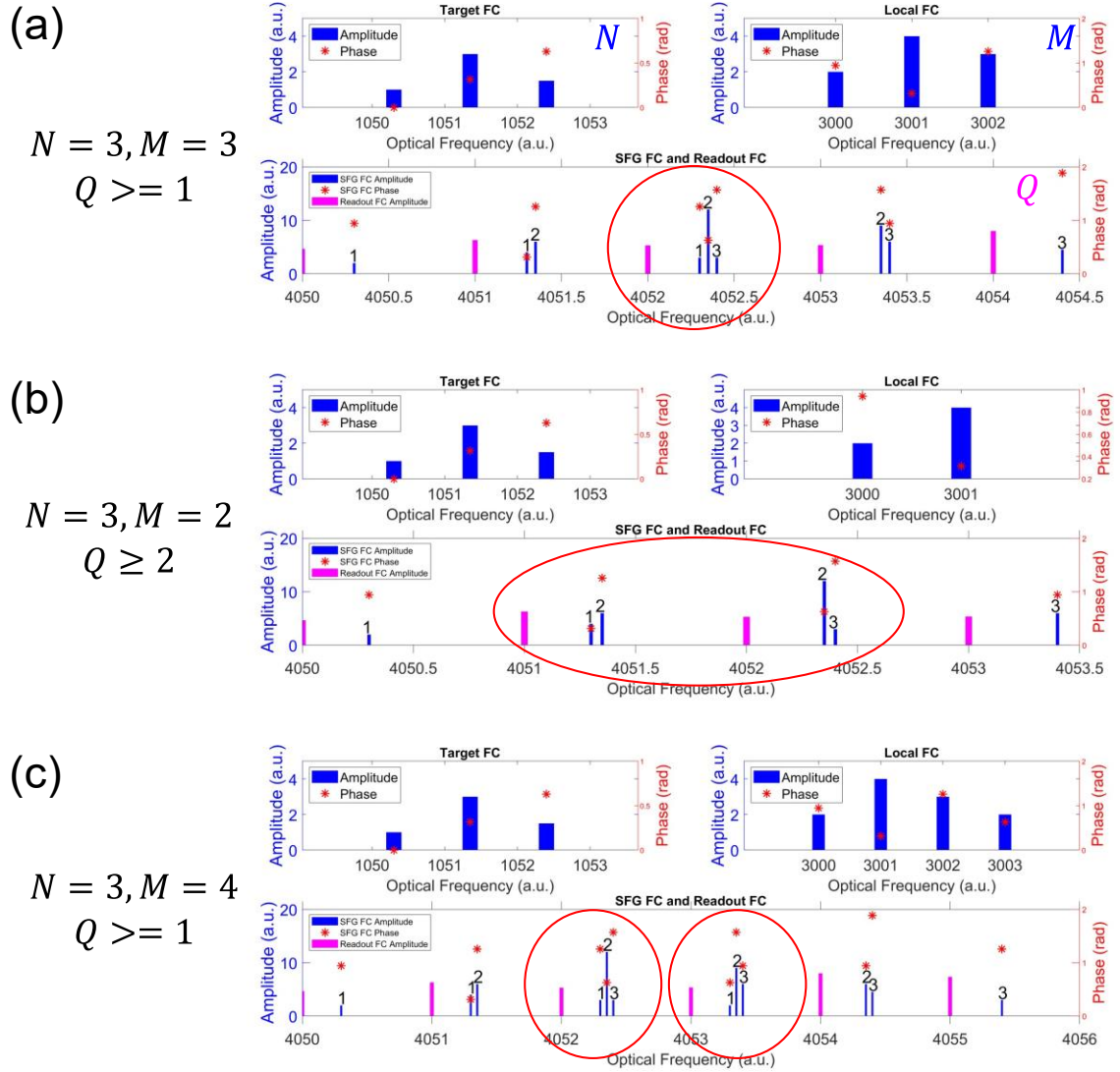
Figure 4.5: **Bandwidth requirements for local FC and readout FC.** M, N and Q denote the number of comb teeth for the target, local, and readout FCs, respectively. **(a)** M=N=3, Q must be >= 1. The only complete SFG group, together with its primary readout tooth, is circled in red. **(b)** N=2, M=3, Q must be >=2. Two incomplete SFG groups circled in red need to be read out by two readout teeth to map all three target teeth. **(c)** N=3, M=4, Q must be >=1. Two complete SFG groups, together with their primary readout teeth, are circled in red.

As shown in the panel (a), when $M = N$, there is only one complete group (circled in red) formed in the SFG FC, which alone contains the information from all target teeth. Thus, to read all target information out, one readout tooth is required at minimum (R>=1), where

the equality holds if and only if the readout tooth is the primary (or secondary) readout tooth of that complete group.

If we have one less local tooth (M=2, panel (b)), there is no complete group formed in the SFG FC, and at least two readout teeth are needed to read all three target teeth out (Q>=2). Similarly, to make the equality hold, the readout teeth need to be the primary (or secondary) readout teeth for those two center SFG groups, which are circled in red.

When there is one more local tooth relative to the number of target teeth (M=4, panel (c)), there will be two complete groups (circled in red) formed in the SFG FC. As in the case of L=3, one readout tooth is enough to read out all the target information (Q>=1). However, because of the availability of more complete groups, the requirement of the location of the single readout tooth to make the equality hold is more relaxed compared to the case of M=3. Here, it can be the primary (or secondary) readout tooth of either complete group.

This discussion can be generalized to any large number of teeth, although the various cases are demonstrated only in small numbers here for simplicity. In short, to realize the one-to-one mapping of all target teeth, the minimum required aggregate bandwidth of the local and readout FCs needs to be equal to or greater than that of the target FC, i.e., $M + Q \geq (N + 1)$. Note that there are two trade-offs behind this equation:

(a) The trade-off between the local tooth number and readout tooth location. If there are more local teeth, the location (frequency) of the readout teeth can be more flexible since there are more complete groups formed. Conversely, the requirement of the readout tooth location will be stricter if there are fewer local teeth. In practice, it is generally much more difficult to accurately control the frequency of the readout teeth with the precision of the repetition rate than to obtain more local/readout teeth. Therefore, the general practical solution could be to make the aggregate bandwidth of local and readout FC moderately larger than that of the target FC and to roughly control the frequency of the readout comb (e.g., with the precision of 0.1 nm). This is what we do in the experiment.

(b) The trade-off between the number of teeth of the local FC and readout FC. As the equation suggests, fewer readout teeth are needed if there are more local teeth, and vice

versa. It should be noted that, although in theory only the sum of the bandwidth of local FC and readout FC is regulated to realize the one-to-one mapping of the target teeth, a relatively broad local FC (short local pulse) will be more beneficial in practice, as it can provides a better time gating (Section 4.6) and a higher upconversion efficiency (Section 4.5).

4.3.7. Bandwidth requirements for repetition rates and carrier–envelope offset (CEO) frequencies

In the last subsection, we discuss the bandwidth requirements on optical side. In this subsection, we discuss instead the requirements on RF side, specifically, $f_{r,L}, f_{r,T}, \delta, f_{ceo,L}$ and $f_{ceo,T}$. Without loss of generality, we continue the assumption that $f_{ceo,L} = 0$; thus, $f_{ceo,T}$ is effectively the relative f_{ceo} between the target FC and local FC.
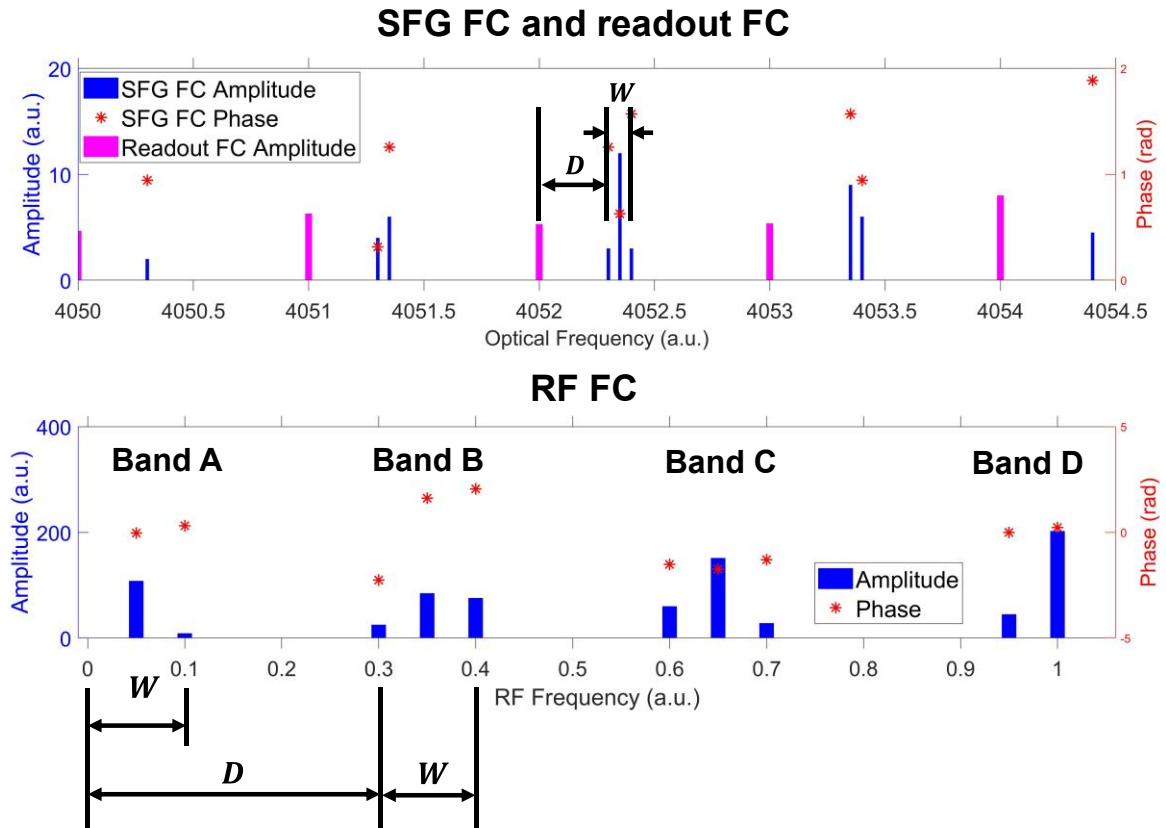
Figure 4.6: **Bandwidth requirements for RF frequencies.** The SFG FC and readout FC are from the Figure 4.4. D: the spectral distance (RF frequency) from the first tooth of an SFG group to its primary readout tooth. W: the spectral width of one complete group.

To quantify the requirements, here we define two important parameters (see the illustration in Figure 4.6):

(a) The spectral (frequency) distance from the first tooth of an SFG group to its primary readout tooth, denoted by D. Note that the "first tooth of an SFG group" refers to the SFG tooth that corresponds to the first target tooth (the tooth with minimum frequency in the target FC).

$$D = mod\left(\left(n_{first} f_{r,T} + f_{ceo,T} \right), f_{r,L} \right) \tag{4.15}$$

$mod(A, B)$ denotes the remainder after division of dividend A by divisor B, and $\left(n_{first} f_{r,T} + f_{ceo,T} \right)$ is the optical frequency of the first tooth of the target FC.

(b) The spectral width of one complete group, denoted by W.

$$W = \left(n_{last} - n_{first} \right) \delta = BW_T \times \frac{\delta}{f_{r,T}} \tag{4.16}$$

BW_T denotes the optical bandwidth of target FC.

Additionally, to realize a one-to-one mapping, two kinds of spectral overlap need to be avoided:

(a) Avoiding overlap between band A(D) and band B(C), which requires:

$$D > W. \tag{4.17}$$

(b) Avoiding overlap between band B and band C, which requires:

$$D + W < \frac{f_{r,L}}{2}. \tag{4.18}$$

Similar to dual-comb spectroscopy (DCS), $\frac{\delta}{f_{r,T}}$ needs to be small enough to provide enough bandwidth in the RF domain, i.e., to satisfy the requirement b. In addition, $f_{ceo,T}$ also need to be determined carefully to satisfy requirement a, which is different with DCS.

Note that the above bandwidth requirements are effective when a single detector is used for heterodyne photodetection. For the case that an ideal balanced detector is used, the requirements are simplified to only one equation:

$$W < \frac{f_{r,L}}{2}. \tag{4.19}$$

This is because the band A and band D are eliminated by the balanced detector since they are common-mode signal from the SFG FC. In another word, the balanced detector can double the bandwidth for RF band B (C) assuming unchanged $\frac{\delta}{f_{r,T}}$, which makes the RF bandwidth requirement effectively same as the general dual-comb.

4.4. Comparison of operating principles between different techniques

In this section, we will compare DCS, C.W. upconversion spectroscopy, electric-optic sampling (EOS), and cross-comb spectroscopy (CCS) (Figure 4.7) using simple mathematical descriptions. Then, we will demonstrate that C.W. upconversion and EOS are essentially two special cases of the cross-comb; the former uses a very narrow-band local "FC" with only one "comb tooth," and the latter uses a very broadband local FC (very short local pulse) which also functions as the readout FC. We will describe them in both the time domain and the frequency domain. Especially, we show that the CCS in a general configuration can utilize the optical bandwidth in a more efficient way, compared to EOS. In all these techniques, if the full electric field profile of the readout FC (local FC) is available, generally acquired by field-resolved measurements (e.g., FROG), the electric field of the target FC can also be reconstructed based on measured correlation signal. This extra information could be helpful in some ways; however, it is not necessary for the goal of general absorption spectroscopy.

To begin with, let us review the cross-correlation theorem:

$$C(\tau) = f(t) \otimes h(t) = \int\limits_{-\infty}^{+\infty} f^*(t)h(t+\tau)dt \quad \Rightarrow \quad \mathcal{F}\{C(\tau)\} \tag{4.20}$$
$$= F^*(\omega)H(\omega)$$

or equally:

$$C(\tau) = f(t) \otimes h(t) = \int\limits_{-\infty}^{+\infty} f(t)h^*(t - \tau)dt \quad \Rightarrow \quad \mathcal{F}\{C(\tau)\}$$

(4.21)

$$= F(\omega)H^*(\omega)$$

where $F(\omega)$ and $H(\omega)$ denote the Fourier transform of $f(t)$ and $h(t)$, respectively.
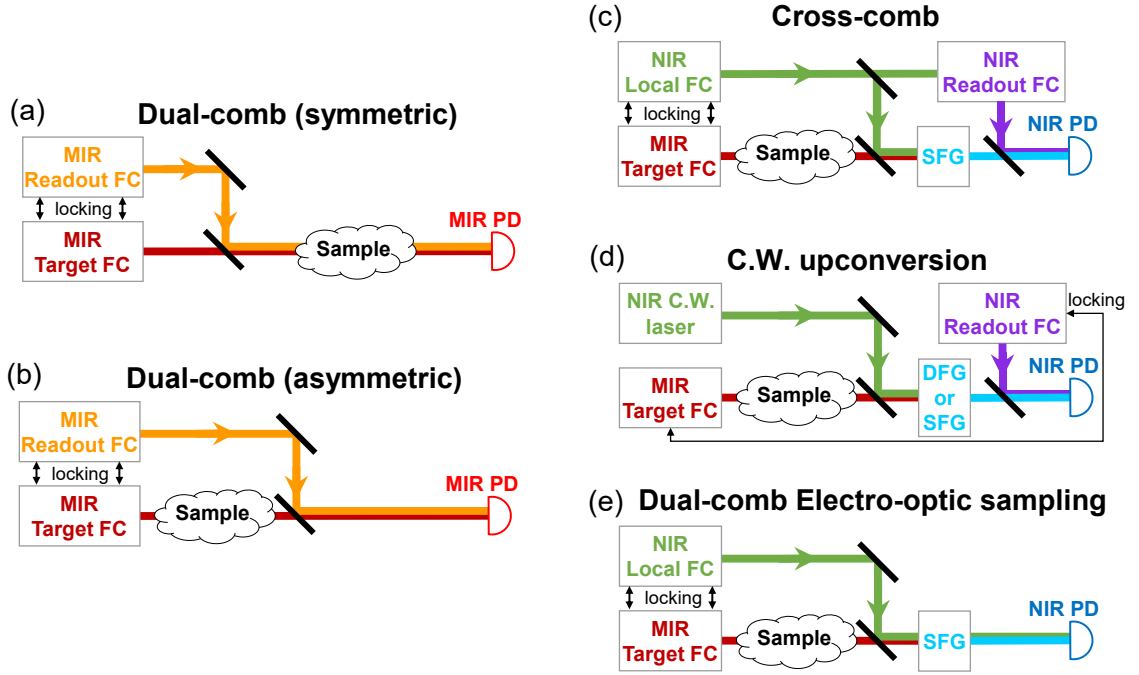
Figure 4.7: **Simplified schematics of different techniques.** Note that generally balanced detectors are used, which are simplified to be single detectors in the schematics. Also, there may be additional equipment before the detector, which is also omitted here; for example, an ellipsometry setup for electro-optic sampling (e).

4.4.1. DCS

Firstly, for DCS with a symmetric (collinear) configuration (Figure 4.7(a)) [19],

$$c(\tau) = \int\limits_{-\infty}^{+\infty} e_T(t)e_R^*(t - \tau)dt$$

(4.22)

$$C(\omega) = \mathcal{F}\{c(\tau)\} = E_T(\omega)E_R^*(\omega)$$

(4.23)

where $e_T(t)$ and $e_R(t)$ denote the electric field of the target FC (pulse) and readout FC without passing the sample (passing the reference cell), while $E_T(\omega)$ and $E_L(\omega)$ denote their Fourier transform, respectively. $c(\tau)$ denotes the cross-correlation signal measured

by the detector in the time domain, and $C(\omega)$ is its Fourier transform in the frequency domain.

Let us assume the sample's spectral response is $S(\omega)$, including both spectral amplitude $|S(\omega)|$ and spectral phase $Ang\ (S(\omega))$. If we use $e(t)$ and $e'(t)$ to denote the electric field of a pulse before and after passing the sample, we have:

$$\mathcal{F}\{e'(t)\} = S(\omega)\mathcal{F}\{e(t)\} = S(\omega)E(\omega). \tag{4.24}$$

Therefore, for the cross-correlation signal $c'(\tau)$, measured when the target pulse and readout pulse pass the sample:

$$c'^{(\tau)} = \int_{-\infty}^{+\infty} e'_T(t)e'^{*}_R(t-\tau)dt \tag{4.25}$$

$$C'(\omega) = \mathcal{F}\{c'(\tau)\} = E_T(\omega)S(\omega)E_R^*(\omega)S'(\omega) = E_T(\omega)E_R^*(\omega)|S(\omega)|^2. \tag{4.26}$$

By comparing those two measurements (with and without sample), we have:

$$D(\omega) = \frac{C'(\omega)}{C(\omega)} = |S(\omega)|^2. \tag{4.27}$$

$D(\omega)$ denotes the comparison between those two measurements. It shows that this measurement can only provide spectral intensity of the sample's response, which lacks the phase information.

In fact, a symmetric DCS measurement is essentially a traditional FTIR (Michelson interferometer), which gives information only about spectral intensity but not spectral phase. Therefore, one cannot get any temporal information on the target pulses which are disturbed by the sample. In other words, the correlation signal $c(\tau)$ is independent of the spectral phase of $e'_T(t)$, which is cancelled as the readout pulse also passes the sample.

Secondly, for DCS with an asymmetric (dispersive) configuration (Figure 4.7(b)),

$$c(\tau) = \int_{-\infty}^{+\infty} e_T(t)e_R^*(t-\tau)dt \tag{4.28}$$

$$C(\omega) = \mathcal{F}\{c(\tau)\} = E_T(\omega)E_R^*(\omega) \tag{4.29}$$

$$c'(\tau) = \int\limits_{-\infty}^{+\infty} e'_T(t)e_R^*(t-\tau)dt \tag{4.30}$$

$$C'(\omega) = \mathcal{F}\{c'(\tau)\} = E_T(\omega)S(\omega)E_R^*(\omega) \tag{4.31}$$

$$D(\omega) = \frac{C'(\omega)}{C(\omega)} = S(\omega). \tag{4.32}$$

Note that in this configuration, the readout pulse does not pass the sample before being combined with the target pulse. In this case, the measured $D(\omega)$ is dependent on the phase of $S(\omega)$; thus, one can get phase information of the sample response.

However, one still cannot recover the full electric field of the target pulse, $e_T(t)$ (or $e'_T(t)$) only by measurement of $C(\omega)$ (or $C'(\omega)$), in which $E_T(\omega)$ (or $E'_T(\omega)$) is modulated by $E_R^*(\omega)$. This is because $E_R^*(\omega)$ is generally unknown unless some other field-resolved measurements (e.g., FROG) are applied to measure it. Nonetheless, general absorption spectroscopy does not require the full knowledge of $e_T(t)$, since what we need to measure is $S(\omega)$ rather than $E_T(\omega)$, assuming $e_R(t)$ does not change for measurements with and without the sample.

Figure 4.8(a) illustrates the spectral amplitudes of $E_T(\omega)$ and $E_R^*(\omega)$ as well as the optical bandwidth requirement for the readout FC. $H^*(\omega)$ denotes the response function of the instrument, which is simply equal to $E_R^*(\omega)$ in this case. Note that this illustration, as well as the following illustrations for other techniques, depicts only the spectral envelopes and thus does not account for individual comb lines. This description simplifies the math without losing any generality since the comb lines can be understood effectively as sampling the envelopes in frequency domain (or equivalently, as a periodic extension in the time domain). The full description of CCS which factors in comb lines is presented in Section 4.3.

(a) Asymmetric dual-comb spectroscopy (DCS)

$H^*(\omega)$: Instrument response function

$H^*(\omega) = E_R^*(\omega)$

Optical bandwidth requirement:
$\Delta\omega_R \geq \Delta\omega_T$

(b) Cross-comb spectroscopy (CCS): general case

$H^*(\omega) = E_L(-\omega) \otimes E_R^*(\omega)$

Optical bandwidth requirement:
$\Delta\omega_R + \Delta\omega_L \geq \Delta\omega_T$
$\omega_T + \omega_L = \omega_R$

(c) Cross-comb spectroscopy (CCS): C.W. upconversion case

$H^*(\omega) = E_L(-\omega) \otimes E_R^*(\omega)$

Optical bandwidth requirement:
$\Delta\omega_R \geq \Delta\omega_T$
$\omega_T + \omega_L = \omega_R$

(d) Cross-comb spectroscopy (CCS): EOS case

$H^*(\omega) = E_L(-\omega) \otimes E_L^*(\omega)$

Optical bandwidth requirement:
$\Delta\omega_L \geq \omega_{T,max}$

Figure 4.8: **Instrument response function of different techniques.** $\omega_T, \omega_L, and\ \omega_R$: spectral center of the target FC, local FC, and readout FC. $\Delta\omega_T, \Delta\omega_L, and\ \Delta\omega_R$: optical

bandwidth of target FC, local FC, and readout FC. Note that we only plot the spectral amplitude (e.g., $|E_L(\omega)|$) for each function and assume zero spectral phase for all of them. Also, the spectral profiles of the local and readout FC ($E_L(\omega), E_R(\omega)$) are simplified to rectangular functions for clarity. **(a)** asymmetric DCS. **(b)** general CCS. The bandwidth requirement agrees with the result of our derivation in Section 2 in which comb teeth are included. **(c)** CCS (C.W. upconversion case). **(d)** CCS (EOS case). $\omega_{T,max}$ ($\omega_{T,min}$), the maximum (minimum) frequency of the target spectrum.

4.4.2. CCS

Thirdly, let us discuss CCS, which has the additional step of frequency conversion (Figure 4.7(c)).

Step 1: nonlinear upconversion

$$e_{SFG}(t,\tau) = e_T(t)e_L(t - \tau) \tag{4.33}$$

where $e_L(t)$ denotes the electric field of the local FC (pulse). Note that this equation is approximated that needs to be based on proper assumptions and approximations, the main of which include slowly varying envelop approximation (SVEA), weak nonlinearity, medium without loss and dispersion, unaffected input beams, and ideal phase-matching. In addition, for clarity, we omit all the proportionality constants since we are mainly interested in the shape of the pulses/spectra. Those conventions are same as what are generally used in the community of ultrafast pulse measurement [112], where more details can be found.

Step 2: linear readout (same as asymmetric DCS)

$$c(\tau) = \int_{-\infty}^{+\infty} e_{SFG}(t,\tau)e_R^*(t - \tau)dt = \int_{-\infty}^{+\infty} e_T(t)e_L(t - \tau)e_R^*(t - \tau)dt. \tag{4.34}$$

Let $h(t) = e_L^*(t)\,e_R(t)$, we can rewrite the above equation as:

$$c(\tau) = \int_{-\infty}^{+\infty} e_T(t)h^*(t - \tau)dt \tag{4.35}$$

$$C(\omega) = \mathcal{F}\{c(\tau)\} = E_T(\omega)H^*(\omega). \tag{4.36}$$

Above is the result for the measurement without sample, and for the measurement with sample we have:

$$c'^{(\tau)} = \int_{-\infty}^{+\infty} e_T'(t)h^*(t-\tau)dt \tag{4.37}$$

$$C'^{(\omega)} = \mathcal{F}\{c'^{(\tau)}\} = E_T(\omega)S(\omega)H^*(\omega) \tag{4.38}$$

$$D(\omega) = \frac{C'(\omega)}{C(\omega)} = S(\omega). \tag{4.39}$$

Like asymmetric DCS, one can get phase information of the sample response, but $e_T(t)$ cannot be fully recovered since $E_T(\omega)$ is modulated by $H^*(\omega)$ in $C(\omega)$. However, this does not impede the measurement of the absorption spectrum $S(\omega)$.

In this case, the response function of the instrument is $H^*(\omega)$. Based on that $h(t) = e_L^*(t)\, e_R(t)$, we have:

$$H^*(\omega) = E_L(-\omega) \otimes E_R^*(\omega) \tag{4.40}$$

which is illustrated in Figure 4.8(b).

4.4.3. C.W. upconversion and EOS

Both C.W. upconversion and EOS can be shown to be special cases of the above CCS description. To describe C.W. upconversion (Figure 4.7(d)), nothing needs to be modified in the CCS equations, except that $e_L(t-\tau)$ denotes a continuous sinusoidal wave instead of a pulse. Also, it should be noted that, using an SFG or DFG process for nonlinear upconversion does not make a fundamental difference here; the equations are equivalent up to a complex conjugation. The illustration is shown in Figure 4.8(c).

EOS (Figure 4.7(e)) requires a more careful discussion. Let us start with equations of CCS.

 Step 1: nonlinear upconversion

$$e_{SFG}(t,\tau) = e_T(t)e_L(t-\tau). \tag{4.41}$$

In the case of ideal EOS, $e_L(t)$ is much shorter than $e_T(t)$. In other words, in the temporal span of $e_L(t)$, $e_T(t)$ varies very little and can be approximated to be constant. Thus, we have:

$$e_{SFG}(t,\tau) = \boldsymbol{e_T(t)}e_L(t-\tau) \cong \boldsymbol{e_T(\tau)}e_L(t-\tau). \tag{4.42}$$

Another way to interpret this is that $e_L(t)$ is approximated to be a Dirac delta function ($\delta(t - \tau)$) that samples $e_T(t)$ in the time domain.

With this approximation, we can continue to derive the next readout step. Note that in EOS the role of readout pulse is played by the local pulse itself.

Step 2: linear readout

$$c(\tau) = \int\limits_{-\infty}^{+\infty} \boldsymbol{e_T(t)}e_L(t - \tau)e_R^*(t - \tau)dt$$

$$\cong \int\limits_{-\infty}^{+\infty} \boldsymbol{e_T(\tau)}e_L(t - \tau)e_L^*(t - \tau)dt \tag{4.43}$$

$$= \boldsymbol{e_T(\tau)} \int\limits_{-\infty}^{+\infty} e_L(t - \tau)e_L^*(t - \tau)dt = K\boldsymbol{e_T(\tau)}$$

$$C(\omega) = \mathcal{F}\{c(\tau)\} = KE_T(\omega) \tag{4.44}$$

$$C'(\omega) = \mathcal{F}\{c'(\tau)\} = KE_T(\omega)S(\omega) \tag{4.45}$$

$$D(\omega) = \frac{C'(\omega)}{C(\omega)} = S(\omega) \tag{4.46}$$

where K denotes the constant that equals to the integration $\int_{-\infty}^{+\infty} e_L(t - \tau)e_L^*(t - \tau)dt$, the core of which is independent of the parameter delay τ. As shown in the equation, under this approximation, the correlation signal $c(\tau)$ is equal to the electric field of target pulse $e_T(\tau)$ up to a constant. Thus, under the approximation of the ideal local pulse (infinitely short pulse width), one can obtain the full electric field of the target pulse $e_T(t)$ in addition to the absorption spectrum $S(\omega)$.

In practice, the finite pulse duration of the sampling pulse always imposes a frequency-dependent instrument response [91,106], which is illustrated in Figure 4.8(d). In this case, the instrument response function $H^*(\omega)$ is the "autoconvolution" of the local spectrum.

$$H^*(\omega) = E_L(-\omega) \otimes E_L^*(\omega) \tag{4.47}$$

In contrast to DCS and CCS, EOS needs the bandwidth of the local FC ($\Delta\omega_L$) to be equal or larger than the maximum frequency of the target FC ($\omega_{T,max}$) to detect the full spectrum of the target FC. This explains why EOS requires a much broader optical bandwidth compared to DCS and CCS. However, the $H^*(\omega)$ band below the minimum frequency of the target FC ($\omega_{T,min}$), is not effectively utilized, resulting from the fact that the same continuous FC is used as both the readout and local FC.

4.4.4. C.W. upconversion and EOS described by comb-tooth mapping

In the previous subsection, we have described C.W. upconversion spectroscopy and dual-comb EOS using the language of CCS without including comb teeth. In this subsection, we do the same thing factoring in comb teeth, following the derivation in Section 4.3.4. Note that Figure 4.3 is a good illustration for this subsection.

Based on what we derived for RF band B in Section 4.3.4, we can write the general formula for j_{th} target tooth mapped in RF band B:

$$I_j = \left(\sum_{m=1}^{M} L_m R_{m+j}^* \right) X_j \tag{4.48}$$

where M denotes the total number of local teeth. Note that all the subscripts denote effective tooth index.

For the case of C.W. upconversion, there is only one "local tooth," so the formula is simplified to be:

$$I_j = L_1 R_{m+1}^* X_j. \tag{4.49}$$

Everything can be described well by the language of CCS.

For the case of ideal EOS, let us review the approximation that we made in the time domain, which is:

"In the span of $e_L(t)$ or $e_R(t)$ (very short local/readout pulse), $e_T(t)$ (target pulse) varies slowly, and thus can be approximated as constant."

Correspondingly, in the frequency domain, we can have such an equivalent approximation:

"In the span of $E_T(\omega)$ (very narrowband, relatively), $E_L(\omega)$ or $E_R(\omega)$ (very broadband, relatively) varies slowly and can be approximated as constant."

With this approximation, we have:

$$R_m \cong R_{m+1} \cong R_{m+2} \cong R_{m+3} \dots \dots \cong R_{m+N} \tag{4.50}$$

where N denote the total number of target teeth. Thus, we have:

$$for\ any\ j,\ \sum_{m=1}^{M} L_m R_{m+j}^* \cong K \tag{4.51}$$

where K denotes a constant.

$$I_j = \left(\sum_{m=1}^{M} L_m R_{m+j}^* \right) X_j \cong K X_j, for\ any\ j \tag{4.52}$$

This result is equivalent to the equation $C(\omega) = \mathcal{F}\{c(\tau)\} = K E_T(\omega)$, which we derived in the last subsection in the time domain. Both results show that, in the limit of ideal EOS, the measured correlation signal (RF heterodyne beating) is equal to the electric field of the target pulse up to a constant.

The case of nonideal EOS is well demonstrated in reference [105].

In summary, both C.W. upconversion spectroscopy and EOS fall into the category of CCS, representing two opposite limits on the bandwidth of the local comb.

4.5. Comparison of detection bandwidth and efficiency between upconversion methods

In the last section, we compared how different techniques work. With the same model and assumptions, in this section and the next one, we further compare some of their important metrics, including detection bandwidth, efficiency, SNR and dynamic range. We will first compare detection bandwidth and efficiency of different upconversion methods, pointing out that the short-pulse CCS is overall more efficient. Secondly, we will present a comparison between DCS and short-pulse CCS in terms of SNR and dynamic range, highlighting the effect of temporal gating [82]. Lastly, some insights into the design rules of CCS systems are provided, based on the results of these sections.

4.5.1. General CCS, symmetric CCS, and C.W. upconversion CCS

In the last section, we defined a response function $H(\omega)$ to describe different methods. Here, we will continue to use it for a more quantitative comparison. With the same mathematical assumptions as before (Figure 4.8), the dimensions of $H(\omega)$ of the general CCS case are calculated, based on the given parameters (heights and width) of $E_L(\omega)$ and $E_R(\omega)$ (Figure 4.9(a)).

In practice, it is more general and convenient to discuss and compare spectral intensity (power) instead of spectral amplitude of the electric field. Thus, the amplitude spectrum is squared to the intensity spectrum, and a power gain function $G(\omega) = |H^*(\omega)|^2$ is defined to describe the detection efficiency of the system (Figure 4.9 (b)).
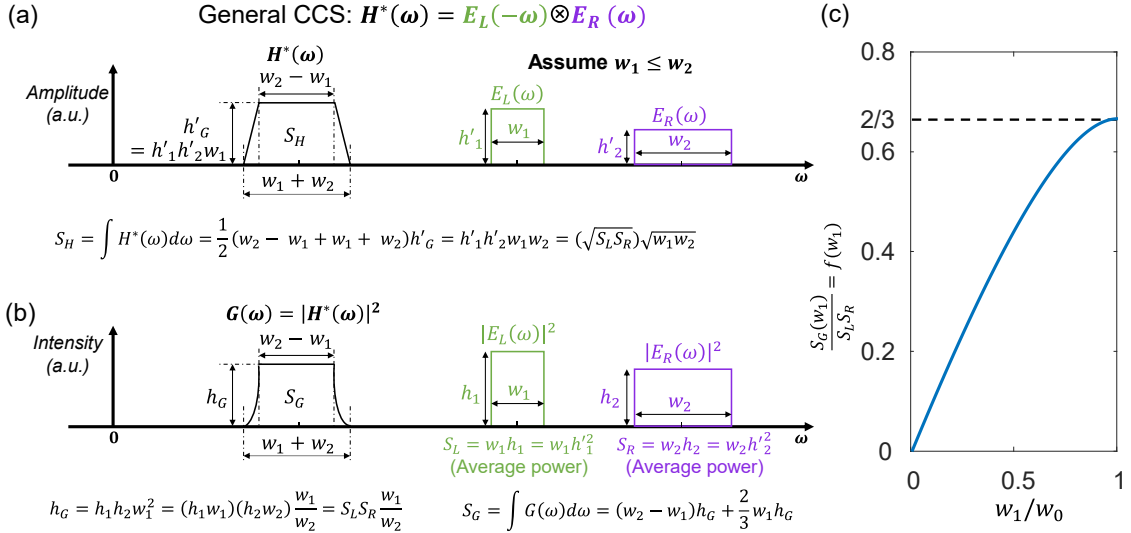
Figure 4.9: **Instrument response function and gain function of general CCS. (a)** Instrument response function $H(\omega)$ spectral amplitude of $E_L(\omega)$ and $E_R(\omega)$. **(b)** Detection gain function $G(\omega)$ and spectral intensity of $E_L(\omega)$ and $E_R(\omega)$. $S_{L(R)} = \int |E_{L(R)}(\omega)|^2 d\omega$. w and h denote the width and height of those spectral profiles, respectively. We assume w_1 (bandwidth of local FC) $\leq w_2$ (bandwidth of readout FC) in this derivation, with no lack of generality for conclusions we draw. **(c)** $\frac{S_G(w_1)}{S_L S_R} = f(w_1) = \left(2w_0 - \frac{4}{3}w_1\right)\frac{w_1}{2w_0 - w_1}$. This function shows how S_G scales with w_1 under the assumptions of constant combined power and combined bandwidth of local FC and readout FC. It monotonically increases with w_1 on the interval $[0, w_0]$.

Three metrics of $G(\omega)$ are used to quantify it:

h_G: the maximum value ("height") of $G(\omega)$, which describe the highest detection gain at the center part of $G(\omega)$.

w_G: the bandwidth of $G(\omega)$. Here we simply use zero points to define the width.

S_G: the area under $G(\omega)$, i.e., $\int G(\omega)d\omega$. This quantifies the total gain of the system.

Under our assumption of rectangular spectral profiles for $E_L(\omega)$ and $E_R(\omega)$, we get:

$$h_G = h_1 h_2 w_1^2 = (h_1 w_1)(h_2 w_2)\frac{w_1}{w_2} = S_L S_R \frac{w_1}{w_2} \tag{4.53}$$

$$BG = w_1 + w_2 \tag{4.54}$$

$$S_G = \int G(\omega)d\omega = (w_2 - w_1)h_G + \frac{2}{3}w_1 h_G = \left(w_2 - \frac{1}{3}w_1\right)h_G$$

$$= \left(w_2 - \frac{1}{3}w_1\right)\frac{w_1}{w_2}S_L S_R \tag{4.55}$$

where we assume $w_1 \leq w_2$.

Please refer to Figure 4.9 and its caption for a detailed definition of variables. Note that $S_{L(R)}$, which denotes the area under $\left|E_{L(R)}(\omega)\right|^2$, is equivalent to the average power of the local (readout) FC.

There are in total four effective free variables: $S_L, S_R, w_1, and \ w_2$. For reasonable comparison later, let us assume a fixed total bandwidth $w = 2w_0 = w_1 + w_2$ and a fixed total power $S = 2S_0 = S_L + S_R$ for the local and readout FC.

Let us first consider the choice of S_L and S_R. Based on the equation of h_G, we have

$$S_L S_R \leq \left(\frac{S_L + S_R}{2}\right)^2 = S_0^2,, where \ "=" \ holds \ when \ S_L = S_R = S_0. \tag{4.56}$$

Thus, we want to make $S_L = S_R = S_0$ to optimize h_G (this also optimizes S_G). In this case, $S_L S_R = S_0^2$, which is a constant.

Secondly, let us consider the choice of w_1 and w_2. To optimize h_G, it is obvious that we want to make $w_1 = w_2 = w_0$, thus we have $h_G = S_L S_R = S_0^2$.

As for S_G, a more careful calculation is needed. Since $S_L S_R$ is already set to a constant, let us consider function $f(w_1, w_2) = \left(w_2 - \frac{1}{3}w_1\right)\frac{w_1}{w_2}$ with the constraint that $w_1 + w_2 = w = 2w_0$, by which $f(w_1, w_2)$ is effectively a function of one variable (w_1 or w_2). Making it a function of only w_1, we plot $f(w_1)$ in Figure 4.9(c), which demonstrates how S_G scales with w_1 under our assumptions here. $f(w_1)$ monotonically increases with w_1 on the interval $[0, w_0]$, and reaches its maxima of 2/3 at $w_1 = w_2 = w_0$. Based on these observations, we name the case where $S_L = S_R = S_0$ and $w_1 = w_2 = w_0$ as "symmetric CCS."
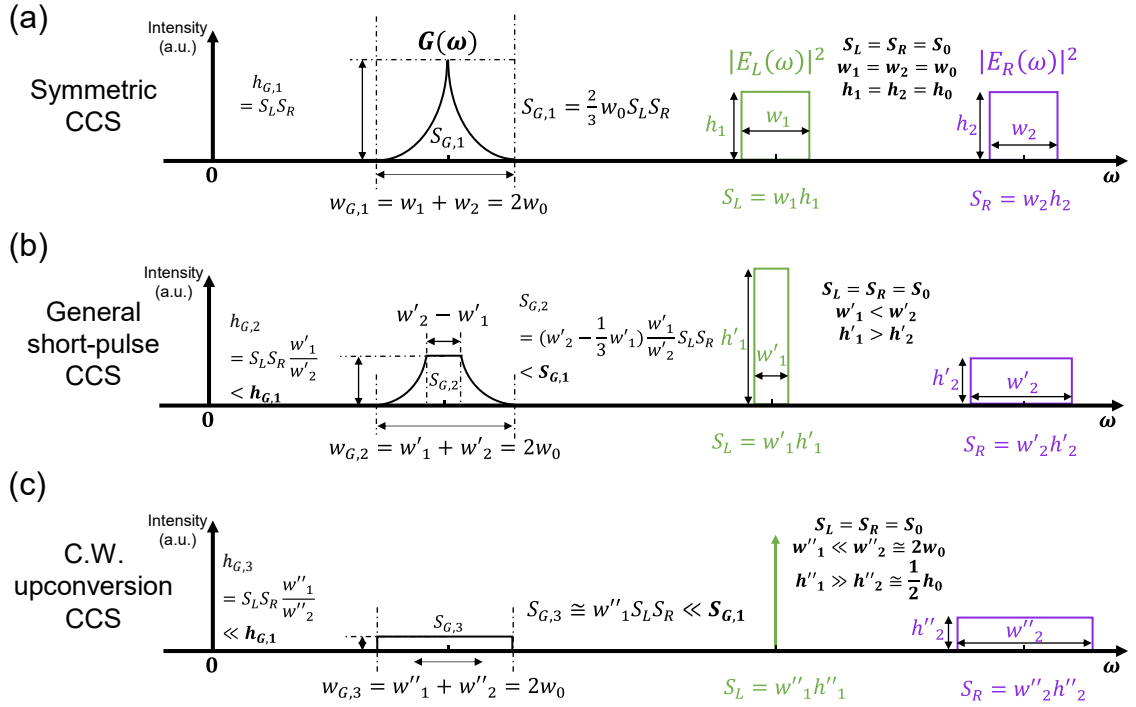
Figure 4.10: **Gain function $G(\omega)$ of symmetric CCS (a), general CCS (b), and C.W. upconversion CCS (c).** In (c), the local FC spectral intensity profile is like a Dirac-delta function, which has a very small width w''_1 and a very large height h''_1, while their product S_L is kept same as the other two cases.

With the derivation above, it is easy to compare the symmetric CCS, general short-pulse CCS (with parameters close to symmetric CCS) and C.W. upconversion CCS, shown in Figure 4.10(a)-(c), respectively. Note that we keep the total bandwidth and power of local and readout FC the same for all three cases. As the bandwidth of the local FC shrinks, symmetric CCS becomes general short-pulse CCS, which finally becomes C.W.

upconversion CCS. During the transition, although the bandwidth w_G stays the same, the maximum gain h_G and the total area S_G monotonically decrease. For the C.W. upconversion case (panel c), the bandwidth of the local FC shrinks to w_1'' that is $\ll w_0$. If we compare h_G and S_G between symmetric case and C.W. upconversion case, we have:

$$\frac{h_{G,sym}}{h_{G,C.W.}} = \frac{h_{G,1}}{h_{G,3}} = \frac{2w_0}{w_1''} \gg 1 \tag{4.57}$$

$$\frac{S_{G,sym}}{S_{G,C.W.}} = \frac{S_{G,1}}{S_{G,3}} = \frac{2w_0}{3w_1''} \gg 1. \tag{4.58}$$

In short, general short-pulse CCS (where local and readout FC both have a broad bandwidth) has a much higher detection gain than C.W. upconversion CCS. This should not be a surprising result if we think about the comparison of conversion efficiency of general nonlinear optics processes between C.W. laser and short pulses. The enhancement ratio here is exactly equivalent to the peak power enhancement ratio between coherent short pulses and a C.W. laser with the same average power. The conclusion we arrive at here has its roots in the same reason why people prefer short pulses over C.W. lasers for nonlinear optics: the much higher peak power of short pulses.

4.5.2. Symmetric CCS and EOS CCS

Here we compare short-pulse CCS with EOS CCS, the former of which is represented by the symmetric CCS, and the comparison is illustrated in Figure 4.11. Still, we keep their total bandwidth and power the same to make a fair comparison.
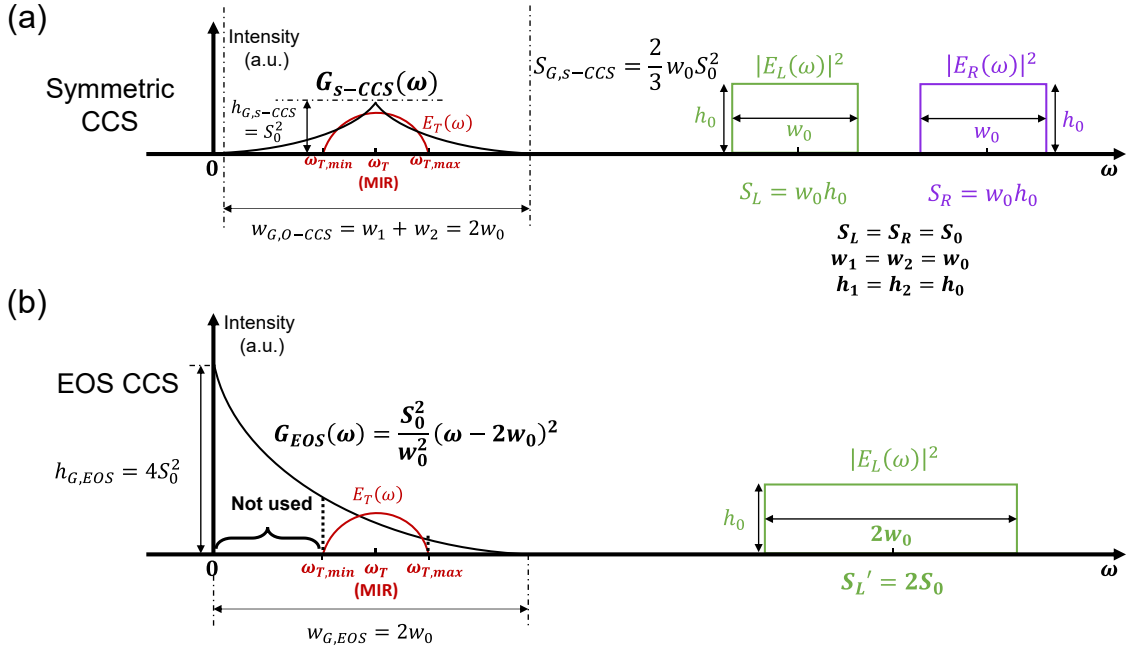
Figure 4.11: **Gain function $G(\omega)$ of symmetric CCS (a) and EOS CCS (b).** Note that the two panels are not on the exact same Y scale. As denoted in the figure, the heights of $G(\omega)$ are $h_{G,s-CCS} = S_0^2$ and $h_{G,s-CCS} = 4S_0^2$, respectively. (The latter is four times of the former.)

Based on the calculation shown in the plot, although the maxima of $G_{EOS}(\omega)$, i.e., $h_{G,EOS}$, is larger than that of the $G_{ccs}(\omega)$, i.e., $h_{G,s-CCS}$, the $h_{G,EOS}$ is at $\omega = 0$, which cannot overlap with target spectrum at all. Actually, $G_{EOS}(\omega)$ monotonically decreases with ω, and the largest part of it in amplitude, i.e., $\omega \in [0, \omega_{T,min}]$, is not effectively used, as shown in the Figure 4.8. A system response curve with a similar shape and trend has been calculated in ref. [106] (see Fig. S1 in its Supplementary Materials). This qualitative behavior already shows that EOS uses resources in a less efficient way compared to general CCS. Nevertheless, we still proceed to give a more quantitative description.

For a fair comparison, we want to calculate $G_{EOS}(\omega_{T,min})$ (the gain at $\omega = \omega_{T,min}$), $G_{EOS}(\omega_T)$ (the gain at the center of the target spectrum, $\omega = \omega_T$), and $S_{G,EOS} = \int_{\omega_{T,min}}^{\omega_{T,max}} G_{EOS}(\omega)d\omega$ (the overall gain that covers target spectrum). Based on the model presented before, we can have an analytical expression for $G_{EOS}(\omega)$:

$$G_{EOS}(\omega) = \frac{S_0^2}{w_0^2}(\omega - 2w_0)^2. \tag{4.59}$$

Of course, the value of the three metrics depends on the value of $\omega_{T,min}$, ω_T, and $\omega_{T,max}$, and different values can result in different conclusions for the comparison. Here, to give an example, let us adopt some values that are close to our experiments.

Let us set $\omega_T = 75\ THz\ (4\ \mu m)$ and assume we are going to detect a 30-THz-broad target bandwidth, that is, $\omega_{T,min} = 60\ THz\ (5\ \mu m)$ and $\omega_{T,max} = 90\ THz\ (3.33\ \mu m)$. If we set the center of the local FC at $200\ THz\ (1.5\ \mu m)$, the bandwidth of the local FC needs to be at least 90 THz, i.e., $w_0 = 45\ THz$, in order to detect the whole target spectrum. This suggests the local FC must span $155\ THz - 245\ THz\ (1.22\ \mu m\ to\ 1.93\ \mu m)$, and is therefore nontrivial to generate. Meanwhile, symmetric CCS only requires 15-THz local and readout FCs (in total 30 THz), which are much less challenging experimentally.

With the assumed values of $w_0, \omega_{T,min}, \omega_T$, and $\omega_{T,max}$, we have $\omega_{T,min} = \frac{4}{3}w_0, \omega_T = \frac{5}{3}w_0, and\ \omega_{T,max} = 2w_0$. Then the three metrics can be calculated and compared.

$$G_{EOS}(\omega_{T,min}) = \frac{4}{9}S_0^2; \quad G_{EOS}(\omega_T) = \frac{1}{9}S_0^2; \quad G_{EOS}(\omega_{T,max}) = 0; \quad S_{G,EOS}$$
$$= \int_{\omega_{T,min}}^{\omega_{T,max}} G_{EOS}(\omega)d\omega = \frac{8}{81}w_0S_0^2 \tag{4.60}$$

$$\frac{G_{EOS}(\omega_{T,min})}{G_{s-CCS}(\omega_T)} = \frac{4}{9}; \quad \frac{G_{EOS}(\omega_T)}{G_{s-CCS}(\omega_T)} = \frac{1}{9}; \quad \frac{S_{G,EOS}}{S_{G,s-CCS}} = \frac{4}{27} \cong 0.15 \tag{4.61}$$

In this case, the maximum value of $G_{EOS}(\omega)$ is just 4/9 of that of the $G_{o-CCS}(\omega)$, and this value is only at the left edge of the target spectrum. If we instead compare the gain at the center of the two functions, the ratio becomes only 1/9. Since they are of different profiles, it is more reasonable to compare their overall gain S_G, and $S_{G,EOS}$ is only ~15% of $S_{G,o-CCS}$. In short, although EOS may require much more experimental effort, its overall detection efficiency can be much lower than symmetric (general short-pulse) EOS.

4.5.3. Comparison of general CCS, symmetric CCS, and C.W. upconversion CCS under a different assumption

Above we compare general CCS, symmetric CCS, and C.W. upconversion CCS under the assumption of constant combined power and bandwidth of local FC and readout FC. While that is a fair comparison in theory, it is not generally realistic since it requires changing the properties of both combs simultaneously, which could be experimentally challenging. Here we provide another way of comparison under a different assumption that we keep the readout FC always the same ($w_R = w_0$ and $h_R = h_0$), and only scale the bandwidth of local FC (w_L) while maintaining its average power a constant ($S_L = S_0$). Like Figure 4.10, gain functions of different cases are illustrated in Figure 4.12(a)-(d). Compared to Figure 4.10, here we include one more different general short pulse CCS (Figure 4.12(a)) in which the local bandwidth ($w_L = w'''_1$) is larger than readout bandwidth (w_0).

As shown clearly, the width of $G(\omega)$, total bandwidth w_G, decreases monotonically with the local bandwidth w_L.

Similarly, the area of $G(\omega)$, total gain S_G, also decreases monotonically with local bandwidth w_L, the trendline of which is shown in Figure 4.12(e).

The scaling of the height of $G(\omega)$, highest gain h_G, is slightly different. It gets maximized when $w_L = w_R$ (Symmetric CCS), as we derived before in Section 4.5.1. However, this metric is less important than the other two.

In short, as the local FC gets broader in frequency domain (shorter in time domain), the overall performance of CCS increased. This agrees with our general understanding that shorter pulses lead to larger peak power, which benefits efficiency of nonlinear process.
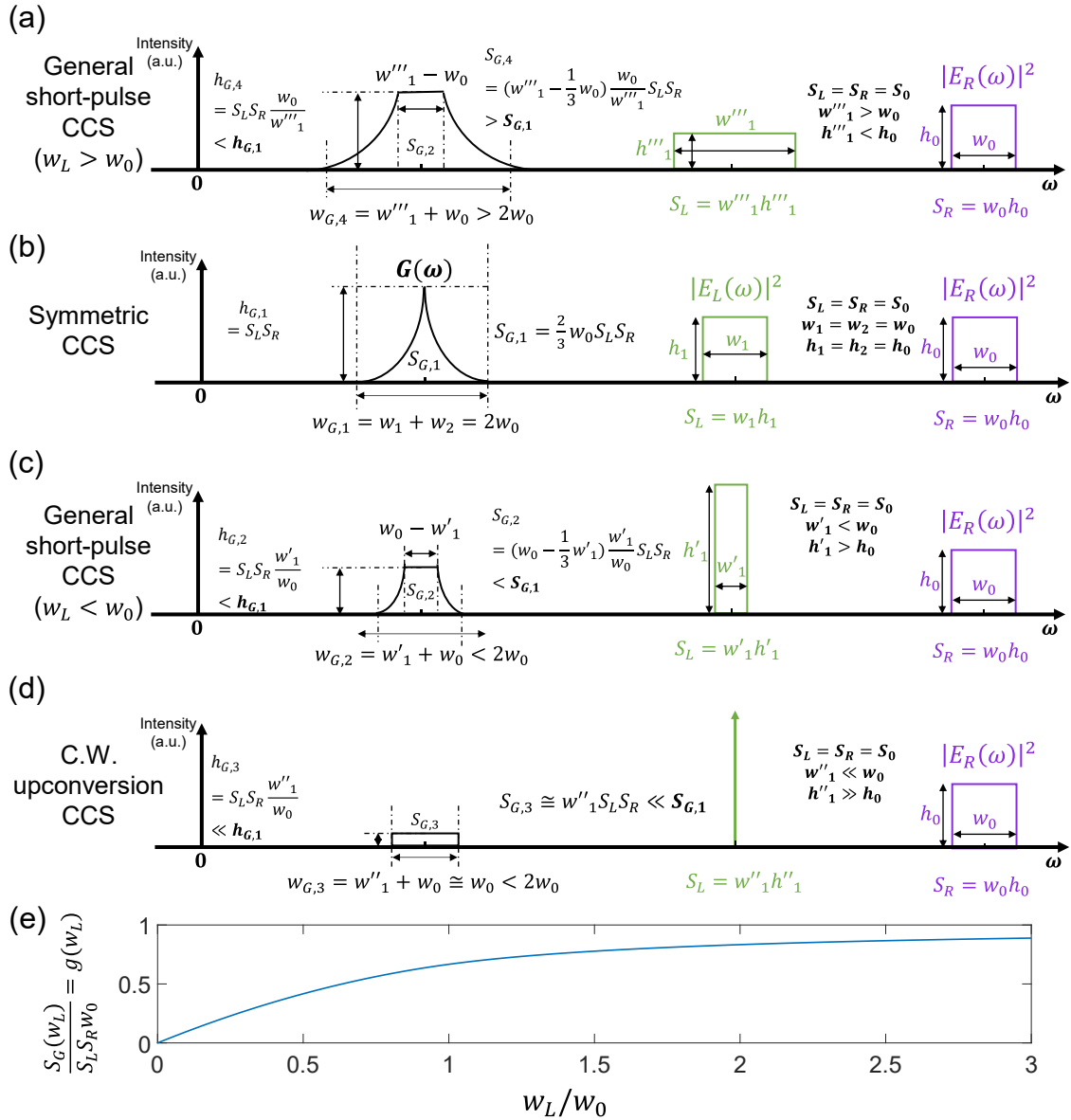
Figure 4.12: **Gain function $G(\omega)$ of symmetric CCS (b), general CCS (a, c), and C.W. upconversion CCS (d), and S_G scaling with w_L (e), under a different assumption.** In (d), the local FC spectral intensity profile is like a Dirac-delta function, which has a very small width w''_1 and a very large height h''_1, while their product S_L is kept same as the other three cases. In (e), note that the abscissa, local bandwidth w_L, is normalized by w_0, and the ordinate, total gain S_G, is normalized by $S_L S_R w_0$.

4.5.4. Summary

In this section we compare symmetric CCS, general short-pulse CCS, C.W. upconversion CCS, and EOS CCS. Compared to C.W. upconversion CCS, general short-pulse CCS can have a much higher detection (upconversion) efficiency, which comes from the

enhancement of peak power of short pulses over C.W. laser. Compared to EOS CCS, general short-pulse CCS (represented by symmetric CCS) can have a much larger detection bandwidth and detection efficiency, although it is much less experimentally demanding. Overall, among different upconversion configurations, short-pulse CCS has advantages in bandwidth, efficiency, flexibility, and experimental complexity.

4.6. Comparison between DCS and CCS: temporal gating, sensitivity, SNR, and dynamic range

4.6.1. Overview

In this part, we will provide a quick qualitative description. In asymmetric DCS, we have the correlation signal:

$$c(\tau) = \int\limits_{-\infty}^{+\infty} e_T(t)e_R^*(t-\tau)dt. \tag{4.62}$$

Note that only the cross term, i.e., the effective correlation signal, is kept in this equation. The background that is omitted in the equation is:

$$B = \int\limits_{-\infty}^{+\infty} |e_T(t)|^2 dt + \int\limits_{-\infty}^{+\infty} |e_R^*(t-\tau)|^2 dt = \int\limits_{-\infty}^{+\infty} |e_T(t)|^2 dt + \int\limits_{-\infty}^{+\infty} |e_R^*(t)|^2 dt. \tag{4.63}$$

This background is equal to the sum of the full power of the target pulse and local pulse, which is independent of the delay, τ. At large delay τ, when the weak tail (optical free induction decay) of the target pulse is being sampled by the local pulse, the effective correlation signal can be much smaller than the constant background. In other words, the extra noise incurred by the background from the strong target pulse can envelop the weak useful signal at the tail. Even in the absence of technical noise, the strong background can saturate the detector, thus fundamentally limiting the dynamic range and SNR of the measurement [82].

In CCS, in which a short local pulse is used (not necessarily as short as in the EOS case), the correlation signal is:

$$c(\tau) = \int\limits_{-\infty}^{+\infty} e_{SFG}(t,\tau)e_R^*(t-\tau)dt = \int\limits_{-\infty}^{+\infty} e_T(t)e_L(t-\tau)e_R^*(t-\tau)dt. \quad (4.64)$$

The omitted background terms are:

$$
\begin{aligned}
B(\tau) &= \int\limits_{-\infty}^{+\infty} |e_{SFG}(t,\tau)|^2 dt + \int\limits_{-\infty}^{+\infty} |e_R^*(t-\tau)|^2 dt \\
&= \int\limits_{-\infty}^{+\infty} |e_T(t)\boldsymbol{e_L}(\boldsymbol{t}-\boldsymbol{\tau})|^2 dt + \int\limits_{-\infty}^{+\infty} |e_R^*(t)|^2 dt.
\end{aligned}
\quad (4.65)
$$

In stark contrast to DCS, the background in CCS is dependent on the delay τ, as the target pulse is "temporally gated" by a short local pulse $e_L(t-\tau)$. At the weak tail of the target pulse, where the effective correlation signal is weak, the background is also very weak, as it is free from the strong power of the center (peak) part of the target pulse. This allows a much stronger target pulse to be used, which promises a higher SNR at the weak tail, compared to the linear DCS. This behavior is well shown qualitatively in Figure 4.1(e).

It is readily seen that the temporal gating effect is better as the local pulse is shorter. Also, a shorter local pulse benefits the power conversion efficiency of the nonlinear process. This is one of the reasons why we use a relatively short local pulse (broadband local FC) in our experiment, although only the total bandwidth of the local FC and readout FC is regulated in theory to fully map the target FC.
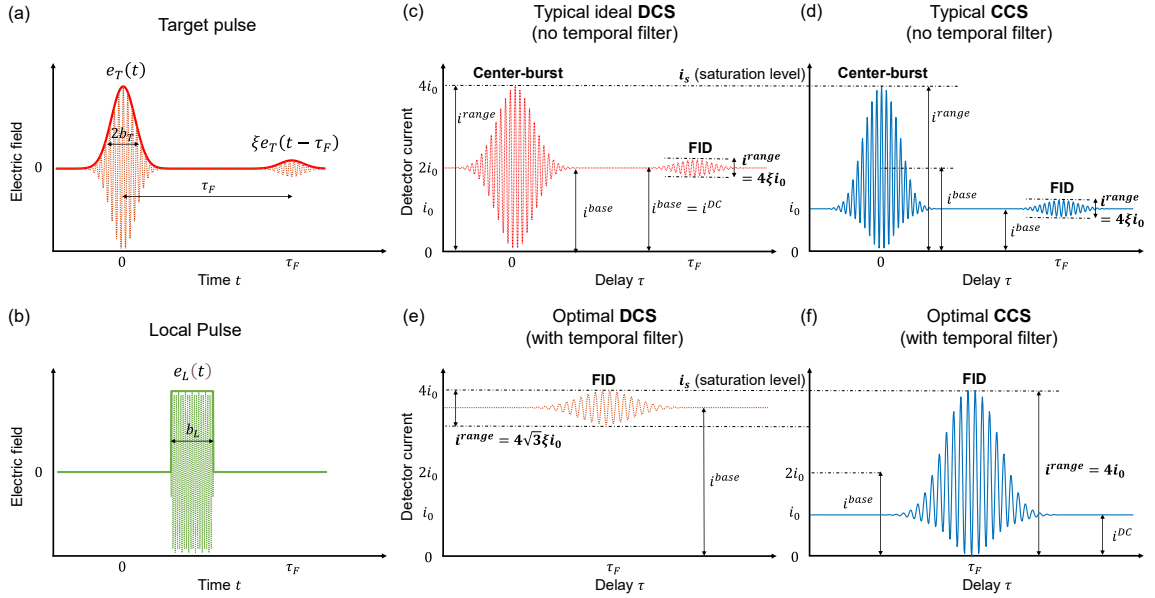
Figure 4.13: **Theoretical model assumptions and comparison between CCS and DCS.**
(a) Electric field of the target pulse $e_T(t)$, followed by its FID part $\xi e_T(t - \tau_F)$. **(b)** Electric field of the local pulse $e_L(t)$. **(c)-(d)** Typical interferograms of DCS (c) and CCS (d), without temporal filtering. **(e)-(f)** Optimal interferograms of DCS (e) and CCS (f) at FID, with a temporal filter to remove their center-bursts.

4.6.2. Assumptions of the model

To compare the SNR and sensitivity of DCS and short-pulse CCS quantitatively, firstly, we need to set up our model (Figure 4.13(a)-(b)):

(1) When the target pulse does not go through sample, we describe it by: $e_T(t) = a g_b(t) \exp(i\omega_T t)$, where a_0 denotes the amplitude, $g_b(t)$ denotes the pulse envelope function. $g_b(t)$, and other functions $g(t)$ to follow, is set to be a gaussian function with a width of b, i.e., $\exp\left(-\left(\frac{t}{b}\right)^2\right)$. Also, we assume a slowly varying envelope, i.e., $\frac{dg(t)}{dt} \ll \omega$.

(2) After the target pulse goes through the sample, we describe it by $e_T^S(t) = \left[a_T g_{b_T}(t) + \xi a_T g_{b_T}(t - \tau_F)\right] \exp(i\omega_T t) = e_T(t) + \xi e_T(t - \tau_F)$ (see panel (a)). The first term denotes the original probing pulse (center-burst), and the second term denotes the FID from the sample. ξ denotes the amplitude ratio between the center and FID, which is $\ll 1$ if assuming a weak absorption measurement. τ_F denotes the time interval between

the FID and the pulse center, and we assume it is $\gg b_T$ (the pulse width of $a_{\tau_T}(t)$), i.e., the FID signal is far enough from the center thus the field amplitude here is not influenced by the term $g_{b_T}(t)$. Indeed, it is not physically sound to assume the FID signal has the same pulse shape as the original excitation pulse. However, what matters for the following calculations is the amplitude ratio ξ between the center-burst and the FID signal, and these assumptions simplify the math without changing the core of the calculation. According to the derivation in part II of the supplementary material of ref. [82], ξ approximately equals the absorption up to a few other factors.

(3) For DCS, we set the readout pulse similar to the target: $e_R(t) = a_R g_{b_R}(t) \exp(i\omega_T t)$ (see $e_T(t)$ in panel (a)). For simplicity we assume $b_R = b_T$.

(4) For CCS, we set the local pulse as a square gating function, i.e., $e_L(t) = rect_{b_L}(t)$. b_L denotes the width of this square function, for which we assume $\tau_F \gg b_L > b_T$ (i.e., a local pulse width larger than target pulse width but much smaller than the interval between the FID and center-burst). Therefore, for the target pulse $e_T^s(t)$, around the center-burst, we have $e_{SFG}(t, \tau \sim 0) = e_T^s(t)e_L(t-\tau) \cong e_T(t)$; around the FID, we have $e_{SFG}(t, \tau \sim \tau_F) = e_T^s(t)e_L(t-\tau) \cong \xi e_T(t-\tau_F)$. This assumption means the gating function effectively separates different temporal parts of the target pulse, and only the part that overlaps with the gating function can influence the detector value at a specific delay τ. As for the readout pulse, we assume it has the same envelope as the readout of DCS, although with a different optical frequency ω.

(5) For both DCS and CCS, we use a single slow detector that samples at a rate f_s, the same as the repetition rate of the readout FC ($f_s = f_{r,R} = f_{r,L} \cong f_{r,T}, T_s = \frac{1}{f_s} \ggg \tau_F \gg b$). Taking DCS as an example, at a delay τ, the detector current can be represented by: $i(\tau) = C_{ip} \int_{-\frac{T_S}{2}}^{\frac{T_S}{2}} |e_T(t) + e_R(t-\tau)|^2 dt$, where C_{ip} denotes a constant parameter that converts the result of the integration (equivalent to optical power) to photocurrent. Note that C_i includes some physical constants related to the electric field as well as the quantum efficiency and responsivity of the detector, which are not main subjects of this study. The parameter, C_{ip},

and integration limits, $\frac{T_s}{2}$ and $-\frac{T_s}{2}$, will be omitted to simplify the equation later, since the calculation is not generally sensitive to them.

(6) There are three kinds of noise that would be generally included in the SNR discussion: detector noise (NEP), shot noise, and relative intensity noise (RIN) [96]. For clarity, we do not include the RIN in this calculation. Therefore, unless the optical power is very low, shot noise is the main noise source here. Since we are going to apply the idea of "temporal gating," we study the SNR of the measurement in the time domain.

Let us first start with a typical ideal DCS measurement (no FID). We assume $e_T(t) = e_R(t) = a g_b(t) \exp(i \omega_T t)$, and $i_a = \int e_T^2(t) dt$. Please refer to Figure 4.13(c) (the center-burst part) for illustration of the following discussion.

When $|\tau| \gg b$, i.e., the two pulses do not overlap, and we have a background signal:

$$i^{DC} = \int e_T^2(t) dt + \int e_R^2(t) dt = 2 i_a. \tag{4.66}$$

At $\tau = 0$, when the two pulses constructive interfere, i.e., the maxima of the interferogram, we have:

$$i^+(0) = \int \left(2 e_T(t)\right)^2 dt = 4 i_a. \tag{4.67}$$

At $\tau \cong 0$, when the two pules destructively interfere, i.e., the minimum of the interferogram, we have:

$$i^-(0) \cong \int [e_T(t) - e_R(t)]^2 dt = 0. \tag{4.68}$$

Thus, the range of the interference here, denoted by i^{range}, is $4 i_a$, which can be understand as the amplitude of the "signal." To evaluate the noise, we define the base current i^{base} around $\tau = 0$ as the average value of $i^+(0)$ and $i^-(0)$, which is:

$$i^{base}(0) = \frac{1}{2}(i^+(0) + i^-(0) = 2 i_a. \tag{4.69}$$

In this case, the base current around the maxima is equal to the background i_{DC}. Since shot noise here increases with i^{base}, to optimize SNR, one wants to optimize the ratio

i^{range}/i^{base}. Actually, this ratio is equivalent to the "interferometric visibility" up to a factor of $1/2$.

The shot noise around $\tau = 0$ can be expressed by:

$$i^{sn} = C_{isn}\sqrt{i^{base}} = C_{isn}\sqrt{2i_a}. \tag{4.70}$$

C_{isn} denote a constant parameter that convert $\sqrt{i^{base}}$ into current noise. Like C_{ip}, C_{isn} includes some physical constants which are not the main subjects of this study.

If the optical power is low, the dominant noise is detector noise, and the SNR of the measurement is:

$$SNR = \frac{i^{range}(0)}{i_{NEP}} = \frac{4i_a}{i_{NEP}}. \tag{4.71}$$

The dominant noise becomes the shot noise when the optical power is higher, and SNR of the measurement is:

$$SNR = \frac{i^{range}(0)}{i^{sn}} = \frac{4i_a}{C_{isn}\sqrt{2i_a}}. \tag{4.72}$$

Apparently, the SNR increases with $\sqrt{i_a}$, and this dependence agrees with general shot-noise-limited measurement since $i_a \propto$ the power of the target (or readout) pulse. Also, the above two equations are equivalent to equation (24) and (25) of ref. [96], although different letter conventions are used, and the RIN and dynamic range terms are not included.

The SNR can be improved by increasing i_a (average power of FCs), which stops when $i^+(0) = 4i_a$ reaches i_s, i.e., the saturation level of the detector. Let $i_0 = \frac{1}{4}i_s$, thus the SNR reaches maxima when $i_a = i_0$ ($4i_0 = i_s$):

$$SNR_{DCS,max} = \frac{4i_0}{C_{isn}\sqrt{2i_0}}. \tag{4.73}$$

4.6.3. SNR at FID, without temporal filtering

To compare the sensitivity for weak absorption, we need to calculate SNR at the FID instead of the center-burst. Let us start with DCS following the last subsection. This time we assume $e_T^s(t) = [a_0 g_b(t) + \xi a_0 g_b(t - \tau_F)]\exp(i\omega_T t) = e_T(t) + \xi e_T(t -$

$\tau_F), e_R(t) = e_T(t) = a_0 g_b(t) \exp(i\omega_T t), i_0 = \int e_R^2(t)dt = \int e_T^2(t)dt.$ See Figure 4.13(c).

At the center-burst, $i^+(0) = 4i_0 = i_S$, and the SNR here reaches maxima, as explained above.

However, at the FID, everything changes. We have:

$$i^+(\tau_F) = \int \left((1+\xi)e_T(t)\right)^2 dt + \int e_T^2(t)dt = [(1+2\xi+\xi^2)+1]i_0 \quad (4.74)$$

$$i^-(\tau_F) = \int \left((1-\xi)e_T(t)\right)^2 dt + \int e_T^2(t)dt = [(1-2\xi+\xi^2)+1]i_0 \quad (4.75)$$

$$i^{range}(\tau_F) = i^+(\tau_F) - i^-(\tau_F) = 4\xi i_0 \quad (4.76)$$

$$i^{base} = \frac{1}{2}[i^+(\tau_F) + i^-(\tau_F)] = (2+\xi^2)i_0 \cong 2i_0 \quad (4.77)$$

$$SNR_{DCS,FID} = \frac{4\xi i_0}{C_{isn}\sqrt{2i_0}} = \xi SNR_{DCS,max}. \quad (4.78)$$

In short, although the amplitude of the signal (the interference) is ξ times weaker than that at the center-burst, the noise level is still the same since the detector can see all the background from the center-burst, i.e., the large energy which contributes to only the noise here but not the signal.

Let us then consider CCS. (See Figure 4.13(d).) At the center-burst, since we assume $e_{SFG}(t, \tau \sim 0) = e_T'(t)e_L(t-\tau) \cong e_T(t)$, its SNR has the same results as DCS. However, at the FID, $e_{SFG} \cong \xi e_T(t-\tau_F)$, we have:

$$i^+(\tau_F) = \int \left((1+\xi)e_R(t)\right)^2 dt = [(1+2\xi+\xi^2)]i_0$$

$$i^-(\tau_F) = \int \left((1-\xi)e_R(t)\right)^2 dt = [(1-2\xi+\xi^2)]i_0 \quad (4.79)$$

$$i^{range}(\tau_F) = 4\xi i_0; \ i^{base} \cong i_0 \quad (4.80)$$

$$SNR_{CCS,FID} = \frac{4\xi i_0}{C_{isn}\sqrt{i_0}} = \sqrt{2} \, SNR_{DCS,FID}. \quad (4.81)$$

This shows a $\sqrt{2}$ SNR enhancement of CCS over DCS, which is not significant. In fact, here we greatly limit the capability of CCS. On one hand, in this simple model we assume

the same detector performance (NEP, responsibility, quantum efficiency, saturation level, and etc.) of the NIR detector of CCS and MIR detector of DCS, the latter of which should be worse the former. On the other hand, we still limit the optical power, especially the local pulse, of the CCS, to avoid detector saturation at the center-burst, which is not necessary for detecting weak absorption.

4.6.4. SNR at FID, with temporal filtering

Now we introduce a temporal filter that throws out the interference signal at the center-burst (before the FID) and only keep the interference around FID for the detection of weak absorption[82]. In this case, we no longer care about the detector saturation at the center-burst; the limits of the SNR at the FID are set by the detector saturation at the FID locally.

For DCS, we can increase both the power of $e_R(t)$ and $e_T(t)$ by 2 times, i.e., $e_R(t) = \sqrt{2}e_T(t), e_T^s(t) = \sqrt{2}e_T(t) + \sqrt{2}\xi e_T(t - \tau_F)$, to maximize the SNR here. See Supplementary Fig. 15 (e). We cannot increase more since $i^+(\tau_F)$ already saturates the detector. We have:

$$i^+(\tau_F) = \int \left((\sqrt{2} + \sqrt{2}\xi)e_T(t)\right)^2 dt + \int 2e_T^2(t)dt$$
$$= [(2 + 4\xi + 2\xi^2) + 2]i_0 \cong 4i_0 = i_s$$
(4.82)

$$i^-(\tau_F) = \int \left((\sqrt{2} - \sqrt{2}\xi)e_T(t)\right)^2 dt + \int 2e_T^2(t)dt$$
$$= [(2 - 4\xi + 2\xi^2) + 2]i_0 \cong 4i_0 = i_s$$
(4.83)

$$i^{range}(\tau_F) = i^+(\tau_F) - i^-(\tau_F) = 8\xi i_0$$

$$i^{base}(\tau_F) = \frac{1}{2}[i^+(\tau_F) + i^-(\tau_F)] = (4 + 2\xi^2)i_0 \cong 4i_0$$
(4.84)

$$SNR_{DCS,FID}^{gated} = \frac{8\xi i_0}{C_{isn}\sqrt{4i_0}} = \sqrt{2}\,SNR_{DCS,FID} = \sqrt{2}\xi SNR_{DCS,max}.$$
(4.85)

Compared to not-gated case, the SNR can only be increased by a factor of $\sqrt{2}$.

For CCS, thanks to temporal gating by the local pulse, the detector signal at the FID is free from the power of the center part of the target pulse (the second term of the RHS of the

above equation of $i^+(\tau_F)$, i.e., $\int 2e_T^2(t)dt$). Thus, we can increase the power of the local pulse by a factor of $(\frac{1}{\xi})^2$, i.e., $e_L'(t) = \frac{1}{\xi}rect_{b_L}(t)$. Then, at the FID: (See Figure 4.13 (f))

$$e_{SFG}(t, \tau = \tau_F) = \xi e_T(t - \tau_F)e_L'(t - \tau_F) = \xi e_T(t - \tau_F)\frac{1}{\xi}rect_{b_L}(t - \tau_F)$$
$$\cong e_T(t - \tau_F).$$

(4.86)

If we keep $e_R(t) = e_T(t)$, we will have an SNR equivalent to that of the center-burst of a typical ideal DCS or CCS measurement, calculated in Section 4.6.3:

$$i^+(\tau_F) = \int \left(2e_T(t - \tau_F)\right)^2 dt = 4i_0 = i_s$$

$$i^-(\tau_F) = 0; \; i^{range}(\tau_F) = 4i_0; \; i^{base}(\tau_F) = 2i_0$$

(4.87)

$$SNR_{CCS,FID}^{gated} = \frac{4i_0}{C_{isn}\sqrt{2i_0}} = \frac{1}{\sqrt{2\xi}}SNR_{DCS,FID}^{gated}.$$

(4.88)

Therefore, a $\frac{1}{\sqrt{2\xi}}$ SNR enhancement is demonstrated for CCS compared to DCS at FID, assuming sufficient upconversion. The weaker the absorption, the stronger the enhancement can be. The reason for this lies in the fact that the DCS signal at the FID always comes with a factor of $1/\xi$ stronger DC background which contributes only to the noise but not the signal, while CCS does not. This comparison is illustrated in Figure 4.2(d) of the main paper.

In practice, one can "infinitely" decreases ξ by decreasing the sample concentration or gas cell length. However, the enhancement ratio $\frac{1}{\sqrt{2\xi}}$ cannot be infinitely increased; the limit is set by two factors, whichever comes first:

(a) The SFG efficiency. To fully reach the SNR enhancement, one needs to upconvert the target pulse by a factor $1/\xi$ stronger using local pulses with a higher peak power. However, this can be clamped by the highest available peak power of local pulses or the damage threshold of the SFG crystal.

(b) The damage threshold of the NIR detector. Although the detector saturation at the center-burst no longer matters if we discard the signal there, we still do not want the power there to damage the detector. Generally, however, the detector is damaged by the average power rather than the peak power, and the average power on the detector mainly depends on that of the readout pulses instead of the local pulses. In other words, just a very small portion of the local pulse average power contributes to the total average power on the detector, the ratio of which is decided by the "duty cycle" of the SFG process (see Section 5.4). In temporal-filtered CCS, the strategy is to use stronger local pulses while keeping the readout pulses unchanged, which adds only a tiny optical average power on the detector. Hence, it is very unlikely that the limit of this factor comes earlier than the former.

4.6.5. Sensitivity and dynamic range, with temporal filtering

Following the SNR calculation, a comparison of sensitivity (the minimal detectable ξ) becomes straightforward. Let us define ξ_{min}, the minimal detectable ξ that makes SNR=1. For DCS at the FID, we have:

$$SNR_{DCS,FID}^{gated} = \frac{8\xi_{min}^{DCS} i_0}{C_{isn}\sqrt{4i_0}} = 1 \tag{4.89}$$

$$SNR_{DCS,FID}^{gated} = \frac{8\xi_{min}^{DCS} i_0}{C_{isn}\sqrt{4i_0}} = 1. \tag{4.90}$$

Clearly it is limited by i_s, the detector saturation ($i_s = 4i_0$).

For CCS, the sensitivity depends entirely on the upconversion capability, as discussed before. Let us assume the upconversion conversion ratio is $1/\xi_0$. Then for an absorption ξ_0, as derived before, we have an $SNR = \frac{4i_0}{C_{isn}\sqrt{2i_0}}$ at the FID if we set $e_R(t) = e_T(t)$. However, this SNR is much larger than 1 and more than enough to detect the absorption signal. Thus, we can further decrease the absorption. Let us assume an extra absorption factor ξ_1 to make the target FID a "small signal." Simultaneously, to maximize SNR, we set $e_R(t) \cong 4\, e_T(t)$. Then, at the FID, we have:

$$i^{range}(\tau_F) = 16\xi_1 i_0; \ i^{base}(\tau_F) = 4i_0; \ SNR_{CCS,FID} = \frac{16\xi_1 i_0}{C_{isn}\sqrt{4i_0}}. \tag{4.91}$$

Assuming this SNR=1, we have:

$$\xi_{1,min} = \frac{C_{isn}}{4\sqrt{i_s}} = \frac{1}{2}\xi_{min}^{DCS}.$$ (4.92)

Adding the ratio ξ_0 back, we have:

$$\xi_{min}^{CCS} = \xi_0\xi_{1,min} = \frac{1}{2}\xi_0\xi_{min}^{DCS}.$$ (4.93)

Therefore, CCS can detect a $\frac{1}{2}\xi_0$ smaller absorption compared to DCS. The detection is limited by the upconversion capability rather than the detector.

It should be noted that, in order to maximize the sensitivity (minimize the detectable ξ) for both techniques, we set their parameters ($e_R(t)$ and $e_T(t)$) to make i_{base} close to detector saturation. However, in such settings, there will not be dynamic range for the detection: a larger absorption will excess the saturation limit, and lower absorption will make $SNR < 1$ thus not detectable. In short, for a detection where we want to get good dynamic range, we do not want to use the settings for the best sensitivity.

We continue to compare their dynamic ranges. In the interest of fairness, we used different power settings for each method to optimize their respective DR while keeping their sensitivity (minimal detectable absorption, the lower limit of the detectable range) the same. The comparison is illustrated in Figure 4.2(e).

In CCS, for an arbitrary low absorption ξ_{low}, we keep powers of readout FC ($e_R(t)$) and SFG signal ($e_{SFG}(t, \tau_F)$) the same and to be a quarter of the detector NEP. Note that SFG power can be tuned by either target power ($e_T(t)$) or local power ($e_L(t)$). In such power setting, the interference range (i^{range}) would be equal to the i_{NEP}, making the absorption just detectable. Note that the dominant noise source in this scenario is detector noise (NEP) rather than the shot noise as readout power and SFG power are both tuned very low. Any stronger absorption would make $e_{SFG}(t, \tau_F)$ larger and more detectable until the detector is saturated. In other words, the interference range can vary from i_{NEP} to i_S, which means the DR of the absorption (ξ) can utilize the full DR of the detector $\left(\frac{i_S}{i_{NEP}}\right)$ and we have

$DR_{CCS_\xi} = \sqrt{DR_{detector}}$. The square root here is simply because we use ξ, a ratio of optical field, to quantify absorption, but detector current is proportional to optical power (square of the field).

In DCS, if we keep the readout power and target power here as same as those of the CCS case, we will get a same interference range $i^{range} = i_{NEP}$, which makes the same small absorption ξ_{low} detectable. However, unlike CCS, a large extra DC background will always be seen by the detector due to a lack of temporal gating. This power can occupy a large portion of the detector DR and therefore limits the range of the detectable absorption. Since this extra background is a factor of $\left(\frac{1}{\xi_{low}}\right)^2$ larger than the interference background in CCS, the dynamic range of DCS would be about a factor of ξ_{low} smaller than that of CCS, i.e., $DR_{DCS_\xi} = \sqrt{(\xi_{low})^2 DR_{detector}} = \xi_{low} DR_{CCS_\xi}$. In fact, this still underestimates the difference between them, since in DCS the dominate noise would become the shot noise at the same ξ_{low} because of the large background. Therefore, even larger target power or readout power has to be used to make the same absorption detectable, i.e., make the interference larger than the total noise, which is now the sum of shot noise and detector noise. This explains why for the same ξ_{low}, in Figure 4.2(e) of the main paper, the interference of the DCS looks larger than that of the CCS; it has to be made larger by a larger target or readout power, to overcome a larger noise. This larger target or readout power will then occupy more $DR_{detector}$. Moreover, the lower the ξ_{low} set to be, the more $DR_{detector}$ has to be occupied as higher target or readout power has to be used in DCS to make the signal detectable, and larger the difference between DCS and CCS will be.

4.6.6. SNR scaling with power of different combs

Here we provide a direct analysis about how temporal SNR of the interferogram scales with powers of different combs, based on the same model and assumptions.

First of all, as the SFG process in our experiment and theoretical model is far from saturation or depletion, the SFG output power is expected to be linear to target power or local power, which is consistent with what we observed in the experiment.

Then the question becomes how SNR scales with the SFG power, which depends on the relative power of the other arm of the interference, readout power, and the current dominant noise source of the detection. This is equivalent to how a typical interference (between two short pulses) SNR scales with the power of one arm. We can use a simple equation to explain this:

$$I = \left(\sqrt{P_{SFG}} + \sqrt{P_r}\right)^2 = P_{SFG} + P_r + 2\sqrt{P_{SFG}P_r} \tag{4.94}$$

with which we have,

$$signal \propto \sqrt{P_{SFG}P_r} \tag{4.95}$$

$$Noise = (shot\ noise + NEP) \propto \left(\sqrt{P_{SFG} + P_r} + P_{NEP}\right). \tag{4.96}$$

Then there are a few different cases:

(a) When SFG and readout power are both low and the dominant noise is the detector noise, the SNR scales linearly with the square root of SFG power or target/local power ($S \propto \sqrt{P_{SFG}}, N = P_{NEP}$).

(b) When SFG power is high, readout power is low, and the dominant noise is the shot noise from SFG power, the SNR does not change with the SFG power or target/local power ($S \propto \sqrt{P_{SFG}}, N \propto \sqrt{P_{SFG}}$).

(c) When SFG power is low, readout power is high, and the dominant noise is the noise from readout power, the SNR scales linearly with the square root of the SFG power or target/local power ($S \propto \sqrt{P_{SFG}}, N \propto \sqrt{P_r}$).

(d) When both the SFG power and readout power are high and comparable, and the dominant noise is shot noise from both the SFG power and readout power, the SNR increases with the SFG power or target/local power ($S \propto \sqrt{P_{SFG}}, N \propto (\sqrt{P_{SFG} + P_r})$).

Note that in above analyses, the roles of SFG and readout FC are equivalent, and the roles of target power and local power are also equivalent. Those analyses are basically equivalent to that of typical optical heterodyne detection.

4.6.7. Summary

The discussion above demonstrates the fact that the sensitivity of short-pulse CCS is limited by upconversion capability (SFG efficiency), which is fundamentally different from DCS, where it is limited by the detector saturation. The beauty of the short-pulse-upconversion CCS is that strong local pulses can greatly enhance the peak power of the signal of interest in a localized temporal window, with minimal increase to the background signal and average power on the detector which add to noise and saturation of the detector. This time gating effect endows CCS advantages in SNR, sensitivity, and dynamic range.

Moreover, it should be noted that, among the three different upconversion configurations, only short-pulse-upconversion CCS can fully have these advantages. Firstly, C.W. upconversion CCS is basically DCS, which does not have advantages we discussed here at all. Secondly, for EOS CCS, one may expect it to have the same advantages since it also uses short pulses for upconversion, but this is not true if no more efforts are taken to independently control the power and spectrum of different spectral parts of the ultrashort pulses. Admittedly, the even higher peak power of the local pulse (because of shorter pulse length) used in EOS CCS can provide even higher upconversion efficiency. However, when the average power of the local pulses is increased to detect weaker absorption, that of the readout part of the local spectrum is also increased, which can saturate the detector unexpectedly, if they are not independently controlled. In other words, in short-pulse-upconversion CCS, you can always use higher local power to amplify a weaker FID signal while keeping the readout power unchanged, and you will never saturate the detector. However, in EOS CCS, you cannot do the same since local and readout are from the same pulse (spectrum), and thus their power cannot be tuned independently.

4.7. Comparison of performance between DCS and CCS by simulation

In previous sections we have compared principles and some performance metrics of different techniques using simplified theoretical models. In this section, we will provide a more quantified comparison by numerical simulation, to further demonstrate the advantages of CCS. We will focus on the SNR and sensitivity of the typical MIR DCS,

MIR CCS without temporal filtering, and MIR CCS with temporal filtering, and how they scale with the sample concentration (absorbance).

4.7.1. Simulation assumptions

Although more quantified and accurate, the assumptions of our simulations are still basically consistent with those of the previous theoretical models. These assumptions will be explained in detail below.

a. Frequency combs

We use femtosecond pulses for both DCS and CCS. For DCS, transform-limited sech^2 pulses of a FWHM of 250 fs centered at 4270 nm (70 THz) are used as the target FC, and the same pulse profile is used for the readout FC. For CCS, the exact same target FC is used, and pulses with the same shape and width but centered at 1560 nm (192 THz) and 1145 nm (262 THz) are used as the local FC and readout FC, respectively. Their repetition rates are set at 250 MHz, and the difference in repetition rates is set at 1kHz. The detection bandwidth is taken to be 125 MHz, i.e., half of the repetition rate.

For DCS, the comb powers are assumed to be enough to saturate the MIR detector (~1 mW), which is practical as many high-power MIR combs have been demonstrated in the past decade. For CCS, we also assume enough MIR power, local power, and nonlinearity, which is interchangeable with higher SFG power, to have a high enough upconverted SFG power to saturate the NIR detector (also ~1mW). This assumption is also practical considering our experimental results, recent progress in related areas, and state-of-the-art techniques as discussed in the main paper.

b. Sample

Here we use 1-meter-long CO_2 of ambient level (~400 ppm) as the sample of unit concentration (relative concentration 10^0 in Figure 4.20), which is used in simulation for different techniques.

We model the CO_2 response using the Lorentz oscillator model [4] in which the refractive index as a function of frequency, $n(\omega)$, is given by the equation:

$$n^2(\omega) = 1 + \sum_{ij} \frac{f_{ij}N_j q^2}{2\varepsilon_0 m_e\left(\omega_{ij}^2 - \omega^2 + i\gamma_{ij}\omega\right)} \tag{4.97}$$

where the indices i, j refer to the upper and lower states of the transitions of interest, N_j is the density of molecules in state j, f_{ij} is the oscillator strength, q is the electron charge, m_e is the electron mass, ϵ_0 is the vacuum permittivity, ω_{ij} is the angular frequency of the transition's line center, and γ_{ij} is the transition linewidth. Line parameters for the CO_2 transitions are taken from the HITRAN database [65]. The absorption and dispersion can be directly computed from the resulting complex refractive index through the relationship:

$$n(\omega) = n'(\omega) - i\kappa(\omega) \tag{4.98}$$

where the dispersion information is contained in *n'(ω)* and the absorption profile is given by κ*(ω)*.

Note that although we use target pulses centered at 4270 nm and CO_2 absorption, this simulation can be adapted to other MIR wavelength easily, which would not fundamentally change the conclusions of this section.

c. Detectors

Detectors are an important factor in considering the differences between MIR DCS and CCS. We choose an InGaAs detector as NIR detector and a HgCdTe (MCT) detector as MIR detector, each of which is a very typical choice in its wavelength region. While different detectors from different manufacturers can have very different performance metrics, we adapt the specifications of two commercial detectors from Thorlabs, FPD510-FS-NIR (InGaAs) and PDAVJ10 (MCT), for the simulation, which can well represent the general metrics of these two kinds of detectors. Note that we also refer to a review paper [113] for D[*] of these detectors.

For the NIR InGaAs detector, we assume:

Spectral responsivity $0.8\ A/W$; Size $(1\ mm)^2$; D[*]$=1 \times 10^{11}\ cm * Hz^{\frac{1}{2}} * W^{-1}$; NEP= $1\ pW/Hz^{\frac{1}{2}}$; $P_{saturation} = 1\ mW$.

For the MIR MCT detector (at room temperature), we assume:

Spectral responsivity $0.01\ A/W$; Size $(1\ mm)^2$; $D^*=5\times10^8\ cm*Hz^{\frac{1}{2}}*W^{-1}$; NEP= $200\ pW/Hz^{\frac{1}{2}}$; $P_{saturation}=1\ mW$.

d. Noise

As before, we include detector noise and shot noise in our simulation. For the assumed NIR detector, the detector noise will dominate at low input powers, while shot noise will dominate at higher input powers. For the assumed MIR detector, however, even at detector saturation, the shot noise will be about the same order of magnitude as the detector noise, as shown by the simulation below, because of its low responsivity and high NEP. Therefore, the shot noise and detector noise are both important at high input powers for the MIR detector. Note that this detector difference is not included in our theoretical model above, making that model effectively less advantageous to CCS.

e. Nonlinearity

For simplicity, we assume an ideal nonlinear conversion process where the upconverted field is the product of the target and local field (the SFG part), which is consistent with the theoretical model. The power efficiency is estimated by the standard SFG model with the assumption of quasi-C.W. operation [114,115]. The nonlinear crystal is assumed to be lithium niobate. Although a more accurate model for the nonlinearity could be used to give a more accurate estimation of upconversion efficiency and bandwidth, these estimates will not affect most parts of this simulation, because generally there will be enough SFG power to saturate the detector. The accurate estimation of upconversion efficiency will only be important to estimate the limits of the CCS with temporal filtering, as we will explain later.

4.7.2. DCS

With all the parameters assumed, the DCS interferograms can be simulated, as presented in Figure 4.14. The average power of the target FC and local FC are both set to one quarter of the $P_{saturation}$, by which the detector will be just saturated (10 µA) at the center peak of the reference interferogram (see panel (a)). The reference interferogram (without sample) and absorbed interferogram (with sample) are present in upper panels (a)-(d) and lower

panels (e)-(f), respectively. As the full interferograms are too long to show, we present the center-burst ((a) and (e)) and one typical part of the FID ((b) and (f)), which can exhibit key signatures of the sample. In (a) and (b) ((e) and (f)), we show only the ideal unbalanced interferogram (signal from one arm of the balanced detector), to better display the relationship between the baseline (D.C.) and the effective interference (A.C.). The corresponding balanced interferograms, as well as noises, are shown in panel (c) and (d) ((g) and (h)). Note that it is because we use a relatively strong absorption here that the effective interference at the FID is fairly observable compared to the background (see (f)) and the noises (see (h)), but the signal could be easily overwhelmed by the noise if a much lower absorption were considered.
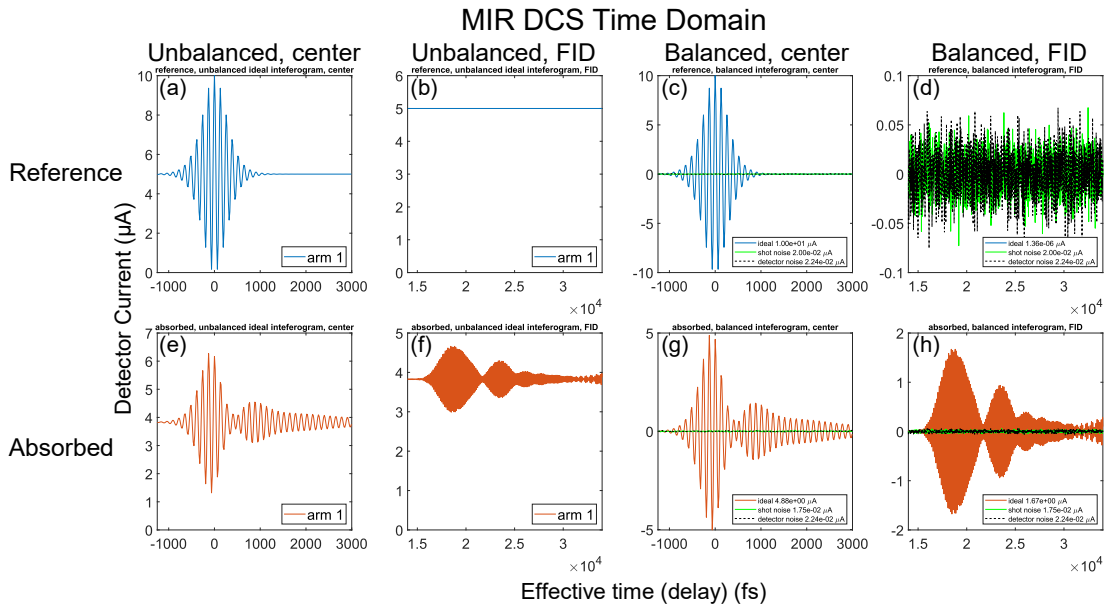
Figure 4.14: **Time domain of MIR DCS.** **(a)** Unbalanced ideal interferogram at the center (-1.25 ps – 3 ps) of the reference measurement (without sample). Note that only the signal recorded by one arm of the balanced detector is shown, and signal at the other arm is of π-phase difference, which is also the case for (b), (e), and (f). **(b)** Unbalanced ideal interferogram at one part of the FID (-14 ps – 34 ps) of the reference measurement. **(c)** Balanced ideal interferogram at the center of the reference measurement, together with noise. The maxima of the ideal interferogram, as well as the average level (standard deviation) of the noise, is denoted in the legend box for the reference; the same is done in (d), (g) and (h). **(d)** Balanced ideal interferogram at one part of the FID of the reference measurement, together with noises. **(e)** Unbalanced ideal interferogram at the center of the absorbed measurement (with sample). **(f)** Unbalanced ideal interferogram at one part of the FID of the absorbed measurement. **(g)** Balanced ideal interferogram at the center of the

absorbed measurement, together with noises. **(h)** Balanced ideal interferogram at one part of the FID of the absorbed measurement, together with noises.

By taking the Fourier transform of those temporal signals and noises, spectra can be obtained, which are shown in Figure 4.15. In panel (a), the spectral amplitude of the ideal reference measurement, the ideal absorbed measurement, and the total noise (sum of the two kinds of noises) are presented, and their average amplitudes are displayed in the legend box. The spectra are truncated to an interval with endpoints where the reference amplitude equals the noise amplitude. Note that the frequency axes are obtained from the direct Fourier transform, which needs to be linearly mapped to real frequencies. However, it is not done in the figures as it is not necessary for our purpose. The spectra of the two noises are presented individually in panel (b). As mentioned before, for this MIR detector, the detector noise is still close to the shot noise even when the detector is saturated in reference measurement, so both are important.

The real "signal," corresponding to "noise," in the absorption measurement, is neither the reference spectrum nor the absorbed spectrum, but the difference between them. The difference spectrum is depicted in panel (c), together with spectra of the reference and the noise. The SNR of the measurement, defined as a spectral average, is the ratio of the average amplitude of the difference spectrum to that of the noise spectrum. The SNR increases with the absorption (sample concentration) as the difference amplitude increases with the absorption and approaches its upper limit. The upper limit, i.e., the max SNR, is the ratio of the average amplitude of the reference spectrum to that of the noise spectrum, because difference amplitude cannot be larger than the reference amplitude. In other words, the difference spectrum approaches the reference spectrum when the absorption is very large, while the SNR approaches its maximum. On the other side, lower absorption would result in a smaller difference amplitude and thus lower SNR, which can approach zero. Note that the SNR here is defined differently with that of ref. [96], however, the max SNR defined here is fundamentally equivalent to the SNR (figure of merit) there.
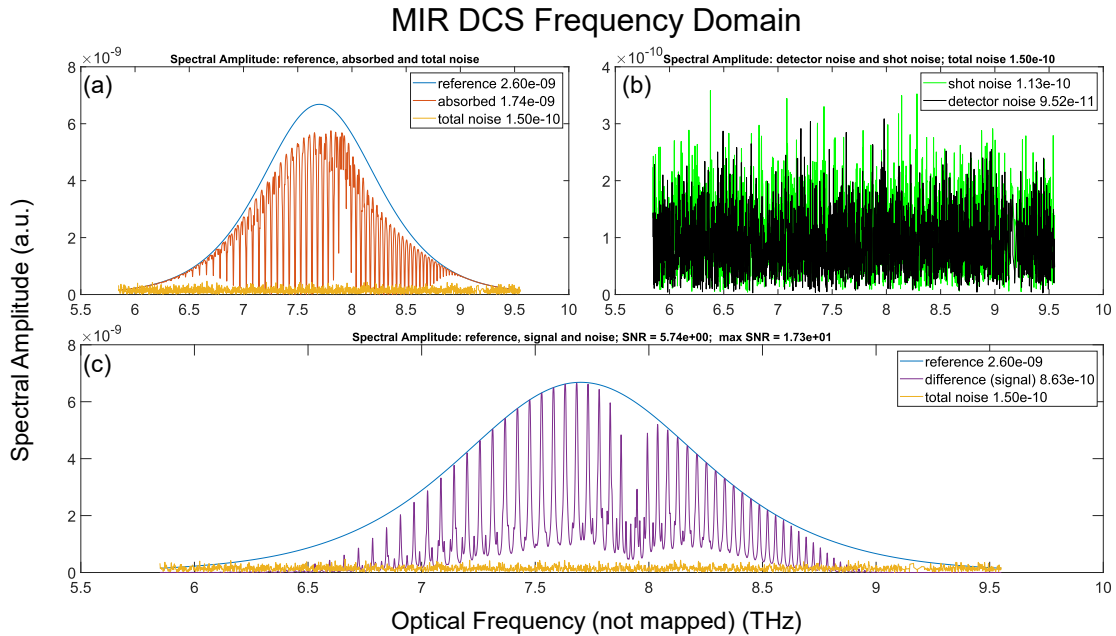
Figure 4.15: **Frequency domain of MIR DCS. (a)** Spectral amplitudes of the ideal reference measurement, ideal absorbed measurement, and total noise. The spectral amplitudes are actually complex values with phase information, but we show only their magnitude in our figures for clarity. The average amplitudes of each spectrum are displayed in the legend box; the same is done in (b) and (c). **(b)** Spectral amplitudes of the shot noise and detector noise. **(c)** Spectral amplitudes of the ideal reference measurement, ideal difference spectrum, and total noise. The spectral average SNR at this (unit) sample concentration (5.74) and its upper limit (17.3) are displayed in the plot subtitle.

4.7.3. CCS (without temporal filtering)

As with DCS described above, the time domain and frequency domain results of CCS are presented in Figure 4.16 and Figure 4.17, respectively. The SFG pulse power at zero-time-delay and the readout power are set to be the same, equal to one quarter of the $P_{saturation}$, meaning the detector will be just saturated (800 µA) at the center peak of the reference interferogram (see Figure 4.16(a)). For this NIR detector, at saturation, the dominant noise is shot noise because of its high responsivity and low detector noise (Figure 4.17(b)). Moreover, although we set the same relative powers here as for the previous DCS case (one quarter of detector saturation), the relative D.C. baseline here (one quarter of the saturation level) is lower than that of the previous case (half of the saturation level), which leads to less relative shot noise. This is the result of temporal gating, which agrees with our discussion before in the theoretical model (Section 4.6.3). A spectral average SNR of 46.8

at unit concentration and its upper limit of 161 are measured, as shown in Figure 4.17(c). The SNR would scale with sample concentration in the same way as that of the DCS above, due to the nature of the interference and measurement.
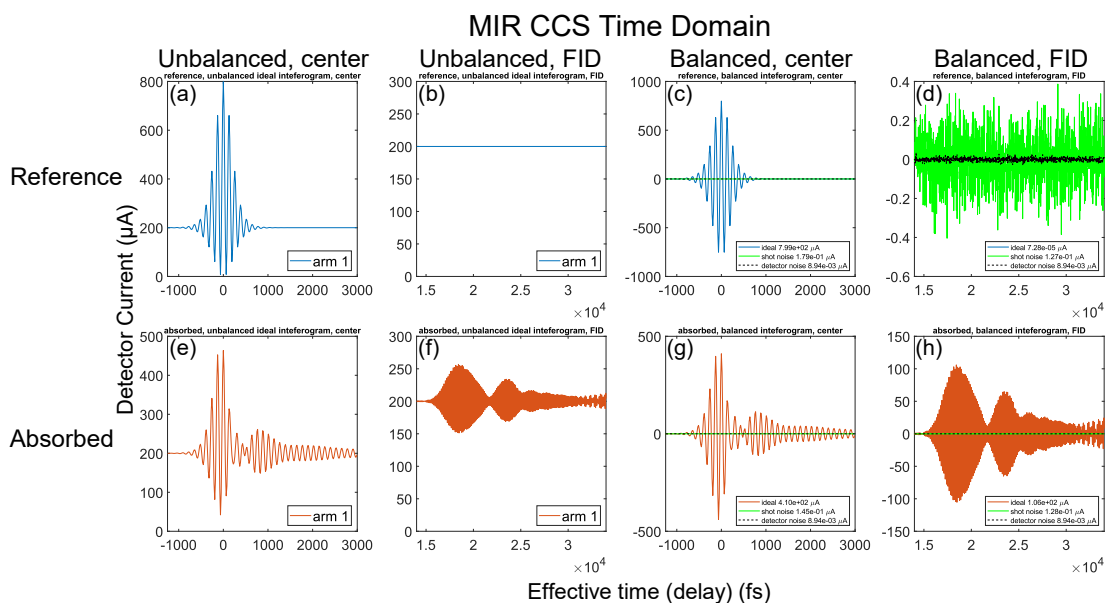
Figure 4.16: **Time domain of MIR CCS. (a)** Unbalanced ideal interferogram at the center (-1.25 ps – 3 ps) of the reference measurement (without sample). Note that only the signal recorded by one arm of the balanced detector is shown, and signal at the other arm is of π-phase difference; the same is true for (b), (e), and (f). **(b)** Unbalanced ideal interferogram at one part of FID (14 ps – 34 ps) of the reference measurement. **(c)** Balanced ideal interferogram at the center of the reference measurement, together with noises. The maxima of the ideal interferogram, as well as the average level (standard deviation) of noises, is denoted in the legend box for reference; the same is true in (d), (g) and (h). **(d)** Balanced ideal interferogram at one part of FID of the reference measurement, together with noises. **(e)** Unbalanced ideal interferogram at the center of the absorbed measurement (with sample). **(f)** Unbalanced ideal interferogram at one part of FID of the absorbed measurement. **(g)** Balanced ideal interferogram at the center of the absorbed measurement, together with noises. **(h)** Balanced ideal interferogram at one part of FID of the absorbed measurement, together with noises.
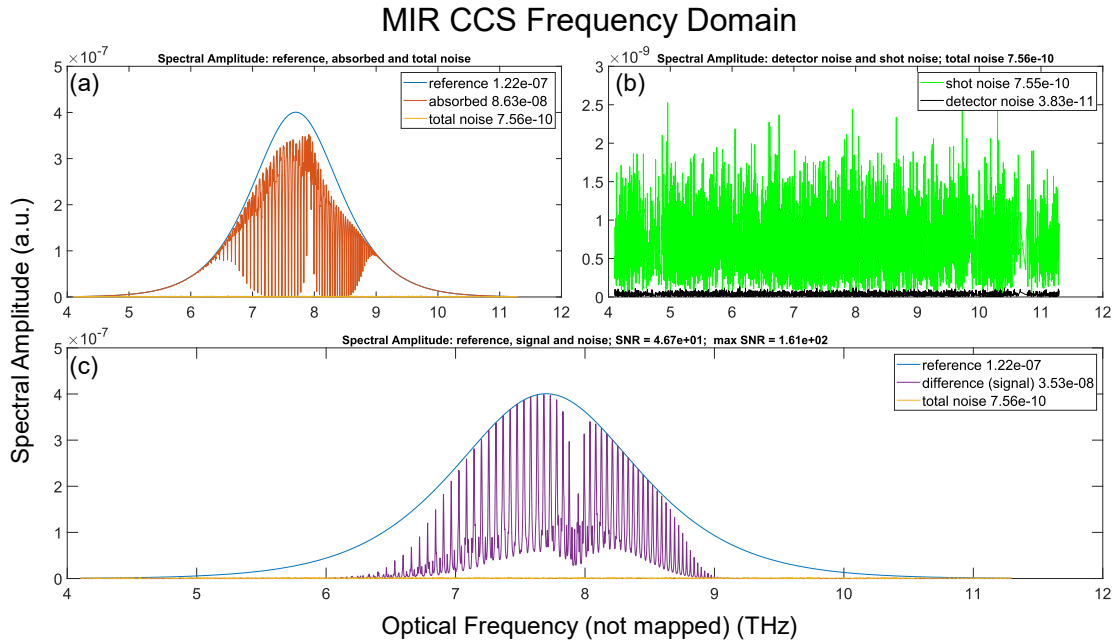
Figure 4.17: **Frequency domain of MIR CCS. (a)** Spectral amplitudes of the ideal reference measurement, ideal absorbed measurement, and total noise. The average amplitudes of each spectrum are displayed in the legend box; the same is true in (b) and (c). **(b)** Spectral amplitudes of shot noise and detector noise. **(c)** Spectral amplitudes of the ideal reference measurement, ideal difference spectrum, and total noise. The spectral average SNR at this (unit) sample concentration (46.7) and its upper limit (161) are displayed in the plot subtitle.

4.7.4. CCS (with temporal filtering)

This detection scheme is different with two cases above, and its basic idea comes from a previous work on EOS [82]. We will cut the interferograms, both reference and absorbed, at a specific delay, τ_c ($\tau_c > 0$), and keep only the part $\tau > \tau_c$ for the detection of the sample. Since the center of the interferogram (around $\tau = 0$) will be cut out, the detection saturation there will be acceptable, and a larger SFG (by tuning target and/or local power) or readout power can be applied. In this example simulation, we keep the readout power the same and increase the target power tenfold and local power fivefold compared to the case (CCS without temporal filtering) in the last subsection. Next, a $\tau_c = 0.5\ ps$ is applied, the results of which in time domain and frequency domain are presented in Figure 4.18 and Figure 4.19, respectively.

In contrast to the two previous cases, here the absorbed amplitude is generally larger than the reference amplitude (Figure 4.19(a)). Although the estimated SNR can be significantly higher than the without-filter case, the signal obtained here is more useful for detecting the presence of the molecule than recovering its complete fingerprint. In other words, as part of the information is excluded by temporal filtering, the original and complete absorption spectrum of the sample cannot be retrieved, at least directly, like in general DCS and CCS.
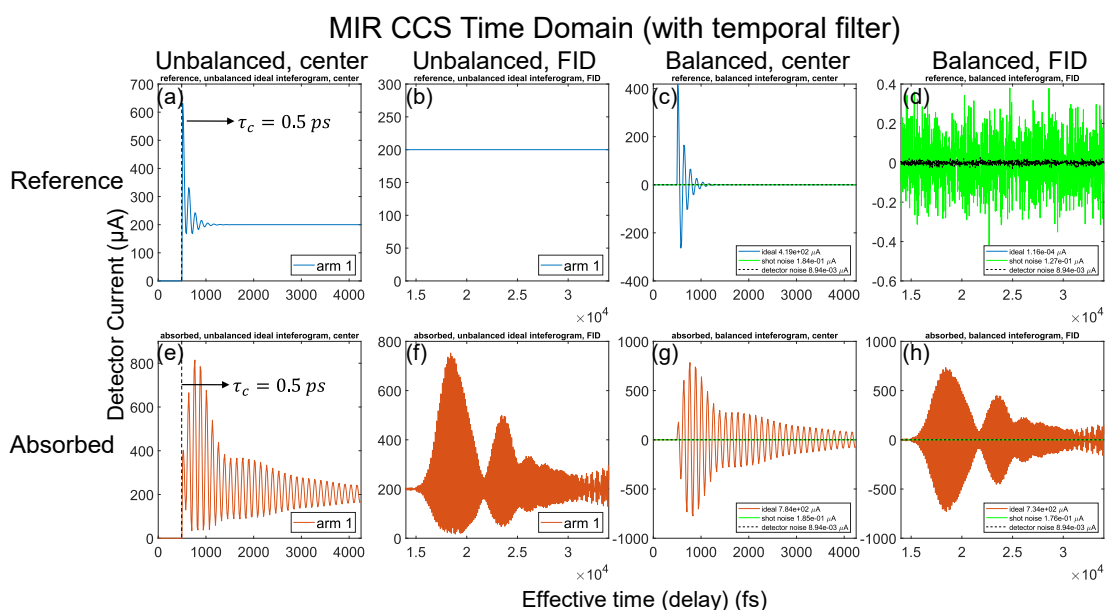
Figure 4.18: **Time domain of MIR CCS (with temporal filtering). (a)** Unbalanced ideal interferogram at the center (0 ps – 4.25 ps) of the reference measurement (without sample), with a $\tau_c = 0.5\ ps$ (same for (e)). Note that only the signal recorded by one arm of the balanced detector is shown, and the signal at the other arm is of π-phase difference; the same is true for (b), (e), and (f). **(b)** Unbalanced ideal interferogram at one part of FID (14 ps – 34 ps) of the reference measurement. **(c)** Balanced ideal interferogram at the center of the reference measurement, together with noises. The maxima of the ideal interferogram, as well as the average level (standard deviation) of the noises, is denoted in the legend box for reference; the same is true in (d), (g) and (h). **(d)** Balanced ideal interferogram at one part of FID of the reference measurement, together with noise. **(e)** Unbalanced ideal interferogram at the center of the absorbed measurement (with sample). **(f)** Unbalanced ideal interferogram at one part of FID of the absorbed measurement. **(g)** Balanced ideal interferogram at the center of the absorbed measurement, together with noise. **(h)** Balanced ideal interferogram at one part of FID of the absorbed measurement, together with noise.

Clearly, different settings of powers and τ_c can lead to different SNR results, and here we only show one possibility. A complete and systematic discussion and optimization of them could be useful but involved, so they are therefore beyond the scope of this section. Nevertheless, the choice of τ_c is still worth additional discussion. While a larger τ_c can further decrease reference amplitude (subtrahend), it also decreases the absorbed signal (minuend) since the FID signal generally decays exponentially in the time domain. In this example, the choice of $\tau_c = 0.5 \, ps$ is a balance between the temporal amplitudes of the reference signal and absorbed signal, on one hand. On the other hand, at this given setting of power and concentration, this choice of timing ensures as much information is preserved as possible without saturating the detector. Moreover, though we highlight the FID signal from 14-34 ps throughout the paper, we do not use a τ_c near there in this simulation for two reasons. Firstly, despite the minimal residual reference signal there, the absorbed signal at such a large time delay is also weaker than that closer to $\tau = 0$ (see Figure 4.18(e)-(h)). A choice of τ_c that is too large, e.g., 10 ps, will eliminate a significant portion of useful signal, for example, signal from 0.5-4.25 ps as shown in panel (e). Secondly, and more importantly, such a distinct peak at such a large time delay is a unique feature of CO_2 (linear molecule) [3,79], which is special compared to more general molecules. Therefore, by using a τ_c much closer to 0 than that unique FID peak, we demonstrate that this method works, and our related claims hold, for more general cases and do not have to rely on such special features, although our theoretical model (Figure 4.1(e), Figure 4.2(d)-(e), and Figure 4.13) assumes a picture more like this feature for clarity.

MIR CCS Frequency Domain (with temporal filter)
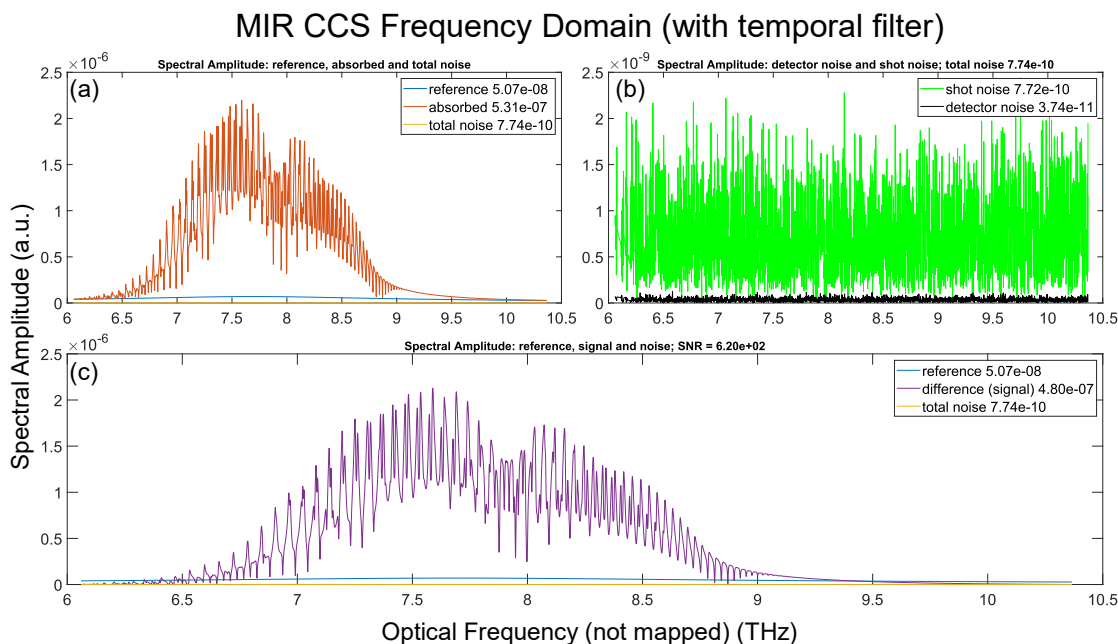
Figure 4.19: **Frequency domain of MIR CCS (with temporal filtering). (a)** Spectral amplitudes of ideal reference measurement, ideal absorbed measurement, and total noise. The average amplitudes of each spectrum are displayed in the legend box; the same is true in b and c. **(b)** Spectral amplitudes of the shot noise and detector noise. **(c)** Spectral amplitudes of the ideal reference measurement, ideal difference spectrum, and total noise. The spectral average SNR at this (unit) sample concentration (620) is displayed in the subtitle.

4.7.5. Comparison

The trendlines between relative sample concentration and SNR for all three schemes are depicted in Figure 4.20. Each data point denotes the highest possible SNR that can be obtained at that concentration. When the SNR is greater than or equal to 1, we assume the sample (absorption) is detectable. Otherwise, it is assumed undetectable, as it would be hard to distinguish the spectral difference from noise. The abscissa (concentration) of the intersection between the line of SNR=1 and each curve can be understood as its sensitivity (minimum detectable concentration, MDC).

Let us first discuss DCS and CCS without temporal filtering. Although a different sample concentration could lead to a different absorbed measurement, their reference measurements, which already saturate their detectors, do not change. Therefore, at different concentrations, neither increasing nor decreasing the optical power would further optimize

the SNR, so that we keep the same power setting for the SNR estimation at different concentrations. In other words, each data point in the curves denotes the highest possible SNR one may possibly get at the given concentration, which is limited by the detector saturation instead of the optical power. Compared to the unit concentration, a higher concentration might lead to a higher SNR because of a larger difference spectrum, until it approaches its upper limit, as explained in Section 4.7.2. A lower concentration would decrease the SNR all the way to zero, with an SNR<1 being regarded as undetectable. Since the SNR would decrease at a certain fixed rate, the sensitivity (MDC) is determined by the max SNR, which fundamentally depends on the detector.
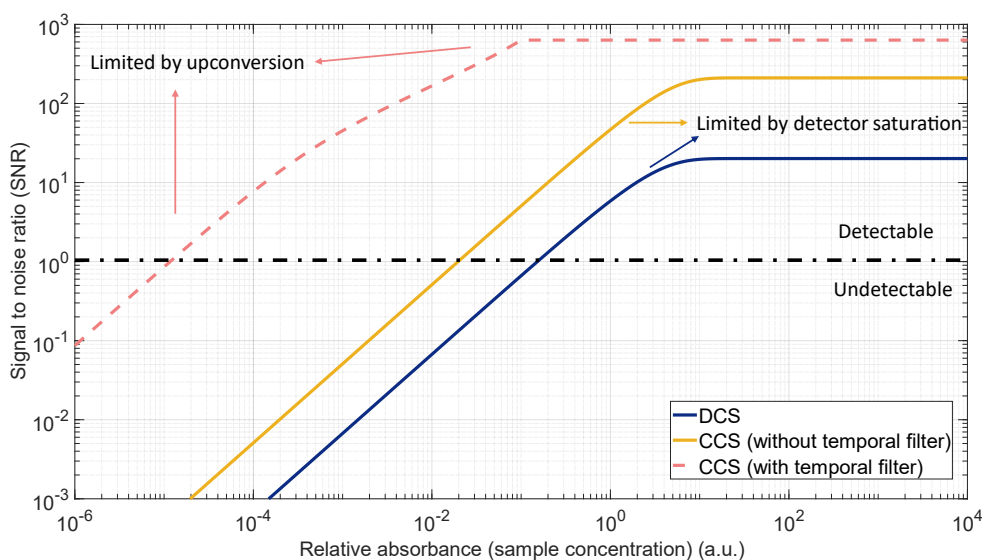
Figure 4.20: **Scaling between relative concentration and SNR for different detection schemes.** MIR DCS (blue solid line), MIR CCS without temporal filtering (yellow solid line), and MIR CCS with temporal filtering (pink dashed line). For MIR DCS and MIR CCS without temporal filtering, their highest SNR is limited by detector saturation, as is their sensitivity (minimum detectable concentration, the intersection between each curve and the line of SNR=1). For MIR CCS with temporal filtering, while its highest SNR is still limited by the detector saturation, its MDC is fundamentally limited by the strength of the nonlinearity, which determines where the SNR starts to decrease with the concentration.

Let us then discuss CCS with temporal filtering, which is slightly different. For a concentration higher than the unit concentration, the SNR could not notably increase despite a stronger FID tail, because the detector is already set to be saturated in the absorbed

measurement at the unit concentration, and the spectral amplitude of the reference measurement is already very low. For a lower concentration, if we keep the same optical power and τ_c, the FID tail will get weaker, so the SNR will decrease. However, if we can apply a higher power (target or local) to compensate the lower absorption, we can keep the amplitude of FID signal the same and still saturate the detector. As such, the SNR is estimated to be the same as that at the unit concentration, which explains the part of the plateau extending to concentrations smaller than 10^0. This plateau can be kept until there is no more optical power (upconversion capability) available, after which the SNR will start to decrease with the sample concentration in a way similar to the other two cases. Therefore, unlike the other two cases, the sensitivity (MDC, the intersection) here is determined by the highest upconversion capability, which is decided by target power, local power, and nonlinear platform together, as claimed and discussed in the main paper. In this simulation, we assume the availability of roughly a factor of 10 higher nonlinear upconversion strength as compared to the parameters used at the unit concentration, to keep the SNR from decreasing until a concentration as low as 10^{-1} (the turning point). The practical values of the turning point and sensitivity will depend on the specific experimental conditions, for which a more accurate estimation would require a more accurate model of the nonlinear conversion process.

4.7.6. Summary

In summary, in this section, we demonstrate that the MIR CCS (without temporal filtering) can have a higher SNR and sensitivity compared to the MIR DCS, thanks to the advantages of NIR detectors and smaller noises due to the reduced background signal. In both cases, we show their SNR and sensitivity are fundamentally limited by the detector saturation and noise if high enough optical power is used, under our assumptions of the noise sources. Moreover, CCS with temporal filtering can provide even higher SNR and sensitivity because of its different detection methodology, which will be fundamentally decided by the upconversion capability instead of detector saturation. However, unlike the other two methods, it cannot provide the full information of the absorption spectrum because some information is lost in the temporal filtering, though it can give a higher sensitivity for the detection of the presence of molecules.

Chapter 5

CROSS-COMB SPECTROSCOPY (EXPERIMENT)

5.1. Overview of setup and experimental results

To experimentally demonstrate CCS in the MIR, we conduct a measurement of ambient carbon dioxide (CO_2) under room temperature and atmospheric pressure around 4.25 µm (2349 cm^{-1}, antisymmetric stretching mode v_3). The target FC consists of 50-fs pulses centered at 4.2 µm with 500 mW of average power provided by two-stage cascaded efficient half-harmonic optical parametric oscillators (OPOs), which are intrinsically phase locked to the pump frequency comb (a mode-locked Yb-fiber laser) at 1 µm[92]. The local FC is a NIR FC centered at 1560 nm (a mode-locked Er-fiber laser) with a 100-nm (400-cm^{-1}) FWHM bandwidth, 100-fs pulse width and a 200-mW average power (Menlo Systems FC1500-250-WG). The f_{rep} of the target FC and local FC are both around 250-MHz and are locked to an RF rubidium (Rb) clock with a shift of 1 kHz. The f_{ceo} of the Yb-fiber laser and the Er-fiber laser are both locked via standard f-to-2f techniques. The readout FC is a band-pass-filtered part of a supercontinuum generated by the local FC, which is centered around 1145 nm with a 6-nm (45-cm^{-1}) FWHM bandwidth and a 2-µW average power. CCS is achieved through SFG of the target FC and the local FC in a 1-mm-long periodically poled lithium niobate (PPLN) crystal followed by its interference with the readout FC, which is measured by a 100-MHz InGaAs balanced detector (Thorlabs PDB415C). The PPLN crystal (Covesion MOPO1-0.5-1) has a 29.52-µm poling period that can provide a ~200-cm^{-1} (~350-nm) quasi-phase-matching 3-dB bandwidth for the SFG. Section 5.2 presents the detailed setup and optical spectra of those FCs.
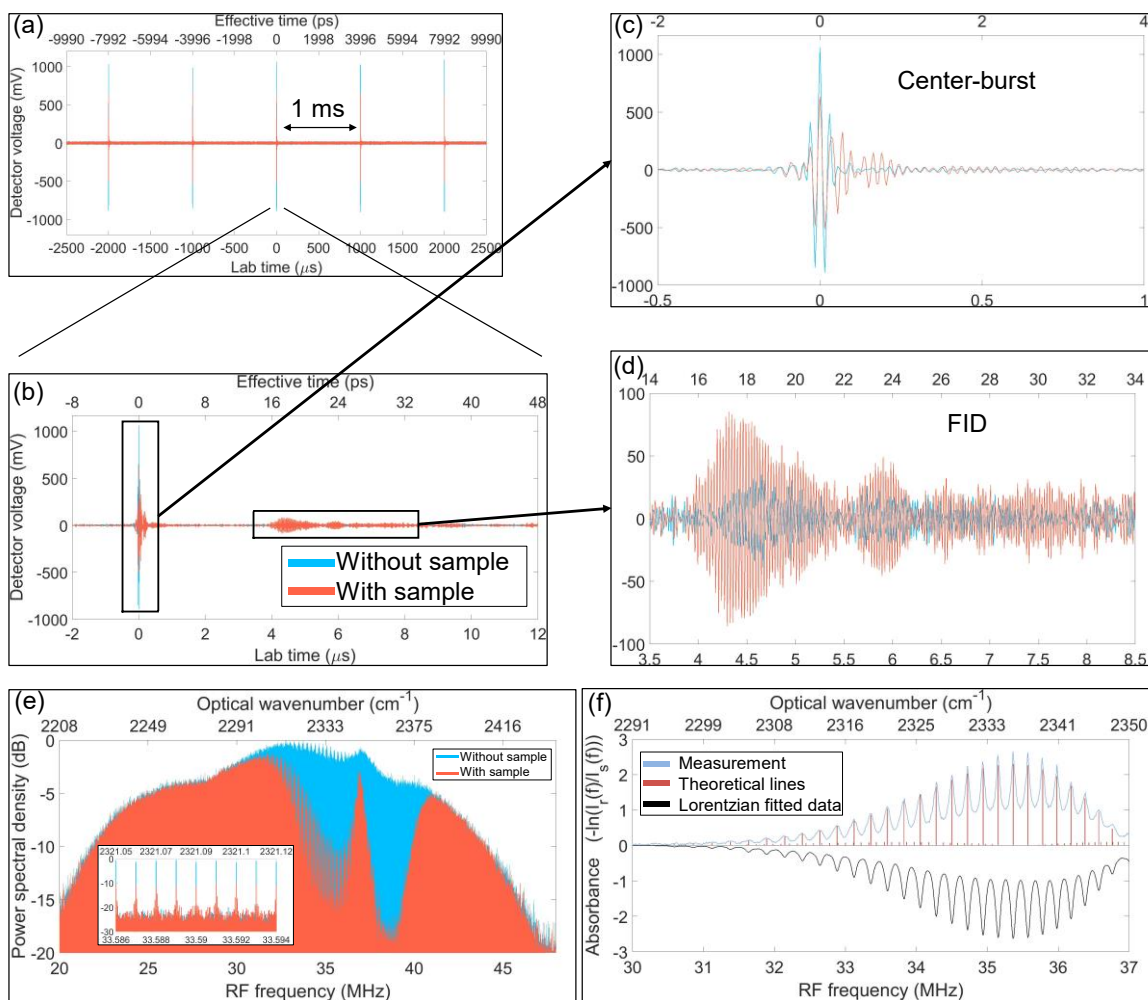
Figure 5.1: **Experimental results of CCS of CO₂.** **(a)** Five consecutive interferograms with a 1-ms temporal spacing, corresponding to $\delta = 1\ kHz$. The "without sample" result (blue) is measured when the optical path is purged with nitrogen (N₂), and the "with sample" measurement (red) is taken when the path is not purged and CO₂ is present. All measurements are carried out at room temperature and atmospheric pressure without extra control. **(b)** The central 14 µs of one example interferogram. Blowups depicting additional details of the center-burst and FID are shown in panel **(c)** and **(d)**, respectively. The lower temporal axes denote the lab time while the upper ones denote the effective time[116], which are related by the equation $t_{Lab}/t_{Effective} = f_{rL}/\delta$. **(e)** Spectra of band B of the RF FC, obtained by Fourier transforms of 498 consecutive unapodized interferograms, for measurements both with and without CO₂, are shown in red ($I_s(f)$) and blue ($I_r(f)$), respectively. The inset is a zoomed-in view to show resolved comb lines, which are separated by $\delta = 1000\ Hz$ in the RF domain corresponding to $f_{r,L} = 250{,}250{,}820$ Hz in the optical domain. **(f)** Measured molecular absorbance spectrum (light blue curve), $A(f)$, defined by $A(f) = -\ln[I_r(f)/I_s(f)]$. The result is obtained from 498 interferograms (for both "with" and "without sample") each apodized with a 100-µs window. The black curve (inverted) denotes the theoretical model, which is derived by fitting the absorption lines

from the HITRAN database (red lines) with a Lorentzian lineshape to the experimental result. The upper axes in both (e) and (f) denote the optical frequency in wavenumber.

Figure 5.1 presents the experimental results. Panel (a) presents five consecutive interferograms with a period of 1 ms, out of which the central 14 µs of one interferogram is depicted in panel (b). The prominent effects due to CO_2 can be observed in both the center-burst (panel (c)) and the tail (panel(d)), which is the result of the coherent addition of molecular FID [94,95]. Note that, thanks to the temporal gating, the background power at the tail (FID) is much weaker than that at the center-burst. This background is not visible in the measurement shown in Figure 5.1 as it is concealed by the balanced detector, but it is prominent if the detector is not well balanced (Figure 5.4). Based on the measurement, we estimate a single-shot time-domain SNR of 167 ($\frac{\pm\ 1000mV}{\pm 6mV}$) in a 28-MHz electrical bandwidth, which is more than four times that of a recent EOS work [91]. On the other hand, we estimate an upconversion (SFG) efficiency of at least 2% mm^{-1}, which is more than two orders of magnitude higher than that of a recent C.W. upconversion DCS work (Section 5.4).

Figure 5.1(e) represents the results in the frequency domain, obtained by the Fourier transform of 498 consecutive interferograms (498 ms) without apodization for both the "without sample" and "with sample" cases, where ~2.78×10^4 comb teeth are present in a 245-cm^{-1} band. The average SNR of the without-sample spectrum is 28.9, which gives a sum of spectral SNR of 8.03×10^5 (the sum of the SNR of all comb teeth). Note that we are only able to acquire 0.5-s data with δ=1kHz, which means the signal spectrum only uses 28 MHz of the whole 125-MHz Nyquist band (half f_{rL}), limited by the memory depth of our data acquisition equipment. If we use a factor of 125/28 larger δ and acquire for 1s, we can get ~9 times as many interferograms, which will scale up the sum of spectral SNR by a factor of 3. This leads to an estimated figure of merit of 2.4×10^6 Hz$^{1/2}$ for this MIR spectrometer (Section 5.4), which is one of the highest among recently reported MIR DCS or EOS works [91,101–103,109]. Note that our SNR can still be further increased since the time-domain signal only reaches about half of the detector saturation ($\pm$ 1V out of $\pm$ 1.8

V), which can be increased through a higher power from any of the target, local or readout FC.

Shown in Figure 5.1(f) (light blue curve), the molecular absorbance spectrum is obtained by comparing with-sample and without-sample measurements (here a 100-µs apodization window is applied to the interferograms before Fourier transform). Only the *P* branch (rotational structure below the band origin) of the measured spectrum of CO_2 is shown here (see Section 5.5). The theoretical absorbance spectrum (black curve, inverted about the x-axis for clarity) is calculated using spectral lines (red lines) from the HITRAN database [117] fitted with a Lorentzian line shape of 0.8-cm^{-1} FWHM linewidth.

Note that these results are obtained by locking the f_{rep} of the target and local combs only individually to a RF standard, which gives fixed f_{rep} values but an uncontrolled broad relative linewidth between two combs [118]. By some post-processing (without external optical referencing), we can correct the without-sample measurements but are unable to fully correct the with-sample measurements (Section 5.5). We believe this is the main reason why the fitted absorption linewidth (0.8 cm^{-1}) is larger than the theoretical pressure broadening (~0.2 cm^{-1}) at room temperature and atmospheric pressure. Similar to other DCS techniques, this problem can be solved by utilizing an intermediate C.W. reference to provide fast phase noise information for either tight-locking using fast actuators [67,95,101–103,119] or error correction by post processing [102,118,120–122].

5.2. Detailed setup and optical spectra

The setup diagram is depicted in Figure 5.2, and the optical spectra are depicted in Figure 5.3.
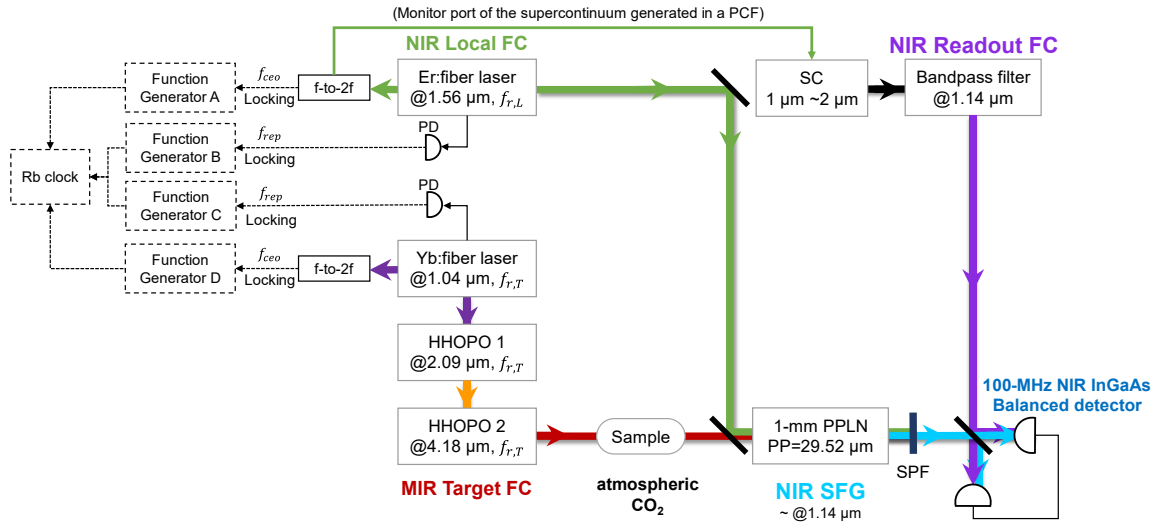
Figure 5.2: **Experimental setup.** PCF: photonic crystal fiber. SC: supercontinuum. PD: photodetector. PP: poling period. SPF: shortwave pass filter. The supercontinuum, used as the readout FC after a bandpass filter, is from a monitor port (tap output) of the PCF pumped by the local FC in its f-to-2f module. The SFG signal and readout FC are mixed in a commercial 2x2 50:50 wideband fiber optics coupler (Thorlabs TW1064R5A2A), before which the two beams are coupled from free space into fiber by commercial fiber collimators. The configuration of the fiber coupler is further illustrated in Figure 5.4(a). For the SFG signal, two commercial freespace shortwave pass filters (Spetrogon SP-1300) are used to block residual NIR local power and MIR target power. For the readout FC, the bandpass filter (Delta Optical Thin Film A/S LF104008) for the supercontinuum is centered at 1140nm with a full-width at half-maximum (FWHM) bandwidth of 15 nm. The NIR detector is a commercial InGaAs fiber-coupled balanced detector (Thorlabs PDB415C).

The target FC is provided by a chain of two cascaded half-harmonic OPOs [92]. Pumped by a commercial mode-locked Yb: fiber laser centered at 1.045 µm, the first half-harmonic OPO generates 2.09-µm pulses, which are then used to pump the second half-harmonic OPO at 4.18 µm. Half-harmonic OPOs feature intrinsic phase and frequency locking of their output to the pump [56]; thus the phase and frequency of the 4.18-µm OPO are intrinsically locked to that of the 1.045 µm pump. Hence, by locking the f_{rep} (f_{ceo}) of the 1.045-µm laser to that of the 1.55-µm Er: fiber laser (local FC), the target FC (4.18-µm OPO) is locked to the local FC. In this experiment, the f_{rep} and f_{ceo} of the local FC and 1.045-µm Yb fiber laser (target FC) and all measurement apparatus are locked to a 10-MHz RF rubidium (Rb) clock, ensuring a common frequency standard.
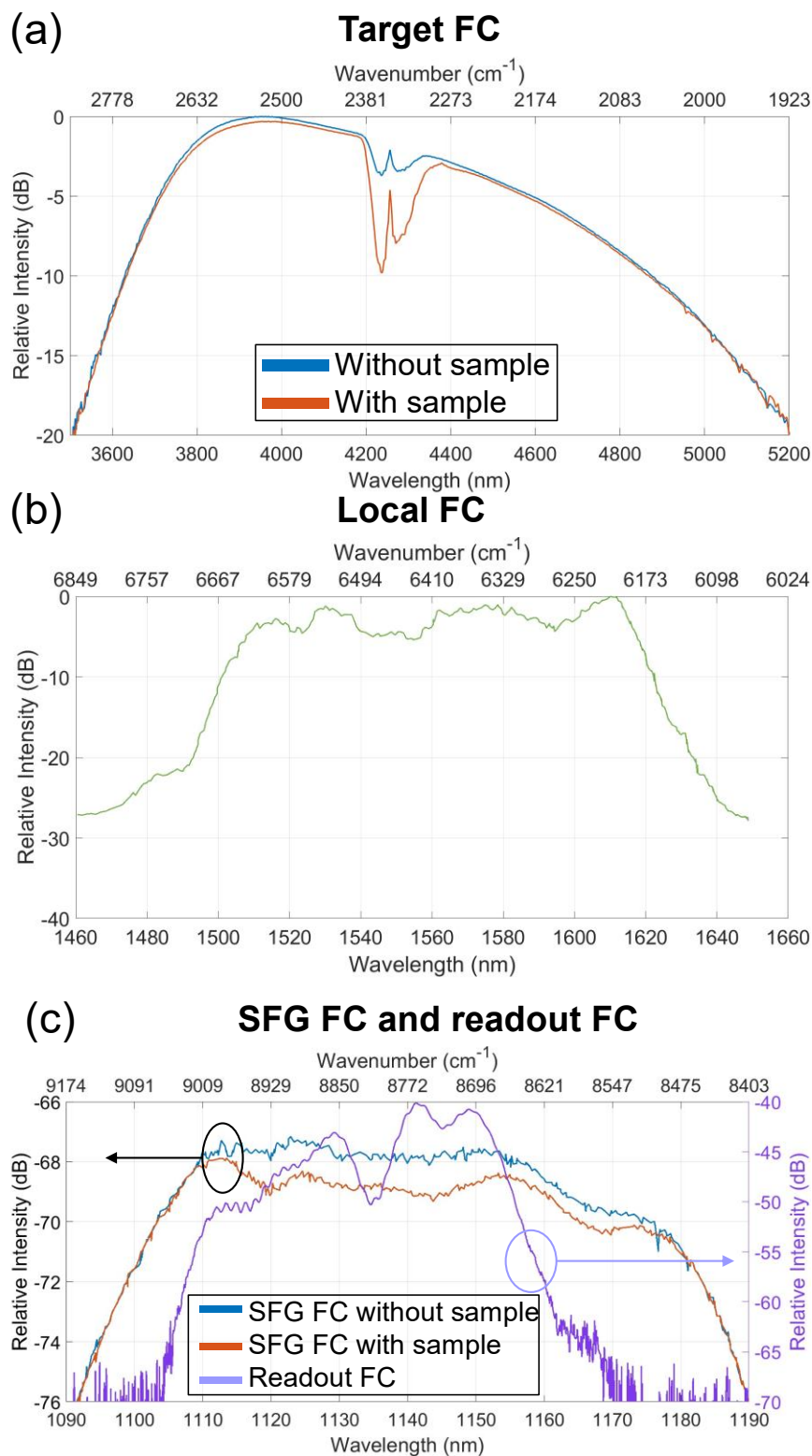
Figure 5.3: **Optical spectra of frequency combs used in the experiment.** **(a)** Target FC for both "without sample" (purged) and "with sample" (unpurged) cases, measured by a

commercial Fourier-transform infrared spectrometer (FTIR) with a resolution of 4 cm$^-$ ^{1}. The residual CO_2 which cannot be fully cleared by purging is the reason why the absorption dip can still be observed in the "without sample" curve. **(b)** Local FC spectrum provided by the manufacturer (Menlo Systems). **(c)** Spectra of SFG FCs (with and without sample) and readout FC measured by a grating-based OSA with a resolution of 0.5 nm.

5.3. Temporal gating

For the same reason as in EOS [82], our cross-comb method can also benefit from the temporal gating (also referred to as "nonlinear gating"), although our local pulse is not as short as that of EOS. However, this effect cannot be seen in the measurement shown in Figure 5.1, because the balanced detection conceals the strong background. Corresponding to band A and band D of the RF FC (see Section 4.3.4), the background is a common-mode signal only from the port of the SFG FC and thus is cancelled by the balanced detection. Note that the background at the center-burst is basically an intensity cross-correlation of the target pulses and local pulses, so it is delay (τ, lab-time)-dependent unlike DCS (See Figure 4.1). As shown in Figure 5.4, if we tweak the coupling of the splitter to the balanced detector (panel (a)) such that it is not well-balanced, the strong background will show up prominently at the center-burst (panel (b)). However, because of the temporal gating, the beating at the tail, which contains useful information, is free from any undesirable background power from the strong pulse center. The complete description of temporal gating can be found in Section 4.4 and 4.6.

Note that the balanced detection can only "conceal" the background in its balanced RF output, but it cannot solve the problem caused by the strong background. Although a well-balanced detector can cancel the common-mode signal and noise in its balanced RF output by comparing the outputs of two photodiodes, there may still be strong optical power incident on each photodiode which is not visible in the balanced output. The strong incident optical power can bring in noise which is not common-mode (e.g., shot noise) and thus cannot be cancelled (indeed they add up), and it will ultimately saturate the photodiodes. This problem exists in detection of weak FID signal for DCS. More illustrations can be found in our simulation (Section 4.7).
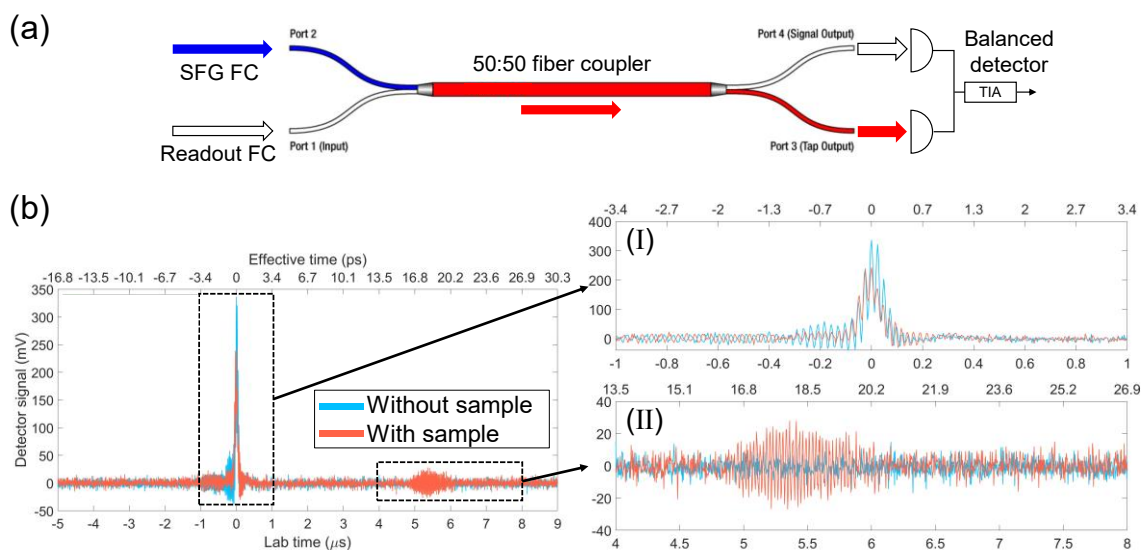
Figure 5.4: **Interferograms of CCS of CO2, measured by an unbalanced detector. (a)** Configuration of the fiber coupler and balanced detection. TIA: transimpedance amplifier. **(b)** Interferograms measured when the detector is not well balanced. The main figure presents the central 14-µs part of one example interferogram in order to highlight the details of the center-burst (inset I) and the tail (inset II). Note that the measurement is done when the detector is tuned to be just slightly unbalanced. The background at the center-burst is actually very strong and can heavily saturate the TIA if the detector is further unbalanced. Note that the result shown here is from an older measurement where local pulses with lower power are used; thus, its FID signal is lower than that of the Figure 5.1.

5.4. Estimation of experimental signal-to-noise ratio (SNR) and figure of merit (FOM)
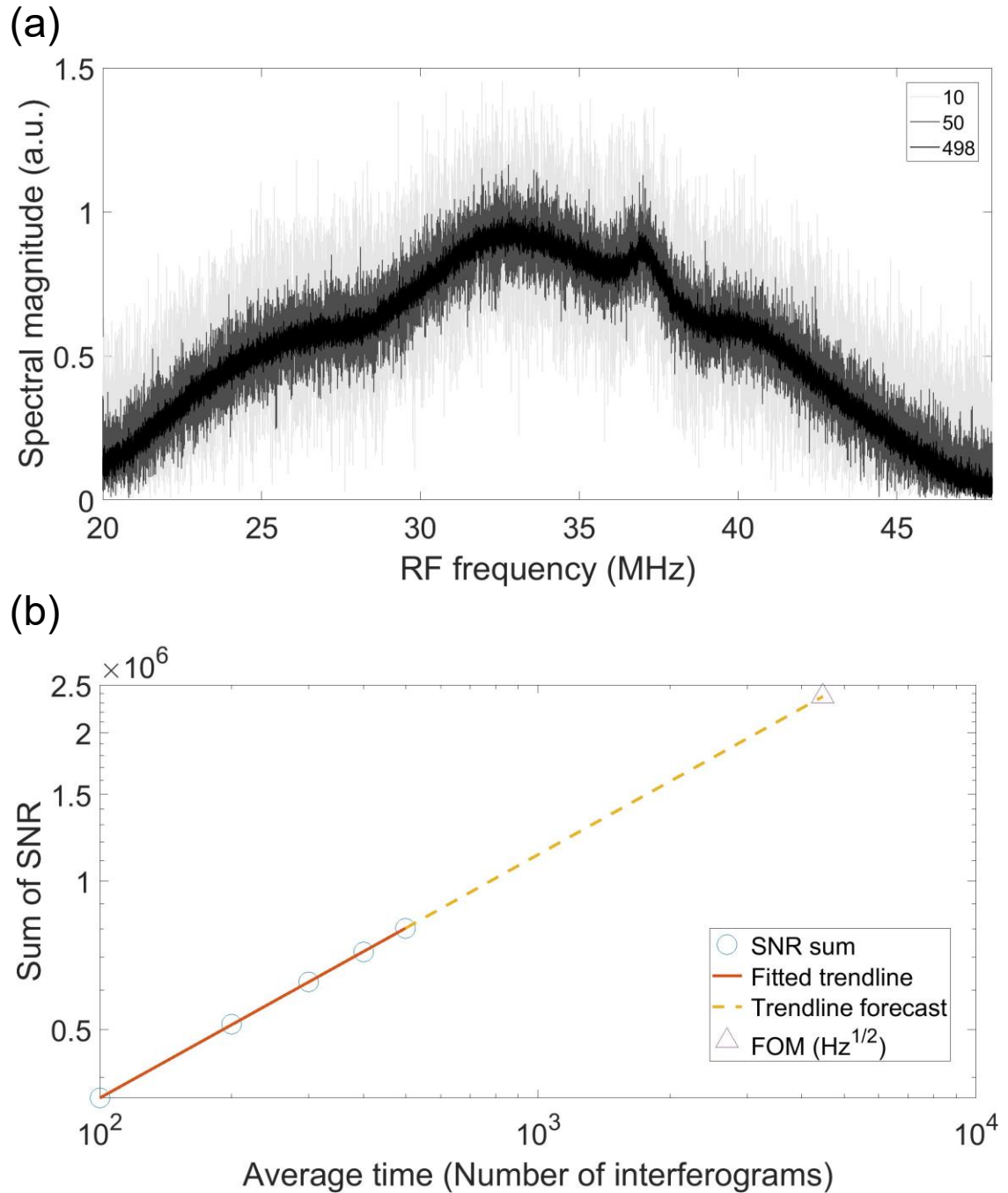
Figure 5.5: **Estimation of SNR and FOM. (a)** averaged without-sample spectra by different numbers of interferograms (10,50,498, denoted by curves with different grayscales). **(b)** Sum of SNR as a function of average time (N), where N denotes the number of averaged interferograms. The red line is a linear fitting of the data points (blue

circle), and the yellow dashed curve denotes the forecast the trendline, which scales the experimental sum of SNR to an estimation of the FOM (purple triangle). Note that the coordinate is in log-log scale.

Figure 5.5 presents the estimation of SNR and FOM of our spectrometer. Panel (a) shows averaged without-sample signal spectra by different numbers of interferograms. Note that a small part of the FID signal in the interferograms is discarded before the Fourier transform is applied to exclude the influence of residual sample absorption. It is readily seen that the SNR of the signal spectrum increases with the averaging time. Panel (b) depicts the spectral SNR sum (the sum of the SNRs of all spectral components) as a function of N (number of averaged interferograms) on a log-log scale, with experimental data denoted by the blue circles. A linear fitting (red line) is conducted for those experimental points, whose slope is 0.4936, indicating the SNR increases as a function of $\sqrt{N}$ as expected.

Because of the reasons mentioned in the main paper, currently we are only able to acquire ~0.5-s data with a δ of 1 kHz, which gives a SNR sum of 8.03×10^5 (the highest blue point). To estimate a figure of merit (FOM), we need to scale the number in two ways. Firstly, we assume data acquisition over a full second, which can give twice as many interferograms. Secondly, the signal currently only takes up 28 MHz out of the whole available 125-MHz spectrum (half repetition rate of the local/target FC). If we could set the δ to be ~4.5 kHz (we did not do that in the experiment due to some limitations of our detector and locking electronics), we would be able to get ~4.5 times more interferograms. In total, we can realistically obtain 9 times as many interferograms in our measurement, which leads to an estimation of FOM of 2.4×10^6 (yellow dashed line and purple triangle).

In addition, here we explain how we estimate the upconversion efficiency of our experiment and how it compares to that of prior work using C.W. upconversion [109]. In that work, a 700-µW MIR FC and a 2.4-W C.W. laser are used to get a 1.3-µW upconverted NIR FC with a 20-mm PPLN crystal. Note that all the power in this subsection refers to average power. Therefore, their upconversion efficiency can be calculated as:

$$\frac{P_{upconverted}}{P_{MIR} \times L_{crystal}} = \frac{1.3\ \mu W}{700\ \mu W \times 20\ mm} = 9.3 * 10^{-3}\ \%\ (mm^{-1}).\qquad(5.1)$$

In our experiments, we use 500-mW target pulses and 200-mW local pules to generate a SFG signal of ~100 nW with a 1-mm PPLN crystal. However, in our case, the 100-fs local pulse scans through the 50-fs target pulse due to their different repetition periods (see Figure 4.1), so the real time interval in which the two pulses overlap (when SFG power is generated) only accounts a very small portion of the full period. Specifically, when we set the $\delta = 1\ kHz$ for the $f_{rep,L} \cong f_{rep,T} = 250\ MHz$, the local pulse will scan through the target pulse in a total of 2.5×10^5 steps with a step size of approximately 16 fs (meaning the relative position of local and target changes by about 16 fs for each local pulse which samples the target) over the course of an interferogram. Since the target pulse is only around 50 fs, there are only 3~4 steps in which the local pulse overlaps with the target pulse well out of those 2.5×10^5 steps, and moreover, there is only at most one step that the two pulses overlap perfectly (the maxima of the interferogram). Therefore, we can estimate an effective overlap coefficient (the "duty cycle" of SFG generation) to be about 10^{-5}, which must be factored into the calculation of the SFG efficiency for a fair comparison. Therefore, the efficiency is:

$$\frac{P_{upconverted}}{P_{MIR} \times L_{crystal}} \times \frac{1}{duty\ cycle} = \frac{100\ nW}{500\ mW * 1mm} \times \frac{1}{10^{-5}}$$

$$= \frac{1}{5 * 10^6} \times \frac{1}{10^{-5}} mm^{-1} = 2\%\ (mm^{-1}).$$

$$(5.2)$$

Our upconversion efficiency is more than two orders of magnitude higher than the C.W. upconversion work, although the average power of our local FC is just one tenth of theirs. Note that we couple the generated SFG from free space to a single-mode fiber and then measure its power with a fiber-coupled OSA. However, there could be a large loss in the free space-fiber coupling which results in an underestimation of the measured SFG power. Therefore, this efficiency could be correspondingly underestimated.

5.5. Phase correction and broadened absorption linewidth
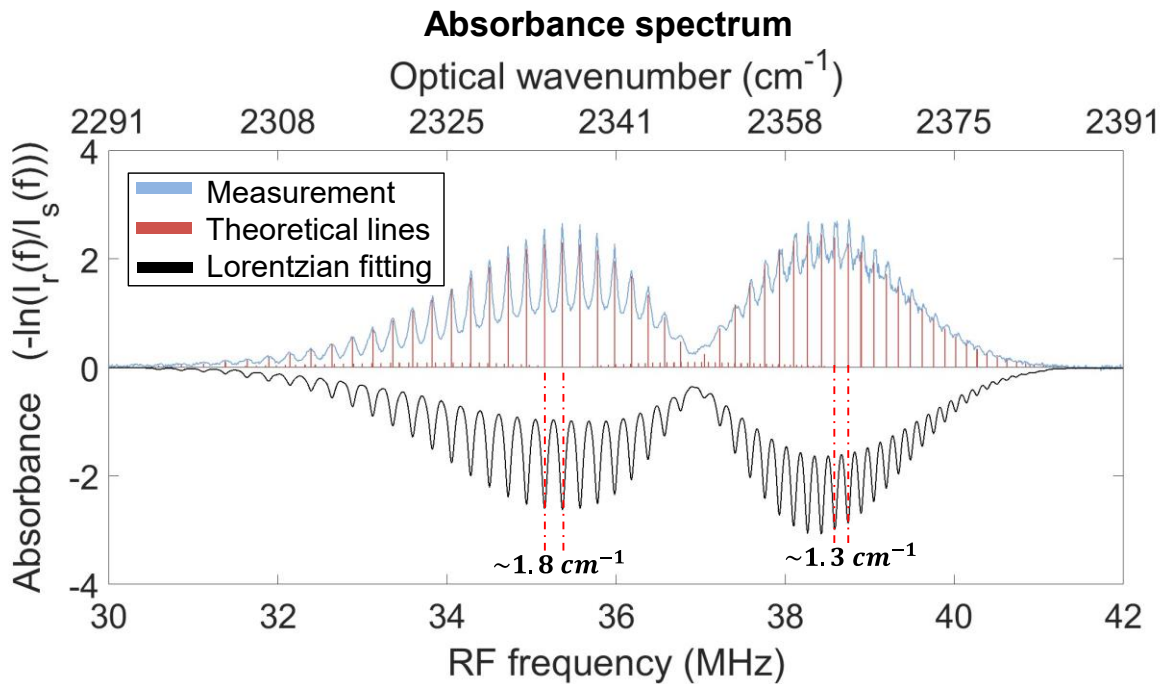
Figure 5.6: **Full measured absorbance spectrum of CO2.** Full measured absorbance spectrum of CO_2 in our preliminary cross-comb measurement, including both P and R branches. The SNR of the R branch is lower than that of the P branch. Also, the absorption lines of the R branch are broader than that of the P branch. The spacing between absorption lines in R branch is smaller than that of the P branch.

Figure 5.6 shows the full measured absorption spectrum, whose right side (higher optical frequency, R branch) has a worse SNR and more broadened absorption linewidth compared to its left-side counterpart (lower optical frequency, P branch). This is because the phase noise (uncontrolled broad relative linewidth) between the target FC and local (readout) FC has a larger effect on the R branch, as explained below.
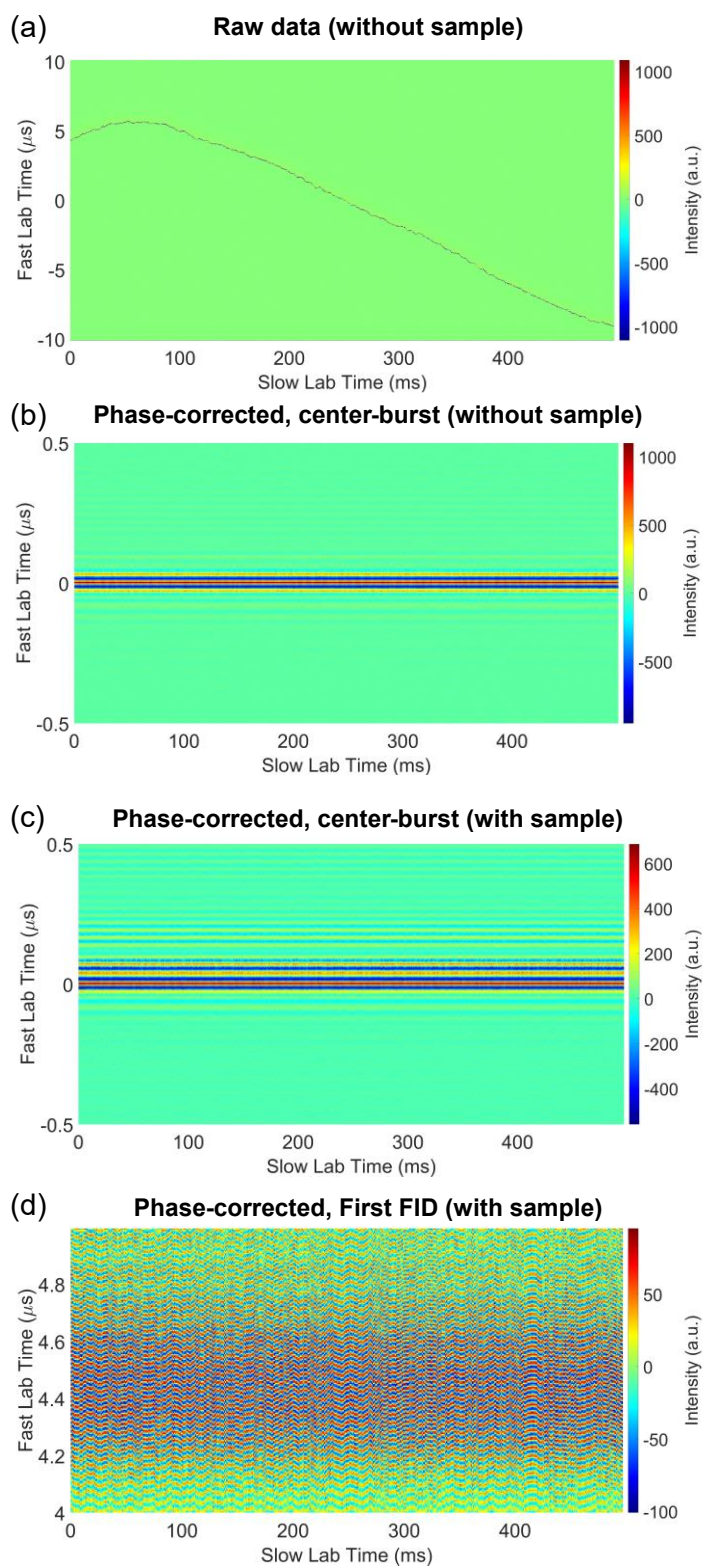
Figure 5.7: **Phase correction process. (a)** 3D interferogram of the raw data of the without-sample measurement. **(b)** 3D interferogram of the corrected data of the without-sample

measurement, around center-burst. **(c)** 3D interferogram of the corrected data of the with-sample measurement, around center-burst. **(d)** 3D interferogram of the corrected data of the with-sample measurement, around first peak in FID at a fast lab time interval of [4,5] μs.

Panels (a)-(d) of Figure 5.7 show the phase correction for the interferograms, where "3D interferograms" are presented. In those 3D interferograms, each column is a single interferogram (detector voltage is denoted by the colormap), and consecutive single interferograms (columns) are plotted from left to right. Therefore, the vertical axis denotes the "fast time" within each single interferogram, and the horizontal axis denotes "slow time" that shows the time spacing between each interferogram.

Panel (a) shows the without-sample 3D interferogram with the fast time zoomed in to [-10,10] μs to show the center-burst. Ideally, the center-bursts of each single interferogram should perfectly align at $t_{fast} = 0$, but they shift due to the phase noise and timing jitter between the two fiber lasers since no tight locking is applied to them [118]. Two steps are taken to correct these shifts. Firstly, the maxima of the envelopes of each interferogram are shifted and aligned to correct the timing jitter (the envelope of the interferograms is obtained by Hilbert transform). Secondly, a zero-order phase term is applied to each interferogram to make its phase at the maxima of the envelope zero to correct the zero-order phase shift between interferograms. The obtained results are shown in panel (b)-(d). At the center-burst of both without-sample and with-sample case (panel (b) and (c)), the corrected interferograms overlap very well and thus can be coherently averaged. This is largely because our correction uses the information from the sharp peak structure at the center-burst of the interferograms and thus provides reasonably good correction over the whole center-burst, since it is generated by the interference of two short, femtosecond pulses. This is sufficient for the without-sample measurement since its information only exists around the center-burst. However, for the with-sample case, although its center-bursts are aligned well and can be averaged, prominent phase error still exists at larger fast times, for example, at the first strong FID peak (panel (d)). This is because the coherence time between the two combs is smaller than 4 μs, so the zero-order phase correction at the center-burst is not able to fully correct the error at the more distant FID. The larger the fast

time (delay τ), the larger the phase error between different interferograms, and the less they can be averaged. In other words, the relative comb linewidth between our target and local (readout) combs remains broad because their repetition rates are independently locked only to a RF standard [118].

This explains why our measured absorption linewidth is larger than the theoretical value; although the center-burst of the with-sample measurement can average well, the FID signal at large delay τ cannot. This is like a window function is applied to the time-domain of the averaged with-sample interferogram, which is equivalent to a Sinc function convolved to its spectrum which broadens all its spectral features. The R branch of the absorption spectrum suffers more from this undesirable effect because its corresponding time-domain information exists at a larger time delay (fast time) due to a smaller spacing of its absorption lines (see Figure 5.6), which means a larger phase error and less averaging. More detailed analysis about temporal and spectral features of the CO_2 absorption can be found in ref. [79]. As mentioned in the main text, this issue can be solved by setting one intermediate C.W. reference to provide information for either tight-locking by fast actuators, or error correction by data processing, as has been well demonstrated in dual-comb spectroscopy.

However, this effect does not influence the without-sample measurements since their information only exists close around the center-burst in the time-domain where phase error and timing jitter can be corrected based on the information from the sharp peak structure of the center-burst itself. Therefore, in terms of SNR, the obtained without-sample measurements after our phase correction are comparable to the results that can be obtained if the relative comb linewidth (phase noise and timing jitter) between target and local combs are ideally controlled. Hence, our estimate of the FOM of our spectrometer using the SNR of the without-sample measurements is fair.

5.6. Discussion
The SNR and sensitivity of CCS are limited by the upconversion efficiency, instead of the detector and background noise (shot noise or RIN at FID from the power of strong excitation pulse center). There are three factors in the upconversion process: the target pulse (generally MIR), the local pulse (generally NIR), and the nonlinear platform

(generally a bulk crystal). The improvement of any of these elements can be exploited to improve the performance and capability of CCS. First, in the past decade, there has been impressive progress in the generation of high-power (>100 mW) MIR FCs [35,36,39,45,48,53,92]. However, MIR DCS has not taken full advantage of this progress yet, as MIR detectors typically saturate at ~ 1 mW. Admittedly, one can always apply additional detectors and bandpass filters to do parallel and sequential detection [96] to alleviate this problem, but they add to the system complexity and cost, and still do not fundamentally address the limitation from the strong background noise at the FID due to the nature of linear interference. Conversely, CCS can reap the full benefits of more powerful target pulses as saturation is not a main problem. Although the target pulse used in our experiment is already among the FCs with the highest power in its wavelength region, it can still be improved [92] and enhance the CCS performance.

Second, for the local FC, we use 1.56-µm local pulses with only a 200-mW average power and 100-fs pulse width, while near-IR combs with orders of magnitude better metrics are available which can directly benefit the demonstrated CCS. Third, a 1-mm commercial bulk PPLN crystal with a poling period of 29.52 µm is used in our experiment as the nonlinear medium, which provides an upconverted MIR bandwidth of 4080 nm – 4530 nm and limits the upconversion efficiency and bandwidth. The total 9 different poling periods of the crystal are expected to provide a combined SFG bandwidth of 2400 nm to 5200 nm, which can cover the whole bandwidth of our MIR target FC 13 (3500 nm to 5200 nm , see Figure 5.2 and Figure 5.3). Recently, developments in lithium niobate nanophotonics have enabled dispersion-engineered waveguides with unprecedented phase-matching bandwidths and nonlinear efficiencies orders of magnitude higher than bulk PPLN crystals [63,70], which can improve CCS performance. One can also envision including several poling periods or a chirped grating in such waveguides to provide a broad SFG bandwidth without sacrificing the efficiency.

Although the power of the local FC and readout FC used in our experiment are relatively low, the NIR detector is already half saturated at the center-burst. The detector can be fully saturated by simply doubling the power of local FC or readout FC. By combining part or

all these above-mentioned state-of-the-art techniques, we expect the FID signal from trace molecules can get close to the saturation limit of the NIR detector so that CCS can provide record-high SNR mode-resolved spectroscopy for record-low concentration samples. This is expected to break the limits of current dual-comb-based techniques and is highly desirable for applications where broadband trace molecular detection plays a significant role, such as breath analysis.

5.7. Summary

In summary, we introduce the new concept of cross-comb spectroscopy, which can not only convert spectral information to a more easily accessible wavelength region but also alleviates the limits of the general dual-comb spectroscopy. In a nutshell, CCS can combine and improve upon many of the merits of other demonstrated techniques while circumventing some of their practical challenges. We experimentally demonstrate a CCS measurement around 4 µm with a broad bandwidth, high SNR, and large figure of merit, which are among the best reported for measurements around this wavelength range. This work opens a simple, flexible, and efficient avenue to high-precision, high-sensitivity, high-SNR, high-speed, and broadband spectroscopy in spectral regions with less developed sources and detectors.

C h a p t e r   6

SUMMARY AND OUTLOOK

Nonlinear optics and frequency combs are rapidly evolving fields. In this chapter, we summarize the thesis and offer a brief overview of some future opportunities stemming from the results and studies presented.

6.1. Summary

This thesis summarizes how we harness nonlinear optics to enhance frequency-comb-based optical spectroscopy in the MIR region. Three key contributions are presented: the generation of a high-power and efficient MIR frequency comb using simulton OPOs; MIR cross-comb spectroscopy; and OPA-enhanced background-free spectroscopy, collectively illustrated in Figure 6.1. On one hand, these methods are independent of each other and can be implemented individually for a wide range of applications under various settings. On the other hand, they are closely related, as they can be threaded by common challenges in optical spectroscopy systems. Indeed, one can employ any two of them, or all three together, and their combination may yield additionally benefits.
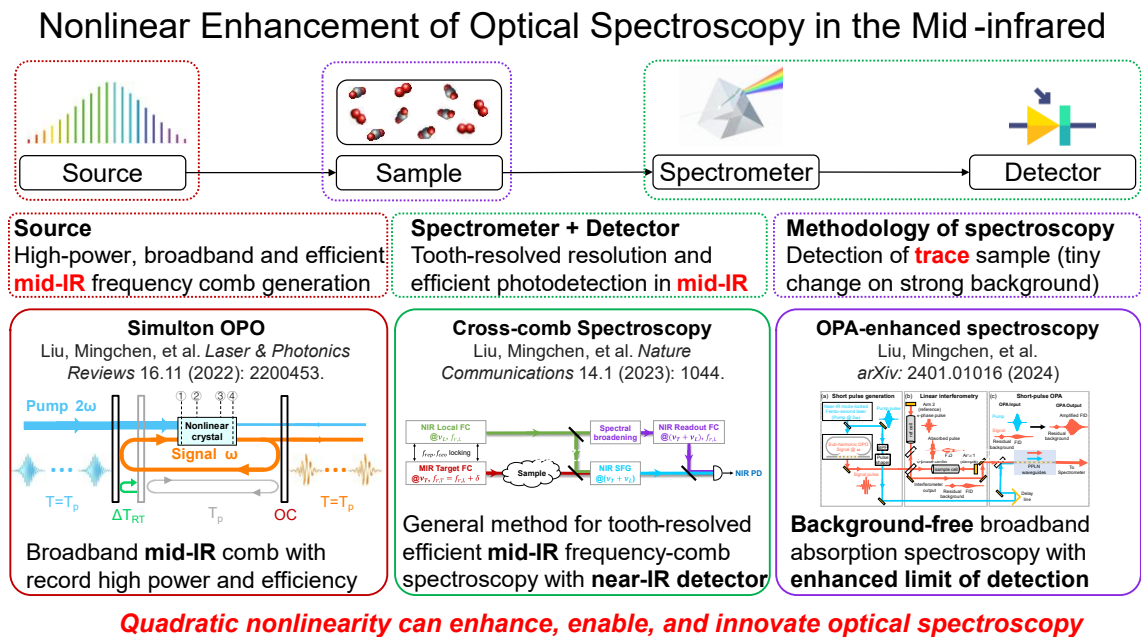
Figure 6.1: **Summary of this thesis.**

6.2. Extension of simulton OPO and cross-comb spectroscopy to longer wavelengths
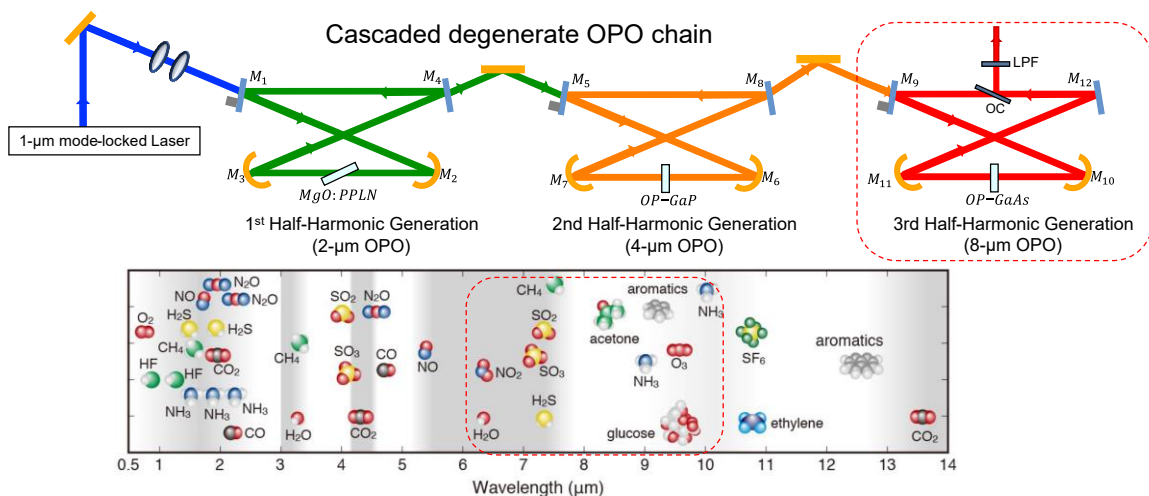
Figure 6.2: **Cascaded degenerate OPO chain and examples of molecular absorption.** Photo credits of the molecular spectrum: Daylights solutions.

The simulton-based OPO can be extended to longer wavelengths following our cascaded degenerate OPO chain, so does cross-comb spectroscopy. There are more important molecules at longer wavelength regions, e.g., around 8 µm.

6.3. Integration of cross-comb spectroscopy
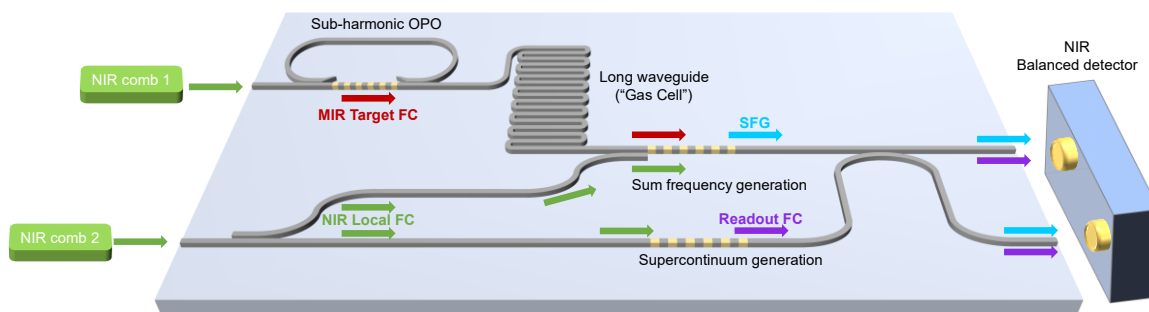
Figure 6.3: **Envisaged on-chip implementation of CCS.** Two NIR comb sources of different repetition rates, which are also possible to integrate, are used to pump a single nanophotonic chip. One of the NIR combs is used to pump an on-chip sub-harmonic OPO for the MIR target FC generation, which may then interact with the sample in a long waveguide. The other NIR comb is split into two parts, which are used to function as the local FC via SFG and generate the readout FC via supercontinuum generation in separate poled regions. The outputs are interfered on chip and measured with a NIR balanced detector, which may also be brought on chip.

Currently, our setup relies on free-space and fiber-based components. However, rapid progress in lithium niobate nanophotonics [123,124] has made it feasible to monolithically integrate most of the components of the entire CCS system into a single photonic chip. In Figure 6.3, we show an envisaged on-chip implementation, in which two NIR combs are coupled to the chip, and one of them is used to pump a sub-harmonic OPO to generate the MIR target FC [125,126]. The other NIR comb plays the role of the local FC in sum-frequency generation [125,127,128], while part of it is used to generate the readout FC via supercontinuum generation [128–131]. A long waveguide is used to increase the interaction area between the target FC and the surrounding environment. Moreover, recent progress in on-chip NIR combs and detectors based on thin-film lithium niobate [123,124] suggests the potential to also integrate both NIR sources and detectors, which can lead to a fully integrated CCS system.

BIBLIOGRAPHY

[1] I. Newton, Opticks, Or, A Treatise of the Reflections, Refractions, Inflections & Colours of Light, Courier Corporation, 1952.

[2] J.C.D. Brand, Lines of Light: The Sources of Dispersive Spectroscopy, 1800-1930, Gordon & Breach Publ., 1995.

[3] P.R. Griffiths, J.A. De Haseth, Fourier transform infrared spectrometry, 2nd ed, Wiley-Interscience, Hoboken, N.J, 2007.

[4] W. Demtröder, Laser Spectroscopy: Basic Concepts and Instrumentation, Springer Science & Business Media, 2013.

[5] R.L. Batchelor, K. Strong, R. Lindenmaier, R.L. Mittermeier, H. Fast, J.R. Drummond, P.F. Fogal, A New Bruker IFS 125HR FTIR Spectrometer for the Polar Environment Atmospheric Research Laboratory at Eureka, Nunavut, Canada: Measurements and Comparison with the Existing Bomem DA8 Spectrometer, Journal of Atmospheric and Oceanic Technology 26 (2009) 1328–1340. https://doi.org/10.1175/2009JTECHA1215.1.

[6] S.T. Cundiff, Phase stabilization of ultrashort optical pulses, J. Phys. D: Appl. Phys. 35 (2002) R43. https://doi.org/10.1088/0022-3727/35/8/201.

[7] S.T. Cundiff, J. Ye, Colloquium: Femtosecond optical frequency combs, Rev. Mod. Phys. 75 (2003) 325–342. https://doi.org/10.1103/RevModPhys.75.325.

[8] T. Fortier, E. Baumann, 20 years of developments in optical frequency comb technology and applications, Communications Physics 2 (2019) 1–16. https://doi.org/10.1038/s42005-019-0249-y.

[9] N. Picqué, T.W. Hänsch, Frequency comb spectroscopy, Nature Photonics 13 (2019) 146–157. https://doi.org/10.1038/s41566-018-0347-5.

[10] Y.-S. Jang, S.-W. Kim, Distance Measurements Using Mode-Locked Lasers: A Review, Nanomanuf Metrol 1 (2018) 131–147. https://doi.org/10.1007/s41871-018-0017-8.

[11] N. Kuse, M.E. Fermann, Frequency-modulated comb LIDAR, APL Photonics 4 (2019) 106105. https://doi.org/10.1063/1.5120321.

[12] T. Udem, R. Holzwarth, T.W. Hänsch, Optical frequency metrology, Nature 416 (2002) 233–237. https://doi.org/10.1038/416233a.

[13] J. Braunfelds, R. Murnieks, T. Salgals, I. Brice, T. Sharashidze, I. Lyashuk, A. Ostrovskis, S. Spolitis, J. Alnis, J. Porins, V. Bobrovs, Frequency comb generation in WGM microsphere based generators for telecommunication applications, Quantum Electron. 50 (2020) 1043. https://doi.org/10.1070/QEL17409.

[14] P.B. Corkum, F. Krausz, Attosecond science, Nature Phys 3 (2007) 381–387. https://doi.org/10.1038/nphys620.

[15] M.-G. Suh, X. Yi, Y.-H. Lai, S. Leifer, I.S. Grudinin, G. Vasisht, E.C. Martin, M.P. Fitzgerald, G. Doppmann, J. Wang, D. Mawet, S.B. Papp, S.A. Diddams, C. Beichman, K. Vahala, Searching for exoplanets using a microresonator astrocomb, Nature Photon 13 (2019) 25–30. https://doi.org/10.1038/s41566-018-0312-3.

[16] A. Schliesser, M. Brehm, F. Keilmann, D.W. van der Weide, Frequency-comb infrared spectrometer for rapid, remote chemical sensing, Optics Express 13 (2005) 9029. https://doi.org/10.1364/OPEX.13.009029.

[17] S. Schiller, Spectrometry with frequency combs, Optics Letters 27 (2002) 766. https://doi.org/10.1364/OL.27.000766.

[18] F. Keilmann, C. Gohle, R. Holzwarth, Time-domain mid-infrared frequency-comb spectrometer, Optics Letters 29 (2004) 1542. https://doi.org/10.1364/OL.29.001542.

[19] I. Coddington, N. Newbury, W. Swann, Dual-comb spectroscopy, Optica 3 (2016) 414–426. https://doi.org/10.1364/OPTICA.3.000414.

[20] M.L. Weichman, P.B. Changala, J. Ye, Z. Chen, M. Yan, N. Picqué, Broadband molecular spectroscopy with optical frequency combs, Journal of Molecular Spectroscopy 355 (2019) 66–78. https://doi.org/10.1016/j.jms.2018.11.011.

[21] P.F. Bernath, Spectra of Atoms and Molecules, Oxford University Press, 2020.

[22] J. Hodgkinson, R.P. Tatam, Optical gas sensing: a review, Meas. Sci. Technol. 24 (2012) 012004. https://doi.org/10.1088/0957-0233/24/1/012004.

[23] M. Metsälä, Optical techniques for breath analysis: from single to multi-species detection, J. Breath Res. 12 (2018) 027104. https://doi.org/10.1088/1752-7163/aa8a31.

[24] A. Parriaux, K. Hammani, C. Thomazo, O. Musset, G. Millot, Isotope ratio dual-comb spectrometer, Phys. Rev. Res. 4 (2022) 023098. https://doi.org/10.1103/PhysRevResearch.4.023098.

[25] J. Westberg, C.C. Teng, Y. Chen, J. Liu, L. Patrick, L. Shen, M. Soskind, G. Wysocki, Urban open-air chemical sensing using a mobile quantum cascade laser dual-comb spectrometer, APL Photonics 8 (2023) 120803. https://doi.org/10.1063/5.0163308.

[26] X. Zhu, J.M. Kahn, Free-space optical communication through atmospheric turbulence channels, IEEE Transactions on Communications 50 (2002) 1293–1300. https://doi.org/10.1109/TCOMM.2002.800829.

[27] A. Schliesser, N. Picqué, T.W. Hänsch, Mid-infrared frequency combs, Nature Photonics 6 (2012) 440–449. https://doi.org/10.1038/nphoton.2012.142.

[28] A. Rogalski, Infrared detectors: status and trends, Progress in Quantum Electronics 27 (2003) 59–210. https://doi.org/10.1016/S0079-6727(02)00024-1.

[29] T. Steinmetz, T. Wilken, C. Araujo-Hauck, R. Holzwarth, T.W. Hänsch, L. Pasquini, A. Manescau, S. D'Odorico, M.T. Murphy, T. Kentischer, W. Schmidt, T. Udem, Laser Frequency Combs for Astronomical Observations, Science 321 (2008) 1335–1337. https://doi.org/10.1126/science.1161030.

[30] J. Bland-Hawthorn, P. Kern, Astrophotonics: a new era for astronomical instruments, Opt. Express 17 (2009) 1880–1884. https://doi.org/10.1364/OE.17.001880.

[31] T. Popmintchev, M.-C. Chen, D. Popmintchev, P. Arpin, S. Brown, S. Ališauskas, G. Andriukaitis, T. Balčiunas, O.D. Mücke, A. Pugzlys, A. Baltuška, B. Shim, S.E. Schrauth, A. Gaeta, C. Hernández-García, L. Plaja, A. Becker, A. Jaron-Becker, M.M. Murnane, H.C. Kapteyn, Bright Coherent Ultrahigh Harmonics in the keV X-ray Regime from Mid-Infrared Femtosecond Lasers, Science 336 (2012) 1287–1291. https://doi.org/10.1126/science.1218497.

[32] S. Ghimire, D.A. Reis, High-harmonic generation from solids, Nature Physics 15 (2019) 10–16. https://doi.org/10.1038/s41567-018-0315-5.

[33] M. Vainio, L. Halonen, Mid-infrared optical parametric oscillators and frequency combs for molecular spectroscopy, Phys. Chem. Chem. Phys. 18 (2016) 4266–4294. https://doi.org/10.1039/C5CP07052J.

[34] B. Henderson, A. Khodabakhsh, M. Metsälä, I. Ventrillard, F.M. Schmidt, D. Romanini, G.A.D. Ritchie, S. te Lintel Hekkert, R. Briot, T. Risby, N. Marczin, F.J.M. Harren, S.M. Cristescu, Laser spectroscopy for breath analysis: towards clinical implementation, Appl. Phys. B 124 (2018) 161. https://doi.org/10.1007/s00340-018-7030-x.

[35] I. Pupeza, D. Sánchez, J. Zhang, N. Lilienfein, M. Seidel, N. Karpowicz, T. Paasch-Colberg, I. Znakovskaya, M. Pescher, W. Schweinberger, V. Pervak, E. Fill, O. Pronin, Z. Wei, F. Krausz, A. Apolonski, J. Biegert, High-power sub-two-cycle mid-infrared pulses at 100 MHz repetition rate, Nature Photonics 9 (2015) 721–724. https://doi.org/10.1038/nphoton.2015.179.

[36] G. Soboń, T. Martynkien, P. Mergo, L. Rutkowski, A. Foltynowicz, High-power frequency comb source tunable from 2.7 to 4.2 µm based on difference frequency generation pumped by an Yb-doped fiber laser, Opt. Lett. 42 (2017) 1748–1751. https://doi.org/10.1364/OL.42.001748.

[37] A.J. Lind, A. Kowligy, H. Timmers, F.C. Cruz, N. Nader, M.C. Silfies, T.K. Allison, S.A. Diddams, Mid-Infrared Frequency Comb Generation and Spectroscopy with Few-Cycle Pulses and $\chi(2)$ Nonlinear Optics, Phys. Rev. Lett. 124 (2020) 133904. https://doi.org/10.1103/PhysRevLett.124.133904.

[38] A. Hugi, G. Villares, S. Blaser, H.C. Liu, J. Faist, Mid-infrared frequency comb based on a quantum cascade laser, Nature 492 (2012) 229–233. https://doi.org/10.1038/nature11620.

[39] J. Faist, G. Villares, G. Scalari, M. Rösch, C. Bonzon, A. Hugi, M. Beck, Quantum Cascade Laser Frequency Combs, Nanophotonics 5 (2016) 272–291. https://doi.org/10.1515/nanoph-2016-0015.

[40] M. Razeghi, Q. Lu, D. Wu, S. Slivken, Review of high power frequency comb sources based on InP: from MIR to THz at CQD, in: Terahertz Emitters, Receivers, and Applications IX, SPIE, 2018: pp. 21–30. https://doi.org/10.1117/12.2326358.

[41] M. Yu, Y. Okawachi, A.G. Griffith, N. Picqué, M. Lipson, A.L. Gaeta, Silicon-chip-based mid-infrared dual-comb spectroscopy, Nat Commun 9 (2018) 1869. https://doi.org/10.1038/s41467-018-04350-1.

[42] D. Grassani, E. Tagkoudi, H. Guo, C. Herkommer, F. Yang, T.J. Kippenberg, C.-S. Brès, Mid infrared gas spectroscopy using efficient fiber laser driven photonic chip-based supercontinuum, Nature Communications 10 (2019) 1553. https://doi.org/10.1038/s41467-019-09590-3.

[43] H. Guo, H. Guo, W. Weng, J. Liu, F. Yang, W. Hänsel, C.S. Brès, L. Thévenaz, R. Holzwarth, T.J. Kippenberg, Nanophotonic supercontinuum-based mid-infrared dual-comb spectroscopy, Optica 7 (2020) 1181–1188. https://doi.org/10.1364/OPTICA.396542.

[44] S. Vasilyev, V. Smolski, J. Peppers, I. Moskalev, M. Mirov, Y. Barnakov, S. Mirov, S. Mirov, V. Gapontsev, Middle-IR frequency comb based on Cr:ZnS laser, Opt. Express 27 (2019) 35079–35087. https://doi.org/10.1364/OE.27.035079.

[45] F. Adler, K.C. Cossel, M.J. Thorpe, I. Hartl, M.E. Fermann, J. Ye, Phase-stabilized, 1.5 W frequency comb at 2.8–4.8 μm, Opt. Lett. 34 (2009) 1330–1332. https://doi.org/10.1364/OL.34.001330.

[46] Y. Kobayashi, K. Torizuka, A. Marandi, R.L. Byer, R.A. McCracken, Z. Zhang, D.T. Reid, Femtosecond optical parametric oscillator frequency combs, J. Opt. 17 (2015) 094010. https://doi.org/10.1088/2040-8978/17/9/094010.

[47] L. Maidment, P.G. Schunemann, D.T. Reid, Molecular fingerprint-region spectroscopy from 5 to 12 μm using an orientation-patterned gallium phosphide optical parametric oscillator, Opt. Lett. 41 (2016) 4261–4264. https://doi.org/10.1364/OL.41.004261.

[48] K. Iwakuni, G. Porat, T.Q. Bui, B.J. Bjork, S.B. Schoun, O.H. Heckl, M.E. Fermann, J. Ye, Phase-stabilized 100 mW frequency comb near 10 μm, Appl. Phys. B 124 (2018) 128. https://doi.org/10.1007/s00340-018-6996-8.

[49] C.F. O'Donnell, S.C. Kumar, P.G. Schunemann, M. Ebrahim-Zadeh, Femtosecond optical parametric oscillator continuously tunable across 3.6-8 μm based on orientation-patterned gallium phosphide, Opt. Lett. 44 (2019) 4570–4573. https://doi.org/10.1364/OL.44.004570.

[50] C. Ning, P. Liu, Y. Qin, Z. Zhang, Continuous wavelength tuning of nondegenerate femtosecond doubly resonant optical parametric oscillators, Opt. Lett. 45 (2020) 2551–2554. https://doi.org/10.1364/OL.390380.

[51] A. Marandi, K.A. Ingold, M. Jankowski, R.L. Byer, Cascaded half-harmonic generation of femtosecond frequency combs in the mid-infrared, Optica 3 (2016) 324–327. https://doi.org/10.1364/OPTICA.3.000324.

[52] E. Sorokin, A. Marandi, P.G. Schunemann, M.M. Fejer, R.L. Byer, I.T. Sorokina, Efficient half-harmonic generation of three-optical-cycle mid-IR frequency comb around 4 μm using OP-GaP, Opt. Express 26 (2018) 9963–9971. https://doi.org/10.1364/OE.26.009963.

[53] Q. Ru, T. Kawamori, P.G. Schunemann, S. Vasilyev, S.B. Mirov, S.B. Mirov, K.L. Vodopyanov, Two-octave-wide (3–12 μm) subharmonic produced in a minimally dispersive optical parametric oscillator cavity, Opt. Lett. 46 (2021) 709–712. https://doi.org/10.1364/OL.403910.

[54] R.A. McCracken, D.T. Reid, Few-cycle near-infrared pulses from a degenerate 1 GHz optical parametric oscillator, Opt. Lett. 40 (2015) 4102–4105. https://doi.org/10.1364/OL.40.004102.

[55] R.A. McCracken, Y.S. Cheng, D.T. Reid, 10-GHz Femtosecond Degenerate Optical Parametric Oscillator, in: Conference on Lasers and Electro-Optics, 2018: p. FTh1M.1. https://doi.org/10.1364/CLEO_QELS.2018.FTh1M.1.

[56] A. Marandi, N.C. Leindecker, V. Pervak, R.L. Byer, K.L. Vodopyanov, Coherence properties of a broadband femtosecond mid-IR optical parametric oscillator operating at degeneracy, Opt. Express 20 (2012) 7255–7262. https://doi.org/10.1364/OE.20.007255.

[57] A. Roy, R. Nehra, S. Jahani, L. Ledezma, C. Langrock, M. Fejer, A. Marandi, Temporal walk-off induced dissipative quadratic solitons, Nat. Photon. 16 (2022) 162–168. https://doi.org/10.1038/s41566-021-00942-4.

[58] A.W. Bruch, X. Liu, Z. Gong, J.B. Surya, M. Li, C.-L. Zou, H.X. Tang, Pockels soliton microcomb, Nature Photonics 15 (2021) 21–27. https://doi.org/10.1038/s41566-020-00704-8.

[59] S. Akhmanov, A. Chirkin, K. Drabovich, A. Kovrigin, R. Khokhlov, A. Sukhorukov, Nonstationary nonlinear optical effects and ultrashort light pulse formation, IEEE Journal of Quantum Electronics 4 (1968) 598–605. https://doi.org/10.1109/JQE.1968.1074933.

[60] S. Trillo, Bright and dark simultons in second-harmonic generation, Opt. Lett. 21 (1996) 1111–1113. https://doi.org/10.1364/OL.21.001111.

[61] R. Hamerly, A. Marandi, M. Jankowski, M.M. Fejer, Y. Yamamoto, H. Mabuchi, Reduced models and design principles for half-harmonic generation in synchronously pumped optical parametric oscillators, Phys. Rev. A 94 (2016) 063809. https://doi.org/10.1103/PhysRevA.94.063809.

[62] M. Jankowski, A. Marandi, C.R. Phillips, R. Hamerly, K.A. Ingold, R.L. Byer, M.M. Fejer, Temporal Simultons in Optical Parametric Oscillators, Phys. Rev. Lett. 120 (2018) 053904. https://doi.org/10.1103/PhysRevLett.120.053904.

[63] L. Ledezma, R. Sekine, Q. Guo, R. Nehra, S. Jahani, A. Marandi, Intense optical parametric amplification in dispersion-engineered nanophotonic lithium niobate waveguides, Optica 9 (2022) 303–308. https://doi.org/10.1364/OPTICA.442332.

[64] J. Wei, J.M. Murray, J.O. Barnes, D.M. Krein, P.G. Schunemann, S. Guha, Temperature dependent Sellmeier equation for the refractive index of GaP, Opt. Mater. Express 8 (2018) 485–490. https://doi.org/10.1364/OME.8.000485.

[65] I.E. Gordon, L.S. Rothman, R.J. Hargreaves, R. Hashemi, E.V. Karlovets, F.M. Skinner, E.K. Conway, C. Hill, R.V. Kochanov, Y. Tan, P. Wcisło, A.A. Finenko, K.

Nelson, P.F. Bernath, M. Birk, V. Boudon, A. Campargue, K.V. Chance, A. Coustenis, B.J. Drouin, J. –M. Flaud, R.R. Gamache, J.T. Hodges, D. Jacquemart, E.J. Mlawer, A.V. Nikitin, V.I. Perevalov, M. Rotger, J. Tennyson, G.C. Toon, H. Tran, V.G. Tyuterev, E.M. Adkins, A. Baker, A. Barbe, E. Canè, A.G. Császár, A. Dudaryonok, O. Egorov, A.J. Fleisher, H. Fleurbaey, A. Foltynowicz, T. Furtenbacher, J.J. Harrison, J. –M. Hartmann, V. –M. Horneman, X. Huang, T. Karman, J. Karns, S. Kassi, I. Kleiner, V. Kofman, F. Kwabia–Tchana, N.N. Lavrentieva, T.J. Lee, D.A. Long, A.A. Lukashevskaya, O.M. Lyulin, V.Yu. Makhnev, W. Matt, S.T. Massie, M. Melosso, S.N. Mikhailenko, D. Mondelain, H.S.P. Müller, O.V. Naumenko, A. Perrin, O.L. Polyansky, E. Raddaoui, P.L. Raston, Z.D. Reed, M. Rey, C. Richard, R. Tóbiás, I. Sadiek, D.W. Schwenke, E. Starikova, K. Sung, F. Tamassia, S.A. Tashkun, J. Vander Auwera, I.A. Vasilenko, A.A. Vigasin, G.L. Villanueva, B. Vispoel, G. Wagner, A. Yachmenev, S.N. Yurchenko, The HITRAN2020 molecular spectroscopic database, Journal of Quantitative Spectroscopy and Radiative Transfer 277 (2022) 107949. https://doi.org/10.1016/j.jqsrt.2021.107949.

[66] L. Maidment, O. Kara, P.G. Schunemann, J. Piper, K. McEwan, D.T. Reid, Long-wave infrared generation from femtosecond and picosecond optical parametric oscillators based on orientation-patterned gallium phosphide, Appl. Phys. B 124 (2018) 143. https://doi.org/10.1007/s00340-018-7001-2.

[67] A.V. Muraviev, V.O. Smolski, Z.E. Loparo, K.L. Vodopyanov, Massively parallel sensing of trace molecules and their isotopologues with broadband subharmonic mid-infrared frequency combs, Nature Photonics 12 (2018) 209–214. https://doi.org/10.1038/s41566-018-0135-2.

[68] M. Liu, R.M. Gray, A. Roy, C.R. Markus, A. Marandi, Mid-Infrared Cross-Comb Spectroscopy, arXiv:2107.08333 [Physics] (2021). http://arxiv.org/abs/2107.08333 (accessed August 8, 2021).

[69] C. Wan, P. Li, A. Ruehl, I. Hartl, Coherent frequency division with a degenerate synchronously pumped optical parametric oscillator, Opt. Lett., OL 43 (2018) 1059–1062. https://doi.org/10.1364/OL.43.001059.

[70] M. Jankowski, N. Jornod, C. Langrock, B. Desiatov, A. Marandi, M. Lončar, M.M. Fejer, Quasi-static optical parametric amplification, Optica 9 (2022) 273–279. https://doi.org/10.1364/OPTICA.442550.

[71] Q. Liang, Y.-C. Chan, P.B. Changala, D.J. Nesbitt, J. Ye, J. Toscano, Ultrasensitive multispecies spectroscopic breath analysis for real-time health monitoring and diagnostics, Proceedings of the National Academy of Sciences 118 (2021) e2105063118. https://doi.org/10.1073/pnas.2105063118.

[72] M. Jamrógiewicz, Application of the near-infrared spectroscopy in the pharmaceutical technology, Journal of Pharmaceutical and Biomedical Analysis 66 (2012) 1–10. https://doi.org/10.1016/j.jpba.2012.03.009.

[73] B. Nozière, M. Kalberer, M. Claeys, J. Allan, B. D'Anna, S. Decesari, E. Finessi, M. Glasius, I. Grgić, J.F. Hamilton, T. Hoffmann, Y. Iinuma, M. Jaoui, A. Kahnt, C.J. Kampf, I. Kourtchev, W. Maenhaut, N. Marsden, S. Saarikoski, J. Schnelle-Kreis, J.D. Surratt, S.

Szidat, R. Szmigielski, A. Wisthaler, The Molecular Identification of Organic Compounds in the Atmosphere: State of the Art and Challenges, Chem. Rev. 115 (2015) 3919–3983. https://doi.org/10.1021/cr5003485.

[74] G.A. West, J.J. Barrett, D.R. Siebert, K.V. Reddy, Photoacoustic spectroscopy, Review of Scientific Instruments 54 (1983) 797–817. https://doi.org/10.1063/1.1137483.

[75] C. Haisch, Photoacoustic spectroscopy for analytical measurements, Meas. Sci. Technol. 23 (2011) 012001. https://doi.org/10.1088/0957-0233/23/1/012001.

[76] R. Lewicki, J.H. Doty, R.F. Curl, F.K. Tittel, G. Wysocki, Ultrasensitive detection of nitric oxide at 5.33 μm by using external cavity quantum cascade laser-based Faraday rotation spectroscopy, Proceedings of the National Academy of Sciences 106 (2009) 12587–12592. https://doi.org/10.1073/pnas.0906291106.

[77] W. Zhao, G. Wysocki, W. Chen, E. Fertein, D.L. Coq, D. Petitprez, W. Zhang, Sensitive and selective detection of OH radicals using Faraday rotation spectroscopy at 2.8 μm, Opt. Express 19 (2011) 2493–2501. https://doi.org/10.1364/OE.19.002493.

[78] J.W. Daily, Laser induced fluorescence spectroscopy in flames, Progress in Energy and Combustion Science 23 (1997) 133–199. https://doi.org/10.1016/S0360-1285(97)00008-7.

[79] A.A. Lanin, A.A. Voronin, A.B. Fedotov, A.M. Zheltikov, Time-domain spectroscopy in the mid-infrared, Sci Rep 4 (2014) 6670. https://doi.org/10.1038/srep06670.

[80] A.A. Lanin, A.B. Fedotov, A.M. Zheltikov, Ultrabroadband XFROG of few-cycle mid-infrared pulses by four-wave mixing in a gas, J. Opt. Soc. Am. B 31 (2014) 1901. https://doi.org/10.1364/JOSAB.31.001901.

[81] H.U. Stauffer, S.W. Grib, S.A. Schumaker, S. Roy, Broadband, background-free methane absorption in the mid-infrared, Opt. Express 29 (2021) 21011. https://doi.org/10.1364/OE.430315.

[82] I. Pupeza, M. Huber, M. Trubetskov, W. Schweinberger, S.A. Hussain, C. Hofer, K. Fritsch, M. Poetzlberger, L. Vamos, E. Fill, T. Amotchkina, K.V. Kepesidis, A. Apolonski, N. Karpowicz, V. Pervak, O. Pronin, F. Fleischmann, A. Azzeer, M. Žigman, F. Krausz, Field-resolved infrared spectroscopy of biological systems, Nature 577 (2020) 52–59. https://doi.org/10.1038/s41586-019-1850-7.

[83] M. Liu, R.M. Gray, L. Costa, C.R. Markus, A. Roy, A. Marandi, Mid-infrared cross-comb spectroscopy, Nat Commun 14 (2023) 1044. https://doi.org/10.1038/s41467-023-36811-7.

[84] T. Tomberg, A. Muraviev, Q. Ru, K.L. Vodopyanov, Background-free broadband absorption spectroscopy based on interferometric suppression with a sign-inverted waveform, Optica 6 (2019) 147–151. https://doi.org/10.1364/OPTICA.6.000147.

[85] T. Buberl, P. Sulzer, A. Leitenstorfer, F. Krausz, I. Pupeza, Broadband interferometric subtraction of optical fields, Opt. Express 27 (2019) 2432–2443. https://doi.org/10.1364/OE.27.002432.

[86] W. Song, D. Okazaki, I. Morichika, S. Ashihara, Broadband background-free vibrational spectroscopy using a mode-locked Cr:ZnS laser, Opt. Express 30 (2022) 38674. https://doi.org/10.1364/OE.470893.

[87] T.T. Fricke, N.D. Smith-Lefebvre, R. Abbott, R. Adhikari, K.L. Dooley, M. Evans, P. Fritschel, V.V. Frolov, K. Kawabe, J.S. Kissel, B.J.J. Slagmolen, S.J. Waldman, DC readout experiment in Enhanced LIGO, Class. Quantum Grav. 29 (2012) 065005. https://doi.org/10.1088/0264-9381/29/6/065005.

[88] T.F. Zehnpfennig, O. Shepherd, S. Rappaport, W.P. Reidy, G. Vanasse, Background suppression in double-beam interferometry, Appl. Opt. 18 (1979) 1996–2002. https://doi.org/10.1364/AO.18.001996.

[89] Z. Guan, M. Lewander, S. Svanberg, Quasi zero-background tunable diode laser absorption spectroscopy employing a balanced Michelson interferometer, Opt. Express 16 (2008) 21714. https://doi.org/10.1364/OE.16.021714.

[90] J. Hayden, S. Hugger, F. Fuchs, B. Lendl, A quantum cascade laser-based Mach–Zehnder interferometer for chemical sensing employing molecular absorption and dispersion, Appl. Phys. B 124 (2018) 29. https://doi.org/10.1007/s00340-018-6899-8.

[91] A.S. Kowligy, H. Timmers, A.J. Lind, U. Elu, F.C. Cruz, P.G. Schunemann, J. Biegert, S.A. Diddams, Infrared electric field sampled frequency comb spectroscopy, Science Advances 5 (2019) eaaw8794. https://doi.org/10.1126/sciadv.aaw8794.

[92] M. Liu, R.M. Gray, A. Roy, K.A. Ingold, E. Sorokin, I. Sorokina, P.G. Schunemann, A. Marandi, High-Power Mid-IR Few-Cycle Frequency Comb from Quadratic Solitons in an Optical Parametric Oscillator, Laser & Photonics Reviews (2022) 2200453. https://doi.org/10.1002/lpor.202200453.

[93] J. Zhang, C. Ning, J. Heng, S. Yu, Z. Zhang, Ultra-Short Pulse Generation From Optical Parametric Oscillators With a Cavity-Length Detuning, IEEE Photonics Technology Letters 34 (2022) 263–266. https://doi.org/10.1109/LPT.2022.3149528.

[94] H. Harde, S. Keiding, D. Grischkowsky, THz commensurate echoes: Periodic rephasing of molecular transitions in free-induction decay, Phys. Rev. Lett. 66 (1991) 1834–1837. https://doi.org/10.1103/PhysRevLett.66.1834.

[95] I. Coddington, W.C. Swann, N.R. Newbury, Time-domain spectroscopy of molecular free-induction decay in the infrared, Opt. Lett. 35 (2010) 1395–1397. https://doi.org/10.1364/OL.35.001395.

[96] N.R. Newbury, I. Coddington, W. Swann, Sensitivity of coherent dual-comb spectroscopy, Opt. Express 18 (2010) 7929–7945. https://doi.org/10.1364/OE.18.007929.

[97] J. Zhang, A.P. Shreenath, M. Kimmel, E. Zeek, R. Trebino, S. Link, Measurement of the intensity and phase of attojoule femtosecond light pulses using Optical-Parametric-

Amplification Cross-Correlation Frequency-Resolved Optical Gating, Opt. Express 11 (2003) 601–609. https://doi.org/10.1364/OE.11.000601.

[98] P.M. Vaughan, R. Trebino, Optical-parametric-amplification imaging of complex objects, Opt. Express 19 (2011) 8920–8929. https://doi.org/10.1364/OE.19.008920.

[99] E. Mimoun, L. De Sarlo, J.-J. Zondy, J. Dalibard, F. Gerbier, Sum-frequency generation of 589 nm light with near-unit efficiency, Opt. Express 16 (2008) 18684. https://doi.org/10.1364/OE.16.018684.

[100] A. Roy, L. Ledezma, L. Costa, R. Gray, R. Sekine, Q. Guo, M. Liu, R.M. Briggs, A. Marandi, Visible-to-mid-IR tunable frequency comb in nanophotonics, Nat Commun 14 (2023) 6549. https://doi.org/10.1038/s41467-023-42289-0.

[101] H. Timmers, A. Kowligy, A. Lind, F.C. Cruz, N. Nader, M. Silfies, G. Ycas, T.K. Allison, P.G. Schunemann, S.B. Papp, S.A. Diddams, Molecular fingerprinting with bright, broadband infrared frequency combs, Optica 5 (2018) 727–732. https://doi.org/10.1364/OPTICA.5.000727.

[102] G. Ycas, F.R. Giorgetta, E. Baumann, I. Coddington, D. Herman, S.A. Diddams, N.R. Newbury, High-coherence mid-infrared dual-comb spectroscopy spanning 2.6 to 5.2 μm, Nature Photonics 12 (2018) 202–208. https://doi.org/10.1038/s41566-018-0114-7.

[103] Z. Chen, T.W. Hänsch, N. Picqué, Mid-infrared feed-forward dual-comb spectroscopy, PNAS 116 (2019) 3454–3459. https://doi.org/10.1073/pnas.1819082116.

[104] G. Villares, A. Hugi, S. Blaser, J. Faist, Dual-comb spectroscopy based on quantum-cascade-laser frequency combs, Nature Communications 5 (2014) 5192. https://doi.org/10.1038/ncomms6192.

[105] R.A. Stead, A.K. Mills, D.J. Jones, Method for high resolution and wideband spectroscopy in the terahertz and far-infrared region, J. Opt. Soc. Am. B 29 (2012) 2861–2868. https://doi.org/10.1364/JOSAB.29.002861.

[106] C. Riek, D.V. Seletskiy, A.S. Moskalenko, J.F. Schmidt, P. Krauspe, S. Eckart, S. Eggert, G. Burkard, A. Leitenstorfer, Direct sampling of electric-field vacuum fluctuations, Science 350 (2015) 420–423. https://doi.org/10.1126/science.aac9788.

[107] S. Ahmed, J. Savolainen, P. Hamm, Detectivity enhancement in THz electrooptical sampling, Review of Scientific Instruments 85 (2014) 013114. https://doi.org/10.1063/1.4862657.

[108] M. Porer, J.-M. Ménard, R. Huber, Shot noise reduced terahertz detection via spectrally postfiltered electro-optic sampling, Opt. Lett., OL 39 (2014) 2435–2438. https://doi.org/10.1364/OL.39.002435.

[109] Z. Chen, T.W. Hänsch, N. Picqué, Upconversion mid-infrared dual-comb spectroscopy, arXiv:2003.06930 [Physics] (2020). http://arxiv.org/abs/2003.06930 (accessed May 18, 2020).

[110] S. Yokoyama, T. Yokoyama, Y. Hagihara, T. Araki, T. Yasui, A distance meter using a terahertz intermode beat in an optical frequency comb, Opt. Express 17 (2009) 17324–17337. https://doi.org/10.1364/OE.17.017324.

[111] M. Huber, M. Trubetskov, S.A. Hussain, W. Schweinberger, C. Hofer, I. Pupeza, Optimum Sample Thickness for Trace Analyte Detection with Field-Resolved Infrared Spectroscopy, Anal. Chem. 92 (2020) 7508–7514. https://doi.org/10.1021/acs.analchem.9b05744.

[112] R. Trebino, Frequency-Resolved Optical Gating: The Measurement of Ultrashort Laser Pulses: The Measurement of Ultrashort Laser Pulses, Springer Science & Business Media, 2000.

[113] A. Fathy, Y.M. Sabry, I.W. Hunter, D. Khalil, T. Bourouina, Direct Absorption and Photoacoustic Spectroscopy for Gas Sensing and Analysis: A Critical Review, Laser & Photonics Reviews n/a (n.d.) 2100556. https://doi.org/10.1002/lpor.202100556.

[114] A. Weiner, Ultrafast Optics, John Wiley & Sons, 2011.

[115] R.W. Boyd, Nonlinear Optics, Elsevier, 2008.

[116] I. Coddington, W.C. Swann, N.R. Newbury, Coherent dual-comb spectroscopy at high signal-to-noise ratio, Phys. Rev. A 82 (2010) 043817. https://doi.org/10.1103/PhysRevA.82.043817.

[117] I.E. Gordon, L.S. Rothman, C. Hill, R.V. Kochanov, Y. Tan, P.F. Bernath, M. Birk, V. Boudon, A. Campargue, K.V. Chance, B.J. Drouin, J.-M. Flaud, R.R. Gamache, J.T. Hodges, D. Jacquemart, V.I. Perevalov, A. Perrin, K.P. Shine, M.-A.H. Smith, J. Tennyson, G.C. Toon, H. Tran, V.G. Tyuterev, A. Barbe, A.G. Császár, V.M. Devi, T. Furtenbacher, J.J. Harrison, J.-M. Hartmann, A. Jolly, T.J. Johnson, T. Karman, I. Kleiner, A.A. Kyuberis, J. Loos, O.M. Lyulin, S.T. Massie, S.N. Mikhailenko, N. Moazzen-Ahmadi, H.S.P. Müller, O.V. Naumenko, A.V. Nikitin, O.L. Polyansky, M. Rey, M. Rotger, S.W. Sharpe, K. Sung, E. Starikova, S.A. Tashkun, J.V. Auwera, G. Wagner, J. Wilzewski, P. Wcisło, S. Yu, E.J. Zak, The HITRAN2016 molecular spectroscopic database, Journal of Quantitative Spectroscopy and Radiative Transfer 203 (2017) 3–69. https://doi.org/10.1016/j.jqsrt.2017.06.038.

[118] Z. Zhu, K. Ni, Q. Zhou, G. Wu, Digital correction method for realizing a phase-stable dual-comb interferometer, Opt. Express 26 (2018) 16813. https://doi.org/10.1364/OE.26.016813.

[119] I. Coddington, W.C. Swann, N.R. Newbury, Coherent Multiheterodyne Spectroscopy Using Stabilized Optical Frequency Combs, Phys. Rev. Lett. 100 (2008) 013902. https://doi.org/10.1103/PhysRevLett.100.013902.

[120] T. Ideguchi, A. Poisson, G. Guelachvili, N. Picqué, T.W. Hänsch, Adaptive real-time dual-comb spectroscopy, Nature Communications 5 (2014) 3375. https://doi.org/10.1038/ncomms4375.

[121] J.-D. Deschênes, P. Giaccari, J. Genest, Optical referencing technique with CW lasers as intermediate oscillators for continuous full delay range frequency comb

interferometry, Opt. Express, OE 18 (2010) 23358–23370. https://doi.org/10.1364/OE.18.023358.

[122] J. Roy, J.-D. Deschênes, S. Potvin, J. Genest, Continuous real-time correction and averaging for frequency comb interferometry, Opt. Express 20 (2012) 21932–21939. https://doi.org/10.1364/OE.20.021932.

[123] D. Zhu, L. Shao, M. Yu, R. Cheng, B. Desiatov, C.J. Xin, Y. Hu, J. Holzgrafe, S. Ghosh, A. Shams-Ansari, E. Puma, N. Sinclair, N. Sinclair, C. Reimer, M. Zhang, M. Lončar, M. Lončar, Integrated photonics on thin-film lithium niobate, Adv. Opt. Photon. 13 (2021) 242–352. https://doi.org/10.1364/AOP.411024.

[124] G. Chen, N. Li, J.D. Ng, H.-L. Lin, Y. Zhou, Y.H. Fu, L.Y.T. Lee, Y. Yu, A.-Q. Liu, A.J. Danner, Advances in lithium niobate photonics: development status and perspectives, Adv. Photonics 4 (2022) 034003. https://doi.org/10.1117/1.AP.4.3.034003.

[125] A. Roy, L. Ledezma, L. Costa, R. Gray, R. Sekine, Q. Guo, M. Liu, R.M. Briggs, A. Marandi, Tunable mid-infrared frequency combs from nanophotonic parametric oscillators, in: Conference on Lasers and Electro-Optics, 2022: p. JTh6B.6.

[126] L. Ledezma, A. Roy, L. Costa, R. Sekine, R. Gray, Q. Guo, R. Nehra, R.M. Briggs, A. Marandi, Widely-tunable optical parametric oscillator in lithium niobate nanophotonics, (2022). https://doi.org/10.48550/arXiv.2203.11482.

[127] C. Wang, C. Langrock, A. Marandi, M. Jankowski, M. Zhang, B. Desiatov, M.M. Fejer, M. Lončar, Ultrahigh-efficiency wavelength conversion in nanophotonic periodically poled lithium niobate waveguides, Optica 5 (2018) 1438–1441. https://doi.org/10.1364/OPTICA.5.001438.

[128] M. Jankowski, C. Langrock, B. Desiatov, A. Marandi, C. Wang, M. Zhang, C.R. Phillips, M. Lončar, M.M. Fejer, Ultrabroadband nonlinear optics in nanophotonic periodically poled lithium niobate waveguides, Optica 7 (2020) 40–46. https://doi.org/10.1364/OPTICA.7.000040.

[129] M. Yu, B. Desiatov, Y. Okawachi, A.L. Gaeta, M. Lončar, Coherent two-octave-spanning supercontinuum generation in lithium-niobate waveguides, Opt. Lett. 44 (2019) 1222–1225. https://doi.org/10.1364/OL.44.001222.

[130] J. Lu, J.B. Surya, X. Liu, Y. Xu, H.X. Tang, Octave-spanning supercontinuum generation in nanoscale lithium niobate waveguides, Opt. Lett. 44 (2019) 1492. https://doi.org/10.1364/OL.44.001492.

[131] T.-H. Wu, L. Ledezma, C. Fredrick, P. Sekhar, Q. Guo, R. Briggs, A. Marandi, S.A. Diddams, Ultraviolet to Near-infrared Frequency Comb Generation in Lithium Niobate Nanophotonic Waveguides with Chirped Poling, in: Conference on Lasers and Electro-Optics, 2022: p. FW4J.2.